



HAL
open science

Multi-modal investigation of hygroscopic granular media at high relative humidity

Ilija Vego

► **To cite this version:**

Ilija Vego. Multi-modal investigation of hygroscopic granular media at high relative humidity. Solid mechanics [physics.class-ph]. Université Grenoble Alpes [2020-..], 2023. English. NNT : 2023GRALI017 . tel-04360890

HAL Id: tel-04360890

<https://theses.hal.science/tel-04360890v1>

Submitted on 22 Dec 2023

HAL is a multi-disciplinary open access archive for the deposit and dissemination of scientific research documents, whether they are published or not. The documents may come from teaching and research institutions in France or abroad, or from public or private research centers.

L'archive ouverte pluridisciplinaire **HAL**, est destinée au dépôt et à la diffusion de documents scientifiques de niveau recherche, publiés ou non, émanant des établissements d'enseignement et de recherche français ou étrangers, des laboratoires publics ou privés.

THÈSE

Pour obtenir le grade de

DOCTEUR DE L'UNIVERSITÉ GRENOBLE ALPES

École doctorale : I-MEP2 - Ingénierie - Matériaux, Mécanique, Environnement, Energétique, Procédés, Production

Spécialité : 2MGE : Matériaux, Mécanique, Génie civil, Electrochimie

Unité de recherche : Laboratoire Sols, Solides, Structures et Risques

Étude multimodale des milieux granulaires hygroscopiques à humidité relative élevée

Multi-modal investigation of hygroscopic granular media at high relative humidity

Présentée par :

Ilija VEGO

Direction de thèse :

Gioacchino VIGGIANI

Professeur, Université Grenoble Alpes

Directeur de thèse

Alessandro TENGATTINI

Maître de conférences, Université Grenoble Alpes

Co-encadrant de thèse

Edward ANDÒ

Principal scientist, Center for Imaging,

École Polytechnique Fédérale de Lausanne

Co-encadrant de thèse

Rapporteurs :

Emilien AZÉMA

Maître de conférences, University of Montpellier

José E. ANDRADE

Professeur, California Institute of Technology

Thèse soutenue publiquement le **31 mars 2023**, devant le jury composé de :

Gioacchino VIGGIANI

Professeur, Université Grenoble Alpes

Directeur de thèse

Gaël COMBE

Professeur, Université Grenoble Alpes

Président

Emilien AZÉMA

Maître de conférences, University of Montpellier

Rapporteur

José E. ANDRADE

Professeur, California Institute of Technology

Rapporteur

Karen E. DANIELS

Professeur, North Carolina State University

Examinatrice

Invités :

Alessandro TENGATTINI

Maître de conférences, Université Grenoble Alpes

Edward ANDÒ

Principal scientist, Center for Imaging,

École Polytechnique Fédérale de Lausanne

Joshua A. DIJKSMAN

Professeur, Universiteit van Amsterdam



Acknowledgements

First and foremost, I would like to deeply thank my supervisors, who inspired me to embark on this journey and whose guidance and support were fundamental throughout these years. I thank Eddy for his enthusiasm and advice. Many thanks to Cino for providing a safe place, but also for constantly encouraging and pushing me to do my best. I cannot thank enough Alessandro, the cornerstone of my PhD, for his patience, care, and honesty.

I sincerely express my gratitude to the reviewers and committee members, for their time, understanding and constructive feedback.

As a member of the Caliper team, I had the pleasure of meeting and working with an amazing and diverse group. Honourable mention to Joshua, a wonderful leader in such unexpected and unpredictable times.

I consider my two-months stay in the Netherlands the turning point of my PhD. I am grateful to Richard, Frank, John, and everyone in Wageningen.

I thank everyone at 3SR for their help and support. Despite the challenges of the past years, I was very lucky to meet such extraordinary people. I especially want to thank Vincent, Nicolas and Pascal, who were always there when help was needed.

While in Grenoble, I had the fortune to meet some of my dearest friends. Many thanks to Gustavo, my Samwise Gamgee during these last years. I thank Angela, who has been around since before the PhD and never left. I thank Edu, Laura and Marta, I will always cherish the laughter and the adventures we had and will have together.

Last but not least, I would like to thank the Vego team, from the ones who have been always there, to the newest members. I cannot express my gratitude for their love and support, no matter what I do, and how poorly I explain it. I am blessed to have you as my family.

Abstract in English

Water strongly influences the behaviour of granular media. However, a distinction can be made based on whether the particles themselves are water-sensitive. For granular assemblies composed of impermeable particles such as sand, the presence of water affects the effective stress and induce capillary forces. But there are many materials where the chemo-mechanical behaviour of the particles themselves mutates in contact with water. Some examples of water-sensitive particles are food, cereals, and pharmaceutical excipients. Namely, even a small increase of water-content can activate chemical reactions causing a relaxation of the polymer chains, and thus, for instance, an increase in size or a loss of mechanical properties of the material. This translates to phenomena observable at the particle scale such as swelling and closing of pores but also opening of fissures and debonding of layers, as well as to a reduction in mechanical properties. Collectively, these particle-scale phenomena lead to agglomeration, and loss of overall strength and granular flow properties. Their extent depends on the material, but affects numerous industrial applications including the processing, storage and transport of this ubiquitous class of materials, specifically in pharmaceutical and food industry. When these properties change to the point of altering product functionality a vast loss in resources generally ensues, which in turn raises important economical and ethical issues. Previous studies focused their attention on either the effect of the increase in water-content on the macroscopic response of several such materials, or, in some cases, on the properties of individual particles driving them. The connection between particle-scale and assembly-scale behaviours appears to be largely ignored in the literature, and is the main focus of this doctoral thesis. Specifically, we investigate the response under compression at high relative humidity (RH) of a widespread hygroscopic granular material: fine couscous. Its particle-scale processes are representative of several other water-sensitive materials and its size is ideal for several of particle-scale approaches employed here. When absorbing water, couscous particles swell, become more deformable, and agglomerate. We conduct this study through a combination of experimental approaches including individual particles mechanical testing, *in-operando* x-ray and neutron tomography, as well as time-domain nuclear magnetic resonance (TD-NMR), as detailed below. Particle-scale numerical approaches complement these observations to explore the role of quantities not directly measurable. We adopt x-ray tomography to characterise in 4D (3D+time) the evolving microstructure and quantify it through bespoke image analysis algorithms. We compare the swelling of each of thousands of individual particles to the volumetric response of their assembly and its porosity, revealing a competition between dilation and loss of mechanical properties. We measure the number, area and orientation of each granular contact and correlate it with both particle swelling and macroscopic boundary conditions. Neutron tomographies, acquired simultaneously to x-ray ones, allow for additionally measuring of the water-content inside each particle to reveal the connection with the kinematic response obtained from the x-rays. Swelling and sorption gradients across the sample are observed and quantified. The particle swelling and contact area growth are then related to the increase of water-content. TD-NMR provides direct insight in the polymer

relaxation process at the molecular scale and complements the neutron imaging information on the sorption rate of the particles. Coupled with x-ray tomography it confirms the swelling - water-content relation from neutron imaging. The results from these campaigns are complemented by other particle-scale mechanical tests. Finally, we develop a DEM (Discrete Element Method) numerical model with swelling particles, and evolving particle stiffness to describe the experimentally observed behaviour. This allows us to explore different boundary conditions but also to assess the role of quantities not directly measurable from the aforementioned experiments.

Résumé en Français

L'eau a une influence considérable sur le comportement des milieux granulaires. Si son rôle dans les systèmes imperméables (par exemple, les sables) est relativement bien compris, de nombreuses autres complexités peuvent survenir lorsque les particules individuelles sont directement affectées par la présence d'eau. Dans les matériaux hygroscopiques ou amorphes, une variation infime de la teneur en eau peut activer plusieurs phénomènes altérant la microstructure, les propriétés mécaniques et la réponse de l'assemblage. Les particules peuvent gonfler, perdre leurs propriétés mécaniques, libérer du mucilage ou de l'amidon. Phénomènes qui peuvent conduire à l'agglomération, à la création de fissures, à la réduction des propriétés d'écoulement granulaire. L'ampleur de ces phénomènes diffère d'un matériau à l'autre, mais conduit finalement à une altération des propriétés mécaniques. Dans l'industrie pharmaceutique et alimentaire en particulier, la capacité à maintenir une fonctionnalité constante d'un produit est essentielle, afin d'éviter d'importants problèmes économiques et éthiques. Malgré la fréquence et la pertinence de ces phénomènes, on en sait que très peu sur eux. Un certain nombre d'études se sont concentrées sur de nombreux matériaux et ont principalement étudié le comportement global de la masse ou les propriétés des particules individuelles. Ce travail de thèse vise à étudier le lien entre le comportement des particules et celui de l'assemblage, et il se préoccupe en particulier des relations entre la teneur en eau des particules et leurs réponses morphologique et mécanique. Une étude expérimentale, utilisant diverses techniques d'imagerie, est menée au moyen de la tomographie à rayons X, de la tomographie à neutrons combinée aux images à rayons X et de la résonance magnétique nucléaire (RMN), pour étudier le comportement d'un matériau granulaire hygroscopique : le couscous fin. Ce matériau "de référence" s'est révélé idéal pour son faible coût, le diamètre de ses particules (compatible avec les installations d'imagerie) et sa simplicité (par rapport au nombre et à la complexité des processus intervenant dans d'autres matériaux hygroscopiques). En absorbant de l'eau, les particules de couscous gonflent, deviennent plus déformables, augmentent les surfaces de contact et s'agglomèrent. Dans les expériences, les particules sont exposées à un environnement à forte humidité relative (HR) et des techniques non-destructives sont utilisées pour mesurer différentes propriétés dans le temps. Les tomographies à rayons X permettent d'étudier l'évolution de la microstructure et de quantifier la porosité, le volume des particules et de l'échantillon, et les zones de contact entre les particules. Le gonflement des particules est mis en relation avec la déformation volumétrique de l'échantillon, révélant une compétition entre l'inflation et le ramollissement des grains sur les changements de volume de l'assemblage. Le gonflement des particules et l'expansion de la surface de contact sont hétérogènes et sont fortement liés aux conditions de contrainte et d'humidité relative appliquées. Les tomographies simultanées aux neutrons et aux rayons X permettent de croiser les informations sur la microstructure à la distribution de l'eau dans l'échantillon. Les gradients de gonflement et de teneur en eau sont observés et quantifiés. Une relation entre la teneur en eau et le gonflement est alors établie. La RMN permet de quantifier le taux d'absorption avec une meilleure précision que les techniques aux rayons X ou aux neutrons. Ces résultats

donnent une indication directe de l'eau absorbée dans l'échantillon, et couplés à une campagne complémentaire de tomographie aux rayons X, permet l'établissement d'une relation gonflement-teneur en eau. Les expériences sont couplées à des essais mécaniques "classiques". Des compressions uniaxiales sur des particules isolées sont réalisés afin de quantifier la dépendance de la rigidité à la teneur en eau. Enfin, un modèle numérique DEM (Discrete Element Method) est développé pour simuler le comportement des particules qui gonflent et se ramollissent, et étudier le rôle de paramètres mécaniques à l'échelle des particules. Les données des campagnes expérimentales sont utilisées pour sa calibration, bien que ce ne soit pas l'objectif final de la modélisation numérique qui a été pensé pour aider à l'interprétation des mécanismes mis en oeuvre.

Contents

1	Introduction	1
1.1	<i>Water-sensitive</i> granular materials	1
1.1.1	Underlying phenomena	1
1.1.2	Particle-scale phenomena	4
	Morphology	5
	Mechanical properties	5
1.1.3	Mesoscopic- and macroscopic-scale response	6
1.1.4	Research interest	8
1.2	Objective of the thesis	9
1.3	Structure of the thesis	10
2	Materials, experimental techniques and apparatus	13
2.1	A reference water-sensitive granular material	13
2.1.1	What is couscous?	13
2.1.2	Why couscous?	14
2.2	Data acquisition techniques	14
2.2.1	Imaging: x-ray and neutron tomography	14
	Beam generation: x-ray and neutron sources	15
	Interaction with matter and attenuation	15
	Image acquisition: radiography and tomography	16
	Imaging setups	18
	X-ray + neutron tomography: recent applications	19
2.2.2	Time-domain Nuclear Magnetic Resonance (TD-NMR)	20
	Fundamentals	21
	NMR signal	21
	NMR equipment	22
	Applications	22
2.3	Experimental apparatus	23
2.3.1	Relative humidity control	23
	RH control with saturated saline solutions	24
	RH control unit from Wageningen University & Research	24
2.3.2	1D compression apparatus	26
	16mm oedometer - design	26
	7mm oedometer - design	26
	Experimental procedure	27
2.3.3	NMR-compatible measurement cell	27
	Experimental procedure	27

3	Data analysis approaches	29
3.1	Image analysis methods	29
3.1.1	Gray-value images and spurious fluctuations correction	29
3.1.2	Particle identification	30
3.1.3	Particle tracking	33
	Basics of Digital Volume Correlation	33
	Discrete DVC	35
3.1.4	Particle and assembly volumetric strain	35
3.1.5	Inter-particle contact detection, orientation and areas	37
3.1.6	Analysis of multi-modal images	38
	Multi-modal registration (MMR)	39
	Particle attenuation	41
3.2	TD-NMR relaxometry	41
3.2.1	FID-CPMG decay analysis	42
4	The effect of high RH on a network of water-sensitive particles (couscous)	45
4.1	Introduction	46
4.2	Experimental campaign	48
4.2.1	Material	48
4.2.2	Experimental conditions	48
4.2.3	Imaging setup	48
4.3	Image analysis: results and discussion	49
4.3.1	Raw grey-scale images	49
4.3.2	Macroscopic sample response	51
4.3.3	Particle-scale response	52
4.3.4	Inter-particle contacts analysis	54
4.4	Conclusions and perspectives	58
5	Heterogeneous swelling of couscous particles exposed to a high RH air	61
5.1	Introduction	63
5.2	Material and methods	64
5.2.1	Gravimetric assessment: experimental procedure	64
5.2.2	TD-NMR relaxometry	65
	Experimental procedure	65
	FID-CPMG decay acquisition	65
	FID-CPMG decay analysis	66
5.2.3	X-ray tomography	67
	Experimental procedure	67
	Imaging procedure	68
5.3	Results and discussion	68
5.3.1	Sorption isotherm	68
5.3.2	Water uptake and molecular mobility increase	68
	Vapour sorption mechanism	69
5.3.3	Particles identification	72
5.3.4	Sample- and particle-scale volumetric response	73
	Pressure induced heterogeneity	76
5.3.5	Free swelling and moisture content relation	77

5.4	Conclusions and perspectives	79
5.5	Appendix: Benchtop NMR experiments: effects of flow rate and RH on sorption	80
5.5.1	Conclusions	82
5.6	Appendix: Evolution of the size distribution with water sorption	82
5.6.1	Conclusions	83
6	The influence of water sorption on the microstructure of couscous	85
6.1	Introduction	86
6.2	Experimental study	89
6.2.1	Material choice: Couscous, a water-sensitive granular medium	89
6.2.2	Experimental procedure	89
	CCRH97-01: experimental procedure	90
	CCRH97-02: experimental procedure	90
	Neutron and x-ray tomographies	91
6.3	Image analysis: methods and results	92
6.3.1	Multi-modal registration and segmentation	92
6.3.2	Volumetric response	94
6.3.3	Water content and its effect on the microstructure	96
6.4	Conclusions and perspectives	103
7	Summary and discussion of the experimental results	105
7.1	Multi-modal investigation	105
7.1.1	X-ray tomography (XT)	106
	Advantages	106
	Disadvantages	106
7.1.2	TD-NMR and x-ray tomography (TD-NMR+XT)	106
	Advantages	107
	Disadvantages	107
7.1.3	Simultaneous neutron and x-ray tomography (NeT+XT)	107
	Advantages	107
	Disadvantages	107
7.2	Microstructure <i>vs.</i> water content	108
7.2.1	<i>Bound or unbound</i> water?	109
7.2.2	Particle <i>vs.</i> water content	109
7.2.3	Sample volumetric response <i>vs.</i> water content	112
7.2.4	Inter-particle contact areas <i>vs.</i> water content	114
7.3	Conclusions and perspectives	117
8	A basic DEM model for hygroscopic swelling particles	119
8.1	The model	120
	Water content increase	120
	Particle swelling	121
	Particle softening	121
	Inter-particle forces	122
8.2	Sensitivity analyses	122
8.2.1	Effect of vertical load	124
8.2.2	Effect of relative humidity	129

8.3	Summary and perspectives	131
9	Conclusions and perspectives	133
9.1	Summary and conclusions	133
9.2	Perspectives	136
A	Technical designs of the experimental apparatus	139
A.1	16 mm oedometer	139
A.2	7 mm oedometer	144
A.3	NMR compatible measurement cell	149
B	Couscous particle stiffness dependency on water content	151
B.1	Experimental procedure	151
B.1.1	Particle compression set-up	151
B.1.2	Sample preparation and test procedure	152
B.2	Results and discussion	154
B.2.1	Simple compression tests	154
B.2.2	Cyclic compression tests	155
B.3	Conclusions	156
	Bibliography	159

Chapter 1

Introduction

This chapter introduces the topic and objectives of this doctoral work. First, we define the category of granular materials of which this study aims to reveal and measure the hydro-mechanical behaviour. We illustrate the phenomena and processes that characterise *water-sensitive* granular materials, and then we present the research interest around them. We then discuss the objectives of this work and the structure of this dissertation.

1.1 *Water-sensitive* granular materials

The behaviour of materials can be strongly affected by the presence of water and granular materials are no exception. Being made of *particles* or *grains*, they are characterised by a high porosity, which facilitates the water uptake. Whether the particles are natural or artificial, their interaction with water can significantly alter the macroscopic response of the material. This can happen because of the effects of water pressure (effective stress), the formation of capillary bridges in partially saturated conditions, or chemical reactions that entail water molecules bonding and solvation.

This study specifically focuses on partially saturated media. There is however another distinction that should be made. Notably, the molecules constituting the *individual* particles can be either hydrophobic or hydrophilic.

The problem regarding the water interaction with hydrophobic particles is quite notorious and widespread. Being of interest in many fields, for example, in soil mechanics, this problem has been thoroughly studied in the last decades [FR93].

Granular materials composed of hydrophilic particles are also very common: cereals, pharmaceutical excipients, fertilisers, are but a few examples. Their behaviour is strongly influenced by the presence of water, as water sorption can alter the molecular structure, which translates to particle scale phenomena and ultimately affects the response at the scale of the product. To include the panoply of possible phenomena that characterise such materials, we define them here as *water-sensitive*. This category is directly related to food, pharmaceutical or chemical industry, which harvest, produce or supply essential goods for numerous anthropic activities. This is why it is essential to study and understand their behaviour.

1.1.1 Underlying phenomena

Obviously, the phenomena that characterise water-sensitive materials are driven by water sorption. In other words, the behaviour of such materials strongly depends on the amount of water entrapped by the particles molecules. The total amount of water in the system is often described in terms of *water content*, which expresses the quantity of water in a material.

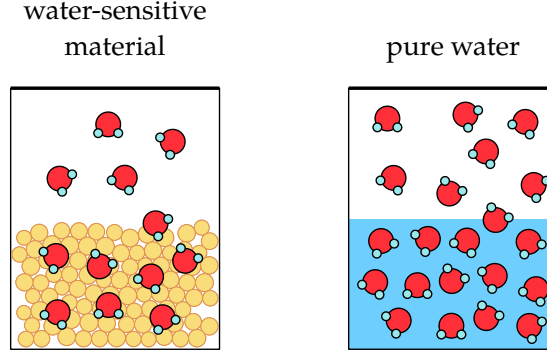


FIGURE 1.1: Water molecules exchange of water-sensitive materials and pure water with the outer environment.

This variable can be determined with respect to a dry basis or a wet basis. The dry basis water content $\omega_{d.b.}$ is measured as the ratio between the mass of water in the system m_{H_2O} and the dry mass m_{dry} :

$$\omega_{d.b.} = \frac{m_{H_2O}}{m_{dry}} \quad (1.1)$$

Conversely, the wet basis water content is defined as:

$$\omega_{w.b.} = \frac{m_{H_2O}}{m_{wet}} \quad (1.2)$$

where m_{wet} is simply the mass of the material and the mass of water. Usually the water mass in the system and the dry mass are determined by placing the material sample in an oven. Hereafter, unless specified, the “water content” term always refers to a dry basis water content.

The water content alone does not provide any information about the chemical state of water in the material. The water molecules can interact with the molecular matrix of the particles, or they can be entrapped, but they do not directly affect the particles properties. We define here these two different conditions of water as “bound” and “unbound” (or “free” water). It should be noted that the use of these terms is a matter of debate [Fen96; DP17], since it is difficult to define their borderline cases. The implications regarding this ill-defined concept are out of the scope of this doctoral work. Therefore, for sake of simplicity, herein we keep this definition.

Water-sensitive granular materials have the potential to entrap great amounts of water, either in liquid state or directly from air. This obviously raises significant issues in industry, where it is desirable to maintain a low water content of the product, to avoid degradation, deterioration of the material properties, and avoid environmental conditions in which microbes proliferate [Fen96; DP17].

In this study, we specifically focus on the water uptake of molecules from outer air, a circumstance rather difficult to prevent. The water content *per se* does not give any indication of the potential molecular interaction of the material with vapour in air. That is why the *water activity* a_w is often utilised to express this potential in food industry [Fen96; Sch04; DP17]:

$$a_w = \frac{n_{H_2O}}{n_{H_2O} + \sum n_{s,i}} \quad (1.3)$$

where n_{H_2O} indicates the molar concentration of water, and $n_{s,i}$ is the molar concentration in each solute i present in the material.

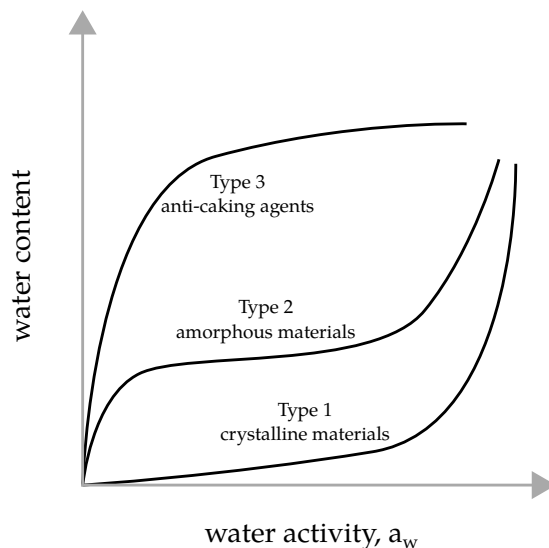


FIGURE 1.2: Schematic representation of the three types of moisture sorption isotherms commonly displayed by (food) materials; from Damodaran and Parkin [DP17].

However, it is generally rather difficult to measure the molar concentration in water-sensitive materials. Therefore, the water activity is often estimated as [Fen96; Sch04; DP17]:

$$a_w = \frac{p_v}{p_{v,H_2O}} \quad (1.4)$$

which is the ratio between the partial vapour pressure above the material p_v and the partial vapour pressure of pure water p_{v,H_2O} , under the assumption of constant temperature and pressure close to the atmospheric one [Fen96; DP17]. As illustrated in Figure 1.1, in a closed system both water-sensitive materials and pure water continuously exchange their water molecules with the surrounding environment. Nonetheless, the overall vapour pressure remains constant, which allows for determining the water activity by means of Equation 1.4. The ratio $p_v/p_{v,H_2O}$, known as *relative vapour pressure*, when in thermodynamic equilibrium, also describes the relative humidity (usually expressed as a percentage) [Fen96; Sch04; DP17]. It is by imposing a flow of higher relative humidity air flow through the sample, that we induce a mismatch in water activity and induce particles hydration, as detailed later and in Chapter 4, 5, and 6.

To describe the water activity of a material, it is common practice to acquire the *moisture sorption isotherm*, i.e., a plot describing the water content as a function of relative humidity at equilibrium [Lab75; Fen96; Lew00; Heb+03; Sch04; EEC05; DP17]. This curve can have different shapes, and they differ from material to material, as highlighted by Figure 1.2. It should be mentioned that the evolution of the isotherm is notably affected by temperature and pressure, and that an hysteresis is often observed when acquiring data in resorption and desorption [Lab75; Heb+03; EEC05; DP17].

At the molecular scale, the water uptake, although reversible, can cause structural changes of the molecular matrix of in water-sensitive materials.

In crystalline structures, e.g., sugar and salt, the solvent (water) can dissolve the material [DP17], a process that usually starts only for high values of water activity (see Figure 1.2, isotherm Type 1).

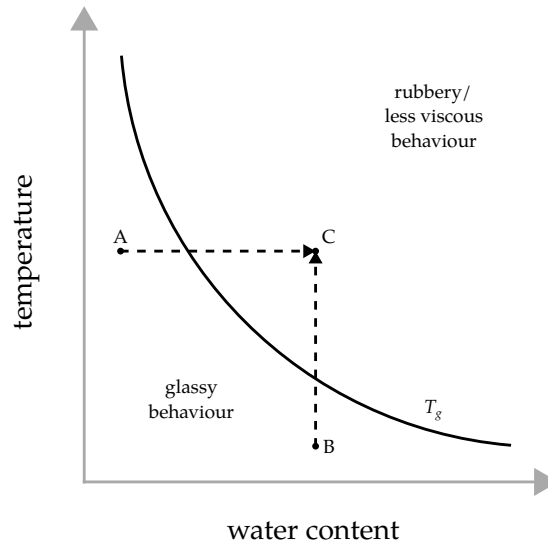


FIGURE 1.3: Hypothetical paths in the state diagram of a water-sensitive material. Upon increase of water content ($A \rightarrow C$) and constant temperature, the material trespasses the limit T_g between glassy and rubbery behaviour, and becomes less viscous. The same transition can occur for an increase of temperature and constant water content ($B \rightarrow C$); adapted from Labuza and Hyman [LH98]:

Conversely, the isotherm typical of amorphous materials (Type 2, Figure 1.2) is characterised by two inflection points, which in turn define three different material responses [Fen96; DP17]. Initially, the water molecules strongly bond with the external regions of the material, *i.e.*, molecules exposed to the outer environment. Then, the additional increase of water content decreases the viscosity of the material and causes swelling, which in turn exposes molecules previously not in direct contact with the outer environment. Finally, the strong final increase of water content further enhances the decrease of viscosity and the material starts flowing [DP17].

The shift of amorphous materials from a glassy behaviour to a rubbery/less viscous response is known as the *glass transition* phenomenon [Fen96; DP17; AVK95]. At relatively low temperatures and water contents, the material is in stable conditions, and the high viscosity allows to sustain its own microstructure. However, an increase of water content or temperature in the system can decrease the material viscosity, thus deteriorating its mechanical properties [AVK95]. The transition is often described by the glass transition temperature T_g , a limit below which the state of the material is glassy, and *vice-versa*, as illustrated in Figure 1.3.

1.1.2 Particle-scale phenomena

The aforementioned underlying phenomena characterising water-sensitive materials naturally affect the *individual* particles properties in granular systems. The water uptake causes significant changes in particle morphology and deterioration of mechanical properties, as detailed in the following paragraphs, which summarise some of the studies carried out to investigate the particle-scale phenomena of these materials.

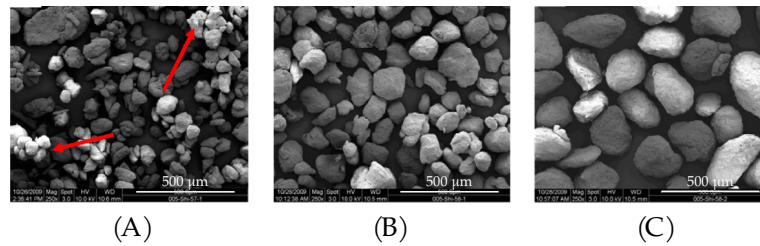


FIGURE 1.4: Evolution of microcrystalline cellulose (MCC) granule morphology with increasing initial moisture content of starting MCC and respective size distribution profiles. 0.9% (A), 7.2% (B), and 10.5% (C); from Shi, Feng, and Sun [SFS11].

Morphology

As mentioned, there are two main processes induced by water uptake that directly affect the morphology of individual particles: material solution and swelling.

The former usually involves crystalline molecular structures. However, restricting the investigation over one single particle, no significant morphology changes are usually measured, except for the possible deposition of solute in internal pores or cracks.

Conversely, the swelling of a particle is much simpler to determine (with the proper tools). For example, Morita *et al.* [MS79] have recorded that increasing the water content from 11% to 22% (wet basis), the length, width and thickness of the soft-rice grains increased respectively of 1.7%, 2.9% and 4.8%. Lentil seeds can also expand [AHR04]; lentils were found 5.73% larger and 13.76% thicker after an increase of water content from 10.3% to 21.0% (wet basis). Shi *et al.* [SFS11] investigated the microcrystalline cellulose granules size at different water content levels and measured an extreme dilation. The reference granular size d_{50} was initially $99.4 \mu\text{m}$ at almost dry conditions, then it increased to $140.9 \mu\text{m}$ and $292.7 \mu\text{m}$ for water contents equal to 7.2% and 10.5% (see Figure 1.4). The swelling of couscous was also investigated. The diameter increased with cooking time (increase of temperature) [BRC18], as well as under submerged conditions (increase of water content) [DR+22]. In submerged conditions, the swelling reached a plateau, after exhibiting a significant expansion in which the final diameter was equal to 1.6 times the initial one.

Mechanical properties

Another phenomenon characterising water-sensitive granular materials is the deterioration of mechanical properties with increasing water content. As detailed previously, the water content (or temperature) increase can shift the material response from glassy to rubbery and less viscous. This translates to measurable decrease of stiffness and strength of particles, as investigated by different studies.

For example, the dependency of wheat kernels strength and stiffness on water content was investigated. The experimental results indicate that the mechanical properties can decrease even down to 10% of their initial values in dry conditions [GYP91; Fig+11]. Figure 1.5 shows the evolution of the tangent modulus E of wheat with water content, as recorded by Glenn *et al.* [GYP91]. The tests were performed on small cylindrical samples extracted from 5 different types of wheat endosperm. For relatively low water contents, the E value remains relatively constant, as the sorption process is still in its initial stage. Later, for higher water content levels, the material becomes softer and softer. Similar mechanical responses were found for rice grains [Kam+02; Cao+04]. Additionally, Sharma *et al.* [SK82] investigated the effect of

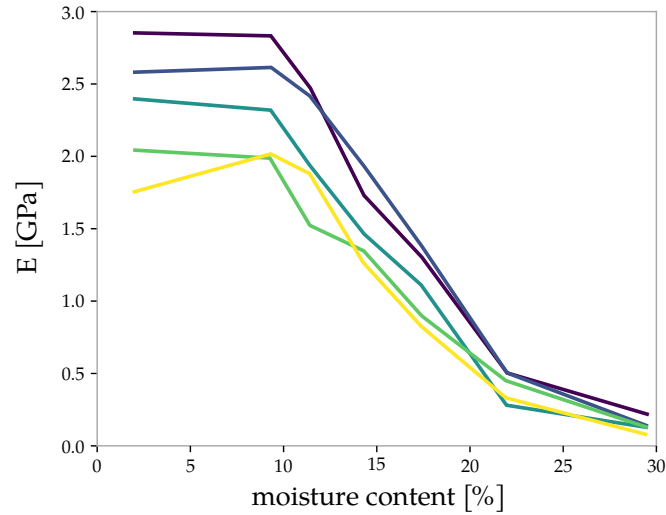


FIGURE 1.5: Tangent modulus of elasticity E of wheat endosperm plotted at moisture levels ranging from 2.0% to 29.6%. The E values decrease at moisture contents above 9.3% for five wheat varieties. Varietal differences in E values diminish with increasing moisture content; from Glenn, Younce, and Pitts [GYP91].

wetting and drying cycles on the structural integrity of rice kernels. It was shown that a higher water content can lead to higher amounts of fissured particles, an undesirable phenomenon in food processing.

Water-sensitive particles can also be the result of the agglomeration or compaction of smaller sized granules (*e.g.*, from microcrystalline cellulose to tablets [SFS11], from semolina to couscous [Abe+12; BRC18]). The initial water content of the prime raw material can also affect the final particle properties. For instance, the tensile strength of tables made of microcrystalline cellulose granules significantly decreases with water content [SFS11].

1.1.3 Mesoscopic- and macroscopic-scale response

The high complexity of water-sensitive materials comes from the inevitable interactions of many particles. The phenomena described in the previous sections may not be severe when only an individual particle is taken into account. On the contrary, the influence of sorption in water-sensitive granular assemblies can be significant. These problems are associated to the continuous and inevitable interaction of particles, and the phenomena characterising water-sensitive materials do nothing but add complexity to the problem.

As previously mentioned, the transition from glassy to less viscous state can induce the particle material to flow. In water-sensitive granular assemblies, this is often associated with agglomeration of particles. Lumps are created and the free flowing properties of the material are lessened [AVK95; Car+16; Zaf+17]. This phenomenon is known as *caking*, *i.e.*, the material shift from a free flowing behaviour to a solid-like behaviour. A proper definition of caking does not exist in literature, regardless, Aguilera *et al.* [AVK95] sought to describe its genesis, as detailed in the following paragraphs.

As shown in Figure 1.6, the material, at low water contents, is initially in *free flowing* conditions. Then, upon water content increase, the material can dissolve, and bridges are formed between the particles, adding overall cohesion to the system. This *bridging* phenomenon is

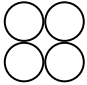
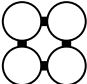
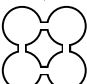

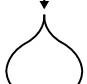
Stage	$\phi(t)/\phi_0$	$D_{bridge}/D_{particle}$	Morphology
Free flowing	1	0	
Bridging	$\rightarrow 1$	$\rightarrow 0$	
Agglomeration	< 1	> 0	
Compaction	$\rightarrow 0$	$\rightarrow 1$	
Liquefaction	0	1	

FIGURE 1.6: Stages during a typical caking process, indicating the changes in porosity ($\phi(t)/\phi_0$), the ratio of inter-particle bridge diameter to particle diameter ($D_{bridge}/D_{particle}$), and morphology at each stage; from Aguilera, Valle, and Karel [AVK95].

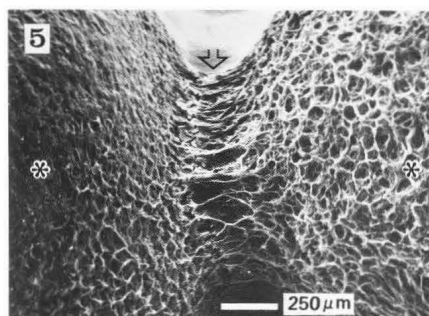


FIGURE 1.7: Mucilage cementing two yellow mustard seeds following their exposure to pure water for 4 h and drying; from Siddiqui *et al.* [Sid+86].

however relatively reversible. A mild shaking can in fact break the inter-particle bonds, (almost) reinstating the free flowing conditions. It should be noted that in case of bridging, the porosity of the system is essentially the same as in free flowing conditions, and the size of the bridge between the particles is null.

The following stage of caking is *agglomeration*, which stands out from bridging because of the irreversibility of the inter-particle bonds. The increase of water content decreases the viscosity of the material, which induces viscous flow between the particles, and with time can lead to particles *sintering* [Sid+86; Bik+05; Pal05; Fit+10; Zaf+17] (see Figure 1.7 and Figure 1.8). Despite the irreversibility of the process, the bulk properties of the material can be relatively similar to the free flowing configuration, and the bridge size is still relatively small.

The material can then undergo *compaction*. In presence of relatively high stresses, the porosity of the system reduces and the diameter of the bridges tends towards the particle diameter, which can indicate the definitive passage from granular/free flowing to solid-like behaviour. Naturally, the assembly compaction is enhanced by the deterioration of mechanical properties

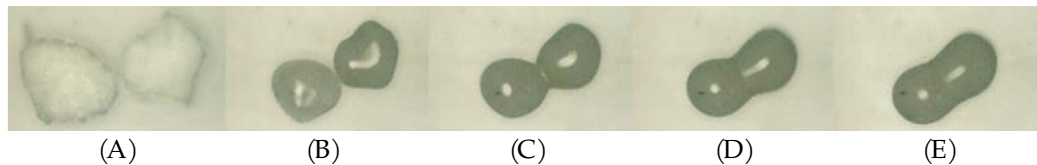


FIGURE 1.8: Sinter bridge formation between two maltodextrin particles when exposed to 76% RH and 25°C, when $t = 0 \text{ min}$ (A), 60 min (B), 90 min (C), 120 min (D), and 150 min (E); from Fitzpatrick *et al.* [Fit+10].

upon increase of water content.

Finally, the final and most extreme case of caking is *liquefaction*, due to extremely high water content and extensive viscous flow. The overall bulk porosity disappears and no more particles can be distinguished in the assembly.

All things considered, the caking phenomenon significantly affects the material response. Specifically, the generated lumps, or more generally, the particle agglomeration, reduce the free flowing properties. Notably, this is not a welcome phenomenon in industrial processing, where maintaining constant product functionality is a major concern [AVK95; Car+16; Zaf+17].

Different studies have focused the attention on the effects of water content on the flow properties of water-sensitive granular materials. For instance, Crouter *et al.* [CB14] investigated the effects of water content on the flowing properties of pharmaceutical excipients, by measuring the avalanche time (*i.e.*, time necessary to observe 128 avalanches in a drum rotating at 0.3 *rotation/min*) and found that the flow properties of microcrystalline cellulose, polyvinylpyrrolidone (PVP), hypromellose (HPMC), and potato starch generally decrease with water content. Conversely, the flowability of corn starch increased with water content, due to lubrication. In a similar test, the flow properties of lactose powder were measured to be lower at high relative humidity levels, as well as for very low levels, due to electrostatic interactions [Lum+16]. In another study, the flow properties of pectin, maltodextrin and modified starch tested powder flow tester revealed a decrease of flow properties with increasing water content [JE+17].

Recently, Brockbank *et al.* [BAC21] measured and quantified the caking extent in some excipients and food products, focusing the attention on the heterogeneity of the process and on the time factor. Cylindrical samples were exposed to different levels of relative humidity. Then, the energy required to break the particles bond with a twisted blade was measured. The authors found that the caking process is highly heterogeneous across the sample height, and that time plays a important role, as it can strongly influence the mechanical inter-particle bond strength.

In other studies, the response of the assembly has been investigated numerically, for different kind of materials, *e.g.*, sugars, fertilisers, super absorbent polymers [Chr+06; Wah+08; Swe+17].

1.1.4 Research interest

The chemo-hydro-mechanical coupling that characterises water-sensitive granular materials makes their investigation and understanding rather cumbersome. On top of that, the number of materials that could be defined as such is quite large and growing. Moreover, each of these materials can be considered as unique, because of its use, the peculiar properties and response, or its origin. Precisely for these reasons, the interest around this class of material is very high.

As mentioned earlier, the harvest, processing, storage and manufacture of materials such as cereals, pharmaceutical excipients and tablets, constitute a large share of anthropic activities, thus, it is fundamental to optimise their production. Studies have reported that inefficiencies in the supply chain can lead to enormous resource loss, sometimes up to 50 % of the product [RW09; Cha+21]. This obviously raises serious economical issues, but most importantly sustainability and ethical issues. One of the major causes of resource waste is the material exposure to water, which entails all the phenomena and processes described above.

Despite the problematic importance and its daily-occurrence, our knowledge of the fundamental behaviour of water-sensitive granular materials is limited. Many studies have focused on the underlying phenomena such as the chemical interactions of such materials with water, on the behaviour of individual particles, or the macroscopic response of the bulk.

Only a few studies have investigated the multi-scale correlation of these phenomena. For example, Wahl *et al.* [Wah+08] carried out an experimental and numerical study which aimed to predict the caking strength of an assembly of urea prills particles (a fertiliser). The bridging and agglomeration processes were measured from optical images. These measurements were complemented with mechanical tensile tests. Then, a contact-dynamics model was implemented numerically, so to estimate the overall strength of an assembly of such particles.

Another example is the study by Haider *et al.* [Hai+14], in which they explored the effects of temperature on the inter-particle contact morphology and mechanical properties in maize starch.

Altogether, our knowledge about the problem is still limited. It is therefore necessary to understand the fundamental behaviour of such materials. Back in 1995, Aguilera *et al.* [AVK95] suggested that the analysis of the microstructure and of images would be beneficial for this scope. Nevertheless, more recent reviews on the caking phenomenon concluded that this goal has not been achieved yet, and what is specifically lacking is a multi-scale characterisation of the phenomenon, from molecular to macroscopic scale [FA05; Car+16; Zaf+17]:

“To successfully predict caking propensity it is vital that the underlying mechanisms that are driving the change are understood and to do this it is critical that the single particle behaviour is understood and linked to the bulk material.” – Zafar *et al.* [Zaf+17].

1.2 Objective of the thesis

The objective of this doctoral work is to experimentally characterise the hydromechanical behaviour of water-sensitive granular materials. In particular, we focus on the relation between the individual response of thousands of particles and the overall response of the assembly, due to the rather limited knowledge of the problem and the need for such studies, as stated by recent reviews on the caking phenomenon [Car+16; Zaf+17].

To achieve this goal, we first select a representative water-sensitive granular material for our experiments, as detailed in Chapter 2. We then carry out different experimental campaigns in which we use different techniques, in order to acquire data about the microstructure of the selected material, from particle- to assembly-scale, but also to quantify the water uptake and the related molecular relaxation. In particular, we investigate the effects of high relative humidity, to mimic a realistic scenario that could be found during product storage.

As highlighted in Figure 1.9, three different techniques are employed in this study:

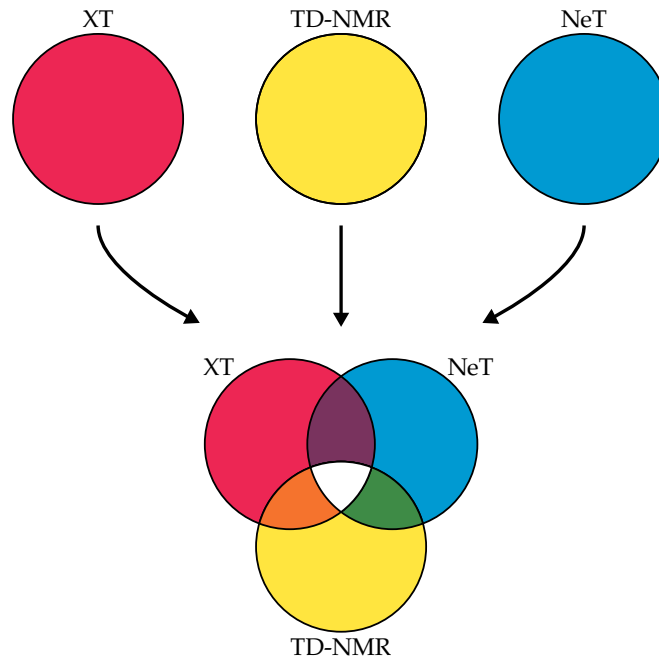


FIGURE 1.9: Multi-modal investigation deployed in this study to investigate the behaviour of water-sensitive granular materials. Data are acquired using and combining three different techniques: x-ray tomography (XT), neutron tomography (NeT), and time-domain nuclear magnetic resonance (TD-NMR).

- *x-ray tomography*: to measure the effects of water content on the microstructure of the assemblies;
- *neutron tomography*: to investigate the water content distribution in the samples;
- *time-domain nuclear magnetic resonance*: to quantify the sorption rate and observe the associated molecular relaxation of the particles.

Combining these techniques whenever possible, we aim to explore the relation between microstructural changes and the water uptake of water-sensitive particles. Attention is paid to the particle morphological changes, the inter-particle contact network evolution and the contact area growth, and to the overall response of the assembly. We finally want to correlate these changes to the variation of water content of the system.

Besides characterising their behaviour, our intention is also to build a future benchmark for the study of water-sensitive granular materials, taking advantage of the high complementarity of the techniques used in this work.

Finally, the experimental results will be used to calibrate a numerical model developed to simulate the behaviour of assemblies of hygroscopic and swelling particles.

1.3 Structure of the thesis

The following chapters are structured as follows:

- in Chapter 2 we introduce the material selected as a reference for this work: couscous. We present the data acquisition techniques (x-ray tomography, neutron tomography and time-domain nuclear magnetic resonance), their fundamentals and some applications. The experimental apparatus are described, with specific emphasis to the relative humidity control;

- Chapter 3 describes the procedures to analyse the images acquired with x-ray and neutron tomography, and then it expands the approach we followed to analyse time-domain nuclear magnetic resonance signal;
- Chapter 4 includes a published study in which we investigated the effect of high relative humidity on an assembly of couscous particles. Attention is paid to the volumetric strain of thousands of particles, as well as to the overall response of the assembly. The study comprises also a comprehensive contact analysis;
- Chapter 5 describes the work behind another paper, which is the result of our collaboration with the Wageningen University & Research and Unilever. The study aims to correlate the particle swelling to the water uptake by complementary deployment of x-ray tomography and time-domain nuclear magnetic resonance. Moreover, the image analysis allows for further investigation of the heterogeneities in the sample;
- Chapter 6 is essentially the third and last paper included in this dissertation. The experimental campaigns presented in this study revolve around the influence that water sorption has on the microstructure of water-sensitive granular assemblies. This investigation is allowed by the simultaneous use of x-ray and neutron tomography;
- Chapter 7 summarises and further analyses the experimental results of the experimental work presented in the three previous chapters. Particular attention is paid to describe the link between water content and particle swelling, response of the assembly, and contact area growth;
- Chapter 8 presents a simple attempt to model hygroscopic swelling particles. A discrete element method approach is used to simulate the behaviour of hundreds of particles, so to qualitatively mimic, but also support, the experimental observations;
- Chapter 9 summarises and highlights the main findings of this doctoral work and finally examines the possible perspectives.

The thesis also includes two appendices:

- Appendix A gives details about the design of the experimental apparatus;
- Appendix B presents an experimental study in which uniaxial compression tests are performed on individual particles to determine the dependency of their mechanical properties on water content.

Information: This doctoral work entitled “Multi-modal investigation of hygroscopic granular media at high relative humidity” has received funding from the European Unions Horizon 2020 research and innovation program under the Marie Skłodowska-Curie grant agreement no. 812638 (CALIPER). The work presented here was mostly carried out at Laboratoire 3SR, Université Grenoble Alpes (France). Experimental campaigns were performed at the Institute Laue Langevin (ILL), in Grenoble (France). Two months were spent on secondment in the Netherlands, at the Wageningen University & Research and Unilever, respectively academic and industrial partners of this thesis project.

Chapter 2

Materials, experimental techniques and apparatus

This Chapter introduces the experimental procedures followed to characterise the hydro-mechanical processes of water-sensitive granular materials exposed to high relative humidity (RH). Specifically, Section 2.1 presents the reference material chosen for this study: couscous. Then, in Section 2.2, general notions about the three main acquisition techniques used in the thesis experimental work are provided. We use a *multi-modal* approach including x-ray tomography, x-ray+neutron tomography and time-domain nuclear magnetic resonance. Section 2.3.1 explains we control the relative humidity, so that we can induce increase of water content, which drives all the changes in material properties. Finally, Section 2.3 describes the multiple experimental apparatus and the developed procedures followed while performing tests. More details about the design of the apparatus are given in the Appendix A.

2.1 A reference water-sensitive granular material

2.1.1 What is couscous?

According to the *Codex Alimentarius* (Codex Standard 202-1995), couscous is “the product prepared from durum wheat semolina (*Triticum durum*), the elements of which are bound by adding potable water and which has undergone physical treatment such as cooking and drying”.

It is prepared by mixing coarse ($475 - 700\mu\text{m}$) and fine ($130 - 183\mu\text{m}$) semolina. Generally, the couscous particle diameter is greater than $630\mu\text{m}$ and not exceed 2mm (with a tolerance of 6%).

Couscous processing comprises three main phases [Abe+12]:

1. *agglomeration*, by wetting, mixing and rolling;
2. *heat treatment*, to strengthen its structure;
3. *stabilisation*, to ensure the product durability.

The correct execution of these stages is fundamental to provide a good quality and a long shelf life to the material [Abe+12].

Commercially, couscous is divided into three groups: fine, medium and coarse, depending on the average particle size. Currently, the production and consummation of couscous remains relatively low when compared to other product derived from durum wheat (*e.g.*, pasta).



FIGURE 2.1: Particles of the fine couscous chosen as the reference water sensitive granular material. The picture highlights the complicated particle shape, formed by several semolina grains gelatinised together.

Nonetheless, these numbers are increasing significantly not only in North African countries, but all around the world [HS20].

2.1.2 Why couscous?

The behaviour of numerous materials is strongly influenced by the presence of water, and many of them are granular (*i.e.*, cereals, pasta, seeds, sugar, food or pharmaceutical powders). We considered several and we carried out exploratory experiments in order to identify the ideal material for this thesis. Preliminary tests were, for example, performed on mustard seeds, sugar, pasta ‘pearls’, and couscous.

The reasons why couscous is finally selected as our reference water-sensitive granular material are diverse. Its particles absorb water, can swell, agglomerate, cake [Abe+12; HS20; DR+22] and potentially lose mechanical properties, as suggested by an experimental study by [GYP91] (and later confirmed by compression tests of individual particles, Appendix B). All these characteristics are typical of water-sensitive materials. At the same time, we try to avoid highly complex phenomena that could be found in other materials, such as germination or husk peeling.

Among the possible size distributions, fine couscous is specifically selected for our studies. The particle size ($0.5 - 1.0\text{mm}$) is near to powder, while still allowing the analyses at particle-scale (and above), as detailed in Chapter 4, 5 and 6.

2.2 Data acquisition techniques

2.2.1 Imaging: x-ray and neutron tomography

In this section we introduce x-ray and neutron tomography, two of the three main techniques employed to acquire data about the chemo-hydro-mechanical interactions occurring when couscous particles are exposed to high relative humidity.

X-ray and neutron are ionising radiation based and non-invasive techniques and can be combined to acquire multi-dimensional images datasets. Thanks to their similarities in spatio-temporal resolution, these techniques make it possible to perform *full-field* observations and measurements, *i.e.* to analyse the spatial distribution of a certain object properties, accounting

also for natural or induced heterogeneities. Moreover, because they are non-destructive, they allow for acquiring sequential images, so that the evolution of the material properties can be observed and measured due to, for example, time dependent phenomena or mechanical loading (in our study case, the effect of relative humidity on hygroscopic couscous particles).

The following paragraphs present a brief introduction to x-ray and neutron generation, detection and image acquisition techniques. Finally, some examples of recent applications the simultaneous use of the two techniques are given.

Beam generation: x-ray and neutron sources

To acquire images with the two techniques, it is first necessary to generate the respective ionising beam.

X-rays are generated when high kinetic energy electrons are decelerated and their energy converted into electromagnetic radiation, *i.e.*, photons [Sei04]. There exist different ways of producing x-rays. The most frequent is the use of vacuum tubes, where electrons are evacuated from a high density filament (cathode) and accelerated towards a metallic target (anode). This can be used to produce a conical *polychromatic* x-ray beam, characterised by a large spectrum of x-ray energy. Another way of producing x-rays is the by deviating electrons from their trajectory using magnetic fields, the common procedure in synchrotron facilities. This beam is characterised a sub-parallel more *monochromatic* beam and high flux, a great advantage when acquiring images in short time and at high resolutions. In this doctoral work, we only employed imaging setups equipped with vacuum tubes.

A high flux of neutron is essential to acquire satisfactory neutron tomographies. This cannot be achieved in common laboratories, but rather in specific facilities. Neutrons can be in fact generated either by fission or spallation [Ten+21]. In our case study, the experiments were performed at the Institute Laue Langevin (ILL), where the neutron beam is provided by fission in the ILL nuclear reactor. Atoms of Uranium 235 (^{235}U) are bombarded with neutrons, and in turn each splits in two atoms (Barium Ba and Krypton Kr), and releases energy and two other neutrons. The neutrons are then transported to a beam line and specifically to the imaging station, as detailed later.

Interaction with matter and attenuation

X-rays and neutron are highly complementary because of the fundamentally different manner in which they interact with matter [MAN11; Ten+20; Ten+21]. X-ray beams interact with the electrons of the atoms, while a neutron beam with their nuclei. The interaction is in our case mainly characterised by two phenomena: absorption and scattering. In imaging, the result of the beam interaction with an object is called *attenuation*, *i.e.*, the loss of beam intensity when encountering an obstacle (*e.g.*, the specimen under investigation). This loss of intensity can be described by the Beer-Lambert law:

$$I(z) = I_0 e^{-\mu z} \quad (2.1)$$

where I_0 is the initial intensity of the beam, μ the material “absorption” and z the thickness of the object.

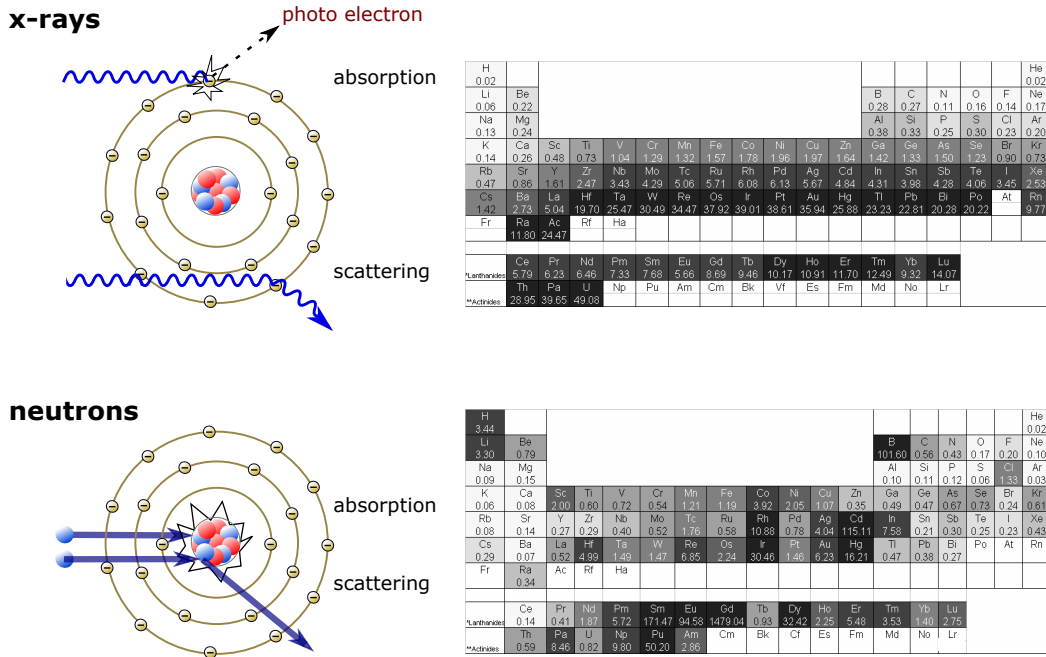


FIGURE 2.2: Periodic tables summarising the attenuation of x-rays and neutron with matter (its opacity being proportional to the attenuation). The x-ray attenuation is proportional to atomic number. Conversely neutrons do not interact the same way. Some elements relatively “transparent” to x-rays strongly interact with neutrons, which highlights the possible complementary study employing the two techniques; from Tengattini *et al.* [Ten+21].

The attenuation has been investigated for the elements of the periodic table. It was found that the x-ray attenuation is proportional to the atomic numbers. On the other hand, the neutron attenuation does not follow the same rule. As shown in Figure 2.2, the attenuation coefficient varies from element to element. In particular, it can be observed how the attenuation of hydrogen is significantly different between the two modalities. This difference can be an advantage when investigating the microstructure of multi-composite materials. In fact, as highlighted in Figure 2.2, several elements have a quite different attenuation between the two techniques. For example, Hydrogen, Lithium, and Chloride are relatively “transparent” to x-rays, while the opposite is true in a neutron beam. Conversely, some metals such as Gold and Lead interact with the beams in the opposite way. In both cases the resulting attenuation of also proportional to the density of the material ρ .

Of the numerous possible element combination, the one of interest for this study is the difference in attenuation of Hydrogen and consequently water (H_2O), as it can be absorbed from, or released to, the outer environment by hygroscopic particles. While x-rays allow for determining the microstructure of the sample under investigation, the change of attenuation caused by the increase of water content is very hard to detect. Neutrons, on the other hand, strongly interact with the water in the material.

Image acquisition: radiography and tomography

X-rays and neutron and neutron intensities are measured by detectors making use of “scintillators”, special materials that, when excited by the radiation re-emit energy under the form of visible light. The produced photons can be then measured by specifically designed panels or cameras. Ideally, when the radiating beam (either x-ray or neutron) does not encounter

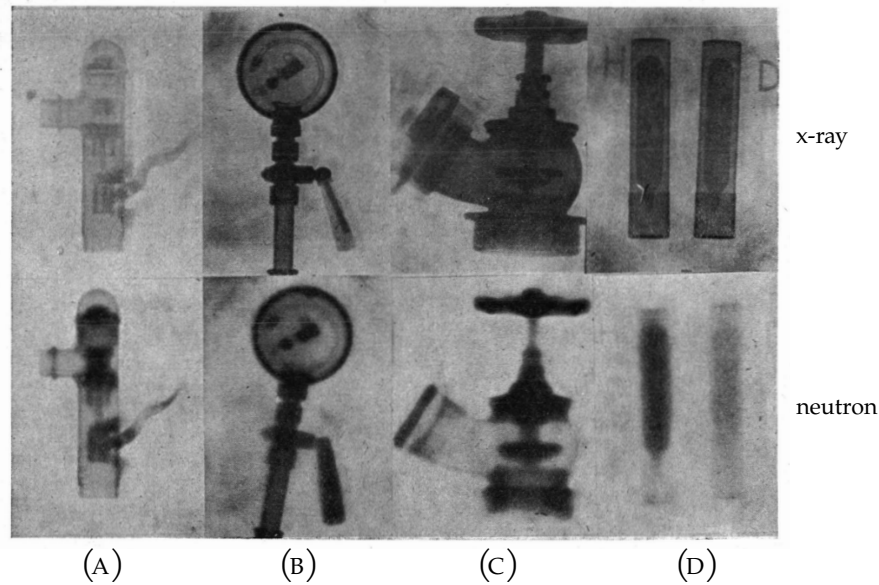


FIGURE 2.3: X-ray (top) and neutron (bottom) radiographies of: (A) pitcher pump, (B) pressure gauge with metal backplate, (C) fire hydrant and (D) test tubes filled with water and heavy water; from Peter [Pet46].

any obstacle, the detector is hit by the same number of photons in time. When an obstacle is placed between source and detector, the beam loses intensity and the detector is able to record, by computing the ratio to the “unencumbered” image, the spatial distribution of attenuation caused by the obstacle (*attenuation map*), thanks to the different number of photons recorded by all the pixels constituting the sample. The two-dimensional map (or image) obtained is referred to as *radiography*. An interesting example of radiographies revealing the complementarity of x-rays and neutrons is given by the first known example of combined use of the two techniques by Peter [Pet46], in Figure 2.3, where the projections of different objects highlight the different attenuation of some elements to x-rays or neutrons.

Generally, lab-scanner x-ray beams are conical in shape. The virtual pixel size is determined by the number of pixels of the detector and by the distance of the investigated object from the source and the detector. Typically, the closer to the source, the higher the resolution (obviously resulting in a small field of view). On the other hand, a neutron beam is (sub-)parallel, and the final resolution of the radiography is the result of the combination of different features: the scintillator-object distance, beam collimation, type of lenses and camera pixel size [Ten+20; Ten+21].

A simple radiography can provide rich information about the microstructure of materials. By acquiring several radiographies (projections) from different angles (in this case by rotating the observed object around its vertical axis), it is possible to obtain the three-dimensional attenuation map of the object, employing specific reconstruction algorithms [FDK84]. This process is broadly known as *tomography* or *computed tomography*. In this study, all the acquired tomographies are obtained by reconstructing the projections with the algorithm proposed by Feldkamp *et al.* [FDK84], and implemented in the software X-Act by RX-Solutions (Annecy, France).

This software is also used to correct for imaging artefacts such as beam-hardening and ring artefacts. The beam-hardening is the phenomenon where lower energy x-rays are attenuated more than high energy ones, and the final energy spectrum mean value is increased (“hardened”) [SB05]. This results with an artefact where some regions of an object appear less

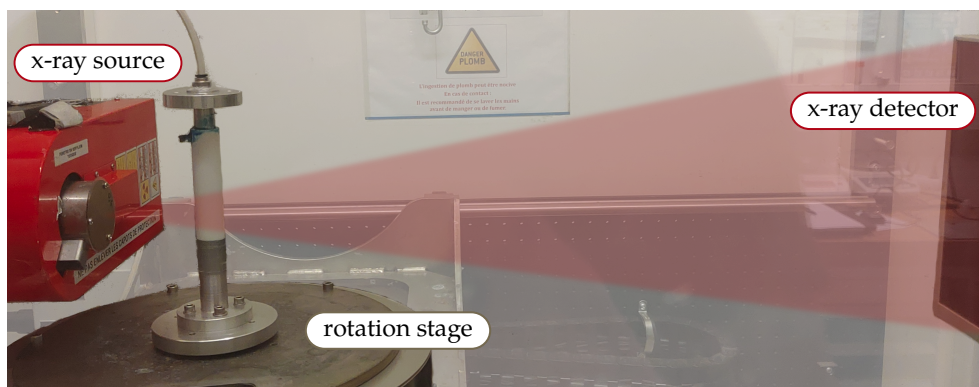


FIGURE 2.4: Main components of the x-ray tomograph at Laboratoire 3SR. On the left, the x-ray source (red box), on the right the x-ray detector. The sample installed on a rotation stage and positioned between the source and the detector in order to acquire several radiographs, that were then reconstructed.

attenuating than they ought be in the reconstructed image. This issue is usually resolved by pre-hardening the beam with a filter between the source and the analysed object, to get rid of the low energy photons that would cause the artefact. Ring artefact instead occur when adjacent detector pixels have different sensitivity (due to bad calibration, filter thickness imperfections, or malfunctioning pixels) [DE06]. Since the pixels remain in the same position during a tomography, the discrepancy is caught in the projections and then by the reconstruction algorithm, resulting in circular marks (*i.e.*, rings) perpendicular to the rotation axis.

Imaging setups

In this work, tomographies are acquired at two different facilities:

- Laboratoire 3SR (Grenoble, France), where only x-ray tomographies are acquired;
- Institute Laue Langevin (ILL) (Grenoble, France), where simultaneous neutron and x-ray tomography images are acquired.

The x-ray apparatus at Laboratoire 3SR was built by RX-Solutions (Annecy, France), and is composed by three main components (see Figure 2.4):

- Hamamatsu Corporation L12161-07 x-ray source;
- Varian PaxScan 2520DX x-ray detector (1920×1536 pixels of $127 \times 127 \mu\text{m}$ in size);
- rotation stage;

This tomograph is employed in different experimental campaigns. Specifically for this study, the results of two experimental campaigns whose images are acquired at Laboratoire 3SR are presented in Chapter 4 and Chapter 5. A picture of the imaging apparatus taken during one of these campaigns is shown in Figure 2.4.

As mentioned, at the ILL, it is possible to acquire simultaneous x-ray and neutron tomographies. Specifically, the experimental campaigns presented in Chapter 6 are carried out at NeXT-tomograph, situated at the end of the H521 ILL beamline. The simultaneous acquisition of neutron and x-ray tomography not only allows for the investigation of two different aspects of the processes occurring during the hydration process of couscous particle, but also their spatial correlation, as detailed in Chapter 3 (Section 3.1.6) and Chapter 6. The NeXT imaging setup used here comprises 5 main elements:

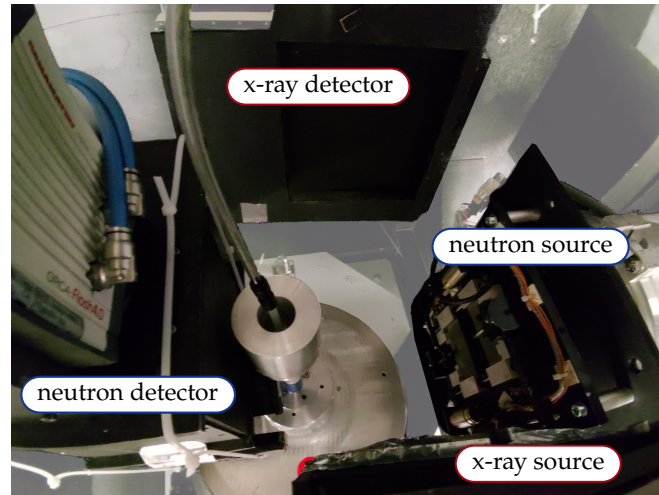


FIGURE 2.5: Main components of the neutron and x-ray imaging apparatus of the NeXT tomograph at the ILL. This picture, taken from above, shows the beam exit with the cold neutron source on the right, and the neutron detection system on the left. A portion of the x-ray source can be seen at the bottom, while the x-ray detector is at the top. The experimental setup of interest is positioned on a rotation stage (center) and then it is aligned at the centre of the two beams.

- x-ray source, identical to the one installed at Laboratoire 3SR;
- Varex PaxScan® 2530HE x-ray detector (1792×2176 pixels $139 \times 139 \mu\text{m}$ in size);
- a $1.4 \times 10^{10} \text{ n cm}^{-2}$ cold neutron source (at the end of the beam line);
- neutron detector comprising a Gadolinium scintillator, mirror, Hamamatsu ORCA-Flash4.0 V2 sCMOS camera and infinity corrected lenses system;
- rotation stage;

The x-ray and neutron setups are mounted (almost) perpendicularly, to minimise crosstalk between the two radiations [Ten+20], and at their center, and on top the rotation stage, the investigated object is placed. The overall structure is of granite, to avoid accidental displacements or thermal expansion/contraction. More details about the operating principles, the components of the NeXT station and some applications can be found in a recent publication by Tengattini *et al.* [Ten+20].

Figure 2.5 is a picture taken before the first experimental campaign presented in Chapter 6, and it shows all the mentioned components of the NeXT tomograph.

X-ray + neutron tomography: recent applications

X-ray tomographs are widespread all around the world. The significant increase in accessibility and image resolution of such instruments is being followed by a large number of studies, in medicine, industrial applications and material science. In the last decades, x-ray tomography has been widely employed to investigate the chemo-hydro-mechanical processes in granular materials, allowing observations and measurements even down to the nano scale ($< 1 \mu\text{m}$). Several comprehensive review were written in order to monitor and summarise the advancements in this field, in geomechanics, food structure, geoscience and many other sectors [VH12; CB13; WS13; Sch+16; Lei+20], to mention but a few.

Fewer facilities exist where it is possible to acquire neutron images [Ten+21], and there are fewer studies employing neutron tomography because of its lower availability. Nevertheless, in the last years, numerous studies used this technique to investigate a broad number of materials and phenomena. The internal structure of corn kernels, the cycle of lithium batteries, the water uptake of plants, the microstructure of concrete, metal-bone implantations, are some examples of all topics that have been investigated with neutron tomography [CI+08; Ban+10; Kar+18; Ten+20; Ten+21; Tör+21]. Often these studies are coupled with complementary and simultaneous x-ray tomography, [Ban+10; Kar+18; Ten+20; Ten+21]. This allows for deeper investigations of the phenomena, in particular when the water distribution and its evolution wants to be observed (and measured).

Here we present two recent applications where 5D (x-ray + neutrons + time) images were acquired to investigate the hydro-mechanical processes related to a specific problem.

The first study case concerns the hydro-mechanical coupling occurring in concrete samples when subjected to high temperature gradients [Sle+21]. Simultaneous x-ray and neutron tomography images were acquired in order to quantify the evolution of the cracking network (from x-ray tomography) due to the increase of temperature of concrete and the migration of the water front (detected with neutron tomography) due to evaporation. The authors also correlated the effect of water migration to the opening of cracks. The combination of the two modalities also allowed for a proper identification of all the microstructural components of the sample (*i.e.*, aggregates, cement paste, pores).

The second study case focuses on the water absorption of Callovo-Oxfordian Claystone [Sta+20b]. The material is characterised by low permeability and self-healing properties, and its behaviour is strongly influenced by water content. From simultaneous x-ray and neutron tomography images, the authors measured the strain field caused by swelling (from x-ray images), and then correlated it to the local water content variation (detected from changes in neutron attenuation).

These studies are examples of the possible uses and potential of x-ray + neutron tomography. In this study, this technique is employed in two different experimental campaigns carried out to investigate the effects of high relative humidity on the microstructure of couscous assemblies, as later detailed in Chapter 6.

2.2.2 Time-domain Nuclear Magnetic Resonance (TD-NMR)

In this Section we present the last technique used in the experimental work of this doctoral work.

Time-domain Nuclear Magnetic Resonance (TD-NMR) is a non-invasive experimental technique (as x-ray and neutron tomography) and it allows the investigation of nano-, meso- and micro-properties of materials. Through the years it has established itself as one of the main investigation tools in pharmaceuticals and food science [van+07; van+10].

The following paragraphs introduce the fundamental notions of this technique and conclude with examples of applications related to the experimental work detailed in Chapter 5, where we use TD-NMR to quantify the water uptake and the molecules relaxation of couscous particles exposed to flows of humid air.

Fundamentals

Nuclear magnetic resonance (NMR) is a physical phenomenon originated by the ability of nuclei to emit an electromagnetic signal, when subjected to a strong magnetic field and the system is perturbed by a secondary magnetic field oscillating near the Larmor frequency.

This frequency is defined by the magnitude of the primary magnetic field and an intrinsic constant named *gyromagnetic ratio*, unique for each kind of nuclei. In our case study, attention is given to the protium isotope (^1H), the most common of the hydrogen isotopes and abundant in organic matter, of particular significance for the study of the hydration process of couscous particles.

The magnetic contribution of a single nucleus is feeble, but the response of many nuclei can be described by a the resultant *magnetisation* vector \vec{M} [Blo46]. The magnitude of \vec{M} is determined as the “net” contribute of all nuclei, meaning that even if not all individual nuclei magnetisations point towards the same direction, their average can still be detected. This conjecture is often necessary when describing the NMR phenomenon through the “classical” interpretations. A more complete quantum one exists but, while more accurate, is not discussed as it is outside the scope of our study.

The magnetisation \vec{M} is parallel to the imposed primary magnetic field \vec{B}_0 , but this alignment can be broken by the secondary magnetic field \vec{B}_1 , commonly named *radio-frequency (RF) field* or *pulse*. By properly tuning the RF intensity and its duration, it is possible to flip \vec{M} by a specific angle, which would then start to precess about the original alignment direction (the \vec{B}_0 direction). With this rotation the magnetisation \vec{M} has a contribute along the direction of \vec{B}_0 (M_{\parallel}), but also one on the perpendicular plane (M_{\perp}). It was found that this phenomenon is transient [Blo46], and that its *decay* could be described with two constant parameters, T_1 and T_2 , called *relaxations times*. T_1 describes the time necessary for \vec{M} to realign with the original direction determined by \vec{B}_0 , while T_2 describes the time for the perpendicular component to fade out (*i.e.*, $M_{\perp} \rightarrow 0$).

Despite the uniqueness of the gyromagnetic ratio, the targeted nuclei do not have necessarily the same relaxation times. The Larmor’s definition states that the ^1H isotopes frequency is related to the gyromagnetic ratio and the intensity of the magnetic field. However, locally, the intensity B_{local} is not equal to the external one (*i.e.*, $B_{local} \neq \|\vec{B}_0\|$). Instead, this perceived magnetic field depends on the contribution of the molecule in which the nucleus resides. Despite being very small, this difference is detectable and it commonly referred to as *chemical shift* [PY50]. Because of this difference, the relaxation times of tightly bound nuclei or of relatively “free” ones (*i.e.*, nuclei in solid, liquid or lipid fraction) are not equal. Therefore, the different components of a multi-phase material can be identified and the nuclei categorised into populations (see Chapter 3 and 5). In practice, nuclei bound to the solid lattice of molecules are usually characterised by very short relaxation times, meaning that their magnetisation tends to realign rapidly with the primary magnetic field. Conversely, the resonance of an unbound nucleus takes longer time to fade out. Conventionally, the population of ^1H nuclei characterised by a longer T_2 relaxation time is referred to as *mobile* population.

NMR signal

The magnetic resonance signal can be detected thanks to the fact that it induces a voltage in a nearby circuit (by Faraday’s law of induction). The NMR phenomenon was initially observed keeping the RF perturbation constant, while changing the intensity of the primary magnetic field [BPP48]. Later, the phenomenon was also observed by pulsing on and off a constant RF

at Larmor frequency [Hah50a; Hah53] and the observed signal, (*i.e.*, a decreasing sinusoidal wave oscillating at the Larmor frequency) is called *free induction decay (FID)*. This decay can be described by the T_2^* relaxation time, which reflects the effect of the previously mentioned T_2 relaxation time, without being its equivalent. Any RF pulse at Larmor frequency would generate nuclear resonance, but to maximise the signal amplitude a 90° pulse must be applied (*i.e.*, a pulse that would rotate the vector \vec{M} perpendicularly to \vec{B}_0). A single RF pulse generates the FID signal, which decays rapidly. Nevertheless, this signal can be revived by applying two consecutive 90° pulses (180° RF pulse), which re-phase precession of the nuclei after a first magnetisation decay. This phenomenon is known as *echo-spin* and was discovered by Hahn [Hah50b]. Their experiments revealed that this phenomenon could not be replicated for long. This issue was resolved by [MG58], who proposed a to apply the 180° RF pulse in two directions alternatively, allowing a prolonged endurance of the echo phenomenon. The signal obtained with this technique is called the *Carr-Purcell-Meiboom-Gill (CPMG)* sequence [CP54; MG58]. The 180° RF pulses can be applied several times (*echo train*). However, the signal eventually decays due to molecular and system heterogeneities. Nonetheless, the peak values of each echo signal would still describe the T_2 relaxation of the material's nuclei.

In our experiments, we analysed the combination of the FID-CPMG sequences to investigate couscous particle components and their evolution during the hydration process. This techniques is often referred as time-domain NMR (TD-NMR).

NMR equipment

For an NMR instrument, the primary field \vec{B}_0 can be either generated with permanent or electromagnetic magnets placed at a distance of few centimetres [van+10]. The perturbation of the magnetic field causes a shortening of the relation times, therefore is it essential to maintain stable environmental conditions of the instrumentation (*e.g.*, constant temperature). The setup is equipped with radio frequency coils, to apply the desired \vec{B}_1 perturbation and to record the induced voltage by the nuclei resonance. In some devices, the input and output RF coils are the same. All the instrumentation is connected to electronic devices that control the tuning and calibration of all the features to obtain NMR sequences. Occasionally, the NMR experimental procedure is controlled by automated algorithms to speed up and facilitate the data acquisition process. In the experimental investigation presented in Chapter 5, we use two different commercial NMR spectrometers: a low-field 20 MHz ^1H (0.47 T) Bruker MiniSpec MQ20 ND and a "Pure Devices" MagSpec 23 MHz 0.55 T.

Applications

NMR is quite a versatile technique, which makes it a remarkably widespread analysis method, from application in material technology to medicine, from pharmaceuticals to food science. The principles of NMR have been employed to build imaging apparatus, capable of acquiring multi-dimensional images taking advantage of the contrast given by the different relaxations times of the components (*i.e.*, Magnetic Resonance Imaging MRI). This technique is not further discussed here, as no images could be acquired due to the typical apparatus sensitivity (exposition time) and the fast decay of resonance in relatively dry materials such as couscous particles.

There exist several comprehensive reviews regarding the use of NMR as a technique to design, process, improve or treat a wide range of products, in pharmaceutical or food industries (*e.g.*, the works by [van+10; Sim+14; Hat19]). Here we introduce some studies on water

sensitive materials, where the molecular structure properties or their variations due to either decreasing or increasing water content were investigated.

It was proven by Le Botlan *et al.* [LBCL98] that the TD-NMR technique could be employed to explore the characteristics of crystalline and "solid" materials, such as sugars. On the other hand, NMR is often employed to investigate relatively wet materials. For example, the water absorption of breakfast cereals was monitored by Lucas *et al.* [LLRM07]. Cereals samples were soaked in water and several CPMG signals were acquired in time. It was observed that the amplitude of water signal in the solid component (*i.e.*, absorbed water) increased with time, a result that was also successfully correlated to gravimetric tests. The T_2 relaxation time of the liquid fraction decreased during the soaking process, as solid molecules would dissolve in it.

Another water sensitive material that has been studied with NMR is corn [RCA99]. The NMR characteristic of *Zea mays* were investigated as a function to the corn maturity (*i.e.*, higher maturity, lower water content). A decrease of T_2 relaxation time was observed for lower water contents, indicating the shift of some molecules from a mobile population to a less mobile one.

The protein, water and oil proportions were determined in seeds by Gambhir [Gam92] and Pedersen *et al.* [PME00], while Mateus *et al.* [Mat+07] analysed the evolution of the T_2 spectrum with water content and temperature in ground roasted coffee. The authors defined three main populations for the nuclei, and found that the most susceptible to water content and/or temperature are the less mobile ones.

The effects of water content on the properties of wheat flour dough-water, starch-water, gluten-water were studied by Doona *et al.* [DB07]. It was observed that by increasing the water content the signal coming from relatively mobile population augments, and so does the mean T_2 relaxation time.

The studies presented above focus their attention of the physical or NMR characteristic of the investigated material. Nevertheless, these are not the only properties measurable by this technique. For example, it was proven that with the NMR material properties could help predict the geographical origin of durum wheat [Lam+11], a reminder of all the hidden additional complexities behind the behaviour of water sensitive granular materials.

2.3 Experimental apparatus

2.3.1 Relative humidity control

During all the experimental campaigns, we investigate the influence of high relative humidity on couscous particles. Although liquid water would have even stronger influence, the tests examine the effects of humid air, a more likely scenario of water exposure during industrial processing and also of a major issue to prevent.

This section presents two custom-built RH unit control that are employed during our experimental campaigns.

The crucial point is to be able to maintain a constant concentration of water in the air, especially when operating close to its saturation point (RH>90%). This choice of extremely high RH levels would be in contrast with the targeted "realistic-case scenario", but couscous being a pre-treated material only exhibits significant changes when exposed to high humidities. It is also necessary to accelerate the natural rate of the processes activate by water sorption, as the time available at imaging facilities is limited. Our results are still likely relevant for materials where even lower water concentrations can activate the phenomena described in Chapter 1.

It should be also noted that RH strongly depends on temperature. A sudden drop of just few degrees can significantly increase the air RH even at ambient temperature (see Figure 2.6).

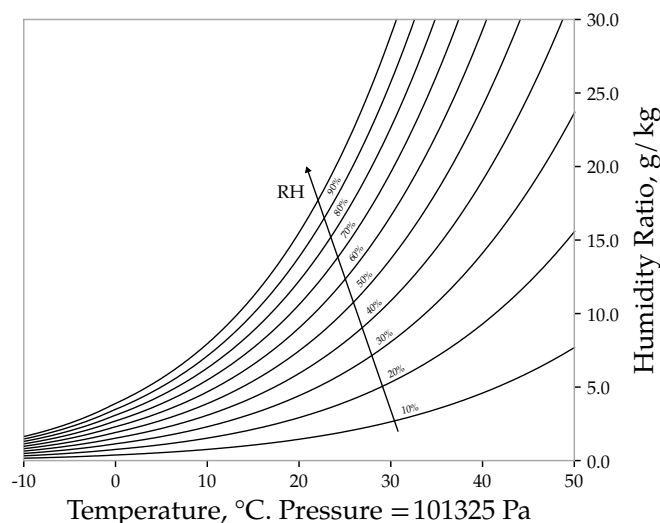


FIGURE 2.6: Chart summarising the relation between temperature and relative humidity; adapted from [Onl].

RH control with saturated saline solutions

In laboratories it is often required to control environmental conditions accurately and saturated saline solutions were found to be particularly useful to achieve this goal. At a given temperature they are able to produce stable RH environment, as was demonstrated by several studies [O'B48; CH49; SR49]. This phenomenon was then further investigated for numerous different aqueous solutions and wide ranges of temperature [WH54; WB60; You67]. A comprehensive review of previous studies was reported by Greenspan *et al.* [Gre+77]. As mentioned, in our studies it is of particular interest to maintain elevated and constant RH, also in the event of accidental temperature changes. Among many possibilities, the potassium sulphate salt is chosen, since its saturated solution ($\text{K}_2\text{SO}_4 + \text{H}_2\text{O}$) produces an environment of $97.30 \pm 0.45\%$ RH at 25°C and it is able to keep this value constant for a relatively large temperature intervals [You67] (see Figure 2.7).

For each of the experiments in which this RH control technique is employed, the solution is prepared by stirring 120 g of K_2SO_4 salt in 1 L of demineralised water, which is then poured in a sealed vessel. This vessel is connected to a Masterflex L/S peristaltic pump (model 7554-85), which transports the air at specified flow rate to the experimental apparatus where the particles are being tested. The air is, after interaction with the sample, transported back to the vessel where the humidity is being generated, to create a close loop. A simple sketch of this RH control method is shown in Figure 2.8.

RH control unit from Wageningen University & Research

The other RH control unit is designed and fabricated at the laboratories of Wageningen University & Research (WUR), in The Netherlands.

A schematic view of the WUR RH control setup is shown in Figure 2.9. A source of compressed, dry air is connected to the inlet of a bigger vessel (26 L Curtec drum). This vessel is equipped with an acrylic flow meter with a needle valve to regulate the incoming dry air flow

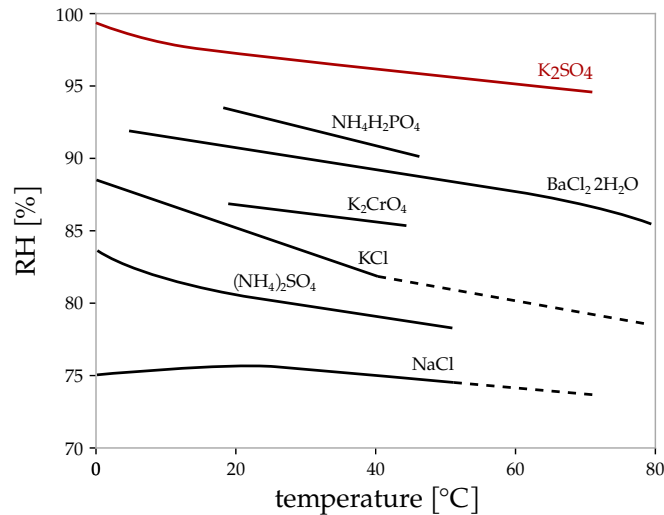


FIGURE 2.7: Variation of relatively high humidities over different saturated salt solution with temperature. The potassium sulphate solution (K_2SO_4) generates a very high RH and can maintain it for a relatively large temperature interval; from [You67].

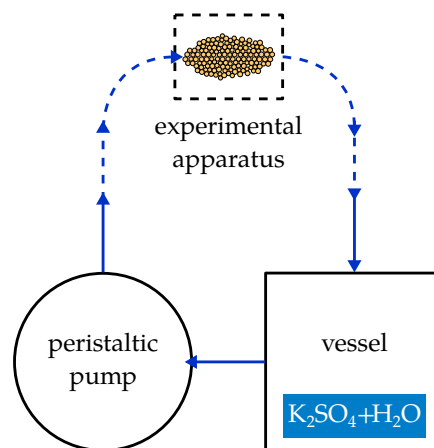


FIGURE 2.8: Schematic view of potassium sulphate solution RH control method. The humidity of 97% (from $K_2SO_4+H_2O$) was generated in a sealed vessel and transported by a peristaltic pump to the experimental apparatus.

(from 0 to 10 L/min). Inside the drum a bottle of demineralised water supplies a Beurer LB12 ultrasound humidifier, which is switched off and on by a custom RH control loop, which adjusts the level of humidity. The vessel is also equipped with a fan, to circulate air and ensure a homogeneous water concentration. The humidified air is transported to a smaller vessel (3.6 L), where a Thorlabs TSP01 RH-T sensor is installed. The sensor communicates with the software in order to control the humidifier switch. The outlet of the smaller vessel is split into two flow meters, one for large flows (up to 10 L/min), and one for smaller ones ($< 1 L/min$). The minimum RH achievable is the one of the dry air used. The WUR RH control set-up is operated at pressures slightly above the atmospheric pressure to minimise leakage. The humid air flow is then transferred into the experimental apparatus.

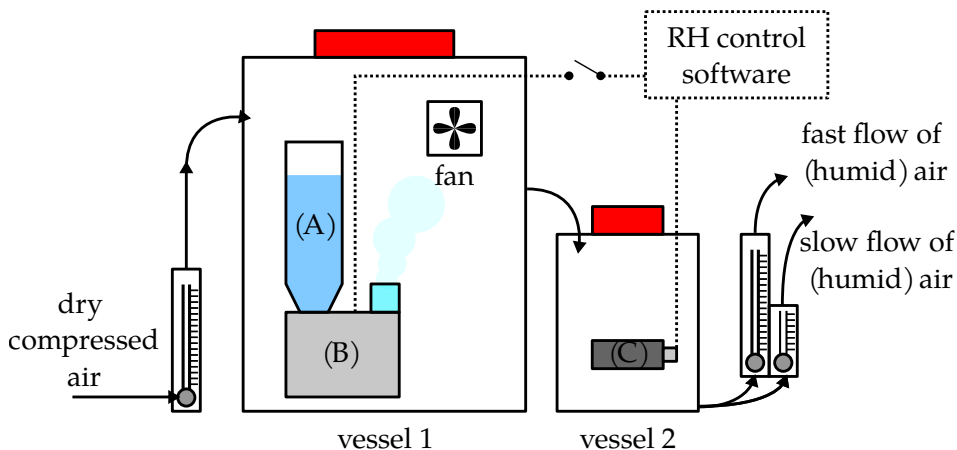


FIGURE 2.9: Schematic view of the WUR RH control unit. Compressed dry air is connected to the inlet of a 26l vessel (vessel 1) and regulated with the needle valve of a flow meter. The RH is increased by the Beurer LB12 humidifier (A+B), depending on the desired humidity and is measured by a Thorlabs TSP01 RH-T sensor (C) in vessel 2 (3.6L). The humid air flow was then split into two channels, one for high flows and one for lower ones.

2.3.2 1D compression apparatus

One-dimensional compression test (or oedometer) is the principal boundary condition used for this study. It is selected as the ideal one to emulate the particles conditions found in a storage-silo. The radial strain is constrained and a constant stress is applied to replicate the self weight of the material stored above (up to a maximum of $\approx 6\text{ m}$ depth). Multiple oedometer cells are built and connected to either RH control unit (see Section 2.3.1).

16mm oedometer - design

One oedometer used during our experimental campaigns was characterised by an internal diameter of 16 mm. It has been designed and fabricated in Laboratoire 3SR, and it comprises three main components: a base, a rigid cylindrical cell and an upper piston. The base is made in aluminium and its purpose is to support and properly align the cylindrical cell, but also to create sealed environment while testing. Two different cylindrical cell are used. One is made in PEEK (rather transparent to x-rays, but not neutrons) and the other one is later fabricated in PTFE (transparent to both x-rays and to neutrons). The piston is also made in aluminium, and it seals the cylindrical cell from top, but it also applies constant vertical stress (dead load) on the sample. Both the base and the ram are hollow, to connect the apparatus to the RH control unit and apply a flow of air (or possibly liquid), see Section 2.3.1. More details of the design are presented by technical drawings in Appendix A, Section A.1.

This 16 mm oedometer is used in the experimental campaigns presented in Chapter 4, Chapter 5 and Chapter 6.

7mm oedometer - design

The design concept of this smaller oedometer is basically the same as the 16 mm one. It is fabricated to reduce the sample diameter and mitigate the neutron beam hardening effect, as detailed in Chapter 6. Its pieces are made in aluminium. It must be noted that in the initial design the cell was fabricated in PTFE, but the material is not rigid enough and the cell could

not remain stable and support the dead load during tomography. Technical drawings of the apparatus and its individual components are presented in Appendix A, Section A.2.

Experimental procedure

The sample preparation is identical for the two oedometers. Based on the internal diameter, the mass of couscous particles is adjusted to achieve the desired sample height. Then, the particles are transferred into the oedomter cell, above a high porosity stone, which prevents the particles from falling into the hollow channels, while ensuring the transit of humid air flow. For the 16 mm oedometer, ceramic porous stones of diameter slightly lower than 16 mm are used, while in the 7 mm oedometer custom borosilicate glass filters of ≈ 6.9 mm diameter are adopted. The high RH air then flows through the sample.

2.3.3 NMR-compatible measurement cell

For the experiments in which data are acquired with the NMR (see Chapter 5), a specific measurement cell is designed. When dealing with NMR-based measurement setups, none of the components of the experimental apparatus can be metallic, due to the presence of strong magnetic fields. This excludes the oedometric conditions as a possible configuration, given that it would be cumbersome to apply relatively high loads with lighter materials. The measurement probe is built as follows. A PTFE cylindrical cell contains at the bottom a glass high porosity stone to prevent particles from falling out. Conversely, at the top the cell is threaded, to connect it to a PEEK rod equipped with an adjustable ring, in order to maintain the particles sample within the homogeneous region of the RF coil of the TD-NMR spectrometer (see Section 2.2.2). No load is applied and the particles are free to swell along the vertical direction.

Experimental procedure

The mass of particles before is measured before each TD-NMR relaxometry test. Then, the couscous is transferred into the PTFE cell, which is attached to the rod. After adjusting the height of the ring, a first FID-CPMG magnetisation decay is recorded for the dry configuration. Finally, the cell is connected to the WUR RH control unit (2.3.1) which generates the high RH air, that flows through the particle and is ultimately released in the outer environment (see Chapter 5).

Chapter 3

Data analysis approaches

In order to discuss the experimental results of this doctoral work presented in the following Chapters, it is first necessary to introduce the tools and techniques employed for the analysis of the data-sets acquired in the experimental campaigns.

This Chapter is divided in two parts. In Section 3.1 we introduce the image analysis procedure followed and developed in this study. Section 3.2 describes the approach used for the analysis of TD-NMR data, specifically of the FID-CPMG decays of magnetisation.

3.1 Image analysis methods

This section presents the approach employed in this work to analyse 3D images acquired with x-ray and neutron tomography. We introduce the fundamentals of each algorithm used in this work, and we discuss its use concerning the measurements of microstructural properties of couscous assemblies and the particles that constitute them.

The analyses are conducted using `spam`, an open source Software for the Practical Analysis of Materials [Sta+20a].

It should be noted that in this study case, the measurements are mainly performed on x-ray tomography images. The signal-to-noise ratio in the x-ray images is higher than in neutron images, due to the fact that the neutron beam is highly attenuated by the dense concentration of hydrogen atoms in materials such as couscous. Nevertheless, the image analysis techniques presented in this Section could be ideally used for any three-dimensional image, regardless its acquisition technique.

3.1.1 Gray-value images and spurious fluctuations correction

The tomography reconstruction algorithms produce 3D images, which can be treated as matrices of elementary units, also known as *voxels*. To each voxel is assigned a *gray-value* that represents the attenuation of the representative elementary volume (REV) defined by the voxel itself.

The name gray-value comes from the common use of gray colors to represent attenuation maps. In tomography, bright tones of gray conventionally indicate a high beam attenuation, while darker tones lower densities. For example, Figure 3.1 shows a horizontal cut (or “slice”) of a 3D x-ray tomography image acquired in the experimental campaign presented in Chapter 5. It can be observed how dark gray represents the air within the sample, while brighter tones indicate the solid fraction, composed by the particles and the cell in which they are being tested. It is important to note that the gray-value represents a specific materials property and that its variation denotes a microstructural change.

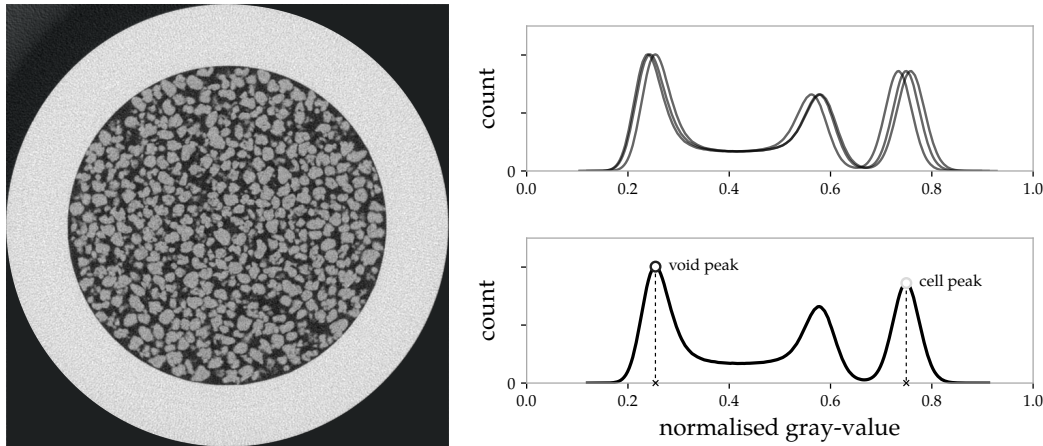


FIGURE 3.1: Effect of spurious fluctuations of the source on the gray-values. When acquiring sequential tomographies, the spurious fluctuations of the source can result in slightly different gray-values in the reconstructed images of ideally stable components. The histograms are linearised with respect to the peak gray-values of elements whose attenuation is theoretically constant (e.g., void and impermeable cell).

Multiple acquisition are necessary to characterise the evolution in time of a certain property or variable. However, when acquiring sequential tomographies it is inevitable to encounter spurious energy fluctuations of the source. This phenomenon can result in substantial variations of the gray-values, even in the ideal case of scanning the same object more times. As shown in Figure 3.1, the histogram of granular or porous system is characterised by the presence of “bells”, each corresponding to a different phase of the material. Typically, the thinner the bell, the better the signal-to-noise ratio. Specifically for the case presented in the figure, three different phases are detected: void, particles and cylindrical cell (see Section 2.3.2). As portrayed, the source fluctuations can alter the gray-value of objects whose attenuation is theoretically constant throughout the test. This issues can be mended with the histogram *linearisation*. First, the local maxima (peaks) of the distribution are determined. Then, the gray-value of two of them is set equal to specific, different values, and all the other gray-values in the interval are adjusted according to a linear transformation. It should be noted that this operation does not affect the histogram counts (or probability), but only the gray-values.

This operation is then run on the whole set of reconstructed images, allowing for a coherent comparison between them at any time-step.

3.1.2 Particle identification

As mentioned in Chapter 1, one of the main objectives of this study is to correlate the particle-scale phenomena to the overall response of the assembly. That is why it is crucial to identify all the particles that constitute the samples, and measure the evolution of their properties (e.g., position and volume).

It is first necessary to classify all voxels, *i.e.* assign them to their respective phase. This procedure is often referred to as *segmentation*, and its here achieved using a thresholding method [PP93]: the voxels are categorised based on whether their gray-value is greater or smaller than a chosen threshold value. In case of a system with two phases (e.g., solid and void phases, couscous particles and air), this approach is also known as *binarisation*. Specifically, we employ here the Otsu’s thresholding method [Ots79], implemented for bi-phase system, that computes the

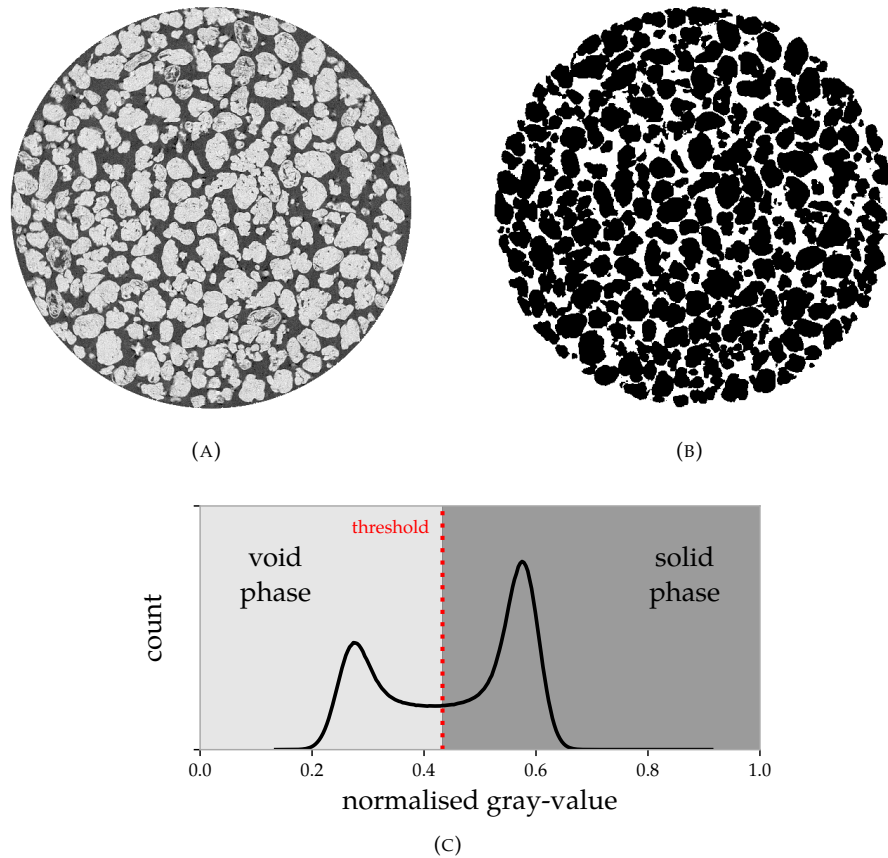


FIGURE 3.2: Image binarisation. Gray-scale image (A), the respective binary image (B), and the Otsu’s thresholding method on a gray-value histogram (C). To identify the solid and void phase in the granular system, the Otsu’s thresholding method is used. All the voxels characterised by a gray-value higher than the threshold are set to be “solid”, while voxels whose gray-value is lower than the threshold are considered as “void”.

thresholding value by minimising the intra-class (*i.e.*, intra-phase) variance or by maximising the inter-class variance.

An example of binarisation *via* Otsu’s thresholding method is shown in Figure 3.2. It must be noted that this approach alone does not consider as part of the solid fraction the intra-particle pores visible in the reconstructed images. These are included afterwards in the image processing with bespoke algorithms [Vir+20]. Straightforwardly, the binary image (Figure 3.2b) allows the measurement of sample-scale properties, such as porosity.

The outlined binarisation procedure does not provide any direct information about individual particles properties. Nevertheless, the binary image is essential for the distance map computation, which assigns to each solid voxel a value equivalent to its euclidean distance (ED) from the nearest void voxel. Figure 3.3a presents an example of distance map computed from a 2D binary image of couscous particles. A voxel close to the particle edge is characterise by a low ED value, while a voxel in the particle core has a high ED . It can be noticed how, for relatively convex shapes, the number of local maxima in a distance map is an indication of the number of particles in the system.

The local maxima location is an essential information for the so-called *labelling* procedure, which assigns to each voxel a unique “label” (typically an integer number), according to the particle to which it belongs (Figure 3.3b).

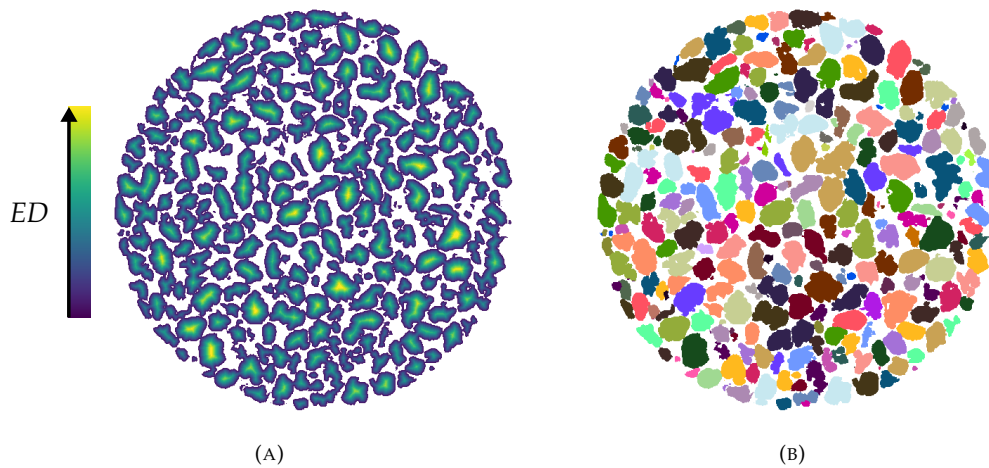


FIGURE 3.3: Euclidean distance map (A) and labelled image (B). The distance map is obtained by assigning to each solid voxel a value indicating its euclidean distance ED from the nearest void voxel. The labelled image is the final result of the particle identification process. To each label is assigned a unique integer number.

In this work, the *watershed* algorithm is employed to label each particle [Beu79; Beu82; VS91]. The logic of this method is illustrated in Figure 3.4. The distance map can be inverted and seen as a topographic relief, and its local minima (maxima in the distance map) allow the separation of particles during the progressive “flooding” of the relief profile. Inter-particle contact points are defined when neighbouring basins touch. Although illustrated for a 1D case in Figure 3.4, the operation is similarly performed in 3D images.

The watershed algorithm is particularly efficient to separate spherical particles. However, when studying irregular shapes such as couscous (Figure 3.2a), the labelling must be refined, in order to fix possible *under-segmentation* and *over-segmentation* issues. With under-segmentation we indicate the spurious assignment of the same label to more than one particle. Conversely, over-segmentation indicates the presence of two (or more) labels within one single particle. To remedy these inaccuracies, we use in this work two bespoke algorithms implemented in `spam`.

To fix under-segmentation issues, a coefficient is assigned to each label, which is equal to the convex volume of the particle and its actual volume. In the specific case of a perfectly convex particle the under-segmentation coefficient is equal to 1. Naturally, this is not the case for couscous particles. When a particle is deemed to be under-segmented (under-segmentation coefficient $>$ chosen under-segmentation threshold), the gray-value subset described by the label is binarised using a higher threshold than the one chosen for the initial segmentation process. If the subset binarisation indicates clearly the presence of more than one local maximum, the label is “split” recomputing the watershed algorithm.

Over-segmentation, which is a quite an ordinary issue in couscous particles because of their shape, is fixed by comparing the characteristic length of a label (*i.e.*, particle diameter) and the characteristic length of its biggest contact area. If the ratio between the two values is found to be higher than an arbitrarily chosen over-segmentation threshold, the two labels are merged together. Clearly, the logic of this approach operates efficiently for rounded particles, because the contact areas are much smaller – ideally punctual – than the average particle size. For example, in case of cubic shapes, this approach would be quite inefficient.

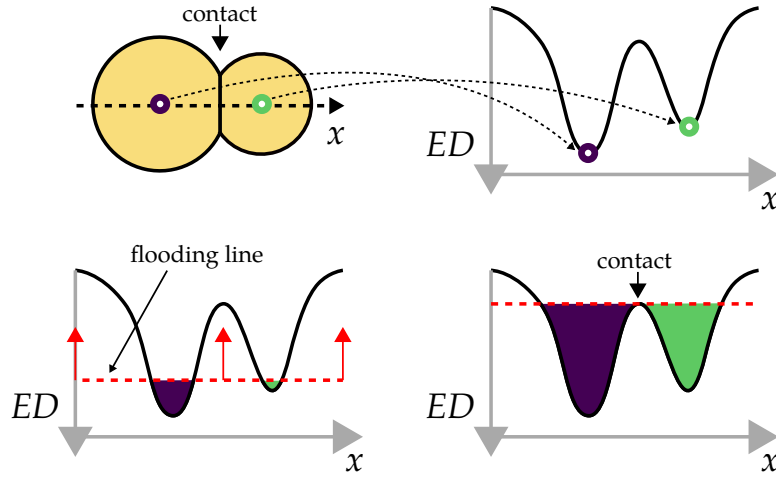


FIGURE 3.4: 1D illustration of the watershed algorithm. Inverting the euclidean distance ED map a topographic relief is described. By “flooding” it, it is possible to separate the particles based on the local maxima previously identified in the distance map. An inter-particle contact is determined when two flooded basins touch.

Once the segmentation issues are solved, the labelled image is ready and it enables particle-scale measurements such as the particle position, orientation, and volume. The particle volume V_p is one of the crucial properties around which revolve most of the analyses and results presented in this doctoral work, and it is calculated as:

$$V_{p,i} = N_i \quad (3.1)$$

where N_i is simply the number of voxels constituting the label i .

3.1.3 Particle tracking

The labelling procedure presented in the previous section allows for measurements of particle-scale properties at a specific time-step, but it does not provide any information about their evolution with time (or water content).

One approach to track the particles kinematics would be to perform the labelling procedure described above for each time-step, and then compare morphological and positional feature of the label to correlate them in time [And+12; Als+17; CW18]. Although efficient in some studies, this approach would be fruitless when investigating the evolution of particles that inherently change in shape and become more deformable (see Section 1.1.2).

That is why, in this study, digital volume correlation (DVC) is employed to track the kinematics of particles. Specifically, we use the *spam* implementation, which is based on the formulations presented in Hild and Roux [HR12] and Tudisco *et al.* [Tud+17].

Basics of Digital Volume Correlation

The basic idea of digital volume correlation (DVC) is to search for a transformation function Φ , that relates the position of material point x in a reference image $f(x)$, to the the position x' in the deformed configuration $g(x')$. Considering that x' is equal to $\Phi \cdot x$, the ideal goal is to find a Φ that satisfies the following equation:

$$f(x) = g(\Phi \cdot x) \quad (3.2)$$

The transformation function is considered as homogeneous and linear, and it can be written as a 4×4 matrix (of 12 unknowns):

$$\Phi = \begin{bmatrix} \Phi_{zz} & \Phi_{zy} & \Phi_{zx} & t_z \\ \Phi_{yz} & \Phi_{yy} & \Phi_{yx} & t_y \\ \Phi_{xz} & \Phi_{xy} & \Phi_{xx} & t_x \\ 0 & 0 & 0 & 1 \end{bmatrix} \quad (3.3)$$

where the terms Φ_{ij} define the deformation gradient tensor F , while t_z , t_y , and t_x describe the rigid translation vector t . The right Cauchy polar decomposition of F allows the computation of the rotation tensor R and the stretch tensor U ($F = R \cdot U$).

Notably, due to image noise, Equation 3.2 cannot be satisfied. It is therefore necessary to define a new “objective” for the DVC algorithm.

The similarity between $f(x)$ and $g(\Phi \cdot x)$, within a domain Ω , can be expressed as the functional \mathcal{T} as follows:

$$\mathcal{T}(\Phi) = \frac{1}{2} \sum_{x \in \Omega} (f(x) - g(\Phi \cdot x))^2 \quad (3.4)$$

The new objective is then to minimise this functional $\mathcal{T}(\Phi)$. This is solved iteratively by means of the Gauss-Newton method, as implemented by Lucas and Kanade [LK81]. At each iteration n , the transformation function is adjoined (Φ^n), and Equation 3.4 can be rewritten as:

$$\eta^2 = \mathcal{T}(\Phi^{n+1}) = \frac{1}{2} \sum_{x \in \Omega} (f(x) - g(\Phi^{n+1} \cdot x))^2 \quad (3.5)$$

The $g(\Phi^{n+1})$ is linearised with a first-order Taylor expansion [LK81], and becomes:

$$g(\Phi^{n+1} \cdot x) = g(\Phi^n \cdot x) + \nabla g(\Phi^n \cdot x) \cdot \delta \Phi^{n+1} \cdot \Phi^n \cdot x \quad (3.6)$$

in which ∇g describes the gradient vector of the deformed image in homogeneous coordinates. Because $x^n = \Phi^n \cdot x$, Equation 3.6 is rewritten as:

$$g(\Phi^{n+1} \cdot x) = g(\Phi^n \cdot x) + \nabla g(\Phi^n \cdot x) \cdot \delta \Phi^{n+1} \cdot x^n \quad (3.7)$$

Calling Equation 3.7 into Equation 3.5, the functional is expanded up to second order in $\delta \Phi^{n+1}$:

$$\begin{aligned} \mathcal{T}(\Phi^{n+1}) &= \sum_{x \in \Omega} (f(x) - g(\Phi^n \cdot x) - \nabla g(\Phi^n \cdot x) \cdot \delta \Phi^{n+1} \cdot x^n)^2 \\ &+ \frac{\partial \eta^2}{\partial \delta \Phi^{n+1}} (\nabla g(\Phi^n \cdot x) \cdot \delta \Phi^{n+1} \cdot x^n) \\ &+ \frac{1}{2} \frac{\partial^2 \eta^2}{\partial \delta (\Phi^{n+1})^2} (\nabla g(\Phi^n \cdot x) \cdot \delta \Phi^{n+1} \cdot x^n)^2 \end{aligned} \quad (3.8)$$

The components of the $\delta \Phi_{ij}^{n+1}$ are relabelled with a single index m , conformly to the Voigt’s notation [Hel01], *i.e.*, $\delta \Phi_m^{n+1} \equiv \delta \Phi_{i(m)j(m)}^{n+1}$.

Differentiating Equation 3.8 with respect to $\delta \Phi^{n+1}$, a linear system is obtained:

$$M_{mp}^n \delta \Phi_p^{n+1} = A_m^n \quad (3.9)$$

where M_{mp}^n and A_m^n are respectively the Hessian and Jacobian:

$$M_{mp}^n = \sum_{x \in \Omega} (x_{j(m)} g(\Phi^n \cdot x_{i(m)})) (x_{j(p)} g(\Phi^n \cdot x_{i(p)})) \quad (3.10)$$

$$A_m^n = \sum_{x \in \Omega} (f - g(\Phi^n \cdot x)) (x_{j(m)} g(\Phi^n \cdot x_{i(m)})) \quad (3.11)$$

in which x_i and x_j refer to the i -th and j -th components of the vector x .

Solving the linear system of Equation 3.9:

$$\delta \Phi_p^{n+1} = (M_{mp}^n)^{-1} A_m^n \quad (3.12)$$

the Φ^{n+1} is straightforwardly computed as:

$$\Phi^{n+1} = \Phi^n (I + \delta \Phi^{n+1}) \quad (3.13)$$

where I is the identity tensor.

The convergence criterion used here for the DVC algorithm is based on the norm of $\delta \Phi$ being lower than a given threshold ($\|\delta \Phi\| < \zeta$).

It should be mentioned that the convergence of DVC rests on the assumption that reference and deformed images are quite similar. However, tomography is often employed to observe relatively large deformations in materials. Therefore, it is crucial to assist the DVC algorithm with an initial guess. In case of sequential images acquisition, DVC is more likely to meet the convergence criterion when supported by a guess transformation function Φ_{guess} . For example, if the correlation of the reference image f_0 and the deformed configuration f_{n-1} is successful, the correlation of f_0 and f_n more likely (and quickly) converges if the Φ_{guess} is set equal to Φ_{n-1} computed in the previous step.

Discrete DVC

The functional \mathcal{T} is defined for a domain Ω . The implementation of the DVC therefore allows the correlation of whole images or of its subsets.

The volume correlation of image subsets can be used to follow the materials points defined by a mesh grid, a beneficial operation often employed to study the strain fields of continuum materials [Len+07; Des+18; Sta+20b]. On the other hand, the DVC can be performed on the domain describing an individual particle [Hal+10]. Known as *discrete* DVC (dDVC), this operation employs the labelled image to define sub-domains for all the particles and compute separately their own transformation function Φ_p .

3.1.4 Particle and assembly volumetric strain

One of the main features of water-sensitive granular materials is the dependency of individual particle properties on water content and its variations. As mentioned in Chapter 1, the particles may undergo morphological changes and deterioration of mechanical properties. Causous particles swell and become softer when exposed to high relative humidity. The effects of these two phenomena on the particle volumetric strain $\varepsilon_{V,p}$ could be computed at once from the deformation tensor F_p of an individual particles resolved using dDVC:

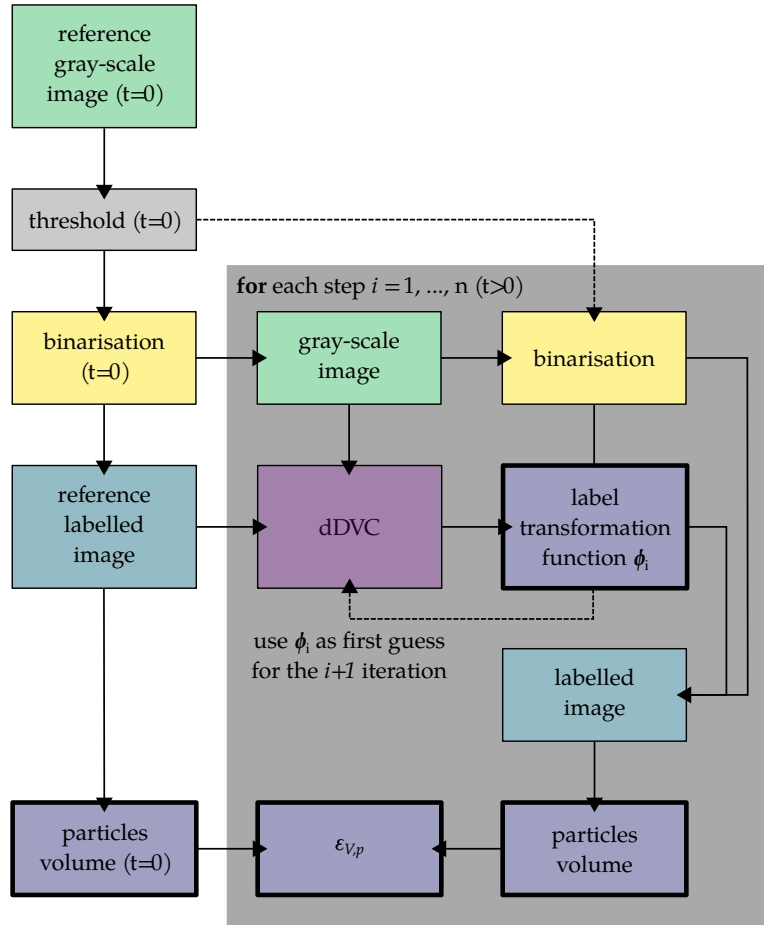


FIGURE 3.5: Flow chart illustrating the image analysis approach employed to determine the particles kinematics and deformation. Boxes highlighted by thicker borders indicate particle-scale measurements obtained in the iterative process.

$$\varepsilon_{v,p}(t) = \det(\mathbf{F}_p(t)) - 1 \quad (3.14)$$

This approach is accurate for relatively small particle strain, or under the assumption of isotropic and free swelling. This is not the case for couscous particles, in particular when samples are subjected to constant stress and the particles are possibly compacted, as detailed later in Chapters 4 and 6. Even though the process is far from the liquefaction stage of caking (see Section 1.1.3), the homogeneous assumption of DVC is not accurate enough to describe the particles morphological changes.

Nevertheless, the dDVC can be beneficial to solve the issue of measuring the volumetric strain of all particles. The computed particle transformation function Φ_p faithfully describes its translation and rotation, especially in case of oedometric conditions that restrain the particles displacement. The labels are then “moved” in a new deformed configuration [Sta+20a], according to their transformation function Φ_p . The deformed labelled image is used to define the “flooding” or “seed” points for a new watershed particle identification, bypassing the distance map local maxima computation and the under- and over-segmentation issues correction. This allows for retaining partial information of the particle shape and for preserving their “identity” (label integer number).

It must be mentioned that the binary images at time-step i are obtained after correcting

the spurious fluctuation of the source, and using always the same threshold selected for and reference image. The threshold is not recomputed at each iteration because the changes in particle density and sample porosity affect the gray-value distribution of the image, and thus the Otsu's threshold would binarise the image i incoherently with respect to the reference configuration previously determined.

Once the labelled images are obtained for all the desired time steps, it is possible to measure the volumetric strain of a particle $\varepsilon_{V,p}$ as:

$$\varepsilon_{V,p}(t) = \frac{V_p(t) - V_{p,0}}{V_{p,0}} \quad (3.15)$$

where $V_{p,0}$ is simply the volume of the particle in the reference configuration.

This approach allows us to more accurately determine the particle swelling, accounting for non-isotropic dilations, but also for the compaction of particles.

The flow chart presented in Figure 3.5 summarises the labelling procedure followed in this work to determine the volumes and volumetric strain of particles.

Objective of this doctoral work is to correlate the particle-scale phenomena to the overall response of the assembly (Chapter 1). To measure the volumetric strain of the assembly $\varepsilon_{V,s}$, we adopt two approaches:

- global DVC on the whole image ($\varepsilon_{V,s}(t) = \det(\mathbf{F}_s(t)) - 1$);
- sample height variation deduced from the vertical displacement of the grains, taking advantage of the oedometric experimental conditions that do not allow radial strain of the sample (see Section 2.3.2).

3.1.5 Inter-particle contact detection, orientation and areas

This study aims to investigate the effects of water content on the contact network and the contact areas, besides the volumetric response of the microstructure. As mentioned in Chapter 1 (Section 1.1.3), the contact area between particles is an indicator of the agglomeration of the system, thus it is an underlying feature of the overall decrease of flow properties in water-sensitive granular materials.

The contact analysis of the assemblies is carried out in two steps: contact detection and contact areas measurement.

An approach to detect whether two neighbouring particles are in contact could be performed using the labelled image [Saa+05; DAAR16]. If any voxel of a particle i touches a particle j , it can be assumed that the two particles are in contact.

However, Wiebicke *et al.* [Wie+17] recently proved that the contact detection based on the labelled image can largely overestimate the number of contacts. In the study, images of 3D spheres were analytically produced [TA15], thus their position and geometry could be perfectly controlled. Different thresholding values were used to binarise the artificial gray-scale images. The image noise and blur, the spatial resolution and the partial volume effect influence the detection algorithms, so that for relatively small particle distance, but higher than zero, a contact is inevitably detected, and the algorithm overestimates the number of contacts. This issue can be mitigated employing a higher thresholding value than the one used for the binarisation (see Figure 3.6). Specifically for the spheres case, on a normalised histogram, where the void peak is set to 0.25 and solid peak to 0.75, the optimal threshold was found to be below 0.7, a value for which the number of contacts would be underestimated.

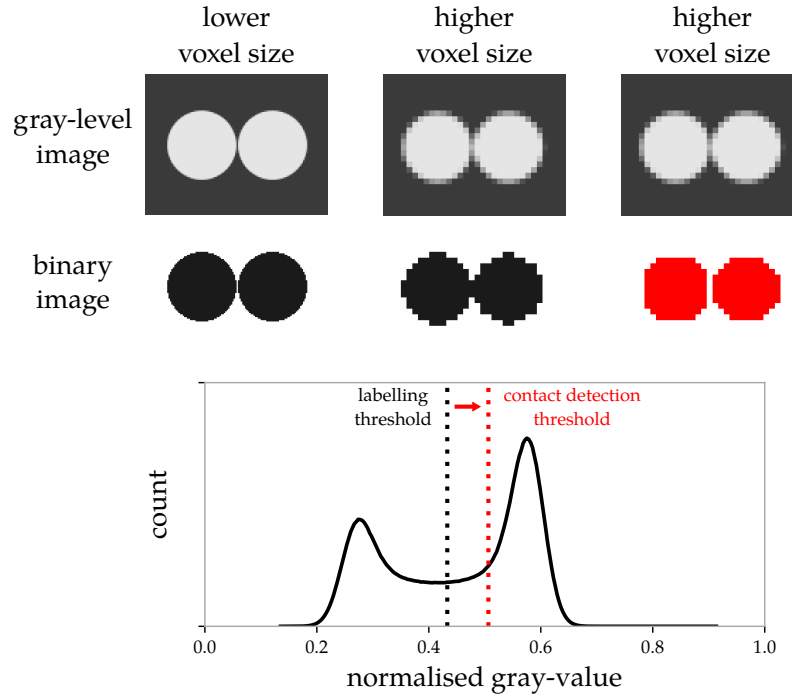


FIGURE 3.6: Use of higher thresholding value for inter-particle contact detection. The use of the labelling threshold can be overestimate the number of contact, especially when the image resolution is relatively low. This issue can be mitigated employing a higher threshold for the contact detection.

Once the contacts are detected, their orientation is computed. This can be achieved by performing a Principal Component Analysis (PCA) of the contact plane between the two contacting labels. In one case, the intersection of two labels in the labelled image can be employed, yet it has been shown that this approach is prone to rather significant error measurements [Wie+17]. Therefore, the use of the Random Walker (RW) segmentation algorithm is recommended [Jaq+13]. Considering two contacting particles, the algorithm creates a probability map of the contact region, assigning to each voxel a value that describes the probability of belonging to either label. The voxels characterised by (almost) equivalent probability ($p_i(\text{voxel}) = p_j(\text{voxel})$), define the contact plane, of which again a PCA is performed. Finally, the normal vector to the contact plane is computed and it describes the contact orientation.

The approach used in this work to assess the contact areas is rather simple. If a contact between two particles i and j is detected, the particle i is dilated once, *i.e.*, the particle volume is augmented by a shell of 1 voxel thickness. The contact area between particle i and particle j is estimated as the number of voxels described by the intersection of the dilated label of i and the label of j (see Figure 3.7).

It can be evinced that the contact area measurement is influenced by the orientation of the contact with respect to the image coordinates. This issue is neglected in this study, and the contact area measurement approach should be refined in the future.

3.1.6 Analysis of multi-modal images

Simultaneous x-ray and neutron tomography allow the observation of the evolution of the microstructure of samples from different perspectives. As detailed in Chapter 2, x-ray tomography images are essentially material density maps and well describe the solid structure of

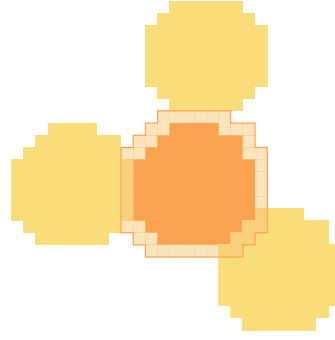


FIGURE 3.7: Contact area measurement approach. Upon contact detection, a reference particle (orange label) is dilated once. The contact area is computed as the number of voxels intersected by the label dilation and each neighbouring particle (yellow labels).

the observed object, while neutron tomography returns, in this study case, hydrogen density maps, from which the variation of water content can be deduced.

To take full advantage of the potential that this technique has to offer, it is essential to spatially correlate the two sets of images, so that the morphology measurements performed on one modality images can be transferred to the other.

Multi-modal registration (MMR)

Multi-modal registration (MMR) is an image analysis tool that allows the correlation of images acquired with different modalities, *e.g.*, x-ray tomography, neutron tomography, magnetic resonance imaging.

MMR can be considered the generalisation of the DVC problem, which is detailed in Section 3.1.3. Its formulation, proposed by Tudisco *et al.* [Tud+17] and implemented in Roubin *et al.* [RAR19], aims to find a transformation function Φ_{MMR} that deforms one modality image f_B so that it matches the other modality image f_A . However, the regular image correlation cannot be applied directly in this case, due to inconsistencies between the gray-values of the images.

That is why MMR computes the *joint histogram*, which is obtained from the gray-values probability distributions of the two images that are being correlated. As shown in Figure 3.8, in our study case of couscous particles investigation, it is rather easy to determine the presence of two peaks (thus phases), which can be traced back to the peaks in the gray-value distributions of the x-ray and neutron images. More generally, when the phases in the system are coarsely distributed (*i.e.*, their gray-values are rather different), the joint histogram hints their total number. It should be noted however, that phases characterised by a relatively small count number might be lost if the images are not properly aligned. It is therefore common practice to “correlate by eye” the images, in order to recognise the presence of minor phases and obviously support the registration algorithm [RAR19].

In addition, the joint histogram can be used to quantify the similarity (or likelihood) \mathcal{L} between images acquired from different modalities:

$$\mathcal{L} = \prod_{x \in \Omega} p(\lambda(x)) \quad (3.16)$$

where Ω is the region of interest (or domain) over which the MMR is computed, and $\lambda(x)$ refers to the images attenuation fields, and $p(\lambda)$ is the joint histogram.

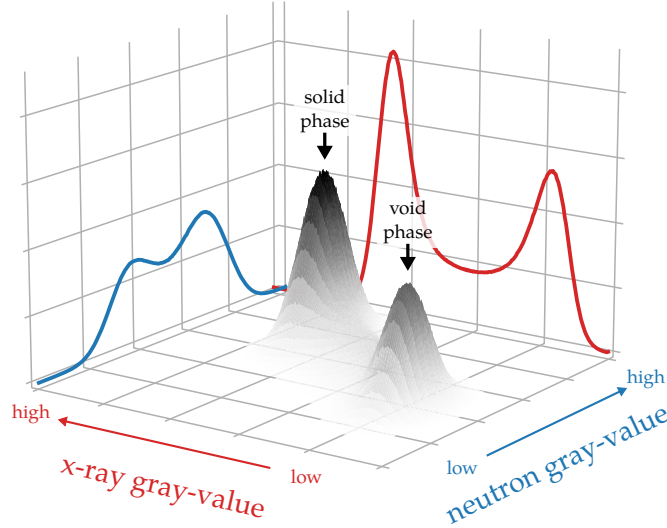


FIGURE 3.8: Joint histogram built with a x-ray (red) and the neutron (blue) gray-value histograms of couscous tomography images. Two peaks can be observed, corresponding to two phases: void/air at low gray-values and solid/particles(+absorbed water) at higher gray-values. This joint histogram is employed in the multi-modal registration (MMR) algorithm to correlate the two images.

In the discrete case, the logarithmic value of the likelihood is expressed as [Tud+17]:

$$\ln(\mathcal{L}) = \sum_{x \in \Omega} \ln(p(\lambda(x))) + \text{constant} \quad (3.17)$$

The objective of MMR is to maximise the likelihood logarithmic value $\ln(\mathcal{L})$, and this can be done by maximising the probability of $p(\lambda)$.

Next, MMR fits N bivariate Gaussian distributions over the joint histogram, where N is the number of assumed phases in the system.

Then, the MMR algorithm essentially determines the transformation function Φ_{MMR} in the same way as for the DVC, as detailed previously. Specifically, the functional \mathcal{T} which expresses the match quality between the images f_A and f_B is written as:

$$\mathcal{T}(\Phi^{MMR}) = \sum_{x \in \Omega} \Lambda^2(f_A(x), f_B(\Phi^{MMR} \cdot x)) \quad (3.18)$$

where:

$$\Lambda^2(\lambda) = -\ln(p(\lambda)) \quad (3.19)$$

which confirms the crucial role played by the joint histogram in the formulation. To be noted that the minus sign is added so to have a minimisation problem, similarly to DVC.

An example of MMR is shown in Figure 3.9, where an image obtained with x-ray tomography and one with neutron tomography are correlated. Prior MMR the images are not aligned. After computing the transformation function Φ_{MMR} , the neutron image is “deformed” and spatially correlated to the x-ray one. Naturally, the MMR operation could be performed so that the x-ray image is deformed to match the neutron one.

Finally, it should be noted that the use of Gaussian distribution to fit the joint histogram and the hypothesised number of phases provides an additional statistically sound segmentation indicator [Tud+17; RAR19], a welcome feature that can be compared to and support the

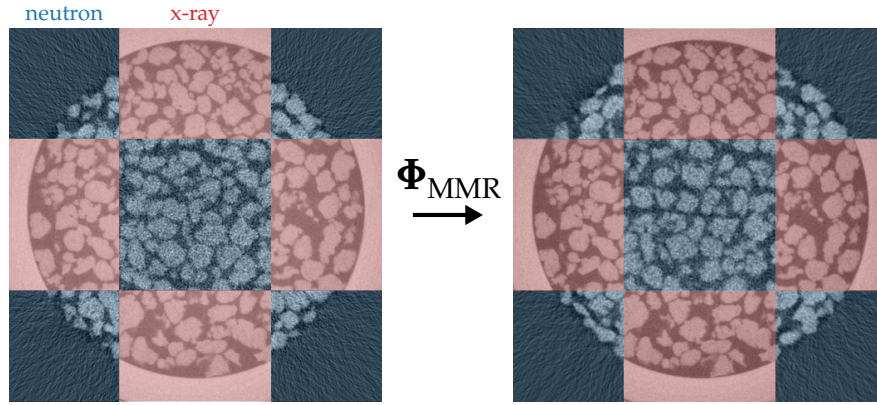


FIGURE 3.9: Result of the multi-modal registration (MMR) algorithm. A transformation function Φ_{MMR} is determined so to spatially correlate images acquired with different techniques, *e.g.*, x-ray (red) and neutron (blue) tomography.

binarisation *via* thresholding method.

Particle attenuation

Of particular interest for this study is the particle attenuation variation in time. As mentioned earlier, x-ray and neutron tomography describe different properties of the microstructure of the analysed samples.

MMR allows for the use of a common coordinate system between the images acquired with different modalities. Therefore, it is possible to compare the gray-values (thus attenuation) of specific regions in the sample, [Tud+17; RAR19; Sta+20b], such as the individual labels. Specifically, we define the global particle x-ray attenuation $\psi_{xr,p}$ as:

$$\psi_{xr,p}(\mathbf{x}) = \sum_{\mathbf{x} \in P} \mu_{xr}(\mathbf{x}) \quad (3.20)$$

while the global particle neutron attenuation $\psi_{ne,p}$ is:

$$\psi_{ne,p}(\mathbf{x}) = \sum_{\mathbf{x} \in P} \mu_{ne}(\mathbf{x}) \quad (3.21)$$

where P indicates the region of interest described by a label, while $\mu_{xr}(\mathbf{x})$ and $\mu_{ne}(\mathbf{x})$ the gray-value (attenuation) of a voxel of coordinates \mathbf{x} , respectively in the x-ray and the neutron images.

3.2 TD-NMR relaxometry

Time-domain nuclear magnetic resonance (TD-NMR) is a technique that allows the investigation of the water uptake in the system and to observe the molecular relaxation with water adsorption, as previously detailed in Chapter 2.

This section presents the analysis approach employed in this work for the analysis of the TD-NMR data, in particular of the FID-CPMG magnetisation decays and their evolution between sequential acquisitions.

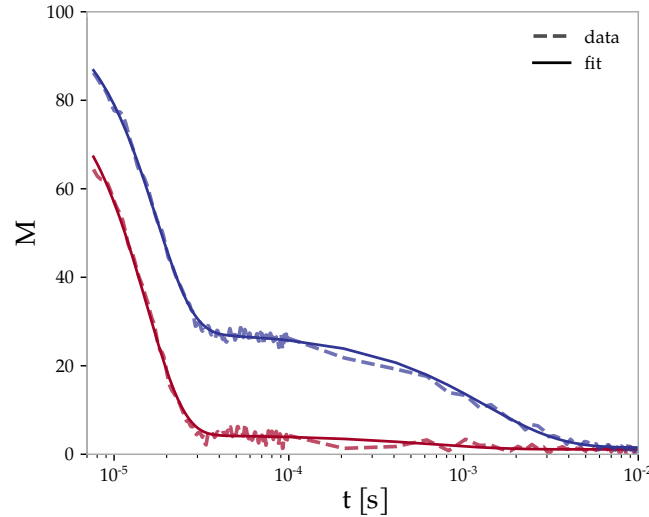


FIGURE 3.10: TD-NMR experimental data analysis. The FID-CPMG decays of magnetisation M obtained from the tests (dashed lines) are fitted with the function in Equation 3.22 (solid line).

3.2.1 FID-CPMG decay analysis

The approach proposed by Trezza *et al.* [Tre+06] suggests to analyse the FID-CPMG decay of magnetisation M by fitting the experimental data with a summation of exponential, Gaussian and “Abragam sinc” [Abr61] functions. The method is based on empirical observations, that demonstrated that specific components show a decay that can be described by one of the mentioned functions. Typically, the populations of nuclei are characterised by the analysis of spectra obtained with the inverse Fourier transform.

In this study, we employ a simplified version of this approach, as the objective of the TD-NMR experiments is simply to capture the water uptake and the associated molecular relaxation, and not to meticulously distinguish all the chemical components of couscous particles, *e.g.*, starch, proteins, oil. Instead of using the whole summation of functions of Trezza *et al.* [Tre+06], the problem is reduced to the analysis of three main terms in the system: solid fraction, semi-solid/liquid-like (*i.e.*, bound water) fraction, and highly mobile (unbound water and oil) fraction. It is deduced that three components are adequate to fit the magnetisation decays, since using more than three did not reduce the residual signal.

The M decay acquired experimentally is therefore fitted with the following function:

$$M(t) = S \cdot e^{-0.5\left(\frac{t}{T_{2,S}}\right)^2} + L \cdot e^{-\frac{t}{T_{2,L}}} + F \quad (3.22)$$

where:

- S represents the signal amplitude of the solid fraction in the system, and $T_{2,S}$ is its respective T_2 relaxation time. The decay of tightly bound ^1H protons is described by a Gaussian function;
- L represents the signal amplitude of the semi-solid/liquid-like fraction (*i.e.*, bound water molecules), and $T_{2,L}$ its associated relaxation time. The function typically employed to describe the M decay of semi-solid fraction is the exponential;

- F represents the signal amplitude of the unbound water and oil fraction. It is here treated as a constant, as no increase of signal is expected from this fraction.

Figure 3.10 shows the result of the fitting procedure for two magnetisation decay curves obtained with TD-NMR. Good agreement is found between the experimental data and the analytical fitting. Further details can be found in Chapter 5, where the results of the TD-NMR experiments are discussed.

Chapter 4

The effect of high RH on a network of water-sensitive particles (couscous)

From the literature review and from the discussions with our industrial partner, it emerges that one of the key features that is currently missing to improve our understanding of the hydromechanics of water-sensitive granular materials is the connection of particle-scale behaviour and phenomena to the overall bulk response [FA05; Car+16; Zaf+17]. Only few studies have focused on the interaction of particles, and often on different and very specific materials (see Chapter 1). For all that, it would be illogical to massively collect data of all the numerous (and growing in number) materials that can be considered as water-sensitive. Instead, it is necessary to understand the underlying processes occurring when such materials are exposed to water.

Nevertheless, to investigate the particle-scale interactions and the related hydro-mechanical processes we need a reference material for our experiments. As mentioned in Chapter 2 (Section 2.1.1), several options could be considered, but finally couscous is selected, since it possesses some critical features that characterise water-sensitive granular materials.

This chapter presents – in the form of a (published) paper – the experimental campaign that can be regarded as the culmination of the material selection process. Specifically, its goal is to observe the phenomenology of an assembly of couscous particles exposed to high relative humidity, by means of (“only”) *in-situ* x-ray tomography (3D images + time).

Full article title

The effect of high relative humidity on a network of water-sensitive particles (couscous) as revealed by *in situ* X-ray tomography

Article status

We submitted the article to the *Soft Matter* journal on March 11th, 2022. It was accepted on May 24th of the same year and published a week later.

DOI: [10.1039/D2SM00322H](https://doi.org/10.1039/D2SM00322H)

Authors

Ilija Vego,^a Alessandro Tengattini,^a Edward Andò,^b Nicolas Lenoir,^a and Gioacchino Viggiani^a

^a Univ. Grenoble Alpes, Grenoble INP, CNRS, 3SR, F-38000 Grenoble, France.

^b EPFL Center for Imaging, École Polytechnique Fédérale de Lausanne (EPFL), Lausanne, Switzerland.

Abstract

Water significantly influences the mechanical behaviour of all granular materials but none as much as hygroscopic amorphous particles. With sufficiently high water content, particles can swell, agglomerate and their mechanical properties can be reduced, having direct effects on the macroscopic response of the material. In food and pharmaceutical industry this can cause loss of product functionality. Despite their relevance, very little is known about the microscopic processes that induce these phenomena. Previous studies focused on single particle behaviour, the strength of agglomerated particles or the material flowability, leaving unexplored the link connecting the particle behaviour and the bulk response. This experimental study aims to investigate this aspect with quantitative measurement at both particle and macroscopic scales. A sample of fine couscous is exposed to high relative humidity (RH) air flow, while being subjected to oedometric conditions, in order to reproduce storage-silo conditions. In the meantime, x-ray tomographies are acquired continuously and the resulting images analysed. The designed spatial resolution allows each particle of the sample to be identified, tracked, allowing volumetric evolution to be compared to the properties of the whole sample. The analysis reveals a dilation-compaction macroscopic behaviour, a result of the competition between the particles swelling and the higher deformability as water content increases. The number, orientations and inter-particle contacts are computed. Their area is related to the applied boundary conditions, and found to be consistent with the particles swelling and dependent on the applied stress direction.

4.1 Introduction

Chemo-hydro-mechanical couplings strongly affect the behaviour of granular materials. While the role played by water in an assembly of impermeable particles has been exhaustively studied (*e.g.*, partially saturated soil mechanics [FR93]), the behaviour of many materials is severely affected by water, either in liquid or gaseous state. Such materials can be defined as *water-sensitive*, and are very common, notably in the food or pharmaceutical industries (*e.g.*, cereals, sugar, salt, excipients). When they are exposed to variations of humidity or moisture their properties can drastically change [AVK95; BAC21; CB14; FA05; Zaf+17].

This variation of properties is driven by a variety of particle-scale phenomena, several of which have been investigated in dedicated studies. For example the volume of individual lentil seeds has been observed to grow with the water content [AHR04]. Similar responses were observed for rice and wheat grains [MS79; Tab03] or even smaller particles, such as Microcrystalline Cellulose Granules [SFS11]. Stiffness and strength are also significantly affected by the water content. Compression tests on cylindrical specimen extracted from wheat kernels highlighted a reduction of both Young's modulus and bearing capacity up to 12% [Fig+11;

GYP91]. A similar behaviour was also observed for individual rice particles [Kam+02]. Different water-content of Microcrystalline Cellulose Granules can also alter the final tensile strength of pharmaceutical tablets [SFS11]. Another process often occurring in water-sensitive materials is the release of starch or mucilage [SM98; Sid+86], which can bridge particles or seeds, thus adding cohesion. Experimental evidence from humidity cycles reveals the non-reversibility of some of these processes [BAC21], leading to the creation of particle fissures, lowering their strength and thus their functionality or customer appeal [SK82]. Most of the aforementioned works focus on the behaviour of individual water-sensitive particles but do not explore the effect that these particle-scale processes have on an assembly. However, in ordinary circumstances, these particles are stored, processed, and interact with, many others. The focus of this work is to study the response of a particle assembly. Notably, one of the key industrial challenges is caking, a deleterious phenomenon caused by the agglomeration of particles. When caking occurs, the particles stop behaving discretely and start exhibiting a solid-like response, critically reducing the flowability and thus functionality [AVK95; Eme+09; JE+17; Zaf+17].

At the molecular level, the reduction of mechanical properties is driven by the evolution of the glass transition temperature, *i.e.*, the transition from a brittle, glassy response to a more viscous one. This is typical in amorphous materials, to which water-sensitive materials generally belong. An increase in water content lowers this glass transition temperature, which can go below the environmental one [AVK95; Zaf+17]. At the particle contact scale this induces inter- and intra-granular plastic deformation, and an increase in contact areas and cohesion [AVK95; Zaf+17]. When this occurs, the assembly transitions from a granular to a 'solid-like' response, leading to major engineering challenges [AVK95; FA05; Zaf+17], and reducing its quality [FA05; SK82].

The aforementioned studies have focused either on the single particle response [AHR04; Fig+11; GYP91; Kam+02; MS79; Tab03], on the macroscopic effect of caking on material flowability properties [CB14; Eme+09; Fit+07; JE+17; Lum+16] or on the hydro-mechanical processes caused by caking over a powder assembly [BAC21; Chr+06; Zaf+17], for numerous materials and environmental and mechanical conditions. As highlighted in a recent comprehensive review, one of the key missing elements is the link between the single particle and bulk behaviour [Zaf+17], which is exactly the main focus of the current contribution.

Specifically this study explores the particle-scale processes that lead to caking, by following an assembly of 2200 couscous particles in 4D (3D+time) through x-ray tomography. This non-destructive technique allowed the tracking of each particle and the corresponding contacts while the sample is subjected to a significant increase of humidity ($> 90\%$) under constant axial load and zero radial strain deformation (so-called oedometric conditions) with *operando* imaging for 103 hours. These conditions are chosen as an analogue to a real-life industrial scenario such as in a silo storage, where the decrease of the glass transition temperature triggers the phenomena that entail caking.

Section 4.2 presents the chosen material, the experimental setup as well as the imaging acquisition settings. Section 4.3 presents the main results of the study. At the sample level (macroscopic), porosity and volumetric strain are quantified. Next, the particle tracking technique is introduced, together with the sample kinematics. Finally, particle number, orientation and size along the test is presented. The conclusions are summarised in Section 4.4, together with possible future developments.

4.2 Experimental campaign

4.2.1 Material

The material selected for this experimental study is fine couscous. Couscous is specifically selected because it presents several interesting micro-mechanical phenomena at the particle scale; notably its particles can swell, they can develop agglomeration (contact adhesion), and their mechanical properties (stiffness, strength) depend on water content. While these features are common in several other materials, additional processes (*e.g.* peeling, highly concave shapes, flat inter-particle contacts) can make the analysis of the images cumbersome. Additionally, the size of fine couscous (about 0.9 mm equivalent diameter) is well within the spatial and temporal resolution of the used imaging system, allowing grain scale analyses.

4.2.2 Experimental conditions

Oedometric conditions are selected to represent in fact the natural conditions in a storage silo, 1.3 g of particles are poured in a rigid (PEEK) cylindrical cell of 16 mm diameter, to give a 8 mm tall sample, with an initial porosity of 50% . To mimic the stress state that could be found in a silo, a dead load applies 25 kPa by means of a metallic ram (corresponding to a depth of approximately 4 meters), with displacement allowed on only one side of the cell (see Figure 4.1).

The sample is subjected to a constant flow of air at 15 mL/min and a relative humidity (RH) in between 95 and 97% depending on room temperature. The temperature is servo-controlled within the experimental room to $24 \pm 1\text{ }^\circ\text{C}$. The humidity is imposed via a peristaltic pump connected to a RH chamber, which contains a saturated saline solution of potassium sulphate, prepared by mixing 115 g of salt in 1 L of demineralised water ($\text{K}_2\text{SO}_4 + \text{H}_2\text{O}$), generating an environment at $97 \pm 1\%$ RH at $20 \div 25\text{ }^\circ\text{C}$ [Gre+77]. This relatively high humidity (when compared to site conditions) is chosen to accelerate the inherent rate of the processes characterising the material, since x-rays scanning time is limited in practice.

In order to allow the flow of the humid air through the sample and prevent particles falling into the air tubes, two high porosity ceramic stones are placed at the boundaries. The diameter of the upper one is slightly lower than the one of the PEEK cell, so as not to obstruct the action of the ram.

4.2.3 Imaging setup

While the sample is being exposed to this high relative humidity air, x-ray tomographies are acquired for about 4 days (103 h) with the tomograph in Laboratoire 3SR (Grenoble, France).

A first tomography is acquired before starting the injection as a reference dry state for the following analyses. Then, the peristaltic pump is turned on and a tomographies are acquired continuously.

Each tomography comprises 1440 projections, each the result of the average of 7 individual acquisitions lasting 0.37 s each, making one single tomography last 1 h . The duration of the acquisition is the result of a compromise spatial and temporal resolution. The voxel-size is of $14\text{ }\mu\text{m}$, in order to have about 64 voxels across a particle.

Each tomography is reconstructed through Feldkamp filtered back projection [FDK84] as implemented in the X-Act reconstruction software by RX-Solutions (Annecy, France), and analysed as detailed in the next sections.

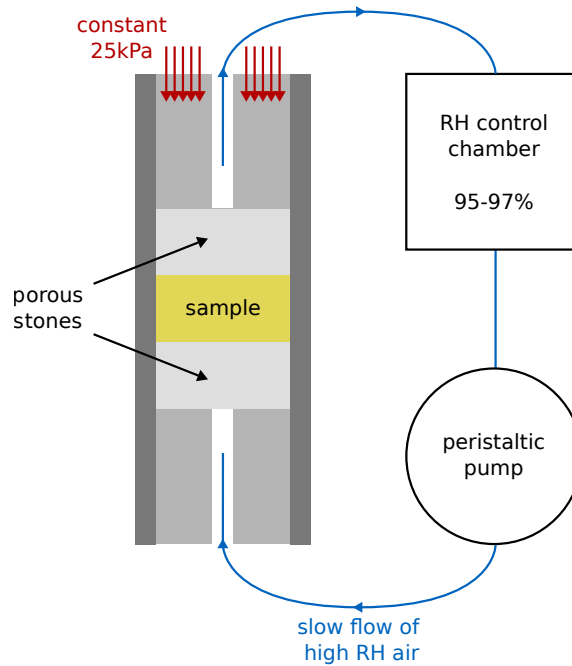


FIGURE 4.1: Sketch of the experimental set-up used to test couscous particles exposed to high levels of RH. The sample is placed in an oedometric cell, subjected to a constant stress of 25 kPa . Meanwhile, a slow flow of high RH air is injected by means of a peristaltic pump from the bottom.

4.3 Image analysis: results and discussion

4.3.1 Raw grey-scale images

A qualitative understanding of the overall process can already be gathered from the reconstructed x-ray tomographies. Figure 4.2 shows a few representative vertical slices of a sequence of 3D images clearly showing a reduction of the porosity, induced by an increase in volume of the individual particles as well as by an overall compaction of the sample.

These reconstructions are simply 3D matrices of attenuation coefficients re-scaled to a 16-bits range. Brighter grey-values are associated with higher attenuation.

The intensity of the x-rays can slightly fluctuate during an experiment, because of minor variations in the x-ray setup. This can be easily compensated assuming that the attenuation of air and of PEEK are constant across the test.

Figure 4.3 shows the histograms of grey-values of the images at different time steps. Each distribution is characterised by two main peaks, corresponding to air and the granular phase, at low and high attenuation/grey-values, respectively. Along the test, the particle swelling and overall sample compaction correspond to a reduction of the counts probability of grey-values typical of voids, matched by a corresponding increase of the solid phase. The peak corresponding to the solid can also be observed to drift to lower values, indicating a progressive decrease in particle density. Nonetheless, the overall sample mass increases by 15% along the test (as measured on a scale before and after the test), due to an increase in water content. This should lead to an *increase* in its grey-values, albeit of modest extent given the very low attenuation of water to x-rays. It can be deduced that the particle dilation is large enough to compensate for this expected increase, resulting in an overall reduction in attenuation. The particle swelling can also be directly measured from the images, as detailed later.

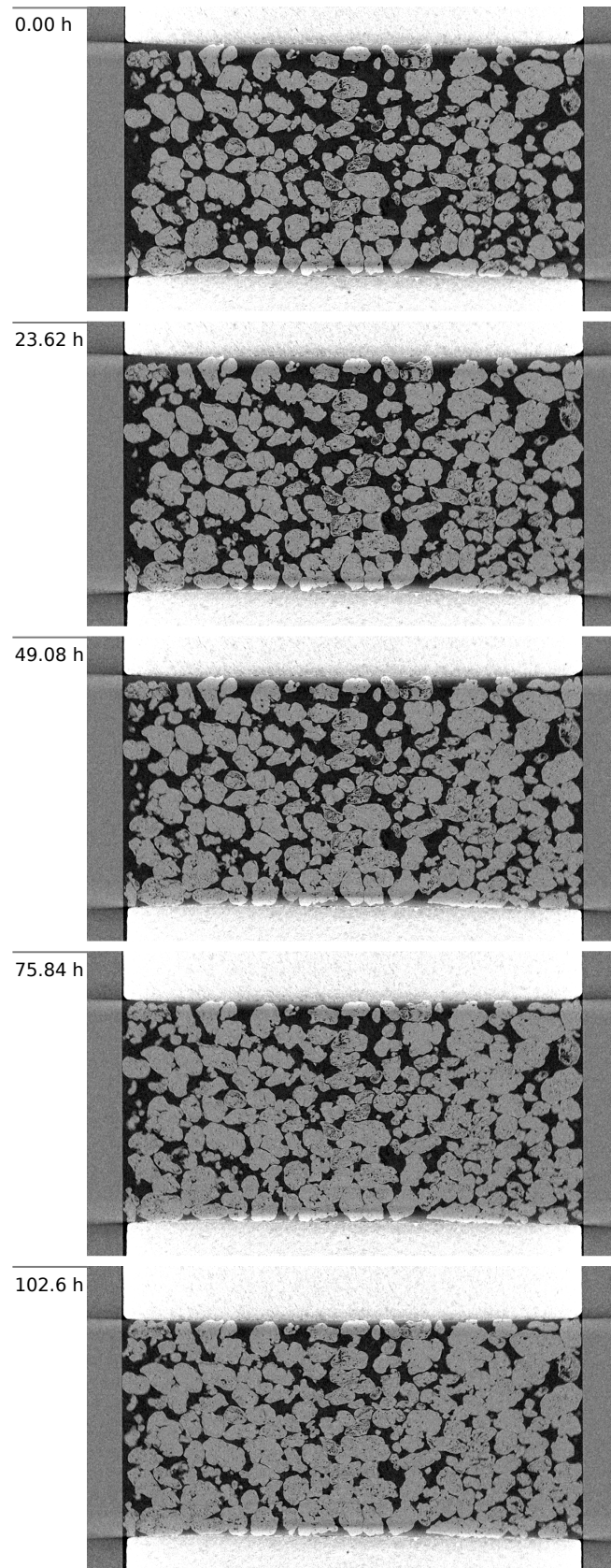


FIGURE 4.2: Vertical slices of 3D grey-scale images of the couscous sample at (from top) 0, 23.62, 49.76, 75.84 and 102.60h hours. The sample porosity decreases as the water adsorption makes the particles swell and become more deformable.

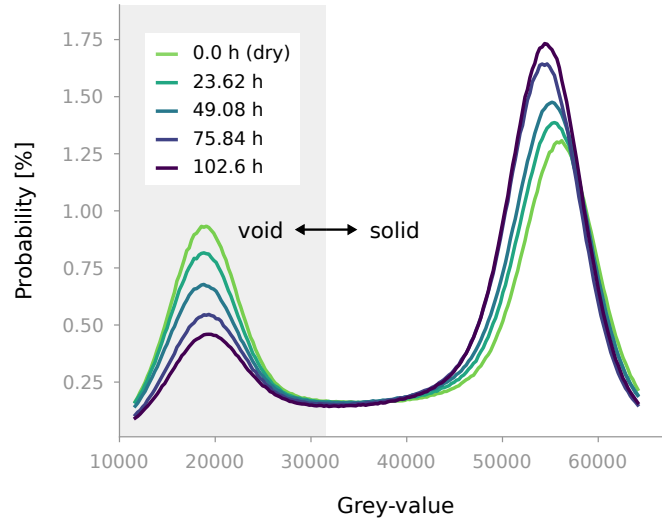


FIGURE 4.3: Grey-values probability distribution of few sequential scans (at 0, 23.62, 49.08, 75.84, and 102.6 h). The probability of finding a voxel belonging to the solid/granular phase increases along the test, while the opposite happens for the void phase. It is noted that low grey-values correspond to dark voxels in Figure 4.2, and vice-versa for the high grey-values, which correspond to particles/porous stones.

4.3.2 Macroscopic sample response

To study the volumetric response of the sample two aspects are of interest, the evolving porosity and the overall sample compaction/dilation. To study the former it is first necessary to identify the granular phases *i.e.*, to “binarise” the sample into void and solid phase. In this case the grey-values of the two phases are sufficiently different from each other that histogram-based techniques are sufficient for this operation. To determine the threshold distinguishing them, Otsu’s method (an approach that minimises the variance between the two classes of voxels) can be applied for the first volume at $t = 0h$ and then maintained throughout the test, since the x-rays fluctuations are compensated – see Section 4.3.1. Once these two phases are differentiated, it is relatively straightforward to measure several properties of the sample, such as the inter-particle porosity, defined as the ratio between the number of “void” voxels outside the grains and the total number of voxels. The evolution of the porosity along the test is reported in blue in Figure 4.4, and can be seen to decrease monotonically with time.

Digital Volume Correlation (DVC) can be used to measure the displacement field in the sample and thus its deformation gradient F . In this work the non-rigid registration implemented in *spam* [Sta+20a] is employed to compute the deformation at each time step with respect to the initial state. Notably, the volumetric strain ϵ_v is measured as $\det(F) - 1$, and is also shown (plain red line) in Figure 4.4.

Unlike porosity, the volumetric strain does not change monotonically during the test. At first, in fact, the sample expands by up to 2.7%, followed by a compaction phase resulting in an overall 5.3% volume reduction, *i.e.*, an 8% compaction from the maximum volume. A possible interpretation of this behaviour is that, while particles with a similar chemo-hydro-mechanical response have a natural tendency to immediately swell in contact with humidity as observed in single-particle studies [AHR04; MS79; Tab03], the variation of their mechanical properties is delayed (as suggested by [GYP91]). This induces a competition between the particles’ natural tendency to swell, which causes the observed initial expansion, and progressive loss of stiffness and strength which yields an overall compaction under the constant applied

load.

4.3.3 Particle-scale response

The spatial resolution of the images is specifically designed to allow the measurement of the kinematics of the individual particles, their deformation, as well as the evolution of the inter-granular contacts. The latter will be discussed in the following Section 4.3.4.

To follow the kinematics of the individual particles it is first necessary to distinguish and assign them a unique label (in this case, an incremental number). This process is sometimes referred to as labelling¹.

Starting from the binary image a distance map can be computed. To each peak of this map is assigned a “seed point”, corresponding to the centre of a particle, which acts as the flooding point of a watershed algorithm [Beu79] as implemented in [Sta+20a]. Ultimately the result of this chain of operations is a matrix where each of the 2230 particles comprising the image is individually labelled. A 3D rendering of the final result is shown in Figure 4.5.

The labelled image of the initial configuration of the sample (dry conditions) is essential to track all particles and measure their kinematics throughout the 4 days of testing. Particle kinematics is measured through discrete digital volume correlation (dDVC), a technique used in granular media for the first time by Hall et al. [Hal+10] in 2010 and now implemented in *spam* [DAD19]. This technique uses the labelled image to create sub-volumes of the reference image and independently performs DIC of each one of these subsets (corresponding to individual particles), measuring for each the displacement vector and interpolating neighbouring nodes to deduce the gradient tensor of each sub-volume. The operation is always performed between the initial reference state and the current one. To accelerate and guide this process, the kinematics measured in the previous step is used as a first guess. In the test presented herein, convergence is reached for all of the 2230 particles, quantifying their displacement, rotation, as well as the internal deformation of each one of them. This information can also be used to guide the labelling process of subsequent scans. The underlying watershed operation can in fact become more cumbersome as the surface of contact between particles increases and the particles start to merge. The moved particles are here instead used as “seeds” to start the watershed algorithms, under the assumption of quasi-staticity of the process.

From these sequential labelled images the volume of each labelled particle can be measured by simply counting the number of voxels comprising it at a given time, thus allowing the computation of the grain-scale volumetric strain. Its evolution can then be compared to the macroscopic volumetric evolution discussed in Section 4.3.2. Figure 4.4 shows how all particles dilate monotonically throughout the test (dashed red line), prompting the initial expansion of the sample, and keep dilating even while the sample macroscopically compacts. The particles dilate by about 20%, significantly less than in free-swelling conditions (where particles can increase by up to 400% in fully submerged conditions, for example De Richter (2022) [DR+22]).

Finally, the spatial distribution of particle swelling and volumetric strain across the sample can be investigated. By “colouring” each particle with a value proportional to its volumetric strain at a given time it can be observed the spatial fluctuations of grain-scale dilation – see Figure 4.6. Specifically, the particles closer to the bottom (*i.e.*, closer to the point of injection of high RH air) swell earlier than the rest, highlighting a gradient of dilation that could be

¹It should be noted that, while the ‘labelling’ naming convention is widespread, it is not universally accepted. This procedure, together with the aforementioned segmentation are at times collectively referred to as segmentation.

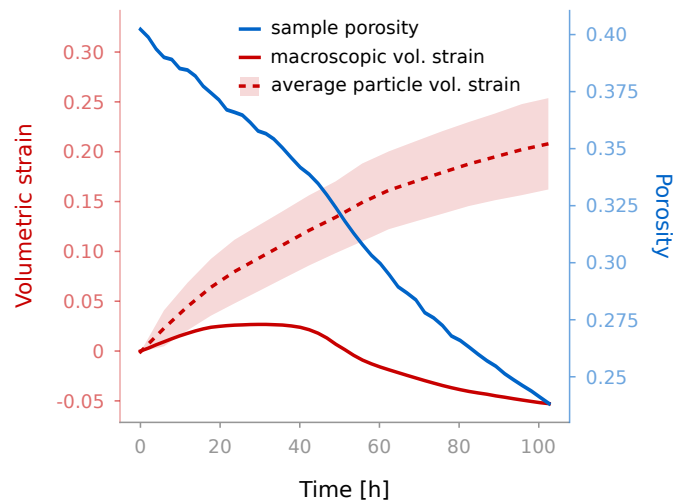


FIGURE 4.4: Sample porosity and volumetric strain evaluations plotted with time. A comparison is made between the average particle and the sample dilation. Despite the monotonic swelling of single particles the sample compacts under the constant stress applied as the increasing water content makes couscous more deformable.

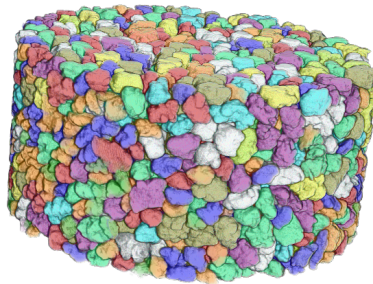


FIGURE 4.5: 3D rendering of the labelled couscous sample. Every single particle has its own label and its kinematics are followed throughout the experiment.

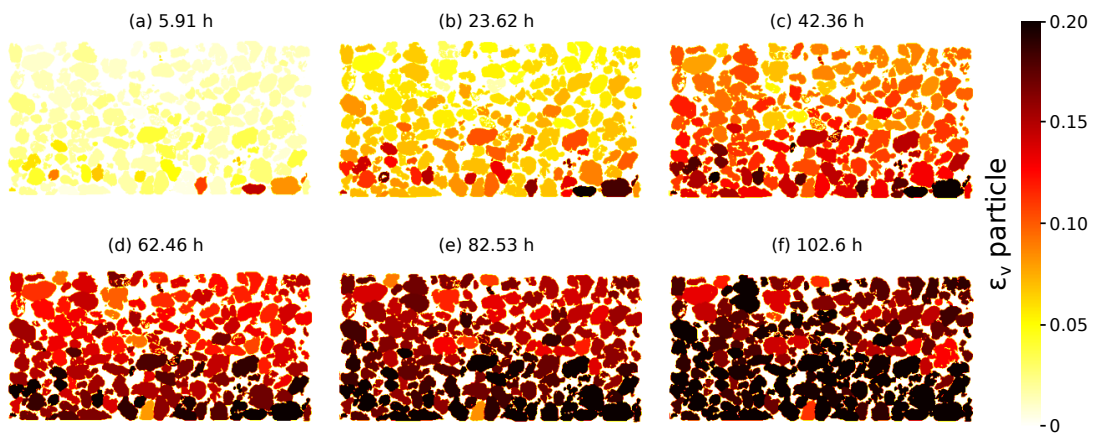


FIGURE 4.6: Maps of the volumetric strain of individual particles throughout the test. A vertical gradient in particle swelling is apparent, with the particles closer to the high RH air injection point dilating earlier than others.

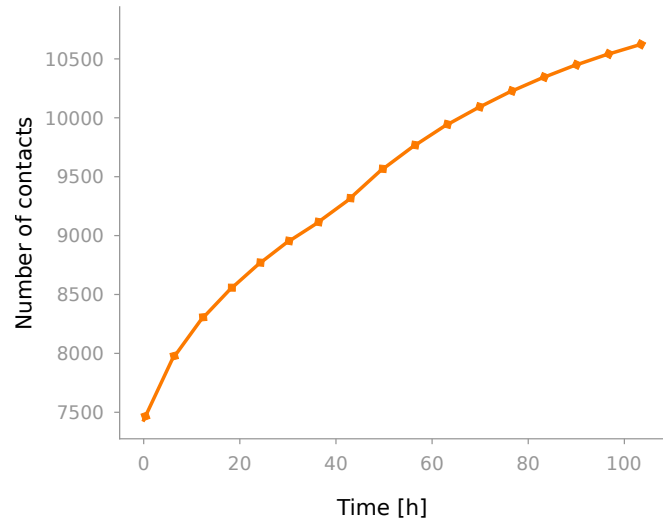


FIGURE 4.7: Number of contacts detected during the 103 hours of testing.

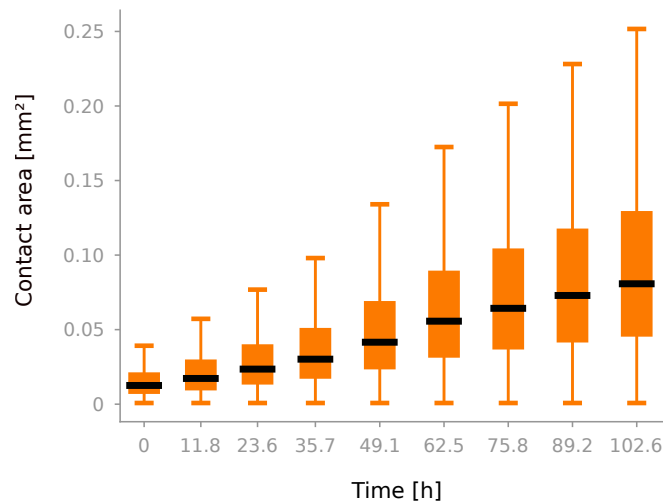


FIGURE 4.8: Box and whiskers plots representing the increase of contact areas of the particles network along time as well as their standard deviation. The black line indicates the median measured value at different time-steps.

associated to a gradient of water-content. This heterogeneity appears to fade towards the end of the test.

4.3.4 Inter-particle contacts analysis

Particle dilatation and higher deformability are key underlying particle-scale processes driving macroscopic agglomeration. Together they induce the macroscopic response detailed in section 4.3.2. This also corresponds to larger contact areas between particles, which in turn increases the adhesion between particles. This likely contributes to the observed increase of overall cohesion of the assembly as well as of the overall cake strength, depending also on the water content of the material [AVK95; Zaf+17].

Given that each individual particle can be tracked throughout the test, the presented dataset also allows the analysis of the evolution of the number of contacts and their areas along the test. A first rough estimate of the contact of a particle to its neighbours can be obtained by simply dilating once (thus adding a 1-voxel thick layer) the labelled particle and verifying

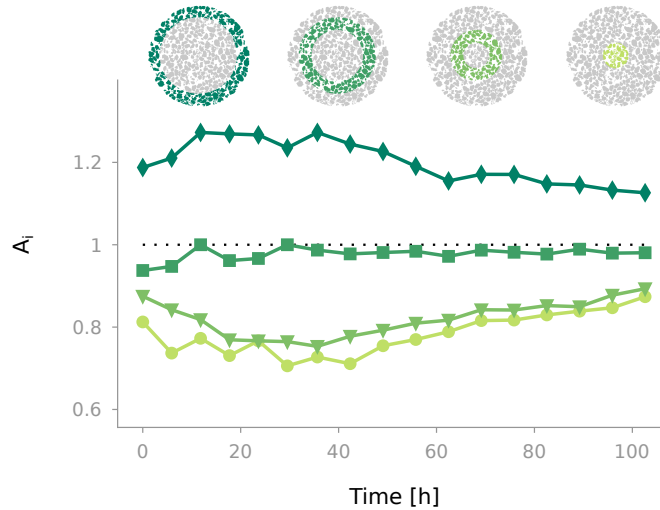


FIGURE 4.9: Evolution of the median area ratio A_i in concentric radial rings. This reveals a modest influence of the radial position in the sample.

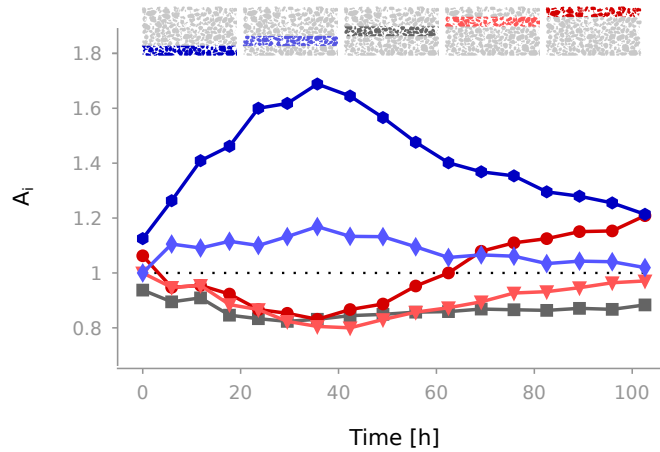


FIGURE 4.10: Evolution of the median area ratio A_i along the height of the sample. Contact areas closer to the high RH air injection point initially increase faster than the rest of the sample. The tendency is then inverted during the macroscopic compression stage.

which other particles it is intersecting. However, it was observed that a simple use of labelled images as a reference results in an overestimation of the number of actual contacts [Wie+17]. Specifically, it was observed that when thresholding particles, the threshold chosen is generally slightly overestimated, thus spuriously increasing their volume and thus their contacts. While the effect on particle volumes is generally negligible, the effect on the contact area can be more significant. To compensate this, and to reduce erroneously attributed contacts, the local grey-value threshold in the normalised histogram is here increased from 0.55 to 0.65 (where the void peak is set to 0.25 and the solid to 0.75), close to the value optimised for spheres [Wie+17].

Figure 4.7 reveals a monotonic increase of the number of contacts in the assembly along the test.

It should be noted that all contacts between particles both belonging to horizontal layers at the ends of the sample are not taken into account for the following analysis, because of the artefacts caused by interaction of the conic beam with the highly attenuating porous stones (compared to the particles or the PEEK cell, see Figure 4.2).

Beside counting the number of contacts, it is of interest to study the evolution of the contact areas. To determine the number of voxels belonging to the detected contacts, the reference label can be dilated once to determine the number of voxels now intersecting the neighbouring particle. This can of course be then converted to mm^2 considering the voxel size.

Figure 4.8 presents the measured evolution of the contact areas throughout the test. The median area of contact increases monotonically with time, and so does also the variance. The area of existing contacts generally always increases, but at the same time new contacts are established and they generally start as small contacts (≈ 1 voxel).

The contact area growth is influenced by several factors, such as the water-content of the particle as well as its boundary conditions, and may vary depending on the particle position inside the sample. To analyse possible inhomogeneities a new variable A_i is here proposed. For each subset i of the sample, $A_i(t)$ can be calculated as the ratio between the the median area within the region at time t and the median across the sample at same time:

$$A_i(t) = \frac{A_{i,median}(t)}{A_{median}(t)} \quad (4.1)$$

It is then possible to study, for example, the radial variation of the area growth A_i , as shown in Figure 4.9. Specifically, four concentric regions are analysed therein, indicating a moderate variation of A_i along a representative horizontal plane. By the end of the test, for each subset, A_i tends toward the asymptotic value of 1, suggesting a tendency towards homogeneity.

Another geometrical factor that could influence the contact areas growth is the vertical position of the contact, *i.e.*, its distance from the injection point. Figure 4.10 shows the evolution of A_i at five different elevations, indicating that there are significant differences in the way the contact area evolves, depending on the distance from the injection point. vertical position, and notably the injection point, highlighted in Figure 4.10. Here the variation of A_i is far more significant. While starting with comparable values, the contact areas in the bottom region (blue and light blue) increase more rapidly than elsewhere the sample. This is consistent with the more pronounced dilation measure in the bottom of the sample, see Section 4.3.3. This suggests that particles closer to injection point swell earlier, showing a faster increase of contact area. However, later in the test, and specifically during the compaction stage, this tendency is inverted and the top subsets (red and pink lines) A_i exhibit an increase of contact areas. The central subset A_i (grey) remains essentially constant along the test, due to its higher distance from the injection point and presumably a lower stress as the upper particles partially unload on the walls of the outer PEEK cell.

Once the contacts have been detected, it is possible also to study their orientation adopting the random walker algorithm, as implemented in *spam* [Jaq+13]. This orientation can be described by the unit normal vector to the plane interpolating the contact surface. For example an horizontal contact would have an orientation vector coaxial to the vertical axis.

The frequency of contact orientation vectors can be represented using a spherical histogram [Sta+20a]. This simply represents the frequency of contact orientations falling within a solid angle, represented as a pyramid pointing towards the centre of the plot and whose height is proportional to their occurrence. The histograms in Figure 4.11 show that in dry conditions there is a higher occurrence of horizontal contact (*i.e.*, vertical vectors). This anisotropy progressively fades as new contacts are generated, up to an essentially isotropic distribution.

It is also interesting to observe that contact orientation affects the contact area growth. To study this, contacts are classified in three groups based on their acute angle θ with respect to the vertical axis. Each group covers 30° as sketched in Figure 4.12.

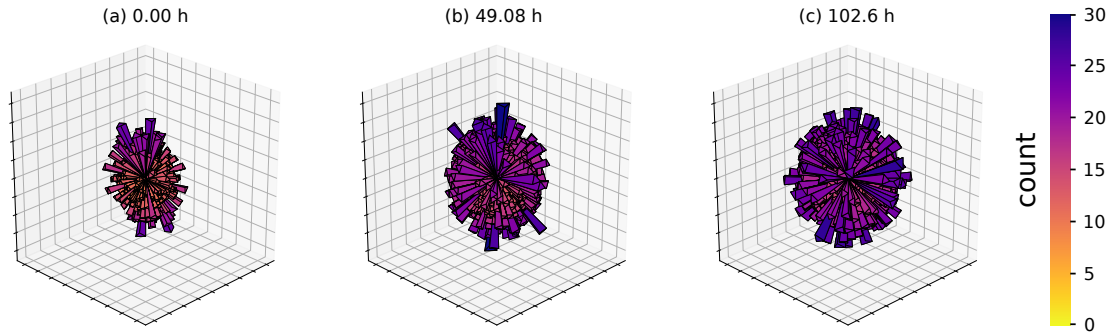


FIGURE 4.11: Spherical histogram of inter-particle contacts in dry conditions (0.0 hours) and after the high RH injection at 49.08 and 102.60 h. The slight contact orientation anisotropy at the beginning of the test disappears as new contacts are generated.

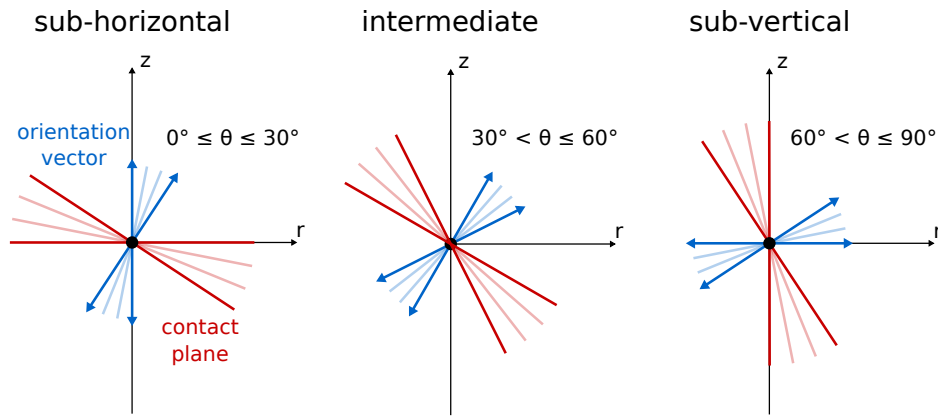


FIGURE 4.12: 2D sketches of the contact orientation angles with respect to the vertical axis, grouped here in three: $0^\circ \leq \theta \leq 30^\circ$, $30^\circ < \theta \leq 60^\circ$ and $60^\circ < \theta \leq 90^\circ$

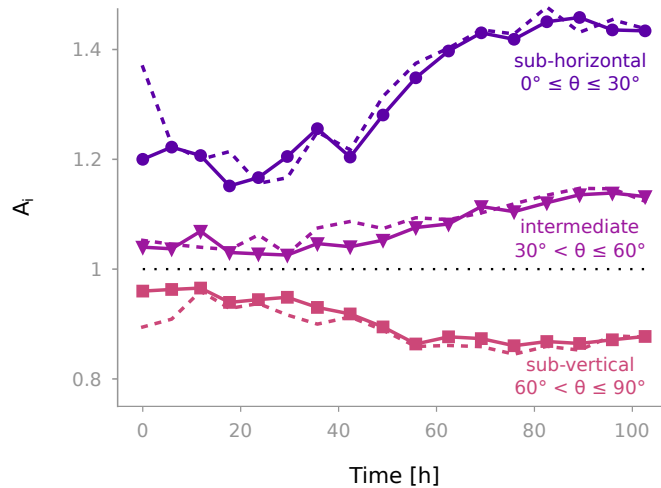


FIGURE 4.13: Evolution of the median area ratio A_i for the three chosen contact orientations subsets. Sub-horizontal contacts are the largest and tend to increase during compaction, while the opposite behaviour is observed for contacts sub-vertical contacts. The same analysis is also performed only for persistent contacts (dashed lines). The evolution of A_i does not vary significantly, except for the initial values in dry conditions, proving that the initial contact anisotropy does not affect the load-dependent increase of contact areas.

Figure 4.13 shows that initially sub-horizontal contacts have larger areas, which combined with the higher frequency of this subgroup (Figure 4.11) suggests an influence of the boundary conditions and ensuing stress transmission. However, while the sample is expanding (*i.e.*, before the particles become more deformable), the difference in total number of contacts between the subgroups does not influence their trend, as their A_i values remain rather constant. However, as soon as the sample starts compacting, sub-horizontal contacts make up a progressively larger fraction of the overall contact area. This indicates how the areas of the contacts coaxial to the loading direction tend to grow more than others. Sub-vertical contacts progressively make up a smaller fraction of the total, while the intermediate ones tend to increase once the sub-vertical ones level off.

The analysis is then repeated only for the persistent contacts (*i.e.*, contacts that persist throughout the whole test). As shown in Figure 4.13 with dashed lines, the evolution of the median ratio of each orientation sub-group does not differ from the non-persistent ones. Moreover, in dry conditions, sub-horizontal contacts have a larger total area (as discussed earlier, Figure 4.11). The difference mitigates during the macroscopic dilation and it emerges again with the following compaction. This again suggests how the increase of sub-horizontal contact areas is induced by the direction of the applied stress, but only during the compaction stage.

4.4 Conclusions and perspectives

This experimental study attempts to study the panoply of complex particle-scale processes occurring in water-sensitive materials exposed to relatively high humidity, and to connect them to volumetric response at the macro level, *i.e.*, at the scale of a particle assembly. To the best of the authors' knowledge it is a first attempt at following a particle assembly and connecting particle-scale a non-trivial macroscopic response.

Macroscopically, the sample gains mass through water adsorption. Overall, the samples undergoes an initial dilation followed by compaction, as the couscous particles become more deformable with higher water content. The individual particles agglomerate into a *caked* pellet, thus losing their discrete granular nature which drives their response in dry conditions.

The particle-scale measurements presented herein provide a unique insight into the particle-scale processes thanks to the use of x-ray micro tomography. Bespoke algorithms are adapted or developed to quantify two key aspects: inter and intra-granular volumetric response and contact fabric evolution.

Couscous particles swell throughout the entire test. Nonetheless, after a certain humidity is adsorbed, they become more deformable. This competition is at the root of the aforementioned inversion in macroscopic volumetric response. The sample compaction adds to the particles swelling to induce a monotonic decrease of porosity. The particle volumetric strain is found to be heterogeneous, perhaps induced by the imposed slow air flow, yielding a vertical swelling gradient from the injection point. The inter-particle contact network is one the main factors influencing the final agglomeration of the sample. Coherently with the particle expansion and macroscopic volumetric response, the total number of contacts increases during the test, as does their area. The radial position of the contacts is found to play a minor role, while their vertical position is observed to influence the speed of contact area expansion.

The contact network is slightly anisotropic at the beginning of the test, albeit it transitioned to isotropic along the test. Nonetheless, the area of sub-horizontal contacts, aligned

transversely to the loading direction, is systematically larger than the rest and increases along the test. Future research will investigate the relation between particles swelling and the water-content, by means of neutron tomography or magnetic resonance imaging (MRI). Furthermore, to better understand the caking phenomenon of the material, it is necessary to quantify its mechanical properties at both the particle and macroscopic scale. Compression tests will be run to assess the effective agglomeration/cohesion of the sample, together with particle-to-particle tests to determine the individual bond strength. These measurements, besides the kinematics presented in this article, will give essential information to implement and calibrate numerical models, so to investigate other features of caking and hopefully predict its occurrence.

Acknowledgements

Laboratoire 3SR is part of the LabEx Tec 21 (Investissements d’Avenir - grant agreement n° ANR-11-LABX-0030). This project has received funding from the European Union’s Horizon 2020 research and innovation program under the Marie Skłodowska-Curie grant agreement No. 812638 (CALIPER).

Conflicts of interest

There are no conflicts to declare.

Author Contributions

- Ilija Vego: Writing - original draft, Visualization, Methodology, Investigation, Conceptualisation, Data curation, Software;
- Alessandro Tengattini: Writing - original draft, Validation, Supervision, Methodology, Investigation, Conceptualisation, Data curation;
- Edward Andò: Writing - review and editing, Software, Funding acquisition;
- Nicolas Lenoir: Investigation, Methodology, Resources;
- Gioacchino Viggiani: Writing - review and editing, Validation, Supervision, Conceptualisation, Methodology, Funding acquisition.

Chapter 5

Heterogeneous swelling of couscous particles exposed to a high RH air

The previous chapter presents an experimental study in which the effects of high RH on the microstructure of an assembly of couscous particles are investigated. The volumetric individual response of thousands of particles and the overall volumetric response of the whole sample are quantified and compared. While each individual particle experiences only swelling, the assembly response undergoes first dilation and then compaction under a constant vertical stress, due to the competition between particle volume increase and the mechanical properties deterioration. A broad statistical analysis is performed to evaluate the contact formation and the growth of contact areas. Altogether, the processes are highly dependent on the imposed boundary conditions. A relatively slow flow of high relative humidity air induces a swelling gradient, even though the sample is relatively short (≈ 8 mm). The contact areas growth is deeply connected to this heterogeneity, but it is found to be strongly influenced by the possible compaction of the sample.

The analysis and results detailed in the previous chapter uncover an interesting behaviour of couscous particles. However, the underlying variable of the observed hydro-mechanical processes is still an unknown of the problem. The water content cannot not be measured simply from x-ray tomography images. The particles attenuation changes with water sorption and it might be argued that the assessment of particle water could be derived from this variation (Section 4.3.1). However, the gray-value (*i.e.*, attenuation) decrease is the result of a density change, to which can contribute numerous factors, such as the size of intra-granular pores and the molecular rearrangement. Therefore, a more direct approach is needed to accurately quantify the variation of water content with time.

This chapter includes a published paper in which we again investigate the behaviour of couscous particles exposed to high RH¹. This time, however, two complementary techniques are used. With the first, data are acquired with TD-NMR to observe and quantify the water uptake of couscous particles, again exposed to high RH. The second campaign is performed under equivalent experimental conditions, and x-ray tomographies are acquired to gather information about the microstructural variations induced by water absorption, following an experimental and analytical approach similar to the one presented in Chapter 4, with two main differences. First, no load is applied to the sample, thus the sample is “free” to swell. Secondly, enough time passes so that system saturates, and no visible variation is detected in water content or microstructure. The final goal is to describe the relationship between particle swelling and increase of water content.

¹For sake of clarity, in this paper we use the term “moisture content”, which is to be considered equivalent to “water content”.

Full article title

Heterogeneous swelling of couscous particles exposed to a high relative humidity air, as revealed by TD-NMR and X-ray tomography

Article status

We submitted the article to the *Food Structure* journal on February 3rd, 2023. It was accepted for publication on June 3rd of the same year and available on-line on June 9th.

DOI: [10.1016/j.foostr.2023.100330](https://doi.org/10.1016/j.foostr.2023.100330)

Authors

Ilija Vego,^a Richard T. Benders,^b Alessandro Tengattini,^{a,c} Frank J. Vergeldt,^d Joshua A. Dijksman,^{b,e} and John P.M. van Duynhoven^{d,e}

^a Univ. Grenoble Alpes, Grenoble INP, CNRS, 3SR, F-38000 Grenoble, France.

^b Physical Chemistry and Soft Matter, Wageningen University & Research, Stippeneng 4, 6708 WE, Wageningen, The Netherlands.

^c Institut Laue-Langevin (ILL), 71 Avenue des Martyrs, 38000 Grenoble, France.

^d Laboratory of Biophysics, Wageningen University & Research, Stippeneng 4, 6708 WE Wageningen, The Netherlands.

^e Van der Waals-Zeeman Institute, Institute of Physics, University of Amsterdam, Science Park 904, 1098 XH Amsterdam, The Netherlands.

^f Unilever Global Foods Innovation Centre, Plantage 14, 6708 WJ Wageningen, The Netherlands.

Abstract

The mechanical behaviour of hygroscopic granular materials is highly influenced by water. The strong dependence of individual particle properties on moisture content affects the response of their packings, which can agglomerate and eventually lead to loss of product functionality. Despite the frequent occurrence of this problem in industry, only few studies tried to explore the underlying phenomena and investigate the fundamental connection between particle and packing behaviour. This work presents an experimental study that aims to link the water uptake to the microstructural changes in assemblies of couscous, a material selected to be representative of hygroscopic granular materials. In the experiments, the samples are exposed to high relative humidity (RH), and the moisture content increase is quantified with TD-NMR, along with the shift in molecular mobility. An analogous test is performed, during which x-ray tomographies are acquired continuously. We analyse the volumetric response of the sample and of thousands of particles. Despite the oversupply of water molecules available to saturate the system, the formation of a swelling heterogeneity is observed, which we attribute to the pressure gradient affecting locally the adsorption kinetics. Combining the results obtained from the two techniques, water uptake and particle swelling are found to be linearly correlated.

5.1 Introduction

The presence of water can significantly affect the behaviour of granular food products. Sugar, seeds, flour are some examples. These are all composed of individual “particles” or “grains” that interact with each other. Hydro-sensitive granular materials can be also found in pharmaceutical industry, where, despite the different application and chemical composition, analogous problems are encountered on a daily basis while processing or storing products.

One of the most common problems encountered during the handling and industrial processing of hygroscopic granular materials, is the accidental moisture content increase due to the mismatch in water activity of those materials with the environment. Water absorption can alter the material properties at the molecular scale, with repercussions at the particle- and, ultimately, the product-scale. The interaction of water molecules with polymer chains inside the hygroscopic materials (e.g., amylose and amylopectin starch chains [SRWG01] and protein matrix) affects their relaxation properties and alters various polymer properties like glass transition temperature T_g [AVK95; Zaf+17]. In granular media, this often translates into particle-scale phenomena such as swelling, release of mucilage, loss of mechanical properties, and creation of fissures. All these have direct effects on the bulk behaviour of the material. The particles can agglomerate or *cake*, a phenomenon that leads to lower product functionality and flowability [AVK95; Car+16; Zaf+17].

Inefficiencies in the supply chain can cause significant loss of resources [RW09; Cha+21], which obviously raises economical and, most importantly, sustainability issues. However, despite the relevance and daily occurrence of the problem, very little is known about the individual particle to product relations, *i.e.*, multi-scale relations, which govern the material behaviour [FA05; Car+16; Zaf+17].

Nuclear magnetic resonance (NMR) is a versatile, non-invasive method that can be used to analyse food stuff in real time at various length scales, ranging from their molecular structure up to the meso-scale [van+10; Hat19]. This technique can be used to understand the fundamental interactions between water and hygroscopic materials. NMR has been extensively used to study drying processes [Pen+20], as well as the absorption of free water by couscous [DR+22]. However, the use of time-domain NMR (TD-NMR) in water vapour-sorption from air at high humidity levels, has received little attention, despite its potential use in understanding the molecular processes that underlie agglomeration and caking in greater detail [Chu+00].

Several studies focused on the behaviour of individual particles. For example, within the domain of food industry, the effects of moisture content increase on the volume or mechanical properties of particles were investigated for lentil seeds [AHR04], rice grains [MS79; SK82; Kam+02; Cao+04; SAH10], wheat kernels [GYP91; Tab03; Fig+11], micro-crystalline cellulose [SFS11], and couscous [Abe+12; DR+22].

The bulk response of hygroscopic materials has also been investigated. For example, the flowability properties for lactose powder were found to be lower in highly dry or highly humid conditions [Lum+16]. Similar responses were observed for micro-crystalline cellulose, pectin, maltodextrin and starch powders [CB14; JE+17]. It was shown that a long exposure to humidity can increase the overall cohesion of different materials and that the agglomeration process is not homogeneous [BAC21].

Few studies have explored the multi-scale relation between hygroscopicity and bulk behaviour. For example, Wahl *et al.* [Wah+08] investigated with experiments and numerical simulations the caking “strength” of a fertiliser (urea prills). The inter-particle contact tensile

strength was measured with respect to the “storage time”, along with the increase of the contact area detected optically. The results were then used to build a contact-dynamics model, which was implemented to numerically simulate the bulk response. Haider *et al.* [Hai+14] carried out experiments to investigate the inter-particle contact genesis in an amorphous reference hydro-sensitive reference material (maltodextrin dextrose) and the role that temperature plays over the contact mechanical strength and morphology. More recently, Vego *et al.* [Veg+22] performed an oedometric test, *i.e.*, radial strain constrained and constant vertical stress, while exposing an assembly of couscous particles to a flow of high relative humidity air to activate the phenomena related to water absorption from the external environment. During the whole experiment, 4D images with x-ray tomography were acquired to explore the effects of humidity and characterise, through image analysis, the microstructural changes such as particle volume and inter-particle contacts, which were found to be correlated and strongly influenced by the applied boundary conditions.

The study of couscous particles can be of great interest, because of its increasing world-wide consumption and production, and also because many other products are made from the same wheat, *e.g.*, pasta [HS20]. Moreover, when in contact with water, couscous presents several of the phenomena described above: its particles absorb water, swell, lose mechanical rigidity and eventually agglomerate [Abe+12; BRC18; DR+22; Veg+22]. Finally, according to *Codex Alimentarius*, couscous particles should have a diameter between $630\ \mu\text{m}$ and $2\ \text{mm}$, which makes them well suited for particle scale measurement in images obtained from the x-ray tomography [Veg+22]. Fine couscous (Ferrero, Groupe Panzani) is selected as a material of interest to perform the study presented in this paper, with the same rationale as in Vego *et al.* [Veg+22]. In this study, the average equivalent particle diameter was found to be $0.9\ \text{mm}$. Moreover, the typical fine couscous size distribution is more representative of the wide range of hygroscopic granular materials [Ham+22], and it provides a larger statistical sample for particle scale measurements. We aim to explore its behaviour when particles are exposed to high relative humidity (RH) environments. By adopting TD-NMR we investigate the water uptake dynamics while also getting insights into whether water gets absorbed or condenses. The complementary use of x-ray tomography allows us to observe swelling kinetics of thousands of particles.

5.2 Material and methods

5.2.1 Gravimetric assessment: experimental procedure

The sorption isotherm of fine couscous is determined at room temperature (20.7 ± 0.5), exposing the particles to air of different relative humidities. The sample mass is continuously recorded by an analytical balance placed inside a plastic, closed container, connected to an conditioned airline, which is equipped with a temperature and relative humidity (RH) sensor (Thorlabs, Inc TSP01 revB). The relative humidity of the air within the setup is servo-controlled by measuring the RH at the sample position and adjusting the humidity of the injected air through an ultrasonic humidifier (Beurer LB12). Specifically, the feedback loop turns on the humidifier when the RH-sensor measures values below the target, thus ensuring control of the RH within the sample chamber. The air pressure is maintained at equilibrium by small holes inside the plastic box, allowing excess air to leak into the surrounding environment.

Initially, the particles are exposed to low humidity air ($11.0 \pm 0.2\%$) for a period of 3 days. Lower RH levels could not be reached due to technical limitations. Afterwards, a series of

12 RH-increments every 24 hours is performed, until reaching a $98.1 \pm 0.5\%$ RH, close to the saturation point of air. Smaller increments are applied when increasing low or high RH levels. The increase in relative humidity of the air, leads to the absorption of water by the couscous particles which is quantified by their change in mass.

Afterwards, the dry matter content m_{dry} of the couscous particles is determined by placing the material in a convection oven for 24 h at 105. The weight loss is then assessed with respect to the mass at the beginning of the experiment [Ros+20]. The moisture content $m.c.$ is determined over the course of the experiment, following Equation 5.1:

$$m.c. = \frac{m_{24h} - m_{dry}}{m_{dry}} \times 100 [\%] \quad (5.1)$$

where m_{24h} is the mass after the 24 h exposure to a specific RH level.

5.2.2 TD-NMR relaxometry

Experimental procedure

At the start of the experiments, couscous particles are dried with a flow of 0% RH air at 21 for 3 days in a sealed vessel. Dry air is used to lower the couscous particles' moisture content, in order to prevent structural changes associated with thermal heating of the couscous in an oven.

Next, the particles are transferred into a custom cylindrical cell made of PTFE with an inner diameter of 7 mm. At the bottom of the probe cell a glass porous stone is placed allowing humid air to pass, while preventing the particles from falling out of the cell. During the experiments, the bed of particles is subjected to a 0.2 L/min flow of 97% RH air, supplied with the same RH unit described in Section 5.2.1. These experimental conditions are selected posterior a preliminary study presented in the Appendix (Section 5.5). A schematic overview of the setup is shown in Figure 5.1.

FID-CPMG decay acquisition

The ^1H NMR transversal relaxation decays are acquired using a combined Free Induction Decay (FID) and Car–Purcell–Meiboom–Gill (CPMG) sequence [Hah53; CP54; MG58]. The first is often used to investigate crystalline or glassy materials, *e.g.*, sugar, characterised by a relatively short T_2 relaxation time, while the CPMG sequence is more suitable for the analysis of liquid-like components, associated with longer T_2 relaxation times [van+10].

In this study, the FID-CPMG decays are acquired using a low-field 20 MHz ^1H (0.47 T) Bruker Minispec MQ20 ND spectrometer equipped with a probehead with a deadtime of $\approx 11 \mu\text{s}$. At this field strength measurements are sufficiently sensitive and the short deadtime allows for assessment of all relevant T_2 NMR relaxation times.

The measurement cell is lowered into the probe head and properly aligned, so that the sample resides within the homogeneous region of the radio-frequency (RF) coil. At the start of the experiment the empty cell is measured to obtain the background signal, *i.e.* signal not associated with the matrix inside the couscous particles (see Figure 5.1a). Next, the dried particles are weighted and transferred into the cell.

The FID is sampled over 100 μs at a frequency of 2.5 MHz. The echo time (TE) of the CPMG sequence is 0.2 ms with a total of 50 echoes. The signal to noise ratio is increased by averaging over 8 scans, with a recycle delay of 8 seconds.

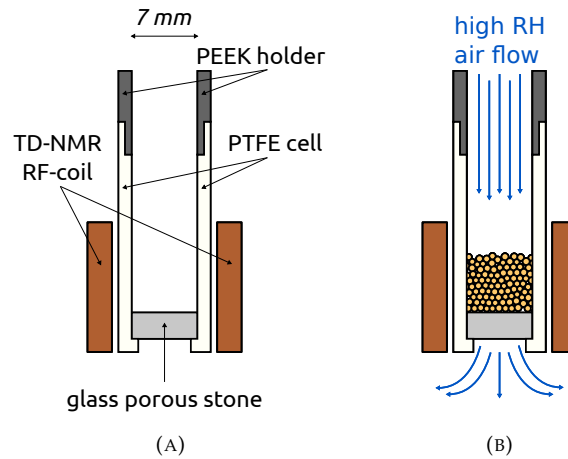


FIGURE 5.1: (A) Schematic view of the measurement cell used for the TD-NMR experiment. (B) Sketch of experimental configuration. The couscous particles are placed in the cell, and attention is paid not to exceed the homogeneous region of the RF coil. A flow of high RH air is circulated through the sample.

The sequence is performed 50 times over a period of 18 hours, starting the first before the high air RH flow is switched on. The timing between the initial sequences is higher compared to those at end of the experiment, to accommodate for the faster change in water content in the early stages of the experiment. The experiment is performed in duplicate. Part of the last data points of the backup test (named here test “B”) have been lost due to a data storage error.

FID-CPMG decay analysis

We analyse the FID-CPMG decays in terms of three main components: one corresponding to the solid fraction, which has a very low proton mobility and thus a short relaxation time T_2 , one with the absorbed water fraction and one to the lipid plus eventual water droplets, with increasingly long T_2 .

To analyse this signal, we subtract the background, and then, using the `scipy.optimize.curve_fit` function [Vir+20], we fit the FID-CPMG decay of magnetisation $M(t)$ with the empirical form:

$$M(t) = S e^{-0.5\left(\frac{t}{T_{2,S}}\right)^2} + L e^{-\frac{t}{T_{2,L}}} + F \quad (5.2)$$

where S describes the overall amplitude of the solid-phase signal, characterised by the relaxation time $T_{2,S}$. The second term corresponds to the semi-solid and/or liquid-like fraction within the sample, with L describing its signal amplitude and $T_{2,L}$ its relaxation time. The last term F describes the components with long relaxation times, like oil and unbound water. This last term is expected to be constant throughout the experiment. The amount of oil cannot change along the experiment and no formation of water droplets or capillary bridges between the particles should be expected, due to the relatively fast flow of air through the bed and the hygroscopic nature of couscous. Nevertheless, the verification of absence of free water is crucial for the interpretation of the results, as detailed later.

It should be mentioned that Equation 5.2 is a simplified version of the approach to analyse TD-NMR results presented by Trezza *et al.* [Tre+06]. Using more than three components to fit

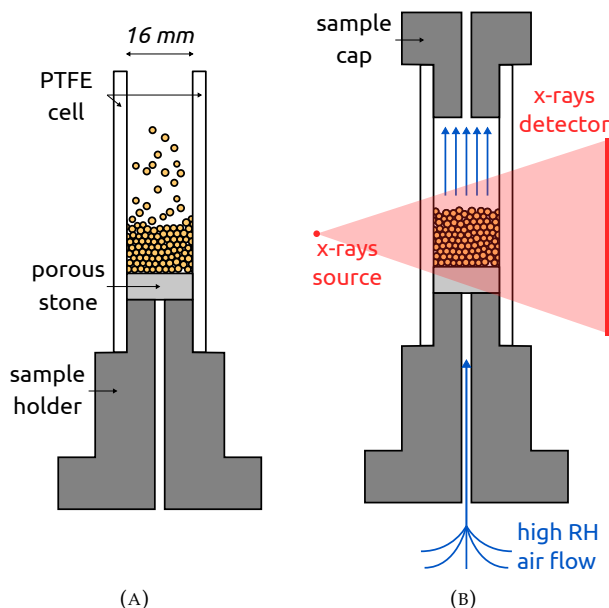


FIGURE 5.2: Schematic view of the x-ray tomography experimental setup. (A) The particles were poured in a rigid PTFE cell, above a porous stone, which functioned as a diffusive filter for the high RH air flow incoming from the bottom. (B) The cell was sealed from top. The particles were exposed to high humidities, and x-ray tomographies were simultaneously acquired.

the relaxation decays does not reduce the residual signal. We therefore conclude that fitting with a Gaussian, an exponential and one constant is adequate to describe the data.

Once the S , L and F contribution is determined, the total proton signal is computed as their sum. This allows for the study of the moisture content evolution, which can be quantitatively evaluated by scaling the $S + L + F$ value increase with respect to the sample mass gain.

5.2.3 X-ray tomography

Experimental procedure

The couscous particles are sieved to obtain a monodispersed size distribution, to simplify the image analysis procedure detailed later. Only particles collected in between $625\mu\text{m}$ and $800\mu\text{m}$ openings are used. It should be mentioned that this sieving procedure is only performed prior the x-ray tomography test, and not the TD-NMR campaigns. The particles are then kept at 13% RH air in a sealed vessel and are “dried” for 3 days, until they reach equilibrium with the surrounding environment. A lower level of RH could not be set due to technical limitations.

The particles are then transferred to a cylindrical PTFE cell (inner diameter $d = 16\text{mm}$), above a high porosity ceramic stone. This functions as a diffusive filter, to provide homogeneous exposure to the flow coming from the bottom, while preventing particles from falling into the bottom channel connecting the cell to the RH control chamber. The chamber contains a potassium sulphate salt solution (120 g of K_2SO_4 and 1000 g of H_2O , 0.69 M molarity). This solution generates humidity in the air and maintains it at a rather constant 97% RH at the room temperature of 24 ± 1 [WB60; Gre+77]. Air is circulated from the RH control chamber to the bottom of the cell, through the sample and back to the chamber by means of a peristaltic pump. The flow rate is set to $0.2\text{L}/\text{min}$, a relatively fast flow, similar to the one above (Section

5.2.2). The experiment is performed once due to restricted access to the x-ray tomograph. A schematic overview of the experimental setup and procedure is shown in Figure 5.2.

Imaging procedure

Tomographies are continuously acquired to capture the evolution of the sample's microstructure along time, employing the x-ray tomograph of the Laboratoire 3SR (Grenoble, France). The x-ray source is operated at 120 kV and 250 μ A, and the pixel size is set to $17 \times 2 \mu$ m, *i.e.*, 17 μ m pixel size in binning 2. Each virtual, binned pixel collects the light of four neighbouring pixels, allowing for a faster image acquisition at the cost of a reduced spatial resolution. We select the binning 2 to increase the temporal resolution of the scans, an imperative choice considering the relatively high humid air flow rate and the ensuing speed of the process. The image 34 μ m pixel size corresponds to an average of 20 pixels per particle diameter, which is deemed sufficient to segment and identify the grains, and characterise their volumetric deformation as detailed later in Section 5.3.3. Each tomography comprises 544 projections, each the result of the average of 10 acquisitions acquired at 10 Hz, lasting therefore approximately 10 min. A first, reference, tomography is acquired before the flow of high RH air is started. In total, 140 tomographies are acquired, which are then reconstructed with the Feldkamp filtered back projection algorithm [FDK84] as implemented in the X-Act software by RX-solutions (Annecy, France).

5.3 Results and discussion

5.3.1 Sorption isotherm

Couscous is a hygroscopic material, thus it can absorb and release water from and into air. A common approach to characterise the water uptake of food is recording sorption isotherms [Heb+03; EEC05], which relates the material's relative increase of mass to the RH of the surrounding environment, all at constant temperature.

Figure 5.3 shows the sorption isotherm of fine couscous particles, obtained by following the experimental procedure described in Section 5.2.1. This sorption isotherm resembles that of other durum wheat products, such as farina or semolina [Heb+03; EEC05]. The moisture content *m.c.* increases progressively for RH. Eventually, the absorption becomes significant for high RH, above 90%. The moisture content is at the beginning of the experiment equal to 4%, at 11% RH. It then increases up to 17.5% when the RH is 98%.

5.3.2 Water uptake and molecular mobility increase

TD-NMR is employed in this study to investigate the changes in ^1H proton signal intensity, *i.e.*, change in proton density and mobility (T_2) of the components. This allows for understanding how water vapour is sorbed by the couscous particles and whether molecular mobilisation occurs inside the solid matrix.

Figure 5.4a shows evolution of the magnetisation decay $M(t)$ of both tests. At the onset of the experiment, the ^1H signal decays rapidly in the FID portion, while the signal almost completely disappears after 0.1 ms, indicating a strong glassy constitution. Later during the sorption process, part of the signal decays significantly slower. The slower decay is associated with a higher mobility of the protons within the sample, due to adsorption of water within the biopolymer matrix of the couscous particles.

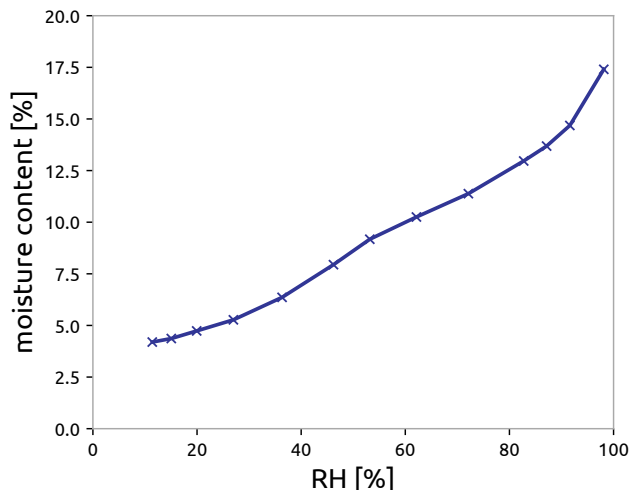


FIGURE 5.3: Sorption isotherm of couscous particles at 20.7. The particles are exposed step-wise to increasing RH and their weight is recorded to evaluate the moisture content.

The magnetisation decay is then interpolated with Equation 5.2. Figure 5.4b reports the results of this operation for the first and last $M(t)$ decay acquisitions of test A. Consequently, the contribution of solid-like S , liquid-like L and oil-like F components is determined. Their and the *total* signal ($S + L + F$) evolution with time are shown in Figure 5.5a. As expected, the total signal increases with time (solid lines), as progressively more water is absorbed by the particles. A slight decrease in the solid signal S (dashed lines) is observed. During the sorption process, water molecules may interact with protons in the solid matrix resulting in an increase of their relaxation time. As a result the $T_{2,S}$ of those protons in the solid fraction is shifting into the solid-liquid-like domain. The reduction of solid fraction signal S is complemented by the increase of the liquid-like one L (dash-dotted line). The oil signal F remains constant and minimal (dotted line), as expected.

The change of the average $T_{2,S}$ and $T_{2,L}$ with time is shown in Figure 5.5b. Both seem to increase monotonically. This suggests that the average molecular mobility increases with moisture content.

After approximately 12 to 13 hours a steady state is reached, when the partial vapour pressure difference between the couscous particles and the humid air diminishes. This results in negligible net-change in water content and hence a plateau in the data. At this point the moisture content of the couscous particles is estimated from the relative weight gain over the experimental runs: 13.8% for test A and 13.2% for test B, assuming the particles to be close to dry (0% *m.c.*) after 3 days of drying at 0% RH.

Vapour sorption mechanism

During the TD-NMR experiments, the increase in moisture content, about 13.5%, is lower than expected, when compared to the gravimetric results (see Figure 5.3). This can be explained by the difference in experimental conditions. The continuous flow of air through the packed bed limits the formation of liquid capillaries between the couscous particles, in contrast to the stationary gravimetric results [LWL21]. This is confirmed by the absence of magnetisation decay signal associated with longer relaxation times (see Figure 5.4a and Figure 5.5a). It can be concluded that no free water is entrapped in the form of capillary bridges or water droplets.

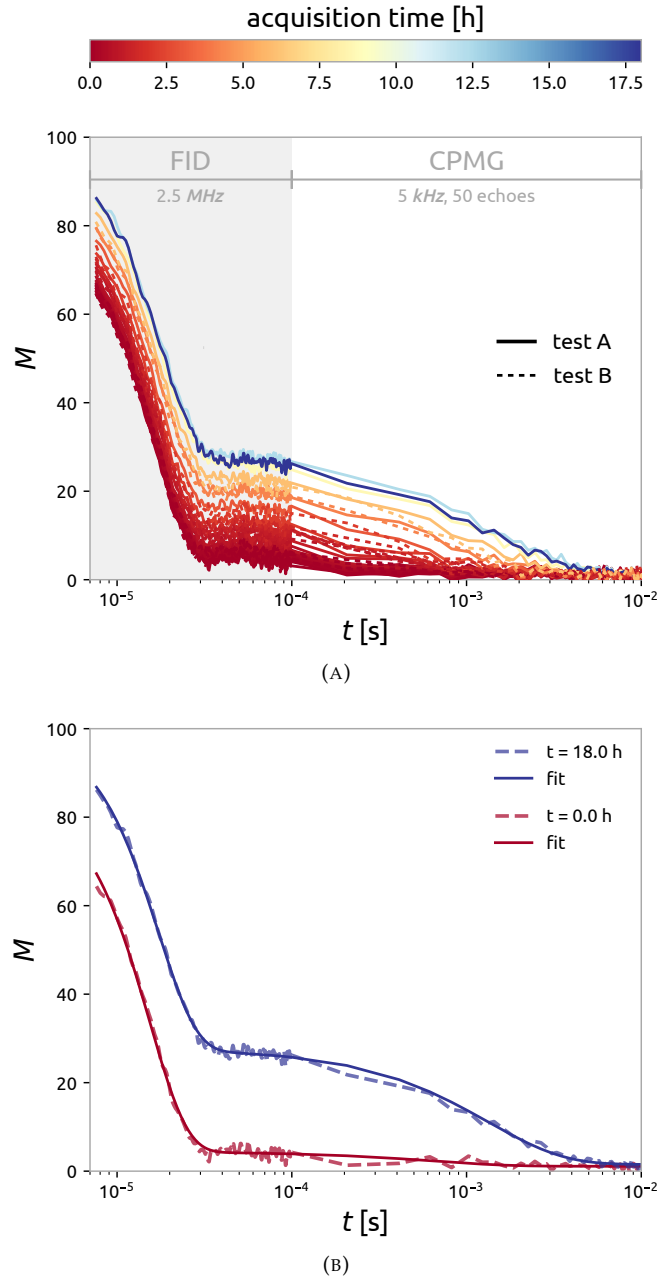


FIGURE 5.4: (A) Magnetisation decay $M(t)$ obtained from the FID-CPMG sequence at different time-steps (from red to blue) throughout test A (plain lines) and test B (dashed lines). (B) Result of this interpolation with Equation 5.2 of the first and last magnetisation decay $M(t)$ acquisitions of test A.

The F proton fraction does not increase over time, and all water vapour that is absorbed by the couscous is hence represented by L , with a short $T_{2,L}$ relaxation time of 1 – 1.5 ms.

Based on the results presented in the Appendix (see Figure 5.12a), it can be deduced that the experimental conditions do not limit the sorption rate by the influx of humid air at a flow-rate of 0.2 L/min. This is confirmed by the initial sorption rate in grams absorbed water per hour from the TD-NMR-data (see Figure 5.10a), which is then compared to the mass flux of water vapour into the packed bed.

At the onset of test A the sorption rate is 9.8 mg/h, whereas, 0.2 g/h of water are supplied

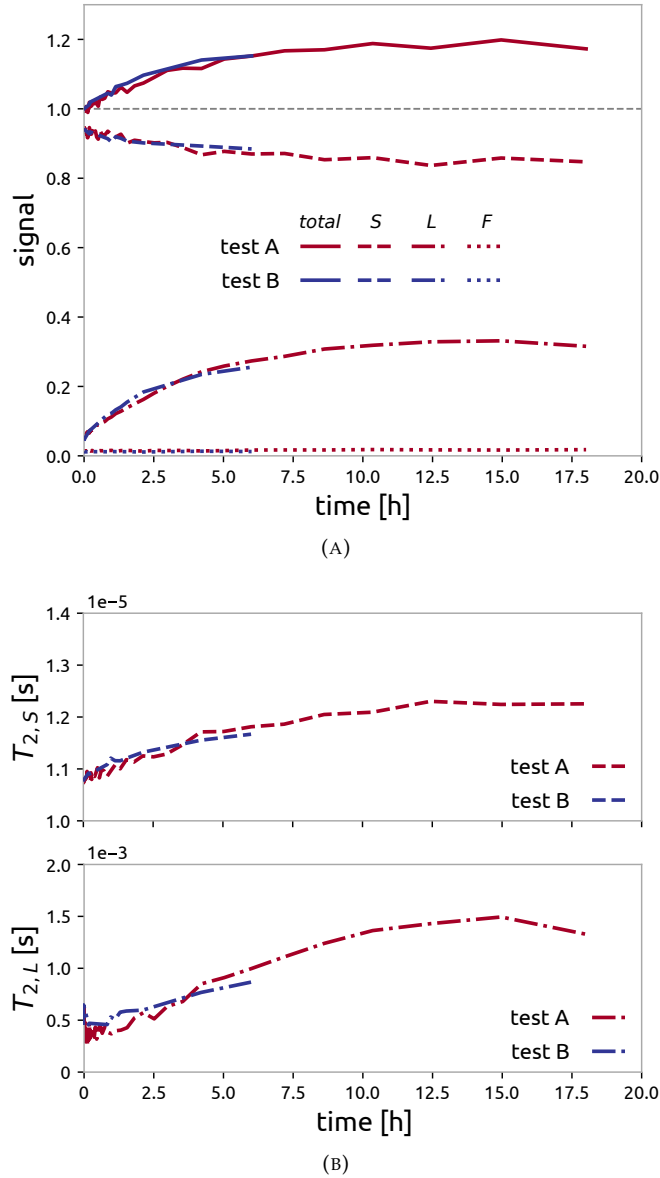


FIGURE 5.5: (A) Evolution with time of the solid fraction S , the liquid/semi-solid fraction L and the oil and mobile water fraction F . (B) Increase with time of the T_2 relaxation times of the solid and liquid fractions S and L .

into the bed, a calculation based on a relative humidity of 97% at 0.2 L/min , and saturation water vapour concentration of 17 g/m^3 . The ratio between the flux of water vapour into the bed and the initial sorption rate of the couscous particles is approximately 20. This suggests that the vapour sorption rate is diffusion limited, as the bed is over-supplied with water vapour. Therefore, the humidity of the air can safely be assumed constant over the packed bed.

Altogether, based on these results, it can be supposed that the couscous particles experience homogeneous air conditions. The water vapour is thereby expected to be absorbed uniformly through the bed. X-ray tomography is used to verify whether a uniform volumetric response is also observed through the sample, as detailed below, since the particle deformation is expected to have a one-to-one relation with absorption.

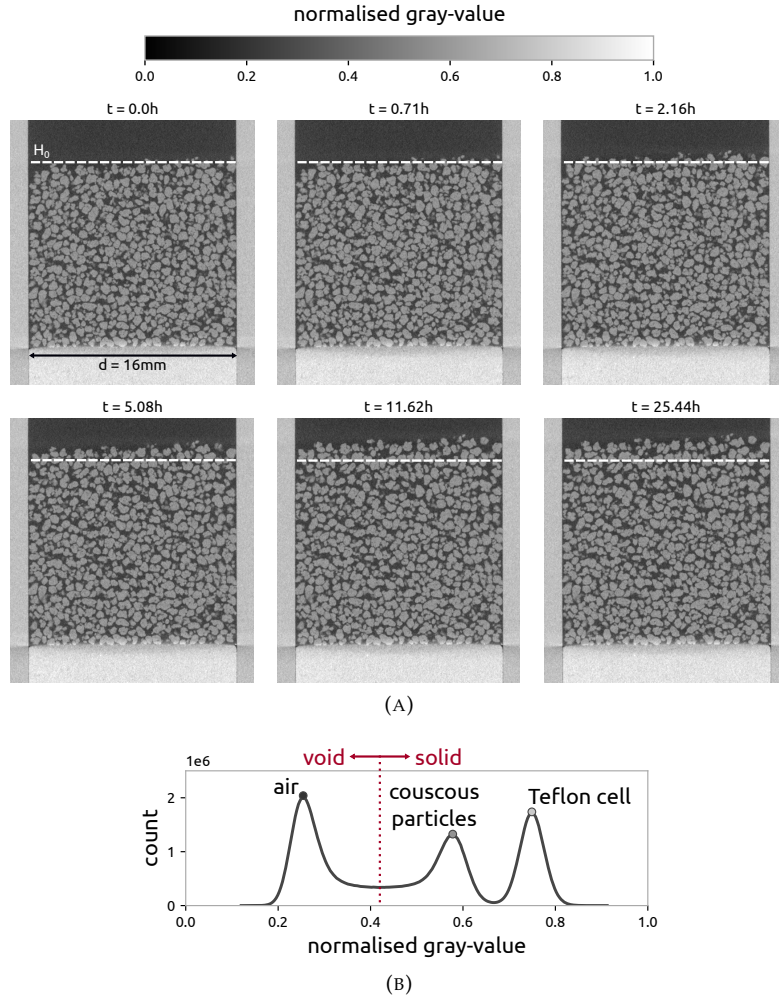


FIGURE 5.6: Evolution of the sample along the test: (A) vertical slices taken in the centre of the sample ($d = 16\text{ mm}$) of the reconstructed x-ray tomography images. The particles absorb water and swell and the sample height increases more than 1 mm . (B) The histogram of the gray-values highlighting the attenuation of the main phases, normalised between zero and one.

5.3.3 Particles identification

The reconstructed 3D images represent the x-ray attenuation (and density) maps of the sample at different time-steps. As shown in Figure 5.6a, darker colours indicate a lower density material, such as air, while brighter colours are for the denser parts, *e.g.*, the ceramic porous stone. The vertical slices anticipate what is later discussed in Section 5.3.4: an increase in sample and particle volume.

The image analysis procedure for this data follows the one in our previous study [Veg+22], adopting functions and algorithms implemented in *spam*, an open source python based software for image analysis [Sta+20a].

First, the effects of spurious fluctuations in x-ray attenuation during the experiment are corrected. As shown in Figure 5.6b for the representative tomography (at $t = 0\text{ h}$), from the gray-value distribution it is straightforward to identify the peaks corresponding to each component (air, couscous particle and cell (PTFE)) and the histogram is normalised between zero and one. We then impose the peak gray-values of air and cell to be constant throughout the entire experiment, as their attenuation is not supposed to change. All the other voxel gray-values

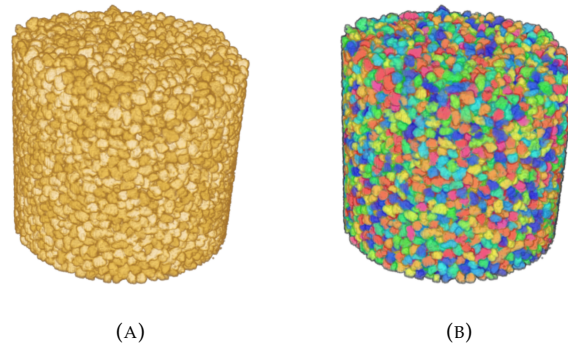


FIGURE 5.7: 3D rendering of the image analysis operations of the reference images ($t = 0h$) of (A) the binary image and (B) labelled image of couscous particles. The labelling procedure revealed the presence of 8543 particles, and to each of them a unique integer value is assigned.

are scaled accordingly. The couscous particles peak cannot be chosen for this operation, since it has been found that its gray-value is affected by increase of moisture content [Veg+22].

All the 140 tomographies are then “binarised”, *i.e.*, the phases in the system are identified, classifying each image voxel in one phase category. The TD-NMR analysis procedure recognises the different components of the couscous solid fraction (S , L and F , see Section 5.2.2 and Equation 5.2). From x-ray tomography images, this distinction is not possible. Nonetheless, the spatial distribution of the solid and void phase in the sample can be identified². This classification is based on whether the attenuation value is below or above a certain threshold, which is calculated via Otsu’s method on the reference image [Ots79] (Figure 5.6b). The result of this binarisation process is shown in Figure 5.7a as a 3D rendering of the couscous sample.

Once the particles are identified it is possible to separate and assign them a unique label, *i.e.*, the value of each voxel belonging to a particle is set equal to an integer number. To perform the former, a distance map is computed, and its relative maxima are used as “flooding” points for the watershed algorithm [Beu82], as implemented in `spam`. We fixed the over- and under-labelling issues common in this kind of approach with the same software. In this case, we identified 8543 different particles. A 3D rendering of this labelled image is reported in Figure 5.7b.

5.3.4 Sample- and particle-scale volumetric response

The labelled image is essential to perform discrete digital volume correlation (dDVC). This technique has been used for the first time by Hall et al. (2010) [Hal+10] and is now implemented in `spam` [DAD19]. It employs the labelled image to extract reference sub-volumes for each particle and perform a digital volume correlation on them, between the reference and “deformed” configurations. This provides a deformation function for each particle, *i.e.*, their 3D displacement and internal deformation, with sub-voxel accuracy. The particle position and its deformation is measured at each time-step [Sta+20a; Veg+22]. Convergence is not reached for only a negligible number of particles (always lower than 0.28 % of the total).

The volumetric strain of the sample $\varepsilon_{V,s}$ is computed as the ratio between the sample height variation at time t and the reference one ($t = 0h$). Only the vertical strain is considered since

²The internal pores of the particle are included into the solid phase fraction, to simplify the analysis.

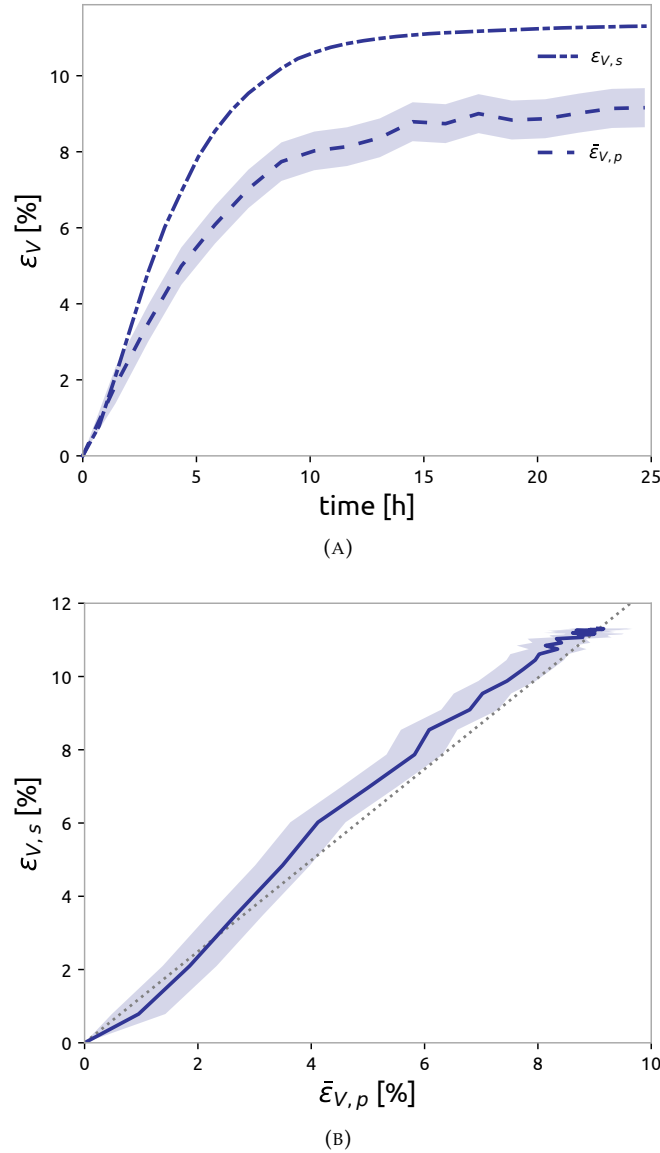


FIGURE 5.8: (A) Evolution of the sample volumetric strain $\epsilon_{V,s}$ and the average particle volumetric strain $\bar{\epsilon}_{V,p}$ in time with its standard error. The particles absorb water from the external environment and swell. This causes a dilation along the vertical direction of the overall sample as the particles rearrange. (B) Relation between $\epsilon_{V,s}$ and $\bar{\epsilon}_{V,p}$. The dilation of the sample is nearly linearly proportional to particle swelling.

the cell's geometry prevents any radial swelling of the sample. The sample dilates up to 11.3% throughout the test.

The volume of each particle is calculated as the sum of all the voxels characterised by the same label. Then, the diameter on a volume-equivalent sphere is measured. The resulting average particle diameter in the sample at the beginning of the experiment is 0.71 ± 0.07 mm, in line with the sieving procedure adopted (Section 5.2.3).

The particle volumetric strain $\epsilon_{V,p}$ can then be measured as the ratio between the particle volume variation and their initial volume [Veg+22]. Overall, the particles swell by 9% by the end of the test. The evolution of the particle size distribution with sorption is presented and discussed in the Appendix (Section 5.6)

Figure 5.8a reports the evolution of the volumetric strain of the sample $\epsilon_{V,s}$ as well as of

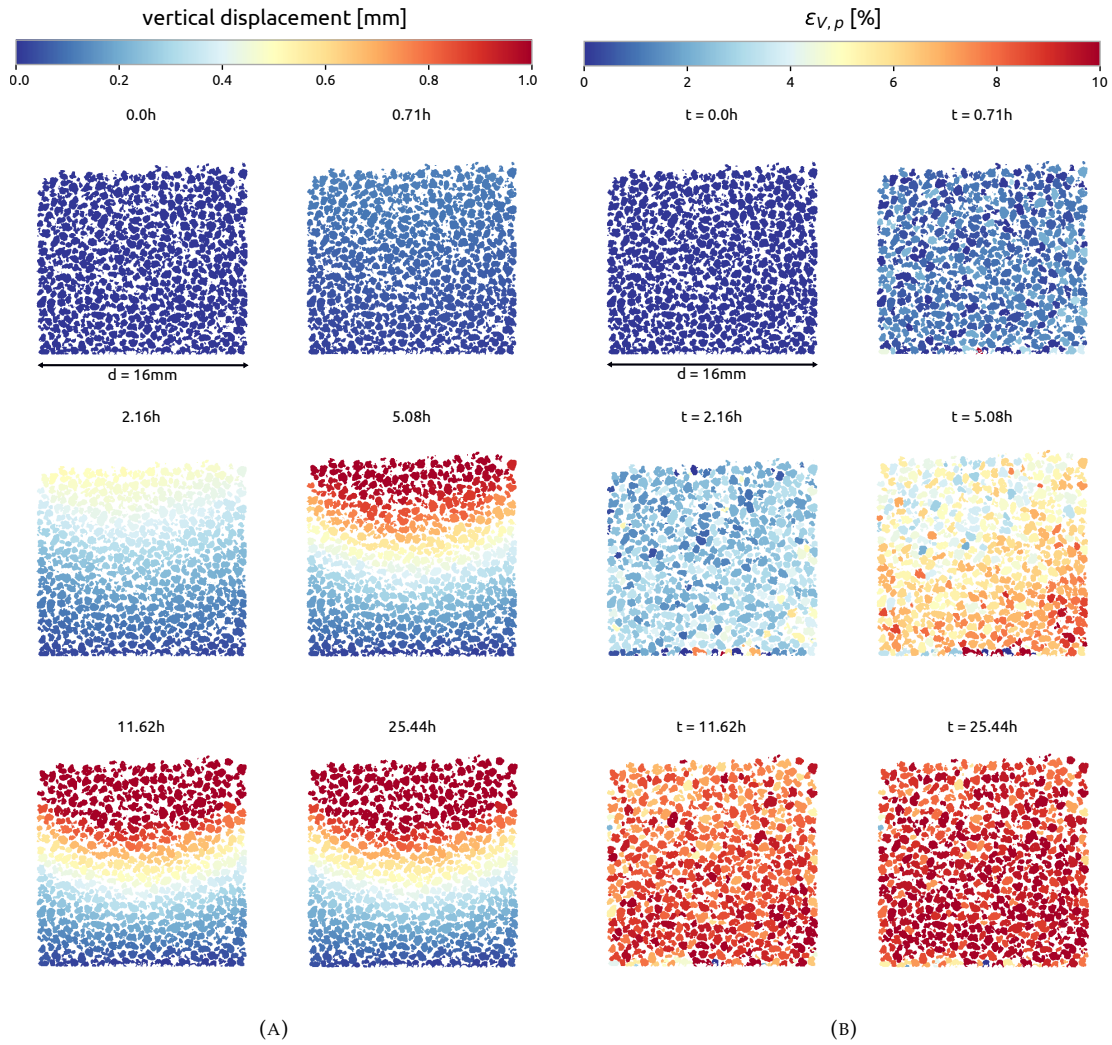


FIGURE 5.9: Vertical slices of (A) the particle vertical displacement and (B) volumetric strain $\varepsilon_{V,p}$ 3D maps. From the vertical displacement map it can be observed how the radial constraints limited the displacement of particles close to the outer boundary. A pressure induced swelling gradient is detected in the intermediate time-steps despite the over-supply of water vapour by the fast flow of humid air. By the end of the test, all particles swell by roughly the same amount.

the average one of the particles $\bar{\varepsilon}_{V,p}$ and its standard error. A similar amount of particle and sample volumetric strain could be expected. Nonetheless, since radial strain is prevented, the constrained particles rearrange, inducing a larger sample dilation than the average particle swelling. It is interesting to observe that after about 12 – 13 h the swelling plateaus, as particles likely reach a steady state with the external environment, similarly to the total signal in the TD-NMR experiment, see Section 5.3.2.

The relation between $\bar{\varepsilon}_{V,p}$ and $\varepsilon_{V,s}$ is found to be (quasi-)linear, as shown in Figure 5.8b. Without constraints in the vertical direction, the sample is free to increase in volume together with individual particles swelling, albeit at a different rate.

Pressure induced heterogeneity

Based on the results discussed in Section 5.3.2, an homogeneous swelling response of the media and no water condensation should be expected, specifically due to the relatively fast flow of high RH air. The X-ray tomography is conducted under similar conditions as the TD-NMR, although on a larger sample (see Section 5.2.2 and Section 5.2.3). The initial mass of the sample is in fact 2.32 g. After 25 h exposure to 97% RH air, the particles absorb 0.21 g of water. Then, the sample is dried in a convection oven for 24 hours at 105, indicating a 4% initial moisture content, which is in agreement with the sorption isotherm and the drying prior testing at 13% RH. Based on this measure, the final moisture content is deduced to be 13.4%, a value analogous to the one recorded in the two TD-NMR campaigns.

The particle vertical displacement map throughout the entire test is then investigated. As highlighted in Figure 5.9a, a significant influence of the boundary conditions is found. Ideally, in unconstrained conditions, the swelling induced displacement should be horizontally uniform. However, lower displacement is measured for particles close to the rigid cylinder wall, limited by friction and arching once the particles start to swell and “push” each other.

Next, the spatial distribution of the particle volumetric strain $\varepsilon_{V,P}$ across the sample is investigated. As shown in Figure 5.9b, the swelling is found to have a gradient along the vertical axis. The particles at the bottom of the sample dilate earlier than the upper ones. This swelling gradient is particularly visible in the intermediate phase of the experiment (in Figure 5.9b, $t = 2.16 h$ and $t = 5.08 h$), while by its end the particles seem to reach a stable maximum swelling capacity for the applied RH level (Figure 5.8a).

As mentioned, a homogeneous particle swelling through the sample is expected occur. Taking into account the higher initial mass of the sample, within the first hour, 300% the water needed to saturate the system is supplied by the humid air flow. Nevertheless, a gradient is clearly measured, suggesting strongly that the water absorption is not only dependent on water vapour concentration, *i.e.*, mass of water per volume. Naively, one would perhaps expect that with homogeneous absorption conditions, higher swelling should be measured in the upper regions, where the mechanical constrains are less severe, as suggested by the vertical displacement maps (Figure 5.9a). Higher inter-particle forces would in fact prevent outward swelling and induce closing of internal pores. On second thought, we can explain the higher particle dilation (hence, absorption) due to the effects of pressure. As the air flows through the couscous assembly, a pressure gradient is inevitably generated [Car97]. In the past, it has been found that air pressure can significantly affect the maximum amount of water that a material can entrap [Sch04; He+09], when the difference is in the order of 10 kPa. In our case, we estimate the air pressure drop from bottom to top three orders of magnitude lower [Car97], quite a small pressure difference, but strong enough to affect the absorption dynamics. Initially, the stronger pressure at the bottom induces a higher vapour pressure, thus a quicker water absorption. This swelling heterogeneity fades in the late stages of the test, as the particle absorption and dilation capacity is reached.

The results also suggest the additional presence of a horizontal gradient (see Figure 5.9b). This is likely produced by small gaps between porous stone and rigid cell, which can create preferential air flow paths. Thus, the pressure distribution is not homogeneous horizontally, and consequently neither are absorption and swelling. Nevertheless, the rather homogeneous swelling spatial distribution in the late stages of the test suggest that the magnitude of the horizontal air pressure gradient is in the order of magnitude of the vertical one previously estimated.

In a previous work, a swelling gradient was found as well [Veg+22]. In that case, couscous particles were also exposed to 97 % RH air flow, but the flow was 10 times slower. In retrospect, it cannot be excluded that the heterogeneity in the previous experiment was prompted by the insufficient air water concentration, besides a pressure difference. Moreover, condensation of water cannot be ruled out due the lower flow rate.

5.3.5 Free swelling and moisture content relation

Next, the relation between the volumetric response of couscous and water absorption behaviour is investigated.

While it is not possible to perform the TD-NMR and the tomography tests at the same time, the two are performed in similar conditions and the final mass variations are equivalent, as detailed above, hence correlations can be established between moisture content and volumetric strain.

A small difference in the initial relative humidity of the materials is nonetheless present in the the two tests. As mentioned in Section 5.2.2, before the TD-NMR tests, the particles are dried for 3 days at 0 % RH, which should induced a moisture content $m.c.$ close to 0 %. The increment measured through TD-NMR coincides then to a 13.8 % final moisture content of test A. In the free swelling experiment with x-ray tomography, the initial moisture content is determined equal to 4 %. For this reason, we correlate here the particle swelling to the TD-NMR data only after 4 % moisture content is exceeded in the latter. The so adjusted evolution in time of the moisture content $m.c.$ from TD-NMR signal increment and the average particle swelling $\bar{\epsilon}_{V,p}$ from x-ray tomography are shown in Figure 5.10a, by red and blue points respectively.

Both variables appear to follow an exponential growth equation:

$$x(t) = X \left(1 - e^{-\frac{t}{\tau_0}} \right) \quad (5.3)$$

where X and τ_0 are two constants characteristic of the material. This model has been found to be a good fit for the sorption behaviour of super-absorbent polymers by Omidian *et al.* [Omi+98] and a recent study showed that it can accurately describe the swelling dynamics of couscous under extreme conditions such as submerged particles [DR+22].

Equation 5.3 can be used to describe the water uptake (and thus the moisture content $m.c.$) as well as the average particle volumetric strain. While τ_0 remains an unknown of the problem, X is simply the asymptotic limit of the plateau. Consequently, the two following Equations describe respectively the water uptake and the average particle swelling:

$$m.c.(t) = m.c.MAX \left(1 - e^{-\frac{t}{\tau_{m.c,0}}} \right) \quad (5.4)$$

$$\bar{\epsilon}_{V,p}(t) = \bar{\epsilon}_{V,p,MAX} \left(1 - e^{-\frac{t}{\tau_{\epsilon,0}}} \right) \quad (5.5)$$

These Equations accurately reproduce the experimental results, as shown in Figure 5.10a (plain blue and red lines).

When particle swelling and moisture content increase are compared it is found that the relation between these two variables can be described by a (quasi-)linear relation, as shown in Figure 5.10b.

The influence of the swelling gradient on the linear coefficient is investigated. The results show a slight increase of the inclination by taking into account only the lower regions of the

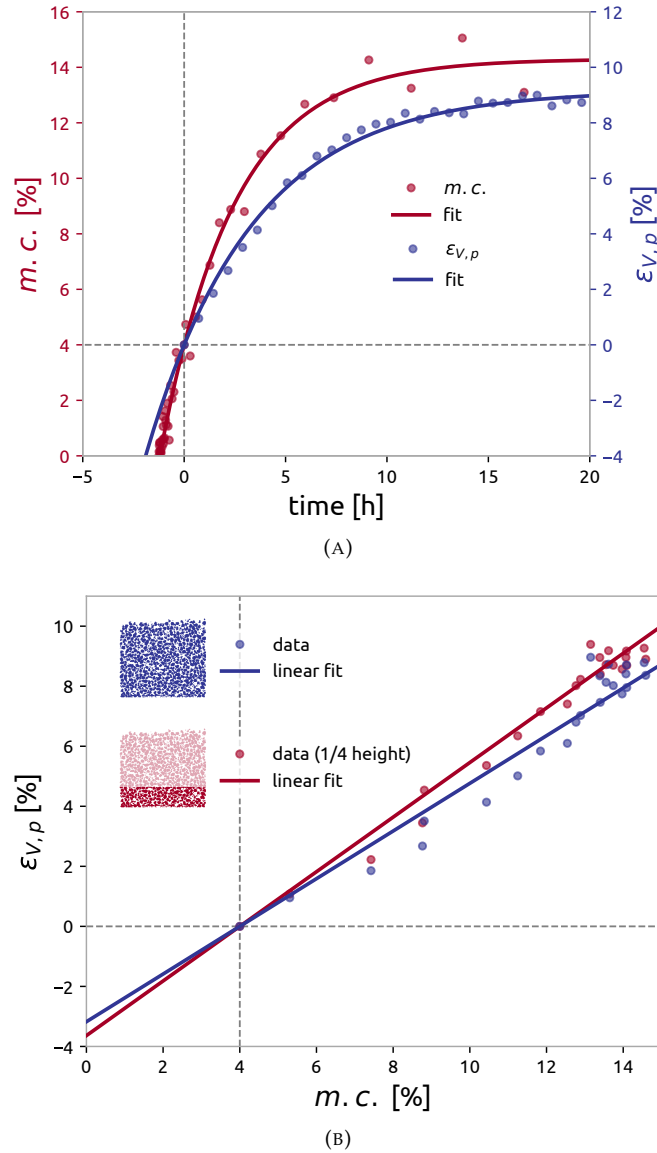


FIGURE 5.10: (A) Evolution with time of the moisture content (in red) and of the particle swelling (in blue) both plateauing. (B) Linear relation between particle volumetric strain $\epsilon_{V,p}$ and moisture content $m.c.$ extracted from experimental data. The $\epsilon_{V,p}$ and $m.c.$ experimental curves with time are interpreted through Equation 5.3. A slight effect of the swelling gradient is observed on the linear coefficient describing the $\epsilon_{V,p}$ and $m.c.$ relation.

sample, which is however within measurement sensitivity interval. As an example, Figure 5.10b reports the evolution for the case in which only the swelling of particles below 1/4 the initial height of the sample are taken into consideration, and the moisture content is still treated as a global variable.

It should be noted that this linearity could be lost in case of water condensation or presence of droplets, as suggested by De Richter *et al.* [DR+22]. The presence of liquid water causes the formation of a gelatinous layer that can decrease the diffusion and, thus, the absorption rate of the internal regions of the particles. Nevertheless, the presence of unbound water can be excluded in this study case. The TD-NMR results do not show a signal from highly mobile ^1H protons (see Figure 5.4a and Figure 5.5a). It can be inferred the same for the complementary campaign, owing to equivalent moisture content by the end of all tests.

5.4 Conclusions and perspectives

Using TD-NMR relaxometry we observe the change in molecular mobility from the increase of the characteristic T_2 relaxation time, as well as the decrease in solid-like signal S and the increase of the bound water signal L . No increase of the signal F of unbound water and oil is observed as the relatively fast flow of air prevents the formation of liquid bridges by capillary condensation.

X-ray tomography allows us to quantify the sample dilation and the volumetric strain of the vast majority of the 8543 particles. The volumetric response shows a similar pattern to the sorption determined by TD-NMR, approaching steady state after about 12 – 13 h at both the particle- and sample-scale.

A modest swelling gradient is observed despite the homogeneous water concentration in the air provided by the relatively fast flow of humid air. This can be explained by gradients inducing a small pressure difference, which in turn influences locally the sorption rate [Sch04; He+09].

A coherent mass gain (*i.e.*, overall change of moisture content) between the TD-NMR and x-ray tomography tests allows us to link the water uptake and the particle swelling in the two tests. The sorption and volumetric response follows the exponential growth model, similarly to other hygroscopic materials [Omi+98; DR+22]. The relation between particle volumetric strain and moisture content increase is found to be (quasi-)linear.

Future research should focus on understanding the physical meaning of the free variable τ_0 in Equation 5.3, and on the effect of different boundary conditions, *e.g.*, isochoric and oedometric. In future works we will explore the spatial distribution of water in the sample, and its effects on the material micro-structure by means of simultaneous neutron and x-ray tomography. A multi-scale mechanical characterisation of the material could complement the morphological information, and provide essential information to understand the underlying phenomena of particles agglomeration and caking. This would also benefit the eventual development and calibration of numerical models aimed at investigating the role played by variables difficult to control or directly measure experimentally.

Acknowledgements

We are thankful to Remco Fokkink, Gert-Jan Goudappel, and Hans de Rooij for the technical support and we thank Julia Vesper for the fruitful discussions during the TD-NMR experimental campaigns. We acknowledge the MAGNEFY NMR facility, which is supported by uNMR-NL, the National Roadmap Large-Scale Facility of the Netherlands (NWO grant 184.032.207). We are grateful to Gioacchino Viggiani and Edward Andò for the advice on the image analysis approach and interpretation of results. We thank Pascal Charrier and Nicolas Lenoir for the technical support with x-ray tomographies acquisition. The Laboratoire 3SR is part of the LabEx Tec 21 (Investissements d'Avenir – grant agreement n-11-LABX-0030). This project has received funding from the European Unions Horizon 2020 research and innovation program under the Marie Skłodowska-Curie grant agreement no. 812638 (CALIPER).

Declarations

There are no conflicts to declare.

Author Contributions

- Ilija Vego: Conceptualisation, Methodology, Software, Validation, Formal Analysis, Investigation, Writing - Original Draft, Visualisation;
- Richard T. Benders: Conceptualisation, Methodology, Validation, Investigation, Writing - Original Draft;
- Alessandro Tengattini: Methodology, Validation, Data Curation, Writing - Review & Editing, Supervision;
- Frank J. Vergeldt: Software, Validation, Formal analysis, Investigation, Resources, Writing - Review & Editing;
- Joshua A. Dijkman: Conceptualisation, Methodology, Resources, Writing - Review & Editing, Supervision, Project administration, Funding acquisition;
- John P.M. van Duynhoven: Validation, Formal analysis, Resources, Writing - Review & Editing, Supervision.

5.5 Appendix: Benchtop NMR experiments: effects of flow rate and RH on sorption

Prior to the TD-NMR relaxometry campaign presented in Section 5.2.2, a series of tests is carried out to settle the optimal experimental conditions. The tests are performed using a spectrometer (Pure Devices MagSpec 23 MHz, 0.55 T), different from the Bruker MiniSpec detailed previously. The same measurement cell as above is used. In order to optimise the data acquisition and achieve high temporal resolution of the hydration process (≈ 500 hundred in one day), we compromise the time interval extent describing the signal decay.

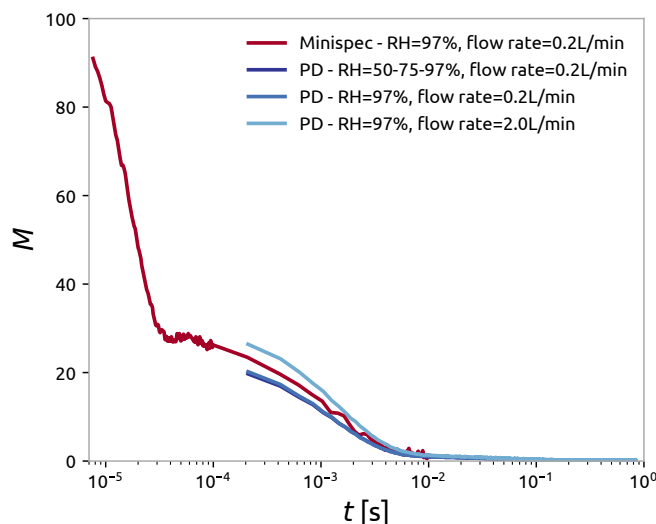
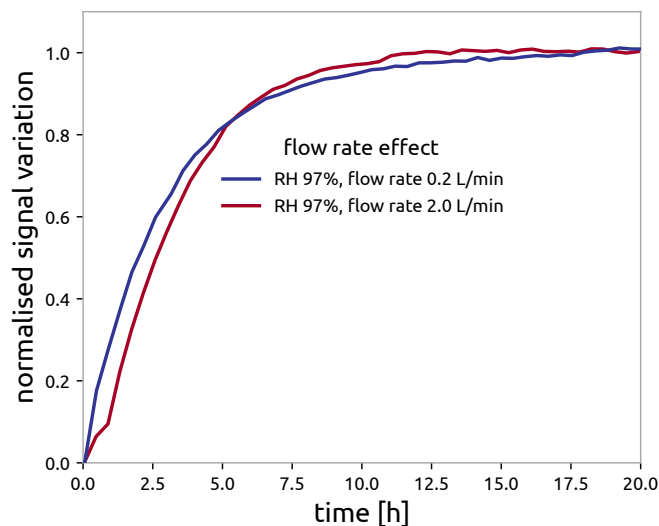
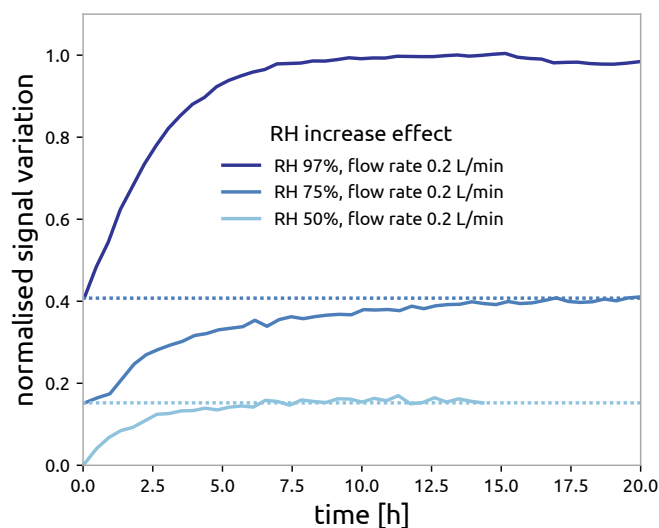


FIGURE 5.11: Comparison between FID-CPMG and CPMG magnetisation decays $M(t)$ obtained from the two experimental campaigns. Representative decay curves at the end of tests are compared. While only the chosen MiniSpec acquisition optimisation allow for capturing the signal of the less mobile protons in the system (solid fraction), both devices agree on the more mobile fraction (semi-solid/liquid phase).



(A)



(B)

FIGURE 5.12: Effects of (A) flow rate and (B) RH from the PD CPMG signal (moisture content). The signal plateaus at 12 – 13 h. No significant effect is observed for two different flow rates, despite one order of magnitude variation. An experiment is performed on the same material for multiple days while the RH is increased progressively once the material reaches a steady state with the external environment. The signal, thus the moisture content, increases upon increasing the RH from 50 to 75 and, finally, to 97%.

Figure 5.11 presents a comparison between the FID-CPMG signal decays obtained by the two spectrometers. With the chosen PD acquisition settings, the sequence decay of the solid fraction is not observed in its entirety. Nonetheless, a good agreement is found between spectrometers for longer T_2 relaxation times. While the chosen setting do not allow for studying directly the solid fraction, the vapour-sorption is analysed from the semi-solid tail and liquid-like fractions contribution on the decay curve (> 0.1 ms).

Figure 5.12a shows the effect of 2 different air velocities on the relative sorption rate, highlighting a negligible effect, despite 1 order of magnitude of difference in flow rate. This indicates that the process was likely limited by the diffusion of water inside the couscous particles themselves rather than the flow rate across the sample.

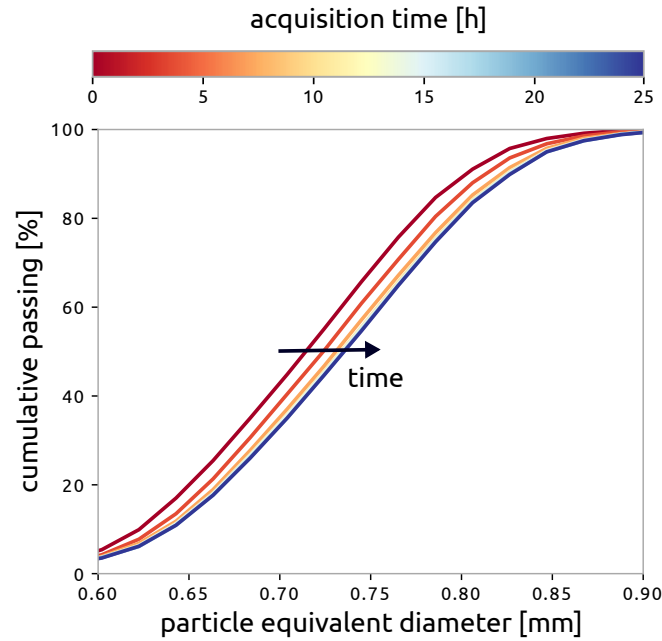


FIGURE 5.13: Cumulative passing particle size distribution at different times obtained from the analysis of the labelled x-ray tomography images.

Furthermore, the sorption signal is analysed at different RH-levels over time (see Figure 5.12b). Starting with a RH of 50 %, a steady state is reached after approximately 12 hours, next the RH was increased to 75 % after which more water vapour was absorbed by the couscous particles. Finally, after 20 hours, the RH is tuned to 97 %, and another steady state plateau is observed after 11 – 12 hours. The relative increments in amount of water at the different RH levels, concur with the gravimetric study results presented in Section 5.2.1.

5.5.1 Conclusions

From these experiments the effects of two different variables in the couscous particles hydration problem are explored. The analysis of the semi-solid tail and liquid-like fractions reveals that there exist a fast flow regime, where the effect of flow rate does not influence the absorption process. Furthermore, the role played by the RH level in the sorption process is investigated. The moisture content (total signal) increases for higher RH, as expected, and it is in agreement with gravimetric studies. Moreover, a plateau is reached after about 12 *h*, similarly to the other tests presented above.

5.6 Appendix: Evolution of the size distribution with water sorption

Particle size distribution (PSD) is a common way of analysing physical properties of granular materials and their change upon mechanical loading or chemical reactions.

As mentioned Section 5.3.3, the analysis of x-ray tomography images allows for the tracking of thousands of particles with DVC and the generation of sequential labelled images. These provide information about the geometry of all particles in the sample and its evolution with

time. It is therefore possible to produce PSD curves directly *via* image analysis, bypassing the more classical sieving method.

Using the dedicated function implemented in the `spam` software [Sta+20a] distributions are obtained from different sequential labelled images, after computing the equivalent diameter of all particles, as shown in Figure 5.13. First, it can be noticed how the results are consistent with the sieving procedure prior the x-ray tomography test (see Section 5.2.3). At the beginning of the test, the vast majority of particles is within the 625 μm and 800 μm range and the distribution is relatively monodispersed. With time, thus with increasing moisture content, the PSD shifts to the right, as the particles swell. Moreover, it can be observed how the size increase is stronger in the initial steps, when the sorption rate is higher (see Figure 5.10a).

5.6.1 Conclusions

The analysis of the PSD confirms a significant swelling of couscous particles with water sorption. The curves, taken at different time-steps, highlight the size increase of the particles and are consistent with the sieving procedure adopted in the sample preparation.

Chapter 6

The influence of water sorption on the microstructure of couscous

The analysis of x-ray images allows to reveal and measure the response of swelling hygroscopic particles exposed to high RH. Joining the results with TD-NMR observations it is possible to correlate microstructural changes to water content variations. In fact, the experimental campaign discussed in Chapter 4 and Chapter 5 constitute a rich data-set. A linear relation is found to link particle volumetric strain and water content. Moreover, the analyses suggest that spatial heterogeneities will inevitably develop, even under “ideal” boundary conditions. Strong heterogeneities are likely to be found in real-case scenarios, but, as revealed by our measurements and other studies, they might develop even in controlled conditions [BAC21] and their influence cannot be ignored.

The data-set can then be improved by linking the heterogeneities to the actual driving process of water sorption, something that was not possible in the previous studies.

This chapter presents a (submitted) paper in which the water content distribution and the volumetric response in couscous assemblies is observed by means of neutron + x-ray tomography. As detailed in Chapter 2, these two imaging techniques are highly complementary and have been successfully used for the full-field measurement of water absorption or migration in materials. Moreover, the simultaneous image acquisition provides essential information to correlate, in space and time, the hydro-mechanical processes, also improving the reliability of the analyses.

The study presented in the paper comprises two tests, both carried out at the NeXT beamline of the Institute Laue Langevin in Grenoble. The samples are tested in oedometric conditions, similarly to the study in Chapter 4, so to observe again the dilation-compaction response.

Full article title

The influence of water sorption on the microstructure of a hygroscopic granular material (couscous) deduced from simultaneous neutron and x-ray tomography

Article status

The article has been submitted to the *Granular Matter* journal on March 7th 2023. The version included here is the result of the first round of reviews, completed on Junend 2023.

Authors

Ilija Vego,^a Alessandro Tengattini,^{a,b} Nicolas Lenoir,^a and Gioacchino Viggiani^a

^a Univ. Grenoble Alpes, Grenoble INP, CNRS, 3SR, F-38000 Grenoble, France.

^b Institut Laue-Langevin (ILL), 71 Avenue des Martyrs, 38000 Grenoble, France.

Abstract

The effects of water on the behaviour of granular materials can be significant. Besides capillary bridges, several other chemo-hydro-mechanical processes can affect the response of hydro-sensitive granular assemblies, when water sorption critically alters the individual particles properties (*i.e.*, swelling, deterioration of mechanical properties). It is very common to find such materials in food and pharmaceutical industries, where water sorption can often lead to important resources waste while processing or storing the product. It is therefore necessary to understand the phenomena that affect the material's functionality, often related to particle agglomeration and degradation. However, despite the relevance of the problem, our knowledge about these phenomena is still relatively poor. With this study we aim to explore the link between water content increase and particle, contacts and assembly scale phenomena. Simultaneous neutron and x-ray tomography allows us to investigate respectively the water uptake and microstructure evolution of two couscous assemblies exposed to high relative humidity while subjected to constant stress, a configuration chosen to simulate the conditions in an industrial silo-storage. We acquire a data-set of images, from which we follow and quantify the variations of water content distribution and the resulting volumetric response of thousands of particles through bespoke algorithms. Despite the abundance of water provided, we observe spatial gradients in water content distribution and consequently in particle swelling. We find that the relation between these two variables can be described as (quasi-)linear. The contact area growth also seems to follow a similar trend.

6.1 Introduction

The presence of water significantly affects the behaviour of granular media. Their response strongly depends on whether the system is in dry, saturated or partially saturated conditions. This problem has been thoroughly investigated for assemblies of impermeable particles (*e.g.*, sands) [FR93]. However, there exist many granular materials whose individual particles are *hydro-sensitive*, meaning that their morphology and mechanical properties vary based on the water content. Clear examples of such materials can be found in food or pharmaceutical industry, *e.g.*, cereals, pharmaceutical powders, flour, tablets, pasta and couscous. These are all hygroscopic, *i.e.*, they can adsorb water molecules from the outer environment. Notably, industries are interested in maintaining constant product properties. Water sorption during processing or storage can alter them, an issue that can lead to severe product or financial loss, sometimes reported to be up to 50 % [RW09].

In spite of the practical relevance of the problem, very little is known about the underlying phenomena that originate at the molecular level, which in turn affect the particle-, assembly- and macroscopic-scale behaviour.

The inherent chemical composition of food stuff or pharmaceutical excipients often endows the material to be in disequilibrium with the external environment (a difference in “water activity”) [Lew00; Sch04]. In this case, the molecular matrix can adsorb large amount of water [DP17], which in turn causes structural changes and also induces the *glass transition* phenomenon that specifically involves the amorphous fraction of the material [AVK95; Sch04]. The material can swell (often due to the dilation of starch molecules) but it can also shift from a “glassy” to a less viscous state, which causes a significant deterioration of mechanical properties.

Naturally, these processes affect the particle properties and make them hydro-sensitive. Several studies were carried out to evaluate the effects of water content on shape and mechanical properties of *individual* particles. Swelling is one of the common phenomena observed when exposing such materials to water. Rice and wheat grains [MS79; Tab03], lentil seeds [AHR04], microcrystalline cellulose granules [SFS11], couscous [Abe+12; BRC18; DR+22; Veg+22] are just some examples of the numerous materials that were found to dilate when increasing water content. Besides the effect on the morphology, water strongly influences also mechanical properties. For example, strength and stiffness of wheat kernels decreased more than 10 % when increasing water content [GYP91; Fig+11]. Similar results were found for rice grains [Kam+02; Cao+04], which also developed fissures upon wetting and drying cycles [SK82]. The tensile strength of microcrystalline cellulose tablets decreased for higher water contents according to a study by Shi *et al.* [SFS11].

These phenomena are not necessarily deleterious by themselves. However, as particles continuously interact with each other, they can agglomerate. Bridges are formed either by material solution accumulated on the contact regions which dries or when a viscous flow occurs between particles (*i.e.*, sintering) [Sid+86; Bik+05; Pal05; Zaf+17]. Relatively high stresses can also enhance the agglomeration and thus decrease the flowing properties of the material [AVK95].

As a whole, these processes can lead to *caking*, a phenomenon in which granular media lose their free flowing properties due to formation of lumps. To prevent this kind of problems is of high interest for the industry [AVK95; FA05; Car+16; Zaf+17], therefore studies have also focused on the bulk/product scale effects of water uptake. As the material picks up water, the caking strength is generally found to be higher and its flowability lower [Fit+07; Lum+16; JE+17; BAC21]. Studies have also showed how the process is not uniform, even for relatively homogeneous testing conditions [BAC21] and it is therefore necessary to take into account heterogeneities to properly model, simulate or predict the behaviour of any hydro-sensitive material.

Altogether, a large number of studies focused on the interaction of water with such materials, and the effects on their properties. However, our knowledge of the problem is still insufficient, either because of its complexity or the impracticality of finding standard references for such a broad class of materials. A few review papers summarised experimental and numerical research related to the caking phenomenon, and they often concluded that it is necessary to investigate and understand the link between particle-scale phenomena and bulk response [FA05; Car+16; Zaf+17]. Nevertheless, few studies aimed to describe the multi-scale response of hydro-sensitive particles. For instance, Wahl *et al.* [Wah+08] investigated optically the bridge formation between two particles of urea prills (a fertiliser) and quantified its mechanical resistance. The Authors then implemented a model describing the particles interaction and predicted numerically the uniaxial strength of the assembly. Haider *et al.* [Hai+14]

examined the effect of temperature on the contact formation, morphology and compressive-tensile strength between maize starch particles. In a recent study [Veg+22], we investigated by means of x-ray tomography the effects of high relative humidity (RH) on the microstructure of a couscous sample subjected to constant stress. We observed the swelling of thousands of particles as they sorbed water and quantified their volume change (up to 20%) as well as the volume change of the whole sample. We found a dilation-compaction behaviour as a result of the particle swelling and deterioration of mechanical properties. Moreover, we found a strong correlation between the inter-particle contact areas growth and the applied boundary conditions (*e.g.*, loading direction and injection point).

With the experimental study presented in this paper we aim to expand our previous work, specifically focusing on the correlation between microstructural changes and water content distribution, a feature that was not possible to capture by means of x-ray tomography only. For this reason, we couple the technique with neutron tomography. The two are highly complementary thanks to the different way in which the beams interact with matter [Pet46; Ten+21]. X-rays interact with the electron cloud of atoms, whereas neutrons interact with nuclei. Of particular interest for this study is the different attenuation of hydrogen atoms, which are basically transparent to x-rays and quite the opposite to neutrons, which as a consequence allows the detection of water. For these reasons, neutron + x-ray tomography is a technique that has been used in several experimental studies to observe the hydro-mechanics of different processes, as detailed in recent reviews [Kar+18; Ten+21]. Recent inspiring examples related to our work are the studies by Stavropoulou *et al.* [Sta+20b] and Sleiman *et al.* [Sle+21]. In the former, the Authors measured the water absorption by a sample of Callovo-Oxfordian claystone and the following microstructural evolution. Via image analysis, the deformation of reference sub-volumes (deduced from x-ray images) was correlated to the local increase of water (from neutrons). In the latter, the drying of concrete samples due to increasing temperature and the resulting cracks opening were investigated.

This paper presents the results of two experimental campaigns similar to the one of our previous study [Veg+22]. We again expose samples of couscous particles to high RH air, while subjected to zero radial strain (oedometric) conditions. This time, instead of using only x-ray tomography, we continuously acquire 5D (neutron + x-ray + time) images, where x-rays provides data about the sample microstructure, while the contrast of neutron images provides information about the water content variation as the molecular matrix of the particles entraps water. Following bespoke algorithms, we measure from x-ray tomography images the volumetric response at the particle- and sample-scale, and correlate them to the water content, which we deduce and quantify from neutron tomography. Finally, we correlate the swelling of particles and the increase of inter-particle contact areas to the water content increase, and to the overall assembly response.

The paper is structured as follows: Section 6.2 describes the material, experimental procedure, set-ups and instruments used in this study. Section 6.3 presents the results we obtained through image analysis. Using the algorithms developed for our previous study [Veg+22], we analyse the volumetric response of the samples during the two experiments. Then, Subsection 6.3.3 introduces the procedure specifically developed to assess and quantify the water content distribution, which is then correlated to the microstructural changes of the couscous assembly.

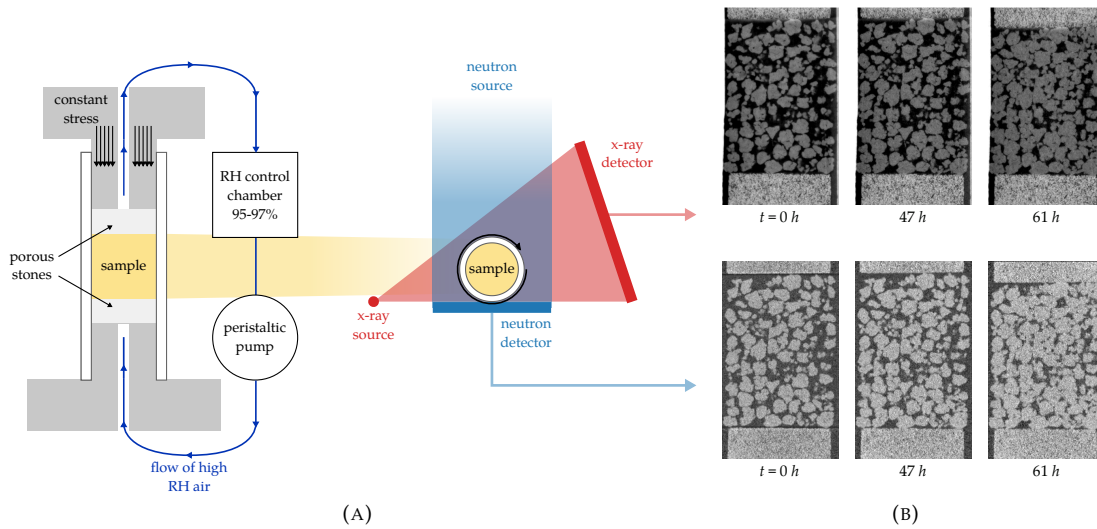


FIGURE 6.1: (A) Sketch of the experiments at NeXT: the samples of couscous are placed in an oedometric cell (sketch on the left, side view) and subjected to a constant vertical stress (dead load). Meanwhile, a flow of high RH air is injected by means of a peristaltic pump from the bottom. Neutron and x-ray tomographies are acquired placing the set-up on a rotation stage (sketch in the middle, top view). (B) Vertical slices of the x-ray (top row) and neutron tomographies (bottom row) at representative states, highlighting the overall processes.

6.2 Experimental study

6.2.1 Material choice: Couscous, a water-sensitive granular medium

Besides its low cost, and commonness, couscous presents several of the phenomena that characterise hydro-sensitive granular materials. When in contact with water its particles can in fact swell, undergo deterioration of mechanical properties, and agglomerate. At the same time, couscous particles do not present some of the more complex phenomena typical of other hydro-sensitive particles, such as peeling or particle breakage (for sufficiently low stresses) – all phenomena that would make the quantification of some microstructural properties studied here cumbersome. Finally, the average particles diameter of fine couscous is $\approx 0.85 \text{ mm}$, a size compatible to the imaging set-up used here: the neutron and x-ray tomograph “NeXT” at the Institut Laue-Langevin (see Sections 6.2.2 and 6.2.2).

6.2.2 Experimental procedure

The particles are subjected to oedometric conditions (no radial displacement) to emulate typical conditions found in storage silos. They are poured in a rigid cylindrical cell, thus, vertical displacement is allowed, and the constant stress applied simulates the action played by the self weight of material stored above. We subject the sample to a flow of high RH air, to study typical phenomena in hydro-sensitive materials exposed to humidity. The air is injected from the bottom of the cell by means of a peristaltic pump, which in turn is connected to a RH control chamber. The environment in this chamber is controlled with a saturated saline solution of potassium sulphate ($\text{K}_2\text{SO}_4 + \text{H}_2\text{O}$), which produces rather constant RH in its environment (95 – 97% for a range of temperatures between 20 and 25 °C [WB60; Gre+77]). At the bottom

and top of the sample two high porosity stones maintain the sample in position and uniformly apply the stress and the humidity.

This paper presents the results of two experimental campaigns:

- CCRH97-01¹;
- CCRH97-02.

Both performed at the NeXT beamline at the Institute Laue Langevin (ILL) in Grenoble (France) [Ten+20], they are analogous experiment to one in our previous study [Veg+22], in which only x-ray tomographies were acquired. These allowed the characterisation of the effects of high RH on the microstructure of a couscous particles assembly. Nonetheless the water content in the particles could not be quantified then, because of the low attenuation (and thus visibility) of water to x-rays. For this reason, in this study we also acquire simultaneous neutron tomographies, to capture the water uptake process and its spatial distribution. A sketch of the experimental set-up and of the process as revealed by the tomographies is presented in Figure 6.1.

CCRH97-01: experimental procedure

To subject the sample to the desired experimental conditions, we use the same oedometer as in our previous study, except for the material of the cell, fabricated here in PTFE (Teflon) and not PEEK to improve its neutron transparency. However, a first preliminary test, although successful, shows us that the high natural hydrogen content of couscous particles causes a strong beam hardening in the neutron tomographies over the 16 mm diameter of the sample [BK04]. The significant amount of scattering spuriously increases the apparent attenuation of the outermost particles. While this artefact can be partly remediated during the reconstruction, it increases the error margin in the estimation of water content. To diminish the influence of this artefact, the cell internal diameter is reduced to 13 mm by inserting a PTFE sleeve of about 17 mm height in the main cylindrical cell, above the bottom porous stone. 1.77 g of couscous particles are then poured in the reduced cell. A smaller porous stones is placed on top (of diameter lower than the “sleeve”) and the piston applying the dead load above it. The diameter reduction means an increase of the applied stress to 35 kPa (to be compared to 25 kPa for the previous study [Veg+22]). Some particles trapped on top of the PTFE sleeve, *i.e.*, between the upper porous stone and the cell wall, might have partly reduced the load actually transmitted to the sample, also due to the expected particle swelling. Air of 95 – 97 % RH is injected at 0.02 L/min for about 49.5 h. The final mass of the sample is 1.91 g, corresponding to an 8 % mass increase.

CCRH97-02: experimental procedure

This second campaign’s goal is to acquire higher resolution images (see Section 6.2.2) to further investigate the processes occurring at the particle scale, but it aims at a reduction of the beam hardening effect. For this reason, a smaller oedometric set-up is designed and fabricated (internal diameter of 7 mm) improving on the previous design. The new cell is in aluminium, because the PTFE would not be stiff enough. The initial mass of the sample is 0.31 g, and, to be consistent with the conditions of CCRH97-01, the dead load applies a vertical stress of

¹‘CC’ stands for couscous, ‘RH’ for relative humidity, ‘97’ for the relative humidity level in percentage applied during the test.

35 *kPa*. High RH air is produced in the same manner as for CCRH97-01 (Section 6.2.2), and the flow rate is initially set to 0.02 *L/min* for 48 hours, indicatively matching the duration of the other test. The flux is then increased to ≈ 0.2 *L/min*, to resolve suspected infiltration of lower RH air from the outer environment due to small defects of the cell. The final mass of the sample is 0.38 *g*. The water content variation is then around 22%. This is a noticeable increase of mass, higher than $\approx 19\%$ reported in previous studies on the sorption isotherms of durum semolina [EEC05]. We suspect that small droplets, perhaps accumulating at the porous stone, are accidentally pushed through the sample by the increase in flow in the later stages of the test. These possible variations in water content are part of the reasons why the addition of neutron imaging is indispensable to correlate the directly measured water content increase in the particles to their strain.

Neutron and x-ray tomographies

During both campaigns, neutron and x-ray tomographies of the sample are continuously acquired.

The cold neutron source at NeXT provides a quasi-parallel beam. The neutrons are detected with high resolution detectors adopting infinity-corrected optics [Ten+20]. The x-ray source is operated at 100 *kV* and 60 μA for CCRH97-01. For CCRH97-02, the parameters are initially set to 140 *kV* and 200 μA to better penetrate the aluminium cell. After 28 h these settings are decreased to 120 *kV* and 68 μA , to further reduce the cross talk between the two radiations, without effective loss of resolution for the x-ray tomographies².

In the CCRH97-01 campaign each tomography comprises 992 projections. Each x-ray projection is the result of the average of 8 individual frames and is acquired at 1.8 *Hz*, without binning. The neutron projections are averaged 3 times and acquired at 0.67 *Hz*, as obtained through a 122 *mm* Heliflex lens combined a 50 *mm* lens, in binning 2, yielding a pixel size of 32 μm . A 20 μm thick Gadolinium Oxysulfides scintillator is used. With an estimated 9 *mm* average sample-detector distance, and pinhole of 30 *mm* at 10 *m*, this yields an estimated 27 μm neutron penumbra, compatible with the pixel size and the desired resolution. This results in the simultaneous acquisitions lasting around 1.24 *h*. In total, 38 tomographies are acquired. The voxel-size for both x-ray and neutron images was 32 μm .

Tomographies are also acquired continuously during the CCRH97-02 experiment. Each one of them comprised 1200 projections. An x-ray projection is acquired initially averaging 27 acquisition at 9 *Hz*. After the aforementioned decrease of the x-rays power (at scan #27), the average and frame-rate is reduced to 7 and 2.3 *Hz*, respectively. Each neutron projection averages 3 acquisitions obtained at 1 *Hz*, in binning 2, throughout the entire test, as obtained through a 55 *mm* Heliflex lens combined with a 50 *mm* lens, in binning 2, yielding a pixel size of 14 μm . A 10 μm thick Gadolinium Oxysulfides scintillator is used. With an estimated 4.5 *mm* average sample-detector distance, and pinhole of 30 *mm* at 10 *m*, this yields an estimated 13.5 μm neutron penumbra, compatible with the (binned) pixel size and the desired true resolution. A single tomography then lasts 1.02 *h*. We acquire in total 60 bi-modal tomographies. The voxel-size of the x-ray and neutron images is respectively 25 μm and 14 μm .

²While the cross-talk between the two was modest, small fluctuations could be observed along time as the x-ray source warmed up. To minimise this possible source of incertitude on the neutron data, the x-ray flux was reduced after verifying that the image quality was comparable. This variation in parameters is not expected to affect the measurements reported in Section 6.3.

In both the experimental campaigns, we take an initial tomography of the “dry” reference sample configuration (counted among the total number of scans) and only then the peristaltic pump was turned on exposing the particles to humid air.

As the experiments go on for 2-3 days, we occasionally interrupt the scanning procedure to re-calibrate the detectors.

Finally, tomographies are reconstructed with the Feldkamp filtered back projection [FDK84] algorithm, as implemented in the X-Act software (RX-Solutions, Annecy, France). Examples of the reconstruction process are shown in Figure 6.1b.

In Table 6.1 we summarise the experimental conditions of the two campaigns and the imaging parameters.

TABLE 6.1: Table summarising the boundary conditions of the two experimental campaigns.

	CCRH97-01	CCRH97-02
sample diameter [mm]	13	7
sample height [mm]	15	9
test duration [h]	49.42	60.86
RH [%]	95–97	95–97 ¹
flow [L/min]	0.02	0.02–0.2
mass _i [g]	1.77	0.31
mass _f [g]	1.91	0.38
$\Delta\text{mass}/\text{mass}_i$ [%]	8	22
vertical stress [kPa]	35 ²	35
tomography duration [h]	1.24	1.02
total scans	38	60
voxel-size _{x-ray} [μm]	32	25
voxel-size _{neutron} [μm]	32	14

¹Possibly because of a defect of the new aluminium cell, the actual level of RH for CCRH97-02 is uncertain before the flow rate increase, as supported by the measurements presented in Section 6.3.2 and Section 6.3.3.

²In CCRH97-01, the PTFE sleeve causes some particle to be accidentally stuck between the porous stone and the cell wall, thus the actual load could be lower due to friction.

6.3 Image analysis: methods and results

In this section we present the image analysis methods proposed in this work as well as the processes quantified thanks to them. The analyses are performed with the open source software for image analysis `spam` [Sta+20a].

6.3.1 Multi-modal registration and segmentation

Firstly, we perform multi-modal registration (MMR, *i.e.*, align the two tomography modalities) at each time-step. This method was proposed in Tudisco *et al.* (2017) [Tud+17] and implemented in `spam` [RAR19]. With this algorithm each neutron tomography is aligned to its corresponding x-ray one, to have a coherent coordinate system between them. This operation

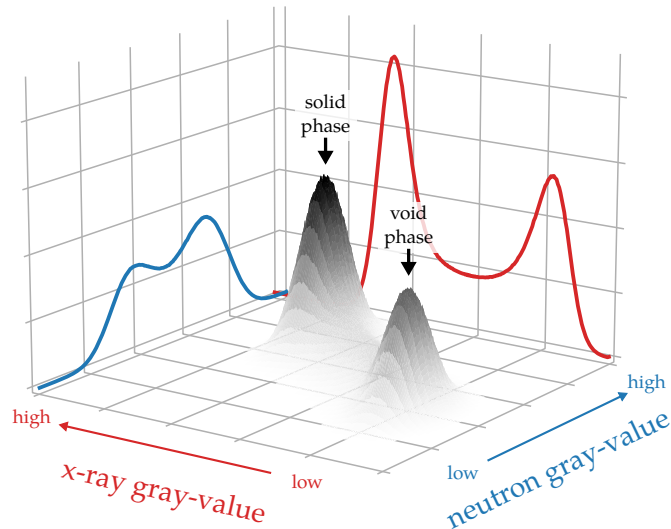


FIGURE 6.2: Joint histogram built with the x-ray (red) and the neutron (blue) gray-value histograms of the tomography of the reference configuration of CCRH97-01. Two peaks can be observed, corresponding to two phases: void/air at low gray-values and solid/particles(+sorbed water) at higher gray-values. This joint histogram is employed in the MMR algorithm to register the two tomographies.

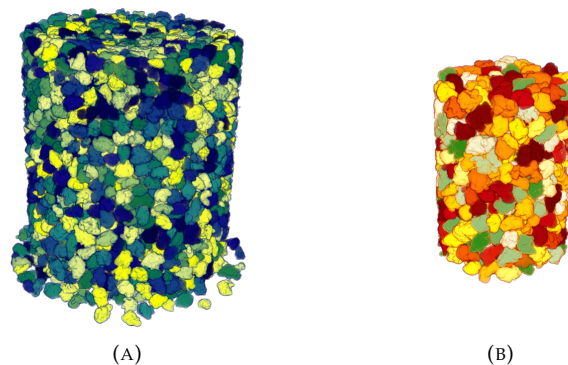


FIGURE 6.3: 3D rendering of the labelled images in their initial configurations of both (A) CCRH97-01 and (B) CCRH97-02 experiments.

requires firstly a “map” of correspondences between the x-ray and neutron gray-values, *i.e.*, the joint histogram. Figure 6.2 reports a representative joint histogram combining x-ray (red) and neutron (blue) gray-value distributions. The two peaks correspond to the two phases in the system: void/air peak and solid/particles(+water). The algorithm describes the joint histogram with a Gaussian mixture model, which is then employed to perform a generalised digital volume correlation (DVC) between images acquired with the two modalities [Tud+17; RAR19]. This allows us to align the tomographies across the test with sub-voxel accuracy, while also segmenting them, *i.e.*, classifying each voxel as either void or particle.

This step is crucial for the following analyses, especially at the particle scale. Combining the MMR segmentation and thresholding of the x-ray image, the sample solid fraction alone is extracted as a binary image. From it the distance map is computed, and the local maxima are used as flooding point for the watershed algorithm [Beu79; Beu82]. Over- and under-segmentation issues are resolved with the dedicated algorithms [Sta+20a].

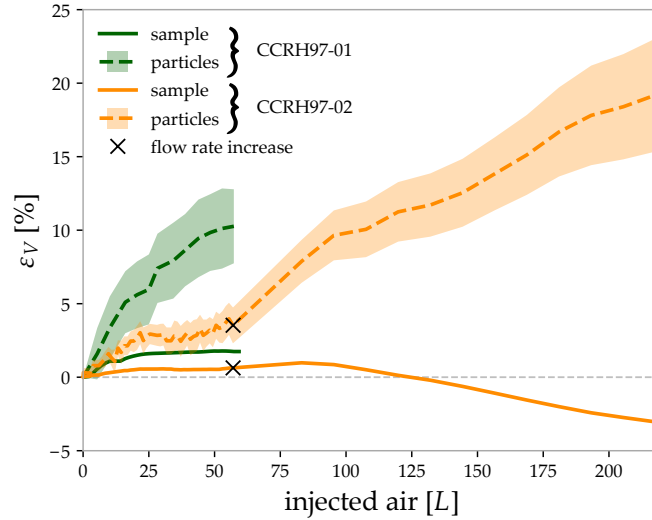


FIGURE 6.4: Volumetric strain ε_V at both sample and particle scale (with standard deviation) of CCRH97-01 (green) and CCRH97-02 (orange) as a function of the injected air volume. High RH air is injected into the system, particles uptake water and swell. These two processes affect the overall sample volumetric strain $\varepsilon_{V,s}$, which increases as the particles are able to lift the dead load. In CCRH97-02, a compaction stage is observed too. The particles become softer with high water content, which causes an overall shortening of the sample.

Once the particles are separated we can assign to each a unique number (a process named “labelling”). We find that 3013 and 527 particles comprise at the end the CCRH97-01 and CCRH97-02 samples and the average particle diameter equal to $0.86 \pm 0.13 \text{ mm}$ and $0.88 \pm 0.12 \text{ mm}$. The 3D renderings are shown in Figure 6.3a and 6.3b.

6.3.2 Volumetric response

We analyse the volumetric response at the assembly and individual particles scale following the procedure proposed in our previous work [Veg+22]. It should be noted that we use the x-rays images for this and the contact measurement presented later in Section 6.3.3, because of their lower noise (see Figure 6.1b).

The sample’s deformation is measured *via* DVC between the reference x-ray image and the sequential ones. Specifically, a *global*, non-rigid registration is performed, as implemented in `spam`. Among the outputs, the operation returns the gradient tensor F between the reference and the deformed configuration, which allows the computation of the sample’s volumetric strain is then computed as: $\varepsilon_{V,s} = \det(F) - 1$. Because of the selected boundary conditions, *i.e.*, no radial strain, no substantial difference is observed when measuring the sample’s deformation using this approach or from the relative displacement of particles.

Measuring the particle-scale volumetric strain requires relatively high resolution images, made possible by a combination of the NeXT beamline specifications, the choice of the material as well as of the geometry of the cell, as detailed above. From the labelled image of the reference configuration, we perform Discrete Digital Volume Correlation (DDVC), as proposed by Hall *et al.*, [Hal+10]. We isolate a sub-volume for each particle and perform DVC on it to measure displacement. To track the particles, the rigid displacements measured from the DDVC is used to move the initial particle labels to their updated position, which then is used

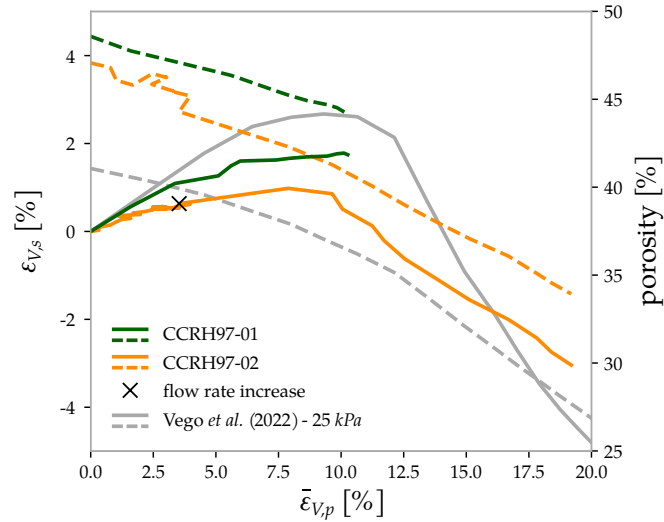


FIGURE 6.5: Relation between the particle $\bar{\varepsilon}_{V,p}$ and sample $\varepsilon_{V,s}$ volumetric responses for the two experimental campaigns presented here (green and orange) and the one in Vego *et al.* (2022) [Veg+22] (gray line). The evolution of porosity in all three tests is shown here with dashed lines for comparison.

as a “seed” for a new watershed algorithm so as to assign the same label to a particle throughout the test. The particles’ volumetric strain is then directly measured from the variation in volume of each labelled particle with respect to the reference configuration.

The volumetric strain of the sample and the distribution of particles for CCRH97-01 as a function of the injected air volume are shown in dark green in Figure 6.4, with solid and dashed line, respectively. Initially the assembly increases in volume until it reaches a constant value ($\varepsilon_{V,s} = 1.7\%$ after injecting $\approx 34\text{ L}$). Meanwhile, the particles (dashed line, arithmetic mean along with the standard deviation value) swell monotonically throughout the entire test, up to 10% from their initial size, despite the plateau in overall sample dilation (*i.e.*, the particles cannot further lift the dead load). The sample porosity decreases from 48% to 44% throughout the experiment (see Figure 6.5). The particle swelling appears to plateau, suggesting an asymptotic value would be reached also for individual particles, at the equilibrium with the external environment.

For CCRH97-02 the same procedure is performed. Figure 6.4 shows the sample and arithmetic average particle volumetric strain, with orange solid and dashed line, respectively. As mentioned in Section 6.2.2, after 48 hours we increase the air flow rate, to study its effect and to compensate a suspected infiltration of lower RH air. The evolution of the curves after this change supports the hypothesis. Before the increase in flow, dilation at the sample and particle scale are lower than for CCRH97-01 (and previous experiments, see Vego *et al.*, [Veg+22]). Once the flow rate is increased (a change highlighted with a cross symbol in Figure 6.4) the particle swelling rate increases significantly. The sample CCRH97-02 also dilates up to 1%, but, as the particles become more deformable, it compacts down to -3.5% of the initial volume. The bulk porosity is initially 47% and it decreases down to 44% at the time-step corresponding to the dilation peak. At the end of the test, the porosity is 34%, as reported in Figure 6.5.

In order to make a consistent comparison between the different experimental campaigns, in Figure 6.5 is reported the volumetric strain at the sample scale $\varepsilon_{V,s}$ as a function of the arithmetic average particle volumetric strain $\bar{\varepsilon}_{V,p}$. The response in CCRH97-01 (green) and CCRH97-02 (orange) are similar. Initially, both samples dilate because of particle swelling. The

curve of CCRH97-01 stops when the experiment is interrupted (end of available beamtime), while CCRH97-02 shows the ensuing compaction stage. This competition between swelling and reduction of mechanical properties is also observed in our previous study [Veg+22], here reported with a gray line (in which the stress applied was 25 kPa and not 35).

The presence or absence of a compaction stage in the volumetric response is linked to the eventual water content increase. In CCRH97-01 the mass gain is $\approx 8\%$ the sample's initial mass, while in CCRH97-02 $\approx 22\%$. The experiments are performed on the same material and at similar environment conditions (temperature and RH), therefore the initial water content can be assumed equivalent in both. We can conclude that the compaction stage is observed only in CCRH97-02, because of the (much) higher water content, which sensibly decreases the mechanical properties of the particles.

Concerning the volumetric response at the sample scale, the differences in peak dilation between the experiments can be explained because of the particles trapped between the porous stone and the PTFE cell (see Section 6.2.2), the friction between the particles and the walls, vertical stress, or even a small difference in initial water content.

Figure 6.5 also reports the evolution of porosity during the experimental campaigns. The void space decreases monotonically in all three cases because of particle swelling, even during the dilation stage. Moreover, the softening of the particles and the consequent sample compaction can accelerate the porosity decrease. Finally, it should be noticed that the curves are essentially parallel, indicating a consistent response between the three tests, with a discrepancy only in the initial porosity value, which can be the result of sample preparation, the sample size, different boundary conditions, and couscous batch.

6.3.3 Water content and its effect on the microstructure

In these experiments, the driving process is the evolving water content in the particles, which originates due to a difference in water activity between the couscous molecules and the high RH air, which in turn alters the particle-scale properties, and thus the sample-scale structure.

Neutron tomography is performed precisely to gather information about the water distribution in the sample. The multi-modal registration procedure in Section 6.3.1, combined with the DDVC in Section 6.3.2 allows us to follow each particle in the neutron tomographies. The average neutron attenuation of each of these particles can be assumed to be the result of the combination of water sorption, increasing their neutron opacity, and particle swelling (reducing it, since the same amount of material, net of the water sorption, would be spread across more voxels). To be able to quantify water content from the neutron attenuation, while neglecting the possible reduction of gray-value because of dilation, we take the global attenuation of each particle ψ_p (thus the integral of its neutron attenuation values, whose variation we can assume to depend on water sorption), which we simply computed as:

$$\psi_p(t) = \sum_{n=1}^N \mu_{ne,n}(t) \quad (6.1)$$

where N is the total number of voxels belonging to the particle and $\mu_{ne,n}$ the gray-value of the n^{th} voxel.

It is possible then to investigate the presence of heterogeneities in attenuation across the sample. The mechanisms that can lead to these heterogeneities are multiple. For instance, the water concentration can gradually decrease as water molecules are entrapped by the particles, as suggested by a former study by Brockbank *et al.* (2021) [BAC21]. The presence of

heterogeneities can also be attributed to a small air pressure gradient that is generated as the injected air flows through the sample [Car97], which in turn affects the water activity of the material and the maximum adsorption [He+09], even with overabundance of water molecules. Ultimately, the stress to which particles are subjected could also affect their sorption capacity.

In this study, we investigate the evolution of vertical gradients, *i.e.*, from inlet to outlet. As observed in our previous study [Veg+22] with similar boundary conditions, the radial variation in volumetric strain is found to be modest, while it is significant along the vertical direction. We therefore study the average particle attenuation $\bar{\psi}_p(h)$ at a given height h . More than the overall attenuation of a particle, which is the product of the natural hydrogen content of the initial skeleton plus the sorbed water, we are interested in its evolution with time, caused by water sorption:

$$\Delta\bar{\psi}_h(t) = \bar{\psi}_h(t) - \bar{\psi}_{h,0} \quad (6.2)$$

where $\psi_{h,0}$ is the hydrogen profile of the reference configuration, assumed to be homogeneous across the sample. It must be noted that the slices close to the porous stones are excluded from this analysis. The interaction of the porous stones (denser than couscous) with the x-ray conic beam creates inevitable artefacts that affect the particles' volume measurement. Since we can measure the overall water uptake of the sample (by measuring its mass at the beginning m_0 and at end of the test m_f) we can calibrate the correspondence between the measured change in attenuation and normalised change in water content. Assuming a linear relationship between the two, the coefficient linking them is evaluated as:

$$\alpha = \frac{\frac{m_f - m_0}{m_0}}{\int_{h=0}^H \Delta\bar{\psi}_{h,f}(t = t_f) dh} \quad (6.3)$$

where $\int_{h=0}^H \Delta\bar{\psi}_h dh(t = t_f)$ is the integral over the sample height H of $\Delta\bar{\psi}_h$ at the end of the test ($t = t_f$) and thus the overall change in attenuation of the particles comprising the sample.

Thanks to α it is possible to convert the vertical profiles of variation of attenuation $\Delta\bar{\psi}_h(t)$ directly to water uptake profiles $\omega_h(t)$ as:

$$\omega_h(t) = \alpha \Delta\bar{\psi}_h(t) \quad (6.4)$$

It is of interest to compare these $\omega_h(t)$ directly to volumetric strain profiles $\varepsilon_{v,h}(t)$, which can be simply computed as the average particle volumetric strain at a given height. It must be noted that later in the article, we use ω to describe the "water content", even though we measure the change in mass with respect to the initial configuration and not to the actual dry mass of the sample.

Figures 6.6 and 6.7 present these profiles for the CCRH07-01 and CCRH97-02 experiments. The increase of particle water content and particle volumetric strain distributions are shown along the (normalised) height of the sample h/H (where $h/H = 1$ indicates the top of the sample). For visualisation purposes, we interpolate the data with a straight line.

The water content increases monotonically during the CCRH97-01 experiment (Figure 6.6a), with an increasing vertical gradient. Particles closer to the injection point uptake in fact more water than the particles at the top of the sample. By the end of the test, the bottom particles pick up $\approx 10\%$ of their initial mass in water, while top particles only 6%. This vertical gradient evolves along the test. At the beginning the profiles' slope indicates higher sorption rate in the lower regions of the sample. However, the difference in water content between lower

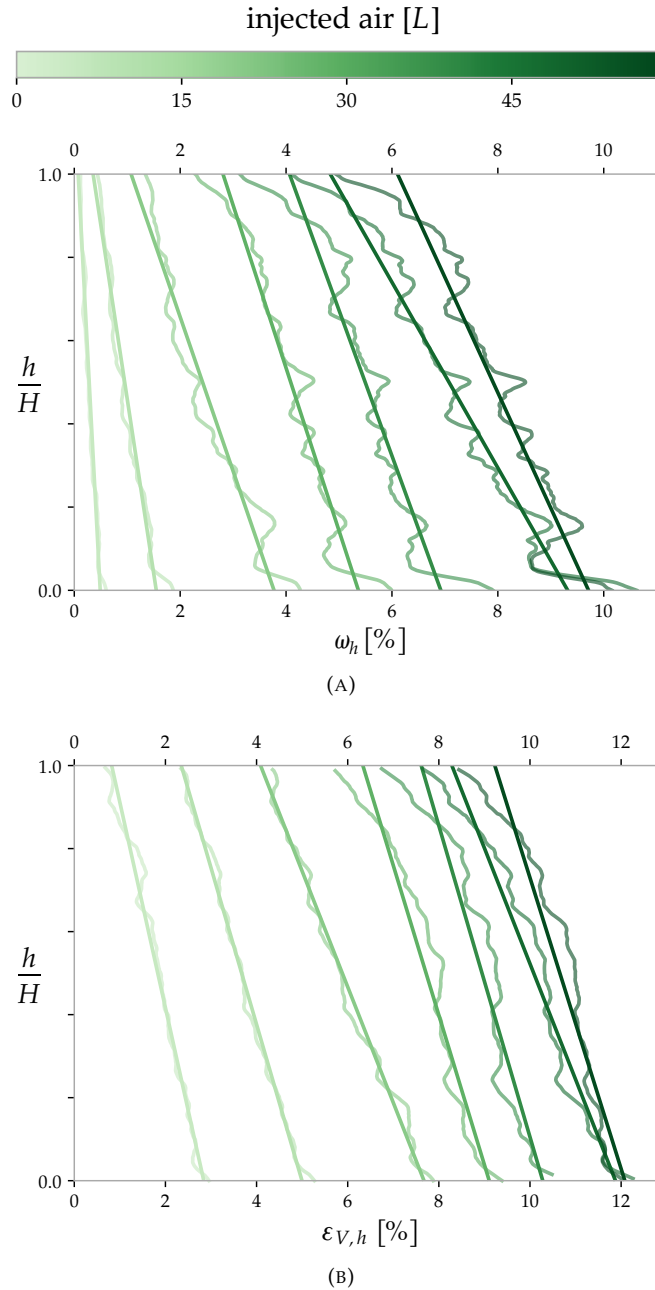


FIGURE 6.6: Vertical profiles of (A) water content (as deduced from neutrons), and (B) volumetric strain (from x-rays), for CCRH97-01. The profiles – and their linear fits – indicate a vertical gradient, where particles closer to the air injection point ($h/H \rightarrow 0$) sorb a higher amount of water than the ones at the top ($h/H \rightarrow 1$). A coherent evolution of the volumetric strain (swelling) profiles is observed.

an upper regions reduces by the end of the test, when the particles are reaching their sorption capacity. Conversely, the particle volumetric strain profiles (Figure 6.6b) evolve coherently to ω_h confirming that swelling is strongly linked to water content increase.

To interpret CCRH97-02, we split the analysis of this experiment in two: before and after the injection speed increase. Figure 6.7a shows the water content distribution profiles, while Figure 6.7b presents the volumetric strain profiles. The two phases of the test are divided by a black line. In the early stages of the test, we observe no significant increase of water content and no major particle swelling. These results support the hypothesis of an infiltration

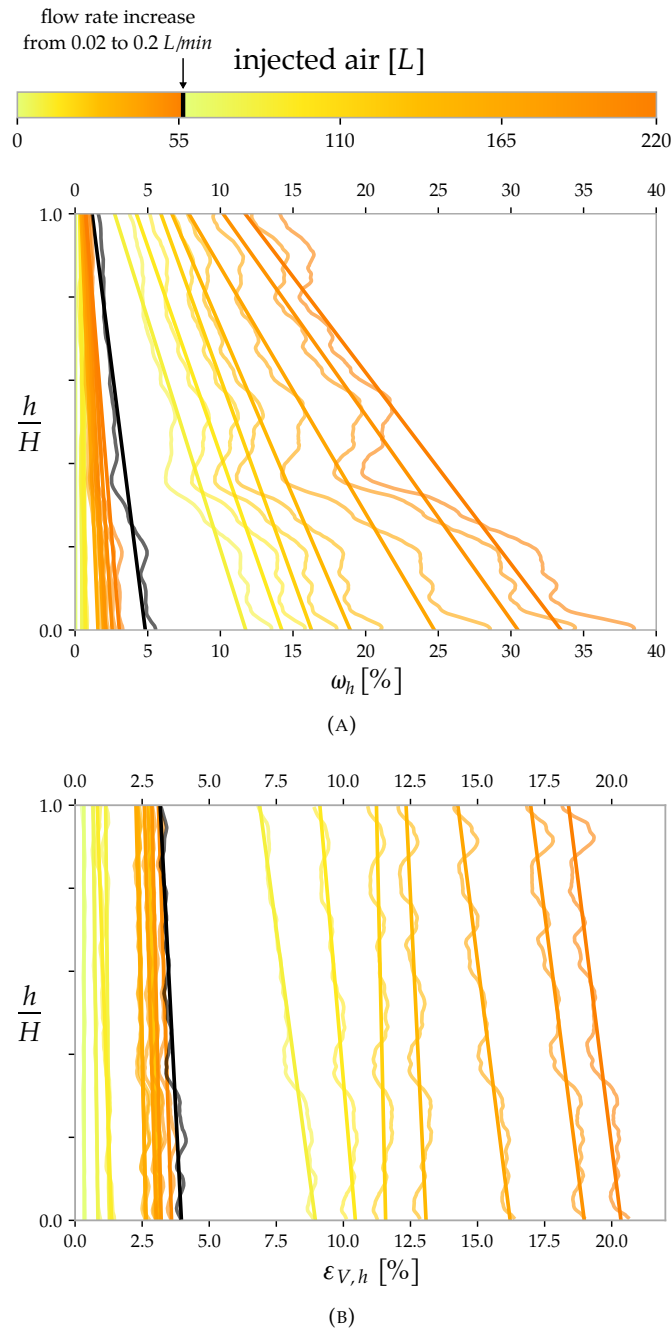


FIGURE 6.7: Vertical profiles of (A) water content (as deduced from neutrons), and (B) volumetric strain (from x-rays), for CCRH97-02. The experiment can be split in two parts: before and after the flow rate increase (black line). The profiles – and their linear fits – in the first stage do not show a significant increase in water content or swelling, and only a modest vertical gradient. In the second stage (higher flow rate), water uptake and swelling accelerate significantly and the particles at the bottom uptake water up to 30 – 35% of their initial mass. Interestingly, the swelling gradient remains less pronounced.

of lower RH air in the oedometric cell or leakage from it (Section 6.2.2). The variations in particle swelling and (thus) volumetric expansion are modest. After we increase the flow rate the process accelerates. The water sorption increases significantly, and a strong vertical gradient can be observed, with particles closer to the injection point sorbing 35% of their initial mass in water, and particles on the top of the sample sorbing less than half of that. In

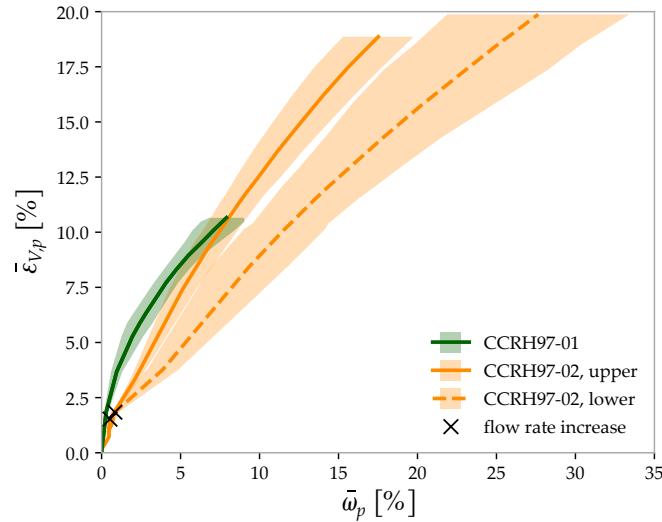


FIGURE 6.8: Average particle swelling $\bar{\varepsilon}_{V,p}$ vs. particle water content $\bar{\omega}_p$. All data-points are displayed with their standard deviation values as “error bands”.

the CCRH97-02 test the increase of water content is exceptionally high when compared to the previous experiment to other studies performed on durum wheat products by Erbaş *et al.*, [EEC05], who recorded an increase of water content of about 19% for semolina and farina at 20 °C. In our case, if we assume an initial dry based water content of 8% (a reasonable value for $\approx 40 - 45\%$ RH), then the final average would be equal to 32.4%, a water content far higher than the one expected from former tests. For this reason, we presume that infiltration of liquid droplets occurred during the experiment. In support of this hypothesis we observe that, while the volumetric expansion also significantly accelerates, the swelling vertical gradient remains modest, hinting possibly at a temporal delay between the water sorption process and the particle dilation. The delay could be caused by the gelatinous barrier that forms when couscous particles are exposed to liquid water [DR+22].

Once the water content distribution and the volumetric strain of the particles are assessed, it is possible to investigate their relative evolution. Figure 6.8 presents the average values of particle volumetric strain $\bar{\varepsilon}_{V,p}$ and average particle water content $\bar{\omega}_p$ (obtained from the respective $\varepsilon_{V,h}$ and ω_h profiles) along with their respective standard deviation at different time-steps³. The green solid line corresponds to the CCRH97-01 experiment, which shows a bi-linear trend. Initially, even a small increase of water content of 2 – 3% causes a 6% swelling. For higher water contents, the swelling slows down (approaching a plateau as shown in Figure 6.4).

The equivalent analysis is performed for the CCRH97-02 sample, but dividing the sample in a top and in a bottom region. As shown by 6.7a, the water content distribution gradient is not constant along the height of the sample, but rather there is a significant variation at $h/H \approx 0.4$. Hence, in Figure 6.8, the results from the upper region are shown with a solid orange line, while the results of the lower region with a dashed one. Once again, for rather low water content variations, we observe a significant increase of volume. However, in later stages of the experiment (after the flow rate increase), a different behaviour emerges in the upper and the lower region. While the top particles, having lower water content, follow the response of

³We only report the water content standard deviation, as the volumetric strain one was much lower thanks to the accuracy of the measurements on x-ray images in this study.

CCRH97-01, the lower ones swell similarly despite their higher water content. For particularly high amounts in water, the swelling behaviour is still directly proportional to water content, albeit at higher values, there is a delay between the two. In a previous work [DR+22] on individual, submerged particles studied optically, it was observed that, while particles can dilate up to 400 %, the rate of expansion progressively slows down. This is caused by the appearance of a gelatinous layer which hinders the water diffusion to the inner layers of the particle. This diffusion-controlled delay could justify the previous results and the loss of linearity between water content and volumetric expansion.

The discontinuity point (or inclination change) could coincide with the saturation of the outer layers of particles and thus the change in regime. However, we cannot confirm this interpretation directly from the images, because of the internal porosity of particles and the relatively high blur on their edges in neutron images. The applied vertical stress or the particle-wall friction could further influence the particle swelling *vs.* water content relationship. More generally, in the images acquired during the two experimental campaigns, no intra-granular water content gradient is observed within individual particles. This suggests that the process is homogeneous at least at the spatial and temporal resolution adopted and for the accuracy of the method – while we cannot exclude that the intra-granular radial gradient plays a role, it does not appear to be a dominant phenomenon in these boundary conditions.

The growth of inter-particle contacts is one of the key factors governing the macroscopically observed agglomeration and thus loss of functionality. The presence and area of the contacts are detected as in our previous study [Veg+22]. Thanks to neutron tomography and the related $\bar{\omega}_p$ measurements presented previously, in this study we focus on the effect of the water content variation onto the median contact area variation $\widetilde{\Delta A}$, *i.e.*, the median of all the contact area variations, defined as:

$$\Delta A_{ij} = A_{ij} - A_{ij,0} \quad (6.5)$$

where i and j are any pair of the contacting particles, A_{ij} is the contact area at that specific time-step and $A_{ij,0}$ the initial one.

Naturally, the number of detected contacts increases with particle swelling and the eventual sample compaction [Veg+22]. We therefore define two different sets of contacts. The first set refers to all the contacts detected throughout the experiment. The second one is a subset of the previous, including only the contacts that are identified since the reference configuration, and is named here as “preserved contacts”. Figure 6.9 presents the $\widetilde{\Delta A}$ evolution for both groups and both the experiments. The relation between contact area variation and water content can be described as (quasi-)linear, similarly to what we observe in the particle volumetric strain *vs.* water content relation (Figure 6.8).

During the test, new contacts are generated, and their contact area is generally quite small. Therefore, these “generated” contacts affect the $\widetilde{\Delta A}$ rate of increase. In this case the discontinuity evidently coincides with the start of the macroscopic volumetric compaction (Section 6.3.2). As expected, the final $\widetilde{\Delta A}$ value is higher for preserved contacts areas, since they are generally larger than newly generated ones. The “error zones” are not reported in Figure 6.9a since the distributions of contact areas are inherently broad, due to the irregular shape of the particles and because of their (re)arrangements. Figure 6.9b shows the distribution of all contact areas at representative water content levels and for both the experiments. These can be interpolated with skew normal distributions, of which the shape, location, and scale parameters are reported in Table 6.2. The distributions broaden at higher water contents, as the swelling of

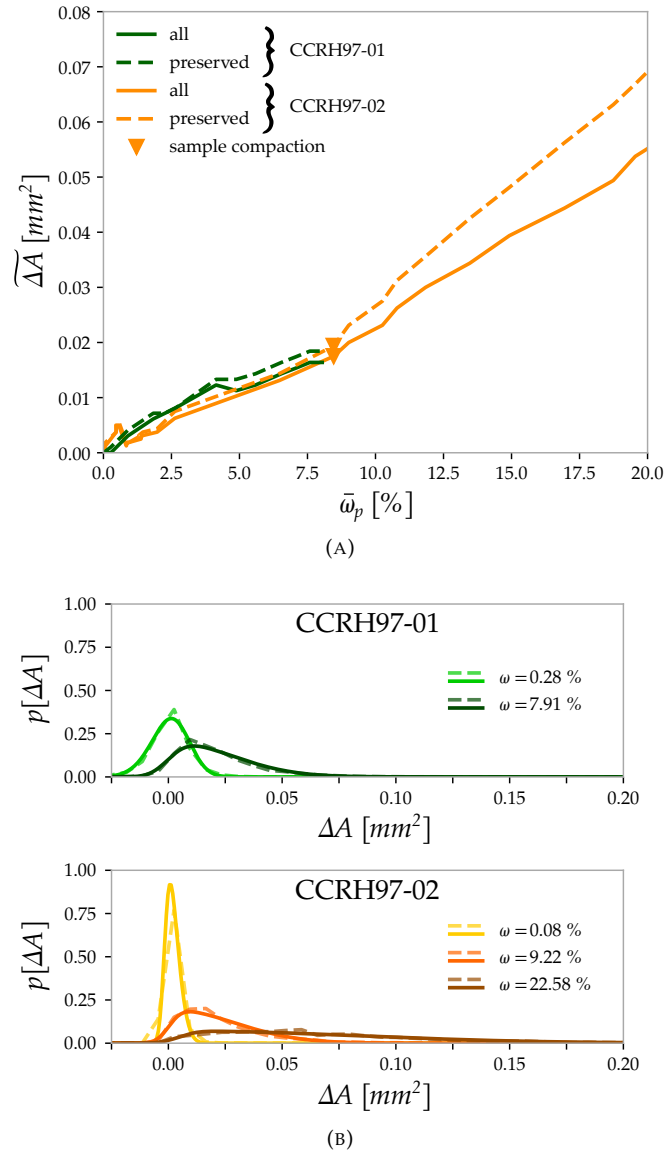


FIGURE 6.9: (A) Evolution of the median contact area variation $\widetilde{\Delta A}$ as a function of water content $\bar{\omega}_p$ and (B) representative statistical distributions of ΔA measured in both the experiments. The analysis is performed both considering only the contacts existing since the beginning of the test (dashed line) and for all the contacts (solid line). In both experiments, the distribution of contact area variation ΔA can be described with a skew normal distribution, whose parameters are reported in Table 6.2, which broadens at higher water contents.

particles and the possible sample compaction induce the growth of existing areas of contact and the generation of new contacts. Moreover, these distributions are comparable between the experiments, suggesting a coherent process and a reliable image analysis procedure.

TABLE 6.2: Statistical parameters obtained by fitting the contact area variation ΔA probability distributions shown in Figure 6.9b with a skew normal distribution.

test	ω [%]	shape	location	scale
CCRH97-01	0.28	-1.217	0.00696	0.01066
	7.91	4.140	0.00001	0.02745
CCRH97-02	0.08	2.480	-0.00159	0.00478
	9.22	6.339	0.00023	0.02854
	22.58	12.228	0.00464	0.07887

6.4 Conclusions and perspectives

In this article we present the results of two experimental campaigns performed on couscous assemblies exposed to high RH, in order to activate the phenomena characterising it as hydro-sensitive. We acquire images with simultaneous neutron and x-ray tomography, from which we quantify the microstructural changes (swelling, contact areas) of thousands of particles driven by the water uptake, as well as the dilation-compaction competition at the sample scale. We observe the presence of sorption and swelling gradients despite the more than sufficient amount of water molecules provided to the system by the high RH air flow. We presume that the heterogeneities are caused by the location of air injection point, the decrease of water concentration due to sorption, air pressure drops from inlet to outlet that influence the material's water activity, and possibly stress gradients. A quasi-linear relation can describe the evolution of particle volumetric strain and contact area variation with respect to the water content increase, although the loss of mechanical properties enhances the trend of the latter. The swelling might be delayed for particularly high water contents, which we think is induced when the particle's external layers are saturated. Altogether, these experiments constitute a unique data-set, which is, to our knowledge, the first attempt to determine the water content of individual particles and correlate it to the particle scale phenomena of hydro-sensitive granular materials. The bespoke developed algorithms combine information from x-ray and neutron images, from which we measure strains and assess the water distribution and their variation with time.

In the future it would be beneficial to further investigate in detail different aspects of the phenomena underlying caking, which is ultimately the final problem to solve in industry. A more accurate control of the initial experimental conditions would help improve the study of the relation between microstructure and water content. The water state (bound or unbound) could be investigated with techniques like Nuclear Magnetic Resonance and thus explain the delay we observed for relatively high water contents. It would be of great importance to study the interaction of particles to understand and quantify how the contact network affects the agglomeration/caking strength. Finally, the problem could be described by analytical models where variables take into account particle scale properties. The process could be then simulated numerically to investigate the role of variables that cannot be measured experimentally and to predict the material's behaviour.

Acknowledgments

The authors want to acknowledge the Institut Laue-Langevin, Grenoble, France for the allocated time at the NeXT-Grenoble beam-line. We gratefully acknowledge Calvin Buckely for the technical support and the fabrication of the experimental set-up. We thankfully acknowledge Edward Andò for the insight on the the image analysis approach. We sincerely thank the reviewers for their constructive feedback and the helpful comments. This project has received funding from the European Unions Horizon 2020 research and innovation program under the Marie Skłodowska-Curie grant agreement no. 812638 (CALIPER).

Data availability

The raw neutron radiography and x-ray tomography data-sets of the CCRH97-01 and CCRH97-02 experimental campaigns are available according to ILL data policy at: <https://doi.ill.fr/10.5291/ILL-DATA.UGA-121> and <https://doi.ill.fr/10.5291/ILL-DATA.1-05-90>.

Conflict of interest

The authors declare that they have no conflict of interest.

Author Contributions

- Ilija Vego: Writing - original draft, Conceptualisation, Methodology, Software, Validation, Formal analysis, Investigation, Data Curation, Visualisation;
- Alessandro Tengattini: Writing - original draft, Conceptualisation, Methodology, Software, Validation, Investigation, Resources, Supervision;
- Nicolas Lenoir: Methodology, Resources;
- Gioacchino Viggiani: Writing - review and editing, Validation, Supervision, Funding acquisition.

Chapter 7

Summary and discussion of the experimental results

Goal of this doctoral work is to understand the response of hygroscopic granular assemblies exposed to high relative humidity (RH). For this reason, several experimental campaigns are carried out using fine couscous as the reference water-sensitive material. As detailed in the previous chapters, different data acquisition techniques are used to investigate the hydro-mechanical processes induced by exposure to high RH. We employ x-ray tomography, neutron tomography and time-domain nuclear magnetic resonance to observe and quantify the phenomena induced by water sorption on couscous particles and link the particle-scale processes to the overall response of the material.

The following sections serve as summary and in-depth analysis of the results from all these different tests. In Section 7.1 we outline the benefits and obstacles encountered when exploring the behaviour of water-sensitive materials with a multi-modal investigation approach. Emphasis is given to the advantages and disadvantages of each technique and why another helps overcome one's limitations. Section 7.2 focuses on the fundamental link between water content and microstructural changes. The relation between particle swelling and water content is further examined merging all the results from different tests. Then, we discuss the response of the assembly and expand the contact analysis.

7.1 Multi-modal investigation

What grants this doctoral work of the "multi-modal" attribute is the use of nuclear magnetic resonance, x-ray tomography, and neutron tomography (and their combination) to acquire data on the hydro-mechanical processes occurring when exposing the chosen reference material to water. In particular, three different combinations are presented in the Chapters, as also highlighted in Figure 7.1):

- (only) x-ray tomography, in Chapter 4;
- time-domain nuclear magnetic resonance (TD-NMR) and x-ray tomography, in Chapter 5;
- simultaneous neutron and x-ray tomography, in Chapter 6.

The following sections summarise the processes and properties measurable with each technique. Moreover, advantages and disadvantages for each study case are discussed.

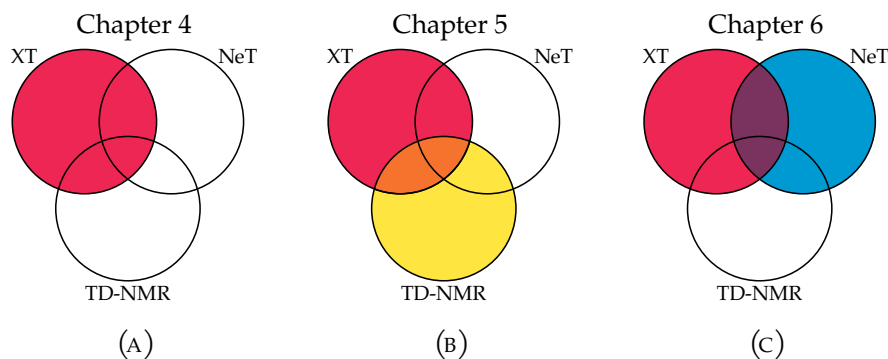


FIGURE 7.1: Outline of the three combinations of the acquisition techniques we used to investigate water-sensitive granular materials. In the first study (Chapter 4), only x-ray tomography (XT) is used to study the volumetric response and contact network evolution induced by RH. In the second (Chapter 5), complementary experiments with TD-NMR and XT are performed to have additional information about the particles water uptake (B). In the third (Chapter 6), simultaneous neutron (NeT) and x-ray tomography (XT) images allow the examination of spatial water distribution during the water sorption process and its impact on the microstructure (C).

7.1.1 X-ray tomography (XT)

X-ray tomography (XT) is the main technique used in this work. The results of all the three experimental campaigns are based on the analysis of XT images and they allow us to evaluate the phenomena induced by water sorption in the material. Thanks to bespoke algorithms detailed in Chapter 3 and in the papers, thousands of particles are identified, tracked, and their volumetric strain quantified, as well as the sample-scale porosity and volumetric response. The technique also allows the observation of possible spatial heterogeneities.

Advantages

In order to properly recognise the advantages offered by XT, it is logical to focus on the results of the experimental campaign in which we used this technique only (see Chapter 4). It was possible to acquire attenuation maps that accurately describe the microstructure of the tested couscous assembly. The obtained images have a very good signal-to-noise ratio, and allow for measurements down to the particle-scale and the contact network.

Disadvantages

The main disadvantage of the XT technique is that no direct information about the actual water content could be retrieved. The *effects* could be observed, but not their *cause*. Another limitation comes from the necessary trade-off between spatial and temporal resolution. In order to achieve higher spatial resolution more time is required to acquire one tomography. Therefore, the imaging settings need to be carefully chosen. It should also be mentioned that the tests are usually days long, and the access to a tomograph can be limited.

7.1.2 TD-NMR and x-ray tomography (TD-NMR+XT)

Chapter 5 presents an experimental campaign in which complementary data-sets are acquired using time-domain Nuclear Magnetic Resonance (TD-NMR) and XT.

Advantages

With TD-NMR it is possible to quantify the overall water uptake of couscous assemblies, something that could not be done using only XT. The technique is based on the magnetic properties of nuclei (Chapter 2) and here it is used to specifically investigate the signal coming from ^1H atoms, and consequently water molecules. TD-NMR also allows relatively high temporal resolution, even hundreds of data-points per day, without compromising with the noise level. Moreover, TD-NMR returns information about the water state (*i.e.*, “bound” and “unbound”) in the molecular matrix of the material. The XT data-set complemented the TD-NMR results with all the advantages described above.

Disadvantages

Two main disadvantages characterise the combined analysis of TD-NMR+XT technique. First, the TD-NMR does not provide any information on the spatial distribution of water. Magnetic Resonance Imaging (MRI) is a tool that is based on the same principles as TD-NMR, and it returns 3D images thanks to the contrast attainable from differences in T_2 relaxation times. However, it could not be used for this study case since it is not suitable for dry matter such as couscous particle, but rather for liquid/fat object, *e.g.*, the human body – which explains its wide use in medical applications. The second limitation of the TD-NMR+XT is that the data acquisition does not occur simultaneously, due to the inherent limitations of the instrumentation, *e.g.*, no metallic pieces can be installed near the TD-NMR magnets. Therefore, analogous tests must be performed separately, forcing the use of expedients in order to have consistent experimental conditions, such as the relatively fast air flow to impose “homogeneous” water concentration (see Chapter 5). However, these compromises often portray unrealistic cases, limiting the study of more significant configurations.

7.1.3 Simultaneous neutron and x-ray tomography (NeT+XT)

Finally, Chapter 6 reports the study in which simultaneous neutron and x-ray tomography (NeT+XT) is carried out.

Advantages

Naturally, this technique holds all the advantages of XT. In addition, it is possible to infer the water content distribution from neutron attenuation variations and spatially correlate these changes to those occurring in the microstructure, from particle- to assembly-scale. This information is crucial to build a relation between particle swelling and water content increase. If the image quality is high enough, the same could be done for contact network.

Disadvantages

Similarly to XT, the NeT+XT combination suffers from constraints caused by the inevitable compromise between spatial and temporal resolution, hindering the investigation of water migration. Another significant limitation is the sample size (*i.e.*, thickness). The materials of interest have inherently a high density of hydrogen atoms per unit volume. The resulting images can be strongly affected by beam-hardening, decreasing the image quality. The problem can be resolved with smaller samples. This implies a lower amount of particles, which in turn might impact the reliability of any statistical analyses. Ultimately, the allocated beam-line time

is even more scarce and precious, thus the tests cannot be run for days and need to be planned with care. This limitation on the other hand highlights the uniqueness and importance of the results obtained with NeT+XT.

All things considered, the multi-modal investigation presented in this work can be considered as an effective and comprehensive method to study water-sensitive granular materials. The processes can be observed and quantified at different scales and correlated to the water content variations in the system. The bespoke algorithms developed for the analysis of images and the TD-NMR data can be used, with small arrangements, to analyse any water-sensitive material.

7.2 Microstructure *vs.* water content

This section summarises the results of the three experimental campaigns detailed in the previous chapters and aims to merge and further analyse them. Before comparing the different tests, the increase of mass in each of them is analysed, so as to recognise the water state in all tests. Then, the relation between particle swelling and water content is analysed and discussed. The effects of particle swelling and softening on the overall assembly response are reviewed. Finally, we examine the contact area growth dependency on water content.

In the previous chapters, a different nomenclature is sometimes used to refer to the same variable or property, because of the different audience towards which each paper is directed. In order to avoid any confusion, the main variables and properties are here re-defined:

- assembly or sample mass: m [g];
- assembly or sample initial mass: m_i [g];
- assembly or sample final mass: m_f [g];
- mass variation during the experiments (*i.e.*, water absorbed): Δm [g];
- water content: ω [%];
- particle water content: ω_p [%];
- dry mass (when $\omega = 0$ [%]): m_{dry} [g];
- particle volumetric strain $\varepsilon_{V,p}$ [%];
- average particle volumetric strain $\bar{\varepsilon}_{V,p}$ [%];
- assembly or sample volumetric strain $\varepsilon_{V,s}$ [%];
- contact area between two grains A [mm^2];
- median contact area between two grains \tilde{A} [mm^2];
- median contact area variation between two grains $\widetilde{\Delta A}$ [mm^2].

7.2.1 Bound or unbound water?

In each test, particles entrap water from incoming flow, so that an increase of mass is always recorded at the end. It is not possible, however, to determine the water state only from a weight measurement. The water can in fact be *bound* or *unbound*. The bound is here defined as the amount of water whose molecules interacting with the particles molecular matrix, and it is the one that actually causes such phenomena swelling and deterioration of mechanical properties. In some cases, the water does not interact with the materials' molecules, but it is simply collected on the particle surface or internal pores – that is why it is defined as unbound. This water is still entrapped, but it does not cause any property variation. It should be noted that in case of particularly high water concentration (*e.g.*, water droplets), the sorption is governed by diffusion, as the unbound water might be absorbed after some time.

TD-NMR is a technique that allows the distinction between the two water states, but it is only employed in the study of Chapter 5. In this case, the relatively fast flow of high RH air hindered the formation of liquid droplets, as deduced by the absence of any signal variation characterised by long T_2 . The final water content measured at the end of this campaign is $\approx 13.5\%$, a relatively small increase, when compared to the other experiments.

In order to correctly compare the final water contents, it is necessary first to impose an initial water content of the samples in the tests presented in Chapter 4 (test XT) and Chapter 6 (Ne+XT), the dry mass (m_{dry}) of which is not determined. An initial ω equal to 8% is assumed for each of them. This value is chosen consistently with the gravimetric study presented in Chapter 5, under the hypothesis of 40 – 45% RH, roughly the storing room conditions. The final water content would then be: 26% for test 1 in Chapter 4, and 16.5% and 32.4% respectively for test 1 and test 2 of Chapter 6.

These results alone can give us some indications about the water state during the experiments. The results are compared to the water content recorded in the gravimetric study and the study wheat farina and semolina by Erbaş, Ertugay, and Certel [EEEC05]. Respectively, the measured maxima are 17.5% and 19%, which are rather similar values.

Any water content above these values could then indicate the presence of liquid water in the system. It is straightforward to notice that this would be the case for test 1 in Chapter 4 and test 2 in Chapter 6. Although accidental, the possible formation of droplets during the experiments does not mean a failed experimental campaign. On the contrary, it actually helps to investigate some aspects that could easily occur. For example, the temperature might suddenly drop, causing an increase of RH, thus leading to condensation. Such scenario could be imagined as an effect of the day-night temperature cycles.

7.2.2 Particle vs. water content

In all the experiments, particular attention is paid to particle swelling. Additionally, the studies in which TD-NMR and NeT+XT are used to examine the relation between particle swelling and particle water content. The results suggest that such relation could be described as linear, especially in the case of absence of unbound water, as detailed in Chapter 5. The linearity could be lost for particularly high water contents, when the outer particle layers are saturated (see Chapter 6).

Before diving into the details of the particle vs. water content relation, the main results are summarised in Table 7.1.

TABLE 7.1: Summary of the data acquisition techniques employed in each experimental campaign, along with the measured initial and final water content and average particle swelling.

Exp. campaign		Technique/s			water content			$\bar{\varepsilon}_{V,p}$
Chapter	test n ^o	XT	TD-NMR	NeT+XT	$\frac{\Delta m}{m_i}$ [%]	ω_i [%]	ω_f [%]	$\bar{\varepsilon}_{V,p,max}$ [%]
4	1	X	-	-	14.5	8 ^a	24.7 ^b	20.8
5	1	-	X	-	13.8	≈ 0	13.8	-
	2	X	-	-	9.1	4.0	13.4	9.1
6	1	-	-	X	7.9	8 ^a	16.5	10.7
	2	-	-	X	22.6	8 ^a	32.4 ^b	22.3
	2*	-	-	X	17.5	8 ^a	26.9 ^b	19.4

^a The hypothesis of initial water content equal to 8% is made based on the room temperature and humidity where the material was stored before the test.

^b The high increase in water content suggests that liquid water might have infiltrated in the sample and influenced the material behaviour.

* As detailed in Chapter 6, two significantly different responses are observed between the upper and lower regions of the sample. Here is reported the upper one, in which the water content is lower.

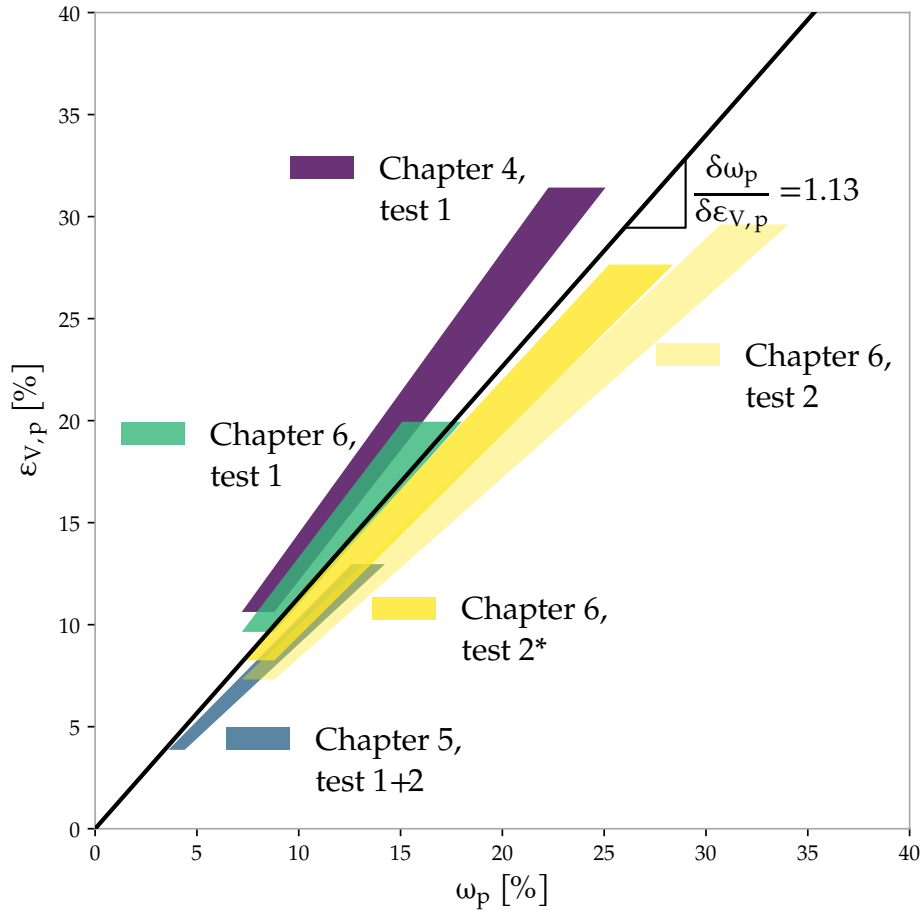


FIGURE 7.2: Evolution of particle swelling $\varepsilon_{V,p}$ with respect to water content ω_p of all experiments, under linearity assumption. The average evolution is highlighted in black and its coefficient is found equal to 1.13.

With the imposition of initial ω equal to 8%, as detailed above, and the assumption of linearity between $\varepsilon_{V,p}$ and ω_p , it is possible to determine *a posteriori* what would have been the particle

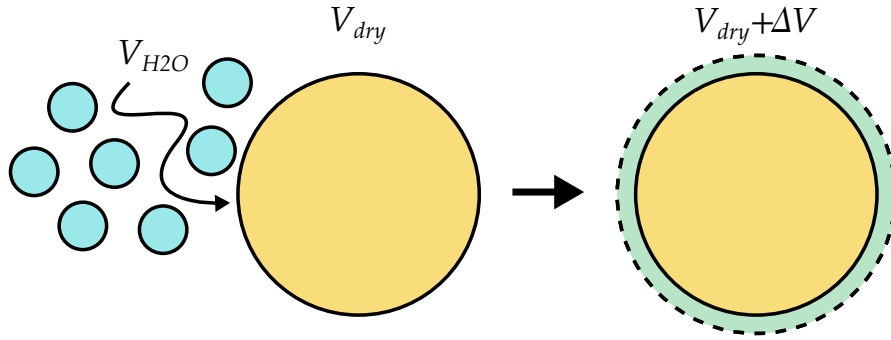


FIGURE 7.3: Schematic view of the water sorption (V_{H_2O}) of a particle (initial volume V_{dry}) and its following swelling ($V_{dry} + \Delta V$).

swelling for that specific initial water content (see Figure 5.10b in Chapter 5 and Figure 6.8 in Chapter 6). The evolution of particle swelling *vs.* water content for all experiments is shown in Figure 7.2. The plot also considers a $\pm 10\%$ error in the estimation of initial and final water content.

Considering that the initial conditions or simply the wheat origin [Lam+11] can significantly affect the behaviour of the material, it seems accurate to state that the response of all tests is similar. Merging together all the results, the average slope is found equal to 1.13.

This linearity assumption might still present itself as a strong but unrealistic hypothesis, even though the experimental results corroborate it. The following discussion aims to give a physical explanation to this quasi-linear response and explicitly determine the variables that govern it.

Recall the water content ω definition:

$$\omega(t) = \frac{m(t) - m_{dry}}{m_{dry}} = \frac{\Delta m(t)}{m_{dry}}. \quad (7.1)$$

Considering that the change in mass is directly related to a specific amount of water absorbed, the previous equation becomes:

$$\omega(t) = \frac{\rho_{H_2O} \Delta V_{H_2O}(t)}{\rho_{dry} V_{dry}} \quad (7.2)$$

where ρ_{H_2O} is the water density, ΔV_{H_2O} the volume of water absorbed, and ρ_{dry} and V_{dry} are respectively the density and volume of the material in dry conditions (*i.e.*, $\omega = 0$).

This last equation can be then rewritten as:

$$\frac{\Delta V_{H_2O}(t)}{V_{dry}} = \frac{\rho_{dry}}{\rho_{H_2O}} \omega(t). \quad (7.3)$$

Assuming that all the sorbed volume of water turns into measurable dilation of the material ($V_{H_2O} = \Delta V$, see Figure 7.3), we can study a limit case of the problem. With this strong hypothesis, which will be later mitigated, the left-hand side is then nothing else than the actual volumetric strain:

$$\varepsilon_V(t) = \frac{\rho_{dry}}{\rho_{H_2O}} \omega(t) \quad (7.4)$$

Thus, it appears that the volumetric strain and water content are linearly related by the ratio between the dry material density ρ_{dry} and the water density ρ_{H_2O} .

Naturally, Equation 7.2 could be generalised, easing the hypothesis that the absorbed volume is totally converted into material dilation:

$$\varepsilon_V(t) = \frac{\rho_{dry}}{\rho(\omega, t)} \omega(t) \quad (7.5)$$

The volumetric strain is now still controlled by water content, but ω also affects the material density as it absorbs water, a real phenomenon, proven by the change in x-ray attenuation (thus, density), as detailed in Chapter 4.

To describe with higher accuracy the dependence of material density on water content would require more tests, a significant effort that might prove to be futile when trying to characterise the behaviour of a large set of materials such as water-sensitive ones. Nevertheless, we can draw some conclusions by simply analysing some particular cases of Equation 7.5.

Supposing the material density to remain constant while absorbing water would mean a balance between overall dilation and internal pores closing. As shown in Figure 7.4, a domain 'A' can be defined where the slope of the linear relation is lower than 1 ($\rho(\omega, t) > \rho_{dry}$). If the response of the material lies within this region, the pore closing or even the collapse of the molecular matrix due to dissolution prevails over the material dilation (*i.e.*, the apparent x-ray density increases).

Conversely, dilation dominates the process when the material density is lower than the dry one ($\rho(\omega, t) < \rho_{dry}$). This other domain can be however divided in two sub-domains 'B' and 'C'. The main difference between the two is the swelling extent. In domain 'C' the dilation would be so large that the material's new density is lower than water density ($\rho(\omega, t) < \rho_{H_2O}$). On the other hand, in domain 'B' the material experiences a constrained swelling ($\rho_{H_2O} < \rho(\omega, t) < \rho_{dry}$). Specifically for couscous, the threshold coefficient between domain 'B' and 'C' is ≈ 1.4 , given that the true density of semolina grains, of which couscous is made, is equal to $1.415 \pm 0.003 \text{ g cm}^{-3}$ [BRC18].

We can deduce that the response of couscous particles lies within the 'B' domain (coefficient equal to 1.13). The water sorption prompts a general swelling that prevails over the internal pores closing and the particles density remains lower than the dry density, as suggested by the x-ray attenuation decrease detailed in Chapter 4. However, we cannot exclude a (temporary) response in the 'A' domain, due to initial pore closing or dissolution at extremely high water contents. It should be noted that the measured response of the material is obtained through image analysis, which depends on the image quality and spatial resolution, which in turn affect the particle segmentation and volumetric strain measurements (Chapter 3). Nevertheless, we can conclude that a response within the 'C' domain is very unlikely to be observed for such materials (the particles would float).

Finally, it should be noted that the possible occurrence of the $\varepsilon_{V,p}$ and water content ω_p response within both 'A' and 'B' domains would make the estimation of water content only from x-ray attenuation inaccurate.

7.2.3 Sample volumetric response *vs.* water content

One of the objectives of this doctoral work is the correlation between particle scale phenomena and the overall response of the assembly. For this reason, in all the experimental campaigns the volumetric evolution of the samples is measured and compared to particle swelling.

Two main configurations are analysed: free swelling and swelling under constant stress. The former is investigated in the TD-NMR+XT study case (Chapter 5). No load is applied on

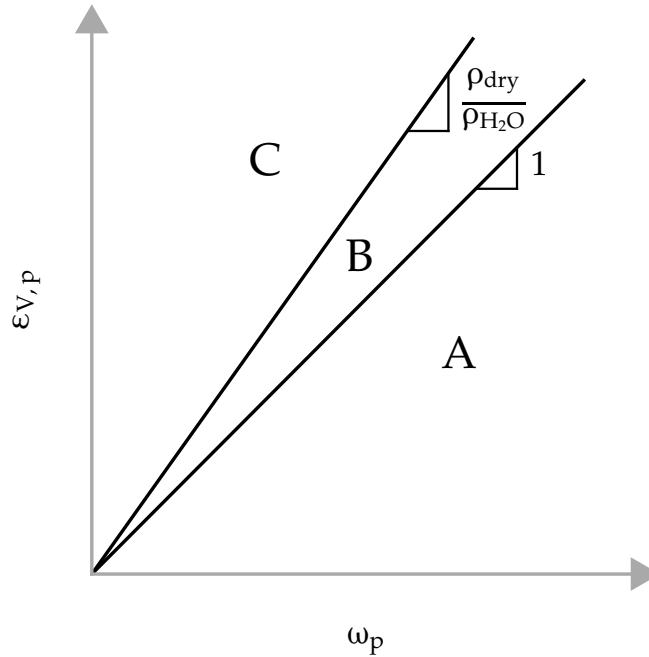


FIGURE 7.4: Particle volumetric strain $\varepsilon_{V,p}$ and water content ω_p domains. Based on the ratio between ρ_{dry} and the new density after water sorption $\rho(\omega, t)$ of Equation 7.5, three domains are defined, which are characterised by different particle swelling dynamics. Domain 'A' describes a behaviour where the pores closing and possible material dissolution prevail over the dilation of the particle. Domain 'B' is characterised by prevalent dilation. Domain 'C' describes an extreme swelling dynamics, where the new material density is lower than the density of water.

the particles exposed to high RH air flow and their swelling and the overall sample dilation are measured. Without any mechanical constraints, analogous particles and sample dilations values could be expected. However, the particles are placed in a rigid cylindrical container preventing any radial strain. The measured $\varepsilon_{V,s}$ is higher than $\bar{\varepsilon}_{V,p}$, due to particle rearrangements. The two variables seem to be linearly related (Chapter 5). Therefore, holding the assumption of a linear relation between particle swelling and water content, the free swelling at the sample-scale is also linearly related to ω .

In the second configuration (swelling under constant stress) the samples are subjected to constant vertical stress (see Chapter 4 and Chapter 6). This additional mechanical constraint allows the observation of a peculiar dilation-compaction behaviour induced by the competition between particle swelling and concurrent deterioration of mechanical properties. For relatively low water contents, the particles are able to resist the load applied and even lift it up. However, as the ω increases, they become more deformable and they reverse the trend and are compacted. In the three tests a consistent evolution is observed, since the the dilation peak is reached for similar water content variations (see Chapter 6). Naturally, this peak is found to be larger when the sample is subjected to lower vertical stress.

One final aspect to be considered is the persistent occurrence of swelling gradients. Although in some cases we suspect infiltration of liquid water, the measurements indicate that heterogeneities inevitably develop, even under well controlled conditions (*i.e.*, over-supply of water by fast flow, small samples). We presume that these heterogeneities are induced by small differences in water activity, which can be affected by little drops in air pressure as the air flows through the assembly or the stress state.

Altogether, more tests would help understand and describe the link between water content and sample volumetric response. An accurate control of the boundary conditions is a complex operation, especially when applying constant vertical stress on the sample. The cell has to be sealed, an aspect that is in contrast with the allowed vertical displacement of the piston. It would be beneficial therefore to use the results of the experimental campaigns to develop and calibrate numerical models, where the boundary conditions are more easily controlled. A first simple attempt to do so is presented in the following Chapter 8, in which a newly implemented DEM model is introduced together with two sensitivity studies.

7.2.4 Inter-particle contact areas *vs.* water content

The contact network is one key aspect that characterises the behaviour of water sensitive materials. In fact, the particle swelling and higher deformability cause the increase of inter-particle contact areas, which in turn can influence the “caking strength” of the material.

Only by means of NeT+XT it is possible to directly measure the evolution of contact areas with respect to water content, as detailed in Chapter 6. The relation between the median contact area \tilde{A} and the average particle water $\bar{\omega}_p$ is found to be approximately bi-linear. The value of \tilde{A} grows linearly with $\bar{\omega}_p$ until the dilation peak is reached. Then, in the compaction stage, the area growth rate increases, but the relation appears to remain linear. In the study presented in Chapter 4, XT allows a comprehensive study of contacts across the sample and the effect of boundary conditions, taking advantage of the particularly good quality of the images. However, the water content of the particles cannot be estimated. Nonetheless, it can be verified whether the contact area growth in different tests (in which contact detection is feasible) is coherent. Figure 7.5a shows the increase of the median contact area variation $\Delta\tilde{A}$ measured in the three tests where the contact analysis is performed (test 1 of Chapter 4, test 1 and 2 of Chapter 6). The evolution is plotted with respect to the average particle volumetric strain $\bar{\epsilon}_{V,p}$, which under the assumption of linearity can be taken as proportional to ω_p . The results show great consistency between the tests, underlying the reliability of the contact analysis algorithms. The contact areas naturally increase with particle swelling, and the growth rate is higher while the sample is compacted ($\bar{\epsilon}_{V,p} > 10\%$).

It should be recalled that the distributions of contact areas are rather large and they expand throughout the test as “old” contacts become larger and larger, but also “new” contacts are generated. The particles shape and arrangement are nor regular. It is therefore rather complex to derive a distinct contact model for such materials. Nevertheless, the investigation of the inter-particle contacts *vs.* water content could be further expanded with numerical modelling, specifically with the DEM, where perfect control of particle geometry is possible (see Chapter 8).

An analytical approach can also be followed. As a first approximation, in the following we attempt to deduce evolution of the contact area between two water-sensitive particles using the widespread Hertzian model.

First, a reference system is described by two contacting particles i and j , as shown in Figure 7.6. The particle geometry is approximated with a sphere for the sake of simplicity.

The harmonic mean radius R^* of the system is defined as:

$$\frac{1}{R^*} = \frac{1}{R_i} + \frac{1}{R_j} \quad (7.6)$$

where R_i and R_j are the radii of the two particles.

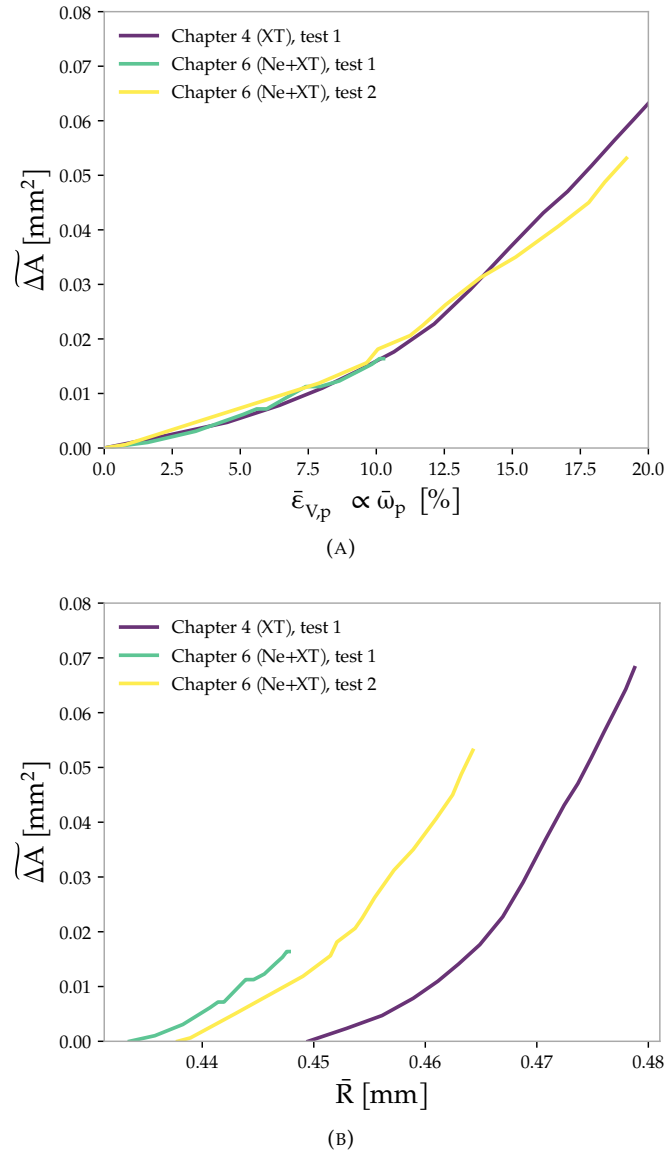


FIGURE 7.5: Median contact area variation $\widetilde{\Delta A}$ as a function of average particle volumetric strain $\bar{\epsilon}_{V,p}$ (thus, particle water content ω_p) (A) and as a function of average particle radius \bar{R} (B).

Upon swelling, the contact between the two spheres (*i.e.*, the circle described by the two overlapping spheres) increase and it is described by a radius a [PHW19]:

$$a(t) = \sqrt{R^*(t) d(t)} \quad (7.7)$$

where d is the indentation. This approximation holds for small deformations (and for $a \ll R^*$) [PHW19]. This means that the model derived should only well represent the very initial steps of the experiments, since by the end of the tests, rather large contact areas are observed.

The contact area between the two spheres is then easily calculated:

$$A(t) = \pi R^*(t) d(t) \quad (7.8)$$

and the same for its variation:

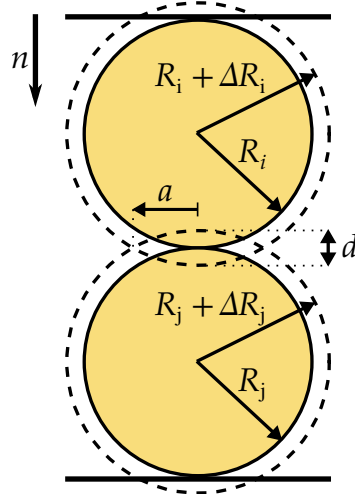


FIGURE 7.6: Schematic view of two contacting spheres used to investigate the contact areas growth with the Hertzian model.

$$\begin{aligned}\Delta A(t) &= A(t) - A_0 \\ &= \pi [R^*(t) d(t) - R_0^* d_0]\end{aligned}\quad (7.9)$$

where R_0^* and d_0 are respectively the harmonic mean radius and indentation of the initial (or reference) configuration.

In the reference configuration, when the contact is ideally a point, the indentation between the particles can be assumed very small, thus $d_0 \simeq 0$, which implies that:

$$\Delta A(t) = \pi R^*(t) d(t) \quad (7.10)$$

After swelling, the configuration evolves into the one described by the dashed lines in Figure 7.6. The radii increase and the indentation evolves too.

If the whole system is confined and no volumetric change can occur along the direction normal to the contact area ($\varepsilon_{V,n} = 0$), the indentation is simply $d(t) = 2\Delta R^*$. Equation 7.10 can be then rewritten as:

$$\begin{aligned}\Delta A(t) &= \pi R^*(t) 2\Delta R^*(t) \\ &= 2\pi [R^{*2}(t) - R_0^* R^*(t)]\end{aligned}\quad (7.11)$$

This equation describes a quadratic function of the radius, in agreement with our observations (see Figure 7.5b). However, it only considers the increase of contact areas because of particle swelling, but not the general dilation-compaction behaviour found experimentally. For this reason, it can be generalised taking into account any volumetric variation ($\varepsilon_{V,n} \neq 0$). Introducing this term, the indentation varies based on system dilation or compaction ($d(t) = 2(1 - \varepsilon_{V,n}(t))\Delta R^*$) and the generalised version of Equation 7.11 reads:

$$\Delta A(t) = 2\pi(1 - \varepsilon_{V,n}(t)) [R^{*2}(t) - R_0^* R^*(t)] \quad (7.12)$$

The evolution is again quadratic, and has the same “shape” as the experimental measurements in Figure 7.5b. Moreover, the model takes into account the possible dilation or compaction of the system. A positive $\varepsilon_{V,n}$ “slows down” the contact area growth, while a compaction enhances it, as observed in the experiments (see Chapter 4 and Chapter 6).

The Hertzian model appears to be a good approximation to understand and describe the evolution of contact areas of our reference material particles, although the assumptions under which it holds are not respected in reality. The swelling and deformations cannot be considered small and surely a (the contact area radius) is not much smaller than the radius. It seems that, thanks to the relatively high internal porosity of couscous particles, the assumed (large) particles indentation is compensated by the compaction of the contacting regions. This suggests that the model might work well for confined configurations (*e.g.*, oedometric conditions), but not necessarily in other cases. It should be also noted that this derivation is (almost) purely geometrical, and no effect on the mechanical properties of the particles and contact regions is taken into account, if not partly by the $\varepsilon_{V,n}$ term and a possible large indentation.

7.3 Conclusions and perspectives

The experimental work carried out demonstrates how the combination of different data acquisition techniques is highly beneficial to study the behaviour of materials. Specifically to this study case, several tests are performed and data are acquired with x-ray tomography, TD-NMR and neutron tomography. These tools are highly complementary and provide the possibility to investigate different aspects of the hydro-mechanical processes occurring in water-sensitive materials and to quantify the particle- and sample-scale phenomena and the water content variations inducing them.

Couscous is found to be a convenient material and an efficient choice to perform the experiments. The experimental and analysis procedure proposed here will hopefully inspire other works on this or similar materials. Currently, most of the studies are carried out with empirical tools conventionally used in industry, such as sieving methods, powder avalanching or the FT4 Powder Rheometer [AVK95; Abe+12; CB14; BAC21]. A multi-modal investigation would help understand the physical meaning of the measurements and what are the variables that govern the problem in industry.

Collectively, the experiments explore several aspects of the behaviour of such materials and specifically focus on the relation between water and microstructure. Particle swelling is linked to the water content variation, and they are found to be directly proportional, the trend being governed by the density of the material. Under the linearity assumption, the analysis indicates the presence of three different domains within the particle swelling *vs.* water content relation. The material density is affected by water content, and it can become higher than the initial one, lower than the dry density, or even lower than water density. In our case, by averaging the results of all experiments, it appears that the swelling dynamics are governed by molecular interactions that slightly lower the overall material density (*i.e.*, particle dilation is greater than the internal pores closing).

The sample-scale volumetric response is the result of particle scale phenomena: swelling and mechanical properties deterioration. In the free swelling case, the sample dilation is directly proportional to the particle swelling. Conversely, when a vertical stress is applied, the

swelling competes with the higher particle deformability, revealing a dilation-compaction response. The image analysis procedure also reveals the recurring presence of swelling heterogeneities in the samples, which might be induced by presence of liquid droplets of water, by the stress distribution or even by small pressure gradients that locally affect the sorption process.

The overall sample deformation also has a significant impact on the evolution of the contact network. The inter-particle contact areas increase quadratically with the particles radii because of the swelling, but possible compaction or dilation can increase or decrease the contact area growth, and likely influence the overall “caking” of the assembly. A quadratic form is also found following an analytical approach to investigate the contact area growth between two particles in contact.

As mentioned, the multi-modal investigation presented here could be of inspiration for future studies. However, given the complexity of the problem, there are some aspects of our work that might/should be improved or further investigated.

First, all future experiments should consider the estimation of the dry mass by the end of the test, to accurately assess the water content and fully characterise the material’s behaviour. Tests involving fewer particles, higher spatial resolution and well controlled mechanical conditions would help investigate the coefficient that links particle swelling and water content. Moreover, such experiments might help improve the contact network development and the evolution of contact areas.

Altogether, the studies presented mostly focus on the morphological and geometrical variations induced by water content. What is necessary and crucial to further understand the behaviour of such materials is a mechanical characterisation. An example is given in Appendix B, where the results of compression tests on *individual* particles are performed to measure the stiffness dependency on water content. The overall sample agglomeration strength (*i.e.*, caking strength) or the mechanical properties of contacts require accurate examination.

There are many other aspects that might be investigated such as the particle size, creep, temperature, wetting and drying cycles. Obviously the list can go on, but as mentioned in Chapter 1, our knowledge about these materials is still rather limited. What could facilitate such studies is the development and calibration of numerical models, suitable for all water-sensitive granular materials, and not only couscous. The next Chapter presents early results obtained with a newly developed model based on the discrete element method (DEM), in which particles volume increase with time, while their stiffness decreases.

Chapter 8

A basic DEM model for hygroscopic swelling particles

The experimental work presented in the previous Chapters allows the quantification of the microstructural evolution of granular hygroscopic assemblies together with water sorption. The observations and measurements reveal different aspects of the peculiar behaviour of couscous particles, and thereby can provide a general reference for water-sensitive granular media. A competition between particle swelling and deterioration of mechanical properties is found for relatively high water contents (see Chapter 4 and Chapter 6). Moreover, it is possible to gain insight into the relationship between the microstructure and water uptake. Specifically, we investigate particle swelling, sample volumetric response, and growth of contact areas as a function of water content, as summarised previously in Chapter 7.

Additional tests could be performed to further investigate the response of couscous particles or, more generally, of other water-sensitive materials, in order to examine which variables govern their behaviour. However, the time dependency of the problem is a complex issue to overcome. Tests can go on for days or even weeks, and maintaining stable experimental conditions can become a relatively difficult issue to deal with. Moreover, technical, time and economic constraints related to the access to imaging or industrial facilities cannot be ignored.

For these reasons, a numerical tool able to investigate the behaviour of these materials can be extremely beneficial. Given the nature of the experimental measurements and the general objective of this doctoral work linking the particle and assembly responses, a numerical model is developed and calibrated to digitally reproduce the behaviour of hygroscopic swelling particles. A discrete element method (DEM) approach is here adopted, which allows the imposition of properties changes to each individual particle and consequently influence overall response of the assembly. At first, the goal is not to replicate with high accuracy the behaviour of couscous, but rather to build a numerical tool that could support the experimental observations and investigate variables that are otherwise not measurable with current or accessible measurements techniques. The model is conceived to be as simple as possible, *i.e.*, defined by a limited number of variables, which allows for a fundamental understanding of the processes occurring. The parameters can be calibrated with respect to the material of interest, with the purpose of guaranteeing a widespread application. The model introduces the possibility of concurrent variation of particle volume and stiffness, an essential feature to simulate the behaviour of water-sensitive granular materials, which is often ignored in literature [Swe+17]. In the future, the model could be used to recognise the role played by variables that are difficult to control or that cannot be measured experimentally (*e.g.*, forces).

The numerical model is developed and implemented in C++ with the help and supervision

of Prof. Vincent Richefeu at Laboratoire 3SR. The code is implemented anew in order to keep control of the variables governing the processes and have direct access to the source code, allowing for quick modifications and improvements when required.

This chapter presents the current state of the model and the preliminary results obtained from two sensitivity studies investigating the effect of vertical stress and of the relative humidity (*i.e.*, maximum water content) on the overall response of the assembly.

8.1 The model

As mentioned, the model design is intended to be simple. Its goal is to capture the phenomenology found experimentally, by using a small number of independent variables. The discrete element method (DEM) is selected as the appropriate approach to simulate the behaviour of hygroscopic swelling particles, given its effective and widespread use to simulate the behaviour of numerous granular materials [GRHM05; et 21] since the work by Cundall and Strack [CS79].

The geometry of couscous particles is simplified and approximated with spheres of the volume measured from the x-ray tomography images (see Chapters 4, 5 and 6). Their kinematics is assumed to be 2D, but the three-dimensional nature of the particles (*i.e.*, mass, volume) is still taken into account. These additional geometrical restrictions are imposed for different reasons. Given the axial symmetry of the configurations investigated experimentally, a two-dimensional configuration simplifies the analysis and the visualisation of the problem, and provides results that can be qualitatively compared to the experimental ones.

Water content increase

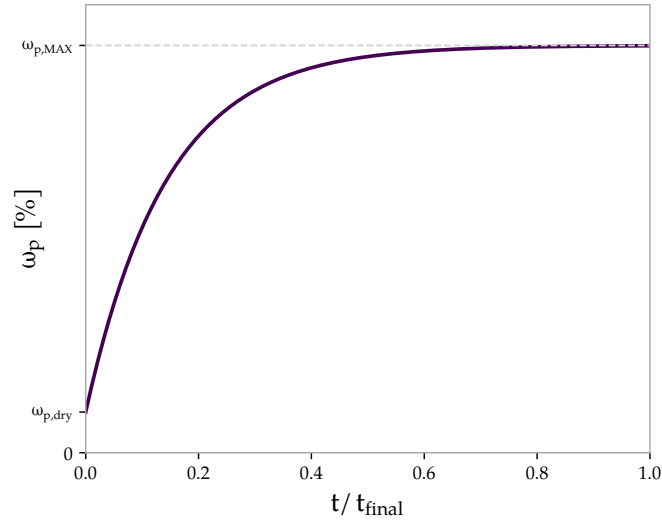
The particle water content ω_p is the fundamental variable of the model, and it increases with time t . The variable “time” does not have equivalent meaning between the experiments and the numerical simulations. Nevertheless, the quasi-static nature of the microstructure evolution is preserved using a relatively small time-step within sequential computations.

In agreement with the sorption model proposed by [Omi+98] and the measurements obtained with TD-NMR (in Chapter 5), the increase of ω_p is modelled by an exponential function:

$$\omega_p(t) = \omega_{p,dry} + (\omega_{p,MAX} - \omega_{p,dry}) \left[1 - e^{-\frac{t}{\tau_\omega}} \right] \quad (8.1)$$

During sorption the water content can only increase, therefore a minimum and a maximum particle values for ω_p are defined: $\omega_{p,MAX}$ and $\omega_{p,dry}$. The sorption rate is controlled by τ_ω , a variable that depends on inherent properties of the investigated material (*e.g.*, diffusion for couscous particles [DR+22]) and it is taken constant for simplicity. It should be noted that the model does not present any limitation in imposing a dehydration process of the particles, although the τ_ω might differ, since an hysteresis is usually found in sorption isotherm curves [Lab75; SW93; Fen96].

For convenience, the model imposes the same water content ω_p to all particles, despite the swelling and water content gradients observed experimentally (see Chapter 4, 5 and 6). However, the ω value is imposed individually to all particles, thus this inaccuracy can and will be resolved in the future. Hereafter, under this (unrealistic) assumption, ω and ω_p are equivalent.

FIGURE 8.1: Evolution of particle water content ω_p with time.

Particle swelling

Once the water content ω is imposed, the model computes the volumetric strain $\varepsilon_{V,p}$ (*i.e.*, swelling) of each particle, based on the experimental observations presented in Chapter 5 (in particular) and Chapter 6, as already discussed in Chapter 7, the proportionality between particle swelling and water content is a reasonable approximation:

$$\varepsilon_{V,p}(\omega) = \beta(\omega - \omega_{dry}) \quad (8.2)$$

where β is a dimensionless coefficient that requires empirical calibration, since it depends on inherent material properties.

The particle radius is then geometrically updated from the computed new volume:

$$R(\omega) = \left[\frac{3}{4\pi} (1 + \varepsilon_{V,p}(\omega)) V_0 \right]^{\frac{1}{3}} \quad (8.3)$$

in which V_0 is simply the initial volume (at $t = 0$).

Particle softening

Another variable that depends on the water content is the particle stiffness. As discussed in Chapter 1, previous experimental studies have proven that the mechanical properties of water-sensitive grains are strongly affected by water. In addition, a series of compression tests on individual couscous particles is performed to investigate the influence of water content on their apparent stiffness (see appendix B). Coherently with these results and with the study by Glenn et al. (1991) [GYP91], the evolution of the particle stiffness k with ω is modelled by an exponential function:

$$k(\omega) = \begin{cases} k_{dry} & \text{if } \omega \leq \omega_{dry} \\ k_{wet} + (k_{dry} - k_{wet}) e^{\frac{\omega_{dry} - \omega}{v_k}} & \text{if } \omega > \omega_{dry} \end{cases} \quad (8.4)$$

An upper limit is imposed for dry particles (k_{dry} if $\omega(t) \leq \omega_{dry}$), while the k_{wet} is a value to which the function tends asymptotically for extremely high water contents. The decrease rate is controlled by v_k , a material-dependent variable.

Inter-particle forces

Once all the fundamental particle properties are set, the inter-particle forces are computed through the so called Hertz-Mindlin contact model. This model is meant to be used to simulate the behaviour of relatively stiff particles remaining elastic. However, here it is used despite the relatively soft particles for convenience: its simplicity and widespread use, the stiffness of two interacting particles is considered at once, and the forces evolve non-linearly with the overlap. In the previous Chapter it is also shown how the growth of contact areas derived under the Hertzian assumption might be a good approximation of what is observed experimentally, as a relatively large overlap (or indentation) compensates the high deformability of particles.

First, the harmonic means of the radii R^* and stiffnesses k^* between two particles i and j are computed:

$$\frac{1}{R^*} = \frac{1}{R_i} + \frac{1}{R_j} \quad (8.5)$$

$$\frac{1}{k^*} = \frac{1}{k_i} + \frac{1}{k_j} \quad (8.6)$$

and the relation of the normal force f_n between the particles is a function of the overlap $\delta_n < 0$:

$$f_n = \frac{4}{3} k^* \sqrt{R^*} \delta_n^{\frac{3}{2}} \quad (8.7)$$

As mentioned, the model allows a relatively large $\delta(n)$ to emulate the high particle deformability. Although physically incorrect, this assumption is kept since it allows for fast computation and also for bypassing the lack of contact laws in literature for these materials.

At each time step, the tangential force variation Δf_t between two particles is computed:

$$\Delta f_t = k^* \sqrt{R^*} \sqrt{\delta_n} \Delta \delta_t \quad (8.8)$$

where $\Delta \delta_t$ is the relative tangential displacement between the particles. The Δf_t term is then added to the tangential force of the previous step:

$$f_t = f_t + \Delta f_t. \quad (8.9)$$

Following the Coulomb criterion, a limit is imposed on the tangential force f_t :

$$\|f_t\| < \mu f_n \quad (8.10)$$

where μ is the frictional coefficient between the particles.

In this preliminary version of the model, the friction coefficient μ is chosen independent of water content ω , and no cohesion is considered.

8.2 Sensitivity analyses

A preliminary sensitivity study is conducted to examine the effectiveness of the newly developed model and to explore the role of some variables that could not be investigated in the experimental work, despite some strong (and occasionally unrealistic) assumptions.

Before running the simulations, a number of 'constant' parameters are defined: particle density ($\rho = 1.3 \text{ g cm}^{-3}$, derived from the experimental data), friction coefficient ($\mu = 0.8$),

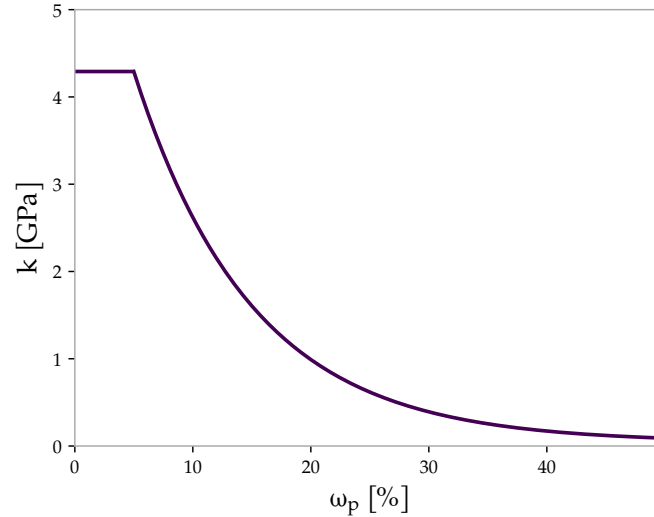


FIGURE 8.2: Evolution of particle stiffness k with particle water content ω_p . For very dry conditions, the stiffness is assumed constant, but when ω exceeds ω_{dry} , the stiffness decreases exponentially.

initial water content ($\omega_{dry} = 5\%$), particle dry stiffness ($k_{dry} = 4.29 \text{ GPa}$) are established, and then the initial configuration is generated.

The stiffness of the particles is calibrated based on uniaxial compression tests performed over individual particles at different water content levels (see appendix B). From these experiments, a value representing the particle apparent stiffness is measured as the ratio between force and displacement, thus expressed in N/m . This variable cannot be used directly in Equation 8.7, therefore we arbitrarily divide it by the particle diameter. We consider this new value to be an indication of the stiffness $k(\omega)$ of the material. It should be investigated whether this expedient to express the particle stiffness in Pa is sound, or if it is necessary to more accurately derive it experimentally.

The resulting evolution of stiffness variable $k(\omega)$ is shown in Figure 8.2. The k_{wet} and v_k variables of Equation 8.4 are calibrated in agreement with the experimental data.

Once all the parameters are set, the initial configuration to run numerical simulations is defined. A box bounded by four “walls” is created to replicate in two dimensions the 3D experimental conditions in the three papers (see Chapters 4, 5 and 6). The left and right walls are fixed, while the displacement of the top wall is allowed along the vertical direction, whilst under the action of a vertical force. The width of the box is set to be equal to 16 mm , which is the internal diameter of the cylindrical cell used in the experiments presented in Chapters 4 and 5. 407 spheres with a diameter between 625 and $800 \mu\text{m}$ are placed and deposited in the box under the action of gravity and the upper wall. The particle size distribution replicates the one obtained upon sieving in the experiment presented in Chapter 5 and the individual particle compression tests (see Appendix B). A schematic view of the initial configuration is shown in Figure 8.3.

The following sections present the results of preliminary numerical studies investigating the role of the vertical load applied over the assembly and of the effect of relative humidity (*i.e.*, maximum water content ω_{max}) on the overall response of the assembly.

The analyses focus on the “surface strain” ε_S , defined as:

$$\varepsilon_S(t) = \frac{\Delta S(t)}{S_0} \quad (8.11)$$

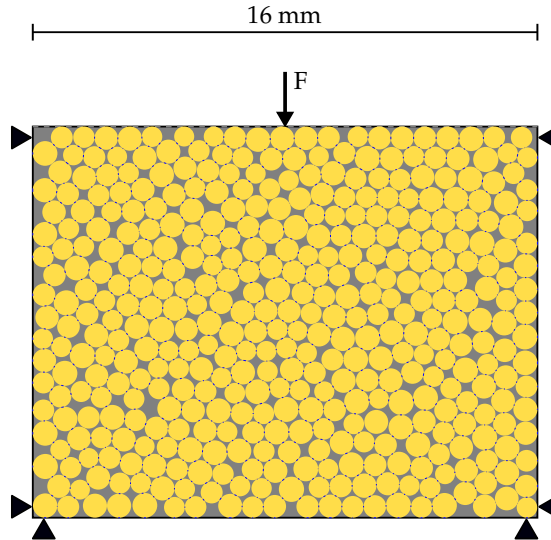


FIGURE 8.3: Initial configuration: the spheres are deposited in a box to mimic oedometric conditions. Bottom, left and right walls are fixed, while the upper one can move in the vertical direction. A vertical force is applied with magnitude is adjusted according to the desired response of the assembly (free swelling or dilation-compaction behaviour).

where S_0 is the surface area described by the four walls and ΔS its variation throughout the test. The surface response describes the overall response of the assembly and it can be qualitatively compared to the three-dimensional volumetric response of the samples in the experiments presented in the previous Chapters.

The sensitivity analysis also examines the evolution of contact areas with increasing water content ω . The contact areas are evaluated as the intersection circle between two contacting spheres.

In addition, when analysing the effect of vertical load, we examine the evolution of inter-particle forces, which is not possible in the experimental studies presented in the previous chapters.

8.2.1 Effect of vertical load

The role of vertical load is analysed by imposing 7 different vertical forces on the top wall: 0.01, 1, 2, 5, 10, 20, and 50 N. These values are chosen in order to observe the free swelling behaviour of the assembly, as well as the dilation-compaction surface response. It should be noted that we cannot impose simply 0 N due to computational instabilities. Therefore, it is implied here that the configuration in which the top force is equal to 0.01 N (much lower than the other forces) represents the free swelling case.

The variables in Equation 8.1 and Equation 8.2 are calibrated, in order to simulate the water uptake and activate the following microstructural changes. The maximum water content ω_{max} is imposed to be 50% (a quite extreme condition for couscous), while τ_ω , the variable that describes the water uptake rate, is arbitrarily set to 700 s^{-1} , so to mimic an equilibrium between the particles and the external environment (see Figure 8.1).

The β parameter of equation 8.2 is set to 1. This value implies that the density of the material does not change with ω , as discussed in Chapter 7.

Figure 8.4 presents the results obtained from the analysis of the evolution of the surface strain, which can be compared to the volumetric strain measurement of the experiments.

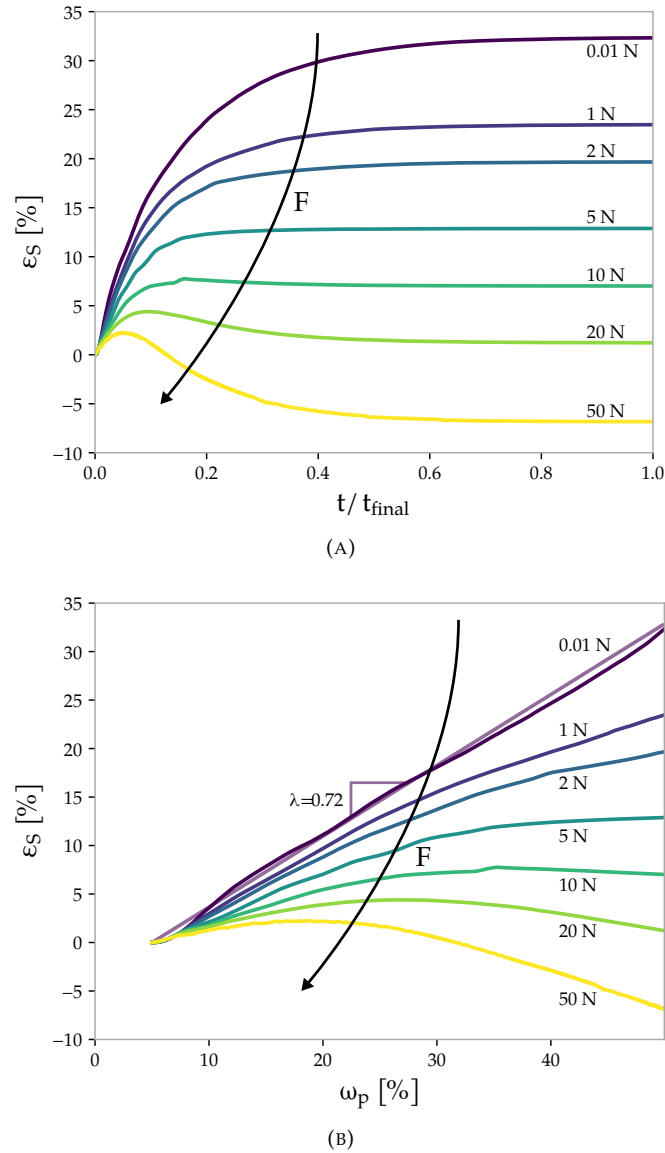


FIGURE 8.4: Effect of vertical load: evolution of surface strain ϵ_S with respect to time t (A) and particle water content ω_p (B). For small loads, the particles are not compacted and the assembly dilates proportionally to water content. However, as the particle stiffness k decreases with increasing ω , higher loads reveal a competition between swelling and deterioration of mechanical properties.

Specifically, Figure 8.4a present the evolution of ϵ_S with time. The volumetric response for very small load (purple lines) shows trends similar to the one observed in the free swelling tests (see Chapter 5). Conversely, as the load increases (green-yellow lines), a competition between particle swelling and mechanical properties deterioration takes place. Initially, the sample dilates, as the particles are able to resist the vertical load. However, as the particle stiffness k decreases upon water sorption, the model allows for higher overlaps between the spheres, leading to a compaction of the assembly under constant load. This behaviour is observed in both the experimental campaign presented in Chapter 4 and in Chapter 6, where high water content variation induces overall compaction of the sample.

Figure 8.4b plots the surface strain ϵ_S as a function of water content ω . For small vertical loads, the ϵ_S increases proportionally to water content. As the particles increase in volume linearly with ω , so does the overall assembly, similarly to the free swelling experimental

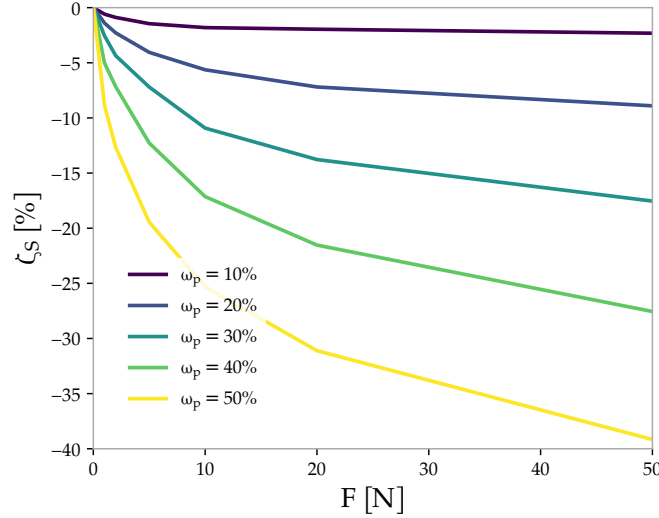


FIGURE 8.5: Evolution of surface strain ζ_S with respect to the vertical force F .

campaign in Chapter 5. The linear relation correlating the system swelling ε_S to the particle swelling $\varepsilon_{V,p}$ is described by a coefficient equal to 0.72. In this case, the dilation of the system is lower than the one imposed on the particle, in contrast with the experimental observations, where the sample volumetric strain is higher than the average particle swelling. This inconsistency might be caused by the two-dimensional restriction of the problem, or likely by the relatively high friction between the particles, which prevents their rearrangement.

As the load increases, the trend is no longer linear, as the assembly is compacted by the action of the top force.

It is possible to quantify the compaction ζ_S induced by a specific load with the following simple expression:

$$\zeta_S(\omega, F) = \varepsilon_S(\omega, F) - \varepsilon_S^{F=0}(\omega) \quad (8.12)$$

where $\varepsilon_S^{F=0}$ refers to the linear evolution of the free-swelling case ($F = 0$ N). Figure 8.5 shows the evolution of ζ_S with the top force F . The plot highlights how the deterioration of mechanical properties can have a major impact on the microstructure of the sample, even at relatively mild stress levels.

The increasing of ω does not affect only the volume of particles and assembly. Similarly to the studies presented in Chapter 4 and 6, attention is paid here to the inter-particle contact areas, specifically to the average variation of contact area $\overline{\Delta A}$. Figure 8.6 shows how the model can capture the increase of contact areas with particle swelling and vertical load. Naturally, higher loads induce larger growth of contact areas than smaller loads. The vertical load magnitude turns out to be a key factor in the contact area increase. In particular, in the cases in which a compaction stage is observed, the behaviour is relatively similar to the quadratic trend that is found for median contact area variation *vs.* water content, proportional to particle swelling, as discussed in Chapter 7. Moreover, in the “compaction” cases, the variation of contact area observed numerically is quite similar (same order of magnitude) to the one measured experimentally. Conversely, no experimental data is available on the contact network evolution in the free-swelling case. Numerically, the response indicates a reduction of the contact area for high ω_p (thus, high particle swelling). This trend is likely influenced by the assumption of zero cohesion, which allows for disengagement and rearrangement of particles once the tangential

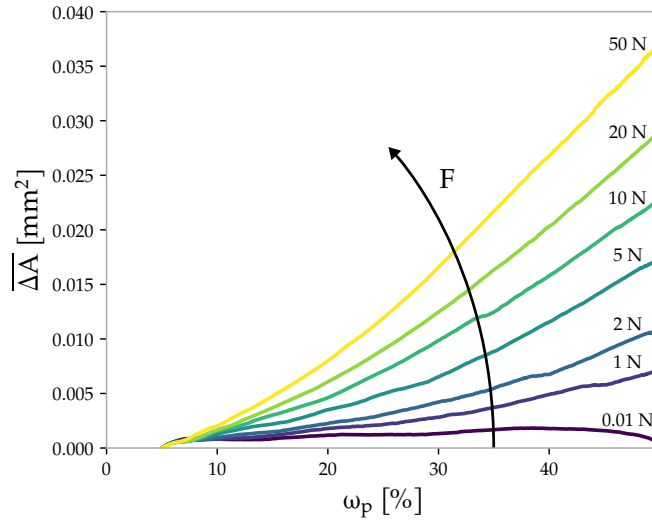


FIGURE 8.6: Effect of vertical load: evolution of the average contact area variation $\overline{\Delta A}$ with particle water content ω_p . The contact area increases as the particles swell and interlock with each other. The growth rate is strongly influenced by the vertical top force.

$F = 0.01 \text{ N}$

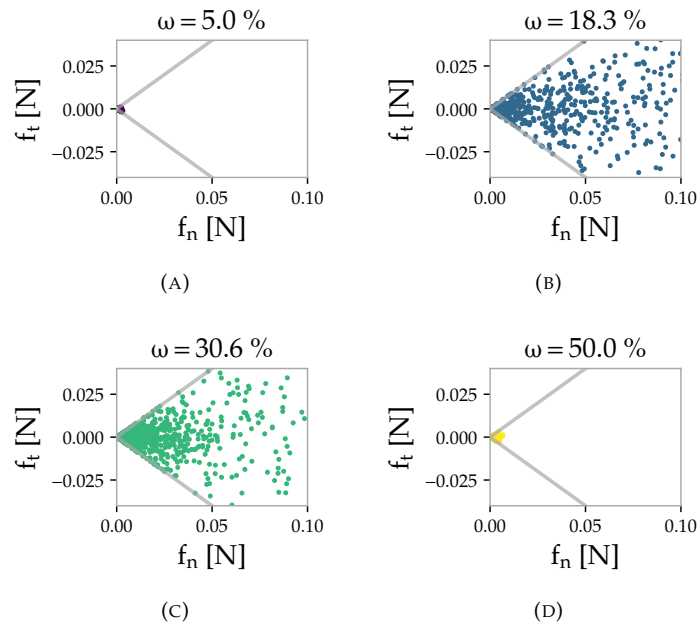


FIGURE 8.7: Effect of vertical load, free swelling case ($F = 0.01 \text{ N}$): inter-particle normal and tangential forces (f_n and f_t) at water content ω equal to 5% (A), 18.3% (B), 30.6% (C), and 50% (D).

force equals the frictional resistance (see Equation 8.10).

We then briefly examine the inter-particle forces and their change throughout the simulations. First, we select three assembly responses: free swelling (0.01 N), constrained dilation (5 N), and dilation-compaction (50 N). For each of them, we analyse the evolution of normal and tangential forces, at different water content levels. The ω values are chosen with respect to the dilation-compaction response of the assembly under 50 N (Figure 8.4b), and they correspond to the first step ($\omega = 5\%$), the dilation peak ($\omega = 18.2\%$), an intermediate step during the compaction stage ($\omega = 30.6\%$) and the final step ($\omega = 50\%$), when the water content

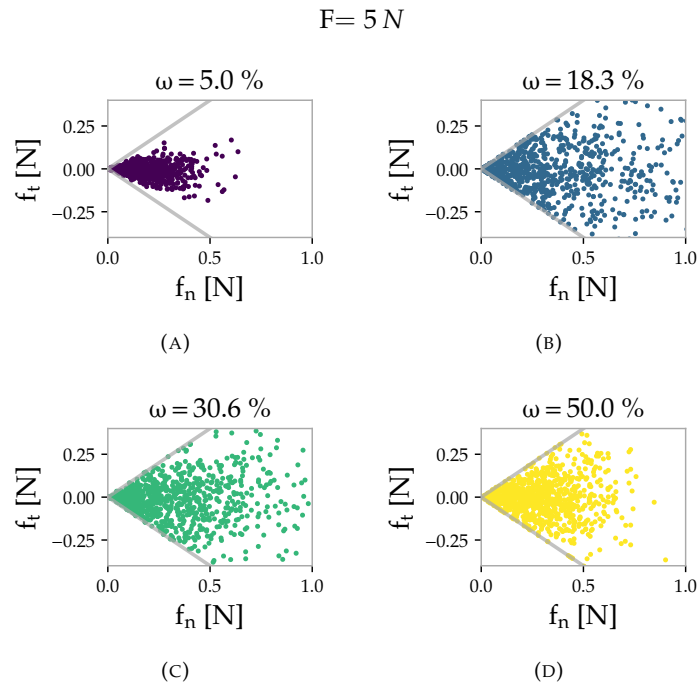


FIGURE 8.8: Effect of vertical load, constrained dilation ($F = 5\text{ N}$): inter-particle normal and tangential forces (f_n and f_t) at water content ω equal to 5% (A), 18.3% (B), 30.6% (C), and 50% (D).

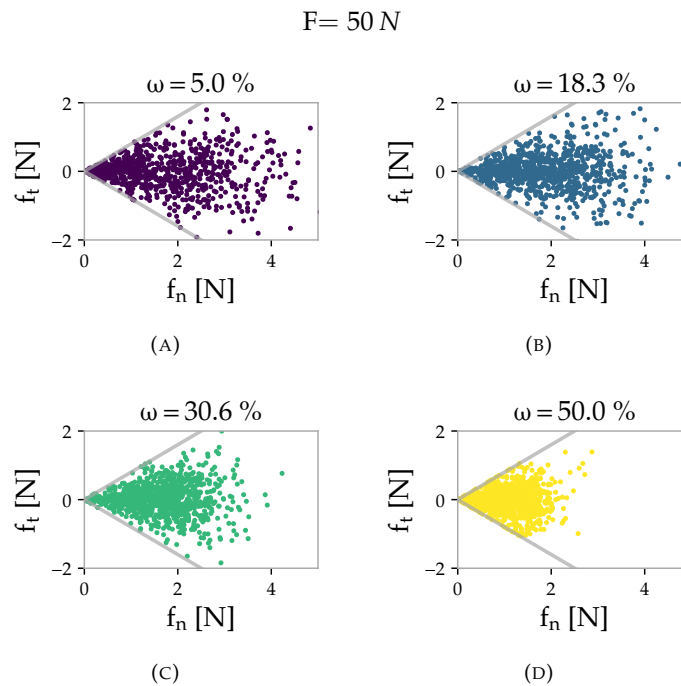


FIGURE 8.9: Effect of vertical load, dilation-compaction ($F = 50\text{ N}$): inter-particle normal and tangential forces (f_n and f_t) at water content ω equal to 5% (A), 18.3% (B), 30.6% (C), and 50% (D).

plateaus (see Equation 8.1 and Figure 8.1).

Regarding the free swelling case, Figure 8.7 shows the evolution of inter-particle forces with four plots, each of them corresponding to one of the reference steps (*i.e.*, water content ω).

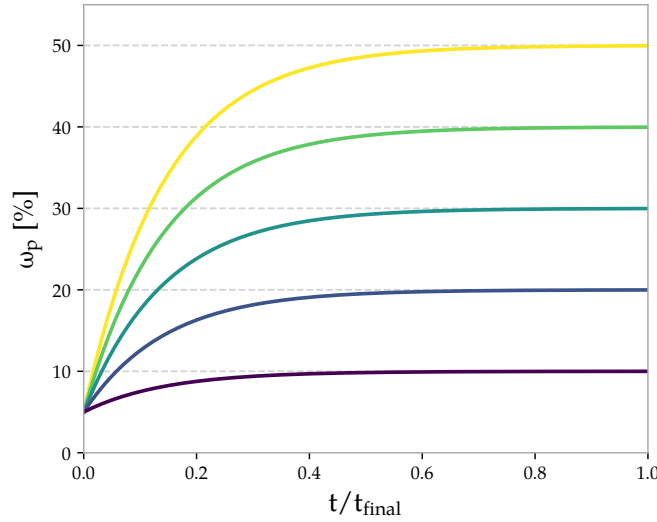


FIGURE 8.10: RH effect: evolution of ω in time for each of the study cases: $\omega_{p,MAX} = 10, 20, 30, 40$ and 50% .

Initially, the forces between the particles are very low as they redistribute among themselves the applied 0.01 N force and their own weight. However, in the following two steps, the inter-particle normal and tangential forces increase considerably (they are comparable to the applied vertical force), as the swelling induces “squeezing” and rearrangements. Finally, in the last step, when the swelling rate is essentially null, the particles stop pushing against each other and the force distribution resembles the initial one.

In the constrained dilation test, we detect a different response (Figure 8.8). Once again, the forces increase with particle swelling. However, this time, the dilation of the sample is limited by the 5 N load, hindering a complete system relaxation. In fact, at $\omega = 50\%$ the results reveal an overall decrease of inter-particle forces, which can be attributed to the higher number of contacts, as well as to the softening of the particles.

We then analyse the third configuration, *i.e.* dilation-compaction (Figure 8.9). It can be noticed that, besides the higher magnitude of the forces, no significant difference is observed between the initial step and the dilation peak, indicating that the process is governed by the vertical load and not by particle swelling alone. Moreover, the relaxation of the system is enhanced in the compaction stage (more contacts and particle softening).

It should be mentioned that the tangential forces are limited by the Coulomb criterion in the model (see Equation 8.10).

8.2.2 Effect of relative humidity

A second sensitivity study investigates the effect of relative humidity.

Water-sensitive materials are hygroscopic, thus they can adsorb water from, or release it to, the outer environment. Notably, this process depends on the RH of the surrounding environment (besides temperature and pressure) [Sch04; EEC05]. By imposing the asymptotic maximum particle water content $\omega_{p,MAX}$ (Equation 8.1), we simulate the effect of relative humidity on the particles assembly.

Two different loading configurations are analysed: $F = 0.01\text{ N}$ and 50 N , respectively

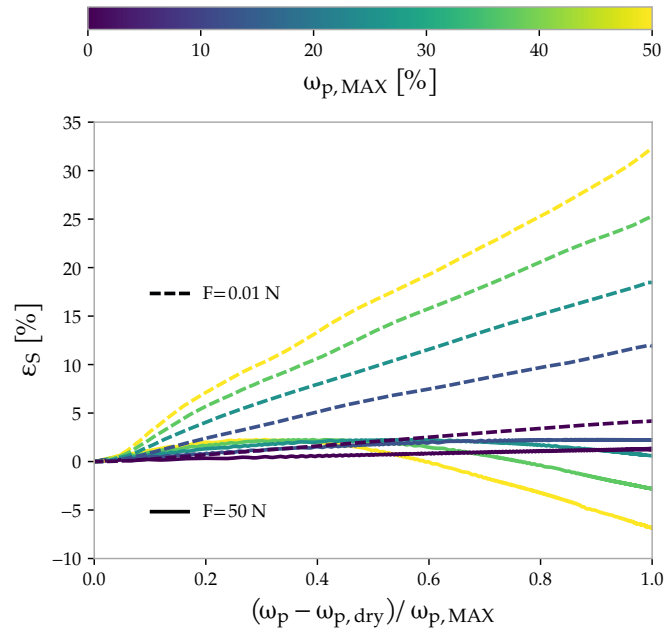


FIGURE 8.11: Effect of RH: evolution of ϵ_S during the numerical simulation for each $\omega_{p,MAX}$ and for both the imposed loads. The response of the assembly was more significant higher water contents. A vertical load could contain the otherwise strong assembly dilation induced by particle dilation and consequent rearrangement.

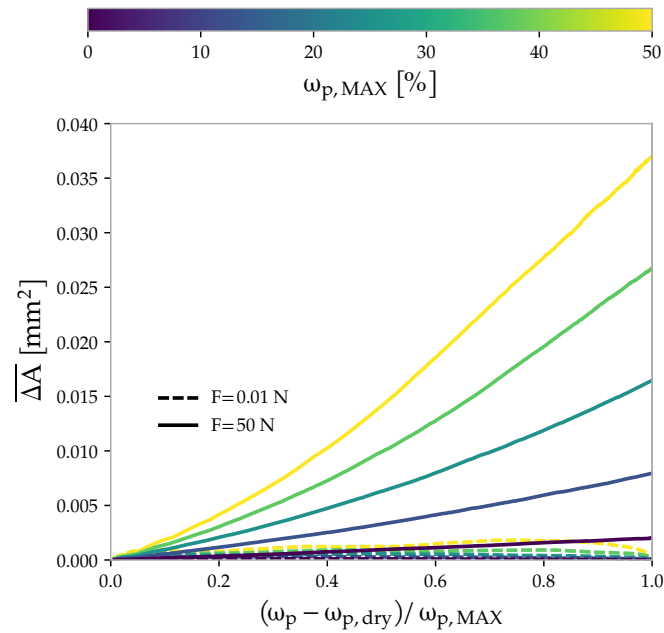


FIGURE 8.12: Effect of RH: evolution of the average contact area \bar{A} during the numerical simulation for each ω_{max} and for both the imposed loads. The vertical load influenced the initial contact areas and their evolution. On the other hand, the maximum water content did not affect the growth, neither in the confined case nor in the free-swelling configuration.

the lowest and highest vertical forces analysed previously. These can be regarded as the extreme cases in the assembly volumetric response: full dilation (*i.e.*, free-swelling) and dilation-compaction.

Numerical simulations are run on both configurations and the effects of five different

$\omega_{p,MAX}$ values: 10, 20, 30, 40, and 50%. Figure 8.10 shows resulting water content ω_p evolutions (the sorption rate τ_ω is kept equal).

In the free-swelling case ($F = 0.01 N$), the trend of ε_S is not significantly affected by $\omega_{p,MAX}$, which, however, influences the dilation peak value (see Figure 8.11). Conversely, the volumetric response is significantly different in the confined configuration. An increase of $\omega_{p,MAX}$ (thus, increase of RH) can have a strong impact on the microstructure of the assembly and result in overall compaction.

Figure 8.12 presents the effects $\omega_{p,MAX}$ on the contact area growth. When no vertical load is applied on the sample, no substantial contact area increase is detected, since particles can easily rearrange due to lower tangential resistance. The opposite happens in configurations where higher loads are applied. In fact, a small increase of water content can induce a significant contact area increase.

8.3 Summary and perspectives

A novel DEM numerical model is adopted to simulate the behaviour of hygroscopic swelling particles. The code is not meant to replicate exactly the behaviour of couscous particles, but rather to provide a elementary tool capable of supporting the experimental results and further investigating the role/variation of variables non-measurable experimentally.

The model is intended to be simple, with a limited number of parameters, which are all function of to the main variable of the problem: the particle water content ω_p . It should be noted that the model we developed could be calibrated also for other water-sensitive materials (and not only couscous).

The current state of the code allows for simultaneous particle volume increase and stiffness decrease, which is, as mentioned, a process often neglected in literature [Swe+17].

The particle interaction is modelled with the Hertz-Mindlin non-linear elasticity law. A large indentation (or overlap) between contacting particles is allowed to simulate the high particle deformability. Concerning the tangential forces, the frictional model proves to be relatively effective to mimic the behaviour of the material, at least for low values of particle water content. No cohesion is taken into account in this preliminary version of the code.

Two sensitivity studies are carried out numerically to investigate the effect of vertical load and relative humidity on the samples.

The vertical load proves to be an element that strongly affects the final response of the material. Based on the vertical force applied on the sample, we observe free swelling and dilation-compaction responses, of which the evolution qualitatively resembles the experimental results. Moreover, the analysis of contact area growth indicates a good agreement between the numerical and experimental results.

It appears that the relative humidity (*i.e.*, maximum particle water content) does not affect the microstructural evolution.

The current numerical model is relatively basic and there is large room for improvements. For example by:

- removing the 2D restrictions, thus allowing for potential quantitative comparison between numerical and experimental results;
- imposing heterogeneous water uptake in the sample, based on experimental evidence;

- including the diffusion variable in the water uptake process [EYDR05; Swe+17];
- refining the particle geometry, since shape has been proven to be a key feature in the prediction of the behaviour of granular materials [Kaw+18];
- verifying the soundness of the Hertzian-Mindlin model for such materials;
- improving the frictional model, where the friction coefficient is function of the particles water content and contact area ($\mu = \mu(\omega_p, A)$);
- integrating the code with one of the major feature of water sensitive granular materials: cohesion [AVK95; Wah+08; Zaf+17; BAC21], allowing the investigation of force chains and overall “caking” strength of the sample [Wah+08; DTR09; Rad+10];
- reproducing the relatively high particle deformation with more advanced models [Can+20; CB+21; CB+22];
- performing targeted experimental campaigns dedicated to its calibration and the characterisation of the investigated material.

Chapter 9

Conclusions and perspectives

9.1 Summary and conclusions

With this doctoral work we investigate the hydro-mechanical response of water-sensitive granular materials, *i.e.*, granular materials whose individual particles have properties that are directly affected by the presence of water.

As discussed in Chapter 1, there exist numerous materials whose particles themselves are hygroscopic, thus they can be adsorb water from, or release it to, the outer environment. The water uptake often induces a shift of the particle bulk behaviour from glassy to rubbery. This phenomenon, known as glass transition, naturally induces changes of particle-scale morphological and mechanical properties. For example, swelling and softening of particles are commonly observed with increasing water content. Such processes are relatively negligible when they only involve individual particles. However, when particles interact with each other, the water sorption sets in motion phenomena such as bridging, agglomeration, and sintering. Lumps are generated and the flow properties of the material are generally reduced. In food, pharmaceutical or chemical industries, such processes can cause severe resource loss in the product supply chain, which obviously raises important economical and sustainability issues.

Therefore, it is necessary to understand the fundamental behaviour of water-sensitive materials, and specifically, the correlation between particle-scale phenomena and assembly response, which is the primary goal of this thesis. To achieve it, we carry out an experimental investigation to characterise couscous particles assemblies and the changes induced by water sorption. Couscous is selected as the reference material because it presents several of the phenomena characterising water-sensitive materials: its particles swell, become softer, and can agglomerate with increasing water content. Moreover, it is well suited for imaging techniques and analysis procedures that are used in this work.

In order to emulate a realistic scenario such as in a storage-silo conditions, we restrict the particles kinematics by means of rigid cylinders. Meanwhile, we expose the samples to high relative humidity ($> 90\%$ RH).

The experimental work is chiefly performed using three different techniques (or modalities):

- x-ray tomography;
- neutron tomography;
- time-domain nuclear magnetic resonance (TD-NMR).

Their high complementarity allows us to observe and quantify the microstructural changes and water uptake inducing them, as detailed in the previous Chapters.

Chapter 4 presents a study in which we employ x-ray tomography alone, and observe the effects of slow flow of humid air on a sample of thousands of couscous particles, subjected to constant stress. *Via* image analysis, we quantify the swelling of the particles (up to 20%) and relate it to the overall response of the assembly. The measurements reveal a peculiar dilation-compaction behaviour, which is the result of the competition between particles swelling and the decrease of their mechanical properties. We observe the presence of a vertical swelling gradient starting from the air injection point. The contact analysis reveals the increase of contact areas induced by swelling and compaction, and that the growth of contact area is strongly related to the particle swelling and the applied stress.

Despite all its advantages, the use of x-ray tomography does not allow the observation of the variable that mainly controls the problem: water content. As detailed in the second paper included in this dissertation (see Chapter 5), we complement the information attainable from x-ray tomography with TD-NMR. We observe the water sorption process and the associated molecular mobility shift. The molecular matrix of the particles interacts with water, activating the material's transition towards less viscous/rubbery state. Thanks to comparable evolutions of water content (obtained from TD-NMR) and particle swelling (from x-ray tomography), as well as of macroscopic mass gain, we correlate the average particle swelling to the water content. We find that these two variables are essentially directly proportional. It should be noted that the test is carried out in free swelling conditions (no vertical stress). We observe that, in this configuration, the overall volumetric response of the sample is proportional to particle swelling. Finally, image analysis reveals again the presence of a swelling gradient across the sample, despite the homogeneous water concentration in the flow of high relative humidity air. We presume that the heterogeneity is induced by pressure drops of the air flowing through the sample, which locally affect the sorption dynamics.

In Chapter 6 we discuss the results obtained by means of simultaneous neutron and x-ray tomography. We perform two more experiments, once again exposing couscous particles to a flow of humid air, while subjecting the samples to constant stress. The concurrent use of x-ray and neutron tomography allows us to spatially correlate the microstructural changes (measured from x-ray tomography) to the variations in water content (inferred from neutron tomography). The analyses reveal a response similar to the one measured in the other studies. We find again that a linear relation correlates particle swelling to the water content, at least for relatively low water contents. In fact, at higher values, it appears that the process is "delayed" by particle diffusion. The effects of water content on the contact network is also investigated. Besides a general and expected increase of number of contacts, we observe that the median variation of contact area is related to water content by a monotonic bi-linear (or quadratic) function. Furthermore, the results suggest again a significant effect of the vertical stress on the contact area growth.

We then summarise and further analyse the experimental results, as detailed in Chapter 7. Attention is paid to the microstructural changes (particle swelling, sample-scale volumetric response, contact areas growth) and their link to an increase of water content.

Assuming linearity between particle swelling and water content (as suggested by experimental evidence), *via* an analytical approach we derive that the swelling dynamics is governed by the changes in particle density. Specifically, the coefficient linking particle swelling and water content is described as the ratio between the dry particle density and the density upon water sorption ($\rho_{dry} / \rho(\omega, t)$). Three major domains characterising the particle response are defined. In the first, the water sorption causes an increase of particle density, due to the internal

pores closing (and possibly the collapse of the molecular structure) prevailing over the overall particle measurable dilation. The second domain denotes a slight decrease of particle density upon water content sorption, induced by a predominant particle dilation (dilation greater than pore closing). The third domain denotes an extreme particle dilation, in which the new density is lower than water density, an unlikely case. Averaging all the experimental results on particle swelling, it appears that the particle volumetric response of couscous particles, for water contents below 30 – 40 %, belongs to the second domain ($\rho_{\text{H}_2\text{O}} < \rho(\omega, t) < \rho_{\text{dry}}$), although a (temporary) response of the material in the first domain cannot be excluded *a priori*.

Regarding the sample-scale measurements, we observe similar volumetric response of assemblies subjected to contact vertical stress. The dilation peak is reached at similar water content levels, and in cases of relatively high water sorption, the assemblies exhibit a dilation-compaction response. As previously mentioned, the free swelling response of the sample is found to be directly proportional to particle swelling (thus, to water content). In general, we can conclude that the sample-scale response is the result of the competition between particle swelling and mechanical properties deterioration. While performing the tests, it is rather difficult to impose a homogeneous air flow injection or to properly install the dead-load applying constant stress on the sample. We believe that the development and calibration of numerical models might help support the experimental observation, thanks to the perfect control of the imposed boundary conditions.

Finally, the experimental work focuses on the contact networks in couscous particles assemblies. The evolution of inter-particle contact area growth with respect to particle swelling (thus, to water content under the linearity assumption discussed above) could be described as quadratic (or bi-linear). We observe also a strong effect of the possible sample compaction on the contact area growth. Following an analytical approach, we then investigate the link between the variation of contact area and average radius of the particles. The relation is found to be quadratic, in agreement with the experimental measurements.

In Chapter 8, we present a novel numerical DEM model to simulate the behaviour of hygroscopic swelling particles. With this tool, we aim to support and supplement the experimental observations. The model is therefore intentionally very simple, with a limited number of variables, and the process governed by the particle water content. It also allows for concurrent variations of particle size and stiffness, a relatively rare feature in DEM numerical modelling. The particle interactions are modelled with the Hertz-Mindlin non-linear elastic law and on the tangential force is imposed the Coulomb frictional criterion. No particle cohesion is taken into account in the preliminary version of the model.

A sensitivity study is carried out to investigate the effects of vertical load and relative humidity on the assembly, but also to verify the soundness of the model. The particle swelling and stiffness decrease are calibrated based on experimental measurement. Despite the 2D restrictions on the particles kinematics, the numerical simulations well mimic the response of the assembly in free swelling and vertically loaded conditions. This allows us to explore the role played by some variables such as the vertical load or the maximum particle water content, which are variables relatively difficult to control in the tests. We then briefly explore the evolution of inter-particle forces, which are not measurable experimentally.

To conclude, in this thesis we present a multi-modal investigation, during which we acquire unique datasets, which are, to our knowledge, first in their kind. The analysis procedure

developed for the analysis of bi-modal images and TD-NMR decay proves to be an effective approach to observe and quantify the microstructural changes occurring when a water-sensitive granular material is exposed to water. Moreover, we can take advantage of accidental hiccups in the experimental campaigns to further characterise the reference material behaviour.

We quantify the effects of water sorption on the microstructure of couscous assemblies exposed to high relative humidity. We measure the swelling of thousands of particles and relate it to the overall volumetric response of the assemblies comprising them. In free swelling case, the volumetric response of the sample is in one-to-one relationship with particle swelling. Conversely, when a vertical load is applied on the sample, we observe a peculiar dilation-compaction response, which is the result of the competition between particle swelling and decrease of mechanical properties. The possible compaction of the assembly accelerates the inter-particle contact areas growth. All the microstructural properties are related to the water content variable. The particle volumetric strain is found to be directly proportional to water content. Contact areas instead are in a quadratic relationship with water content and thus particle swelling, and *vice versa*.

The newly developed numerical model appears to be already a powerful tool to investigate the hydro-mechanical processes in water-sensitive granular materials, and it can/should be refined.

9.2 Perspectives

The doctoral work presented here naturally has room for improvements and further research.

The behaviour of couscous particles is studied here only for a rather specific configuration, *i.e.*, oedometric conditions and high relative humidity. The effects of the boundary conditions on the microstructure could be further investigated, using different relative humidity levels, or other mechanical conditions (for example, an isochoric test). Moreover, the desorption/drying is an important process that has strong influence on the material behaviour, and it requires more attention. Another relatively overlooked variable of the problem is time, which plays an important role, due to the viscous nature of hydrated water-sensitive particles, or simply because of diffusion, which controls the sorption dynamics.

Our multi-modal investigation focuses on the kinematics and deformation of particles and assemblies. However, to fully describe the material fundamental behaviour, a mechanical characterisation becomes an essential requirement. In Appendix B we present a study aimed at describing the couscous particle stiffness dependency on water content. This is but an example of experimental studies necessary to understand in detail the link between micro-scale phenomena and assembly-scale response. Moreover, in this thesis we do not explore explicitly particles agglomeration, although this is a key feature of the caking phenomenon, a major issue in industrial storage and processing. More generally, a proper analytical modelling of the behaviour of water-sensitive granular materials could also help interpret the conventional tests performed to determine certain product properties.

Numerical models would obviously benefit from all these additional studies. The empirically set parameters could be still related to fundamental variables, such as water content. At the same time, attention should be paid not to entangle the different variables only to simulate the response of a specific material, subjected to very specific conditions.

Finally, it should be mentioned that coudous is only as a possible reference material that we find suitable for the experimental work presented here. Nothing forbids the use other materials, because of higher industrial interest or consistent response. We genuinely hope that this doctoral work will inspire other studies to characterise the behaviour of water-sensitive materials.

Appendix A

Technical designs of the experimental apparatus

This Appendix describes the technical designs of the experimental apparatus presented in Chapter 2. The two oedometer designs are detailed in Section 2.3.2, while that of the NMR compatible measurement cell in Section A.3.

A.1 16 mm oedometer

The 16mm oedometer has been designed and fabricated by Nicolas Lenoir at Laboratoire 3SR in Grenoble, before the start of this doctoral work project.

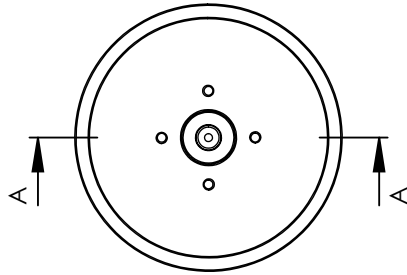
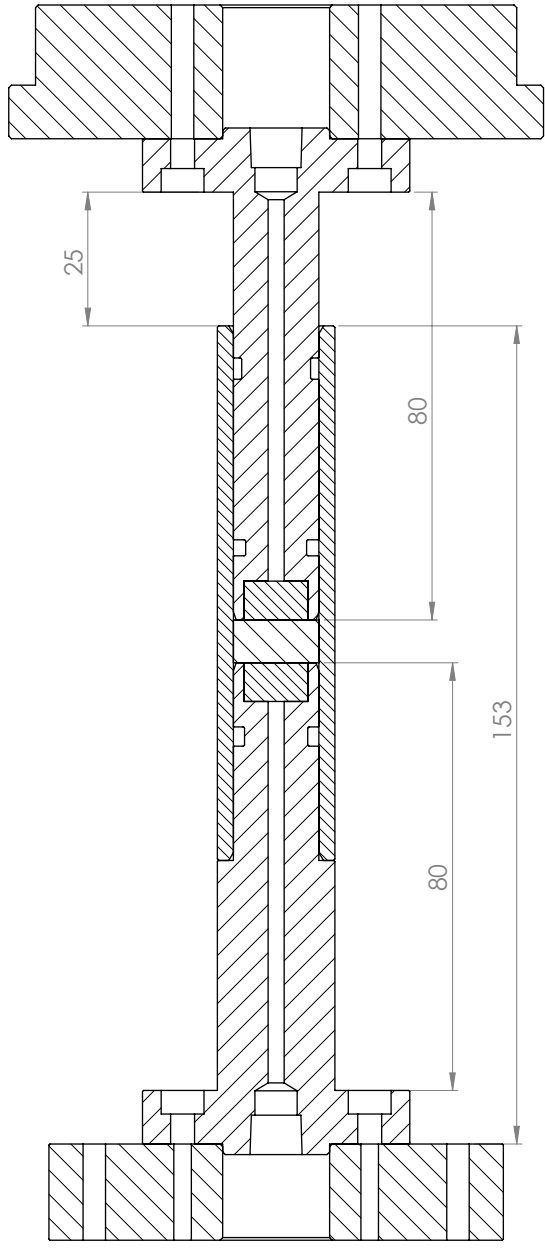
It is composed by three main components:

- an aluminium bottom base, designed to hold the specimen in position on the rotation stage while acquiring a tomography. The whole piece is hollow, in order to allow the circulation of a fluid flow through the sample (*e.g.*, high relative humidity air through a packed bed of couscous particles);
- a PEEK cylindrical cell of 16mm internal diameter ensures the radial strain constraints and the “transparency” to x-rays. Another one has been fabricated in PTFE that make sure it is transparent both to neutrons and x-ray beams;
- an aluminium piston would seal the cylindrical cell and possibly apply a constant load (dead load) on the samples.

A small pin is installed on the upper piston, which would reside in a short guide drilled on the cylindrical cell. This modification allows for coherent rotation between the top and the bottom pieces of the apparatus.

The apparatus is equipped with elastomer O-rings installed on the bottom base, and X-rings installed on the piston, in order to prevent fluid leakage, while allowing the vertical displacement of the piston.

The following pages are presented the drawings of the three main oedometer components.



COUPE A-A
ECHELLE 1 : 1

SAUF INDICATION CONTRAIRE: LES COTES SONT EN MILLIMETRES		FINITION:		ECHELLE 1 : 1		REVISION	
ETAT DE SURFACE:				Chantreins 0,5mm x 45°			
TOLERANCES:							
LIGNES: ±0,2mm							
ANGULAIRES: ±0,5°							
AUTEUR	NOM	SIGNATURE	DATE	TITRE:			
LEHOR			05/2019				
VERIF.							
APPR.							
PAB.							
QUAL.							
				MATERIAU: ALU 5083		No. DE PLAN	
						A3	
				MASSE: 3		FEUILLE SUR 1	

Set_up

No. DE PLAN

ALU 5083

MATERIAU:

MASSE:

3

4

5

6

7

8

1

2

3

4

5

6

7

8

1

2

3

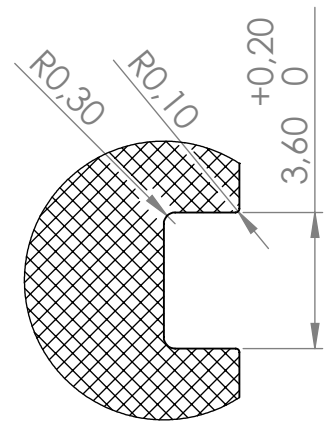
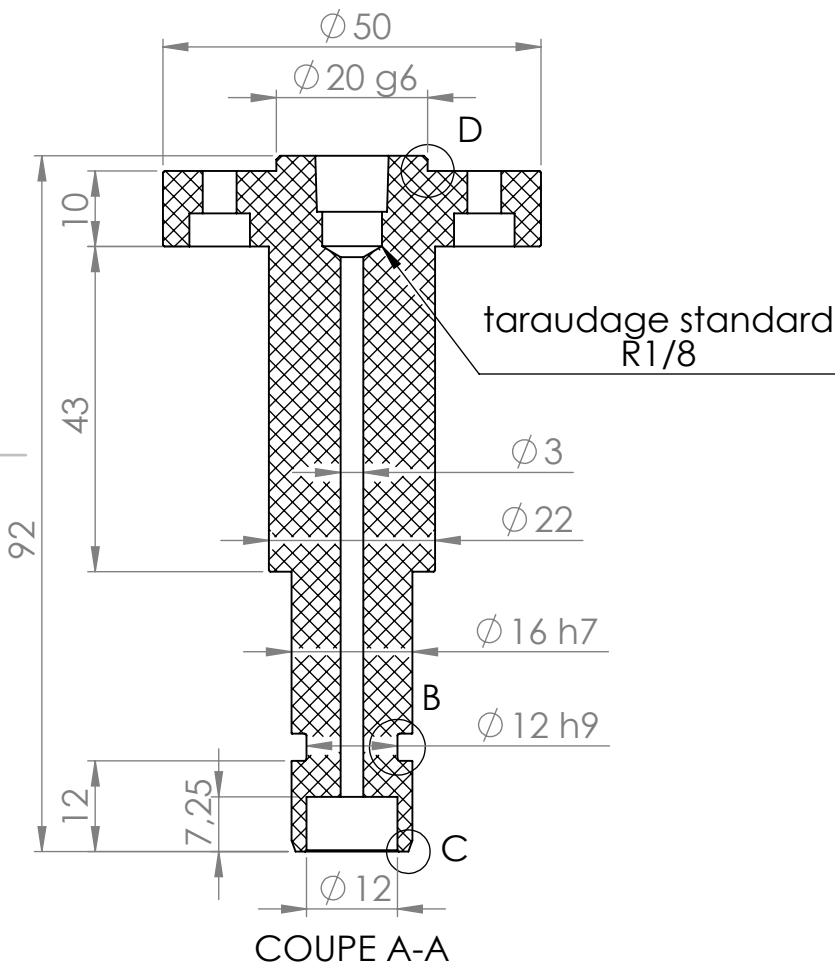
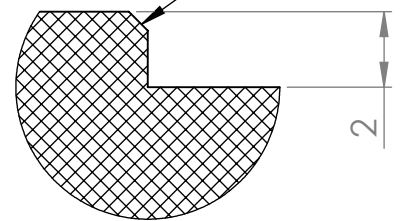
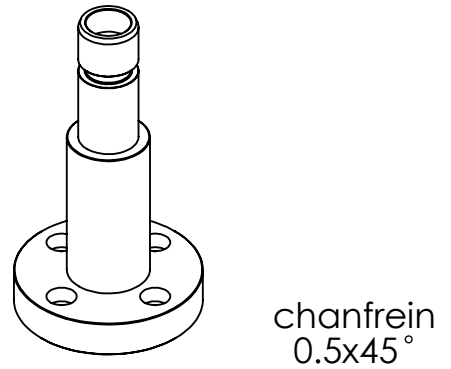
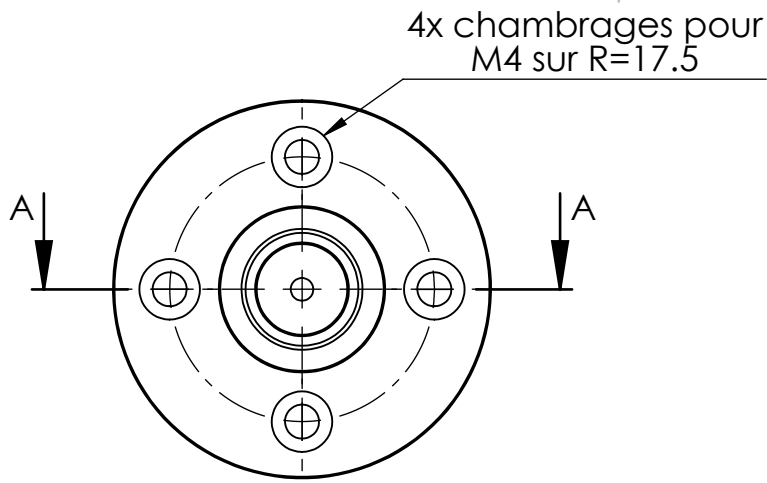
4

5

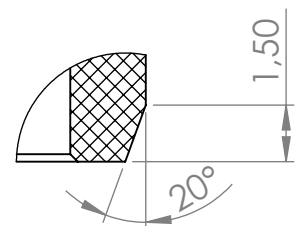
6

7

8



DÉTAIL B
ECHELLE 5 : 1



DÉTAIL C
ECHELLE 5 : 1

SAUF INDICATION CONTRAIRE:
LES COTES SONT EN MILLIMETRES
ETAT DE SURFACE:
TOLERANCES:
LINEAIRES: +/- 0.2mm
ANGULAIRES: +/- 0.5°

FINITION:

casser les angles

ECHELLE 1 : 1

REVISION

NOM	SIGNATURE	DATE	TITRE:
AUTEUR LENOIR		05/2019	
VERIF.			
APPR.			
FAB.			
QUAL.			
MATERIAU: PEEK			No. DE PLAN Bottom_base
MASSE:			ECHELLE:1:1

No. DE PLAN

Bottom_base

A4

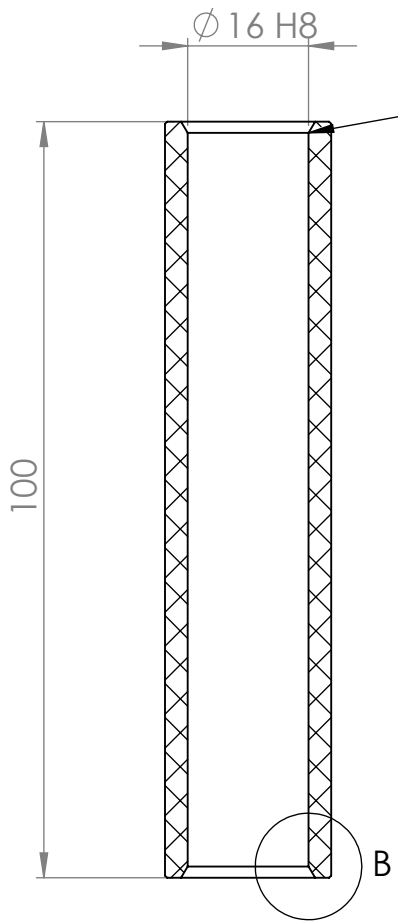
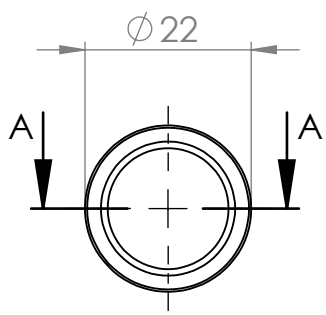
ECHELLE:1:1

FEUILLE 1 SUR 1

4 3 2 1

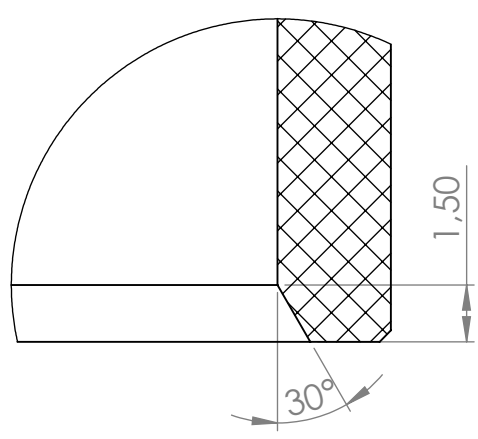
F
E
D
C
B

F
E
D
C
B

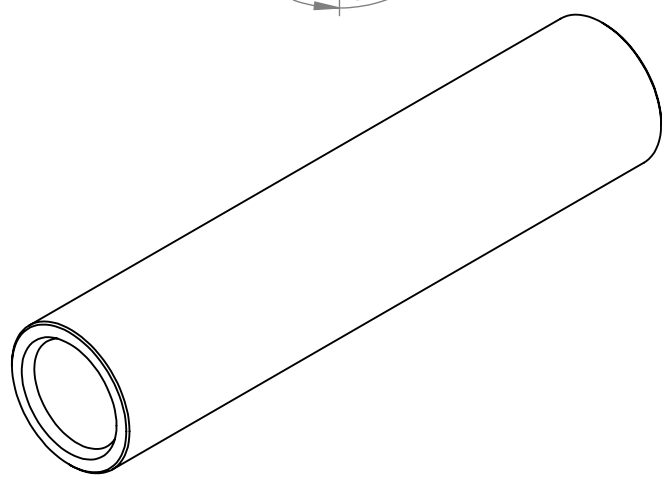


chanfrein à 30° sur 1.5mm
comme indiquée sur vue B

DÉTAIL B
ECHELLE 5 : 1



COUPE A-A



SAUF INDICATION CONTRAIRE:
LES COTES SONT EN MILLIMETRES
ETAT DE SURFACE:
TOLERANCES:
LINEAIRES: +/- 0.2mm
ANGULAIRES: +/- 0.5°

FINITION:

casser les angles

ECHELLE 1:1

REVISION

NOM	SIGNATURE	DATE	TITRE:
AUTEUR LENOIR		05/2019	
VERIF.			
APPR.			
FAB.			
QUAL.			
MATERIAU: PEEK		No. DE PLAN	
MASSE:		ECHELLE:1:2	

Cell

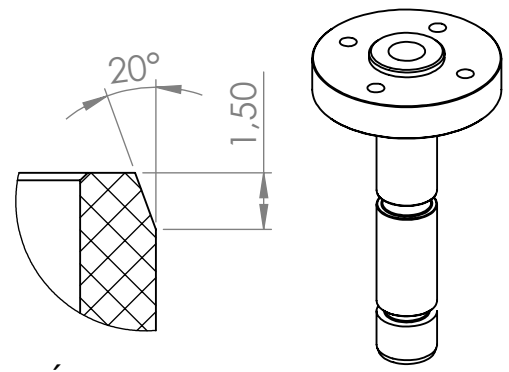
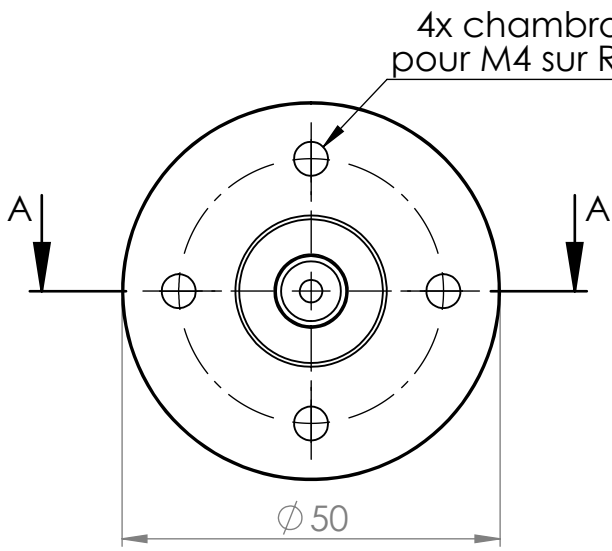
A4

FEUILLE 1 SUR 1

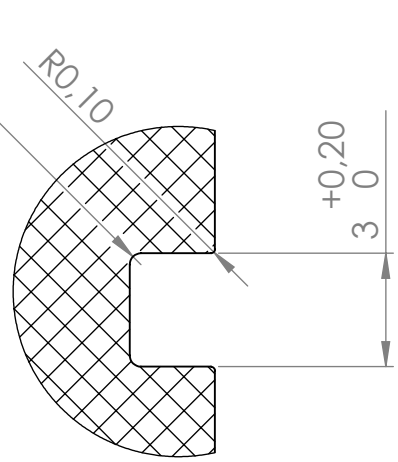
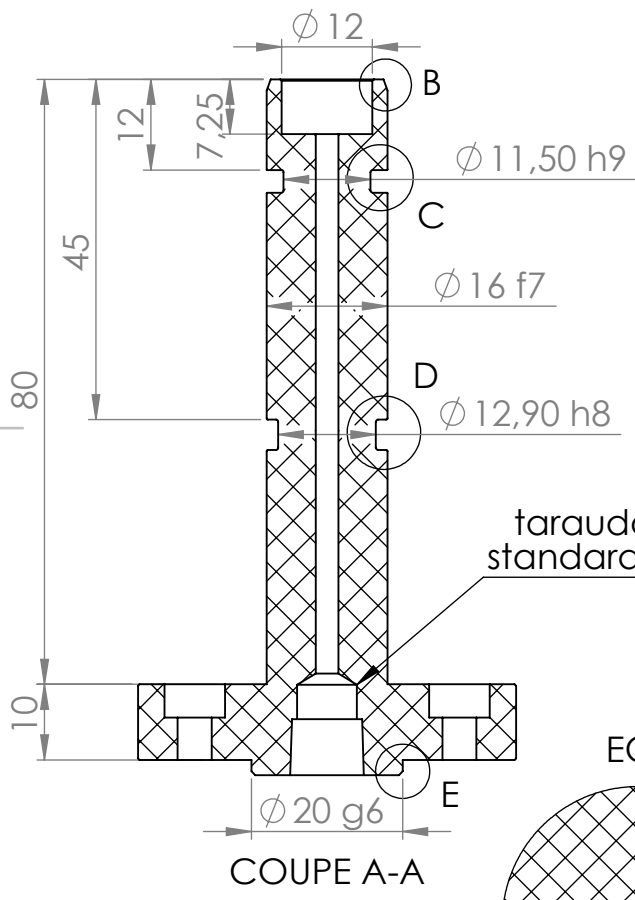
4 3 2 1

A

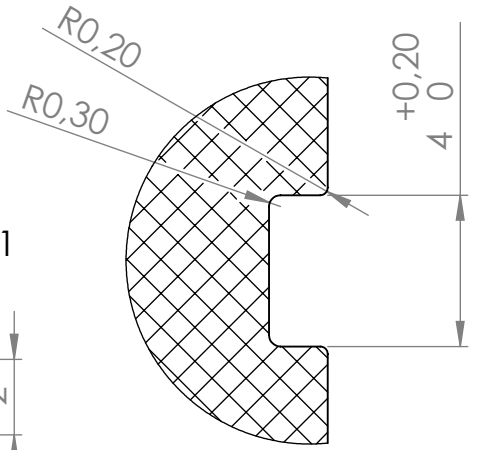
A



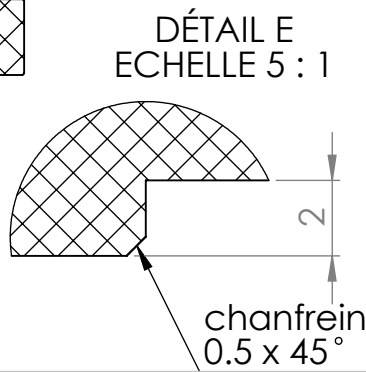
DÉTAIL B
ECHELLE 5 : 1



DÉTAIL C
ECHELLE 5 : 1



DÉTAIL D
ECHELLE 5 : 1



SAUF INDICATION CONTRAIRE:
LES COTES SONT EN MILLIMETRES
ETAT DE SURFACE:
TOLERANCES:
LINEAIRES: +/- 0.2mm
ANGULAIRES: +/- 0.5°

FINITION:

casser les angles

ECHELLE 1 : 1

REVISION

NOM	SIGNATURE	DATE	TITRE:
AUTEUR LENOIR		05/2019	
VERIF.			
APPR.			
FAB.			
QUAL.			
MATERIAU: PEEK		No. DE PLAN Ram	
MASSE:		ECHELLE:1:1	

Ram

A4

FEUILLE 1 SUR 1

A.2 7 mm oedometer

The 7mm oedometer is essentially a smaller scale version of the 16mm oedometer.

However, it presents additional pieces so that it could properly installed in the imaging stations at the Institute Laue Langevin (ILL) in Grenoble (France).

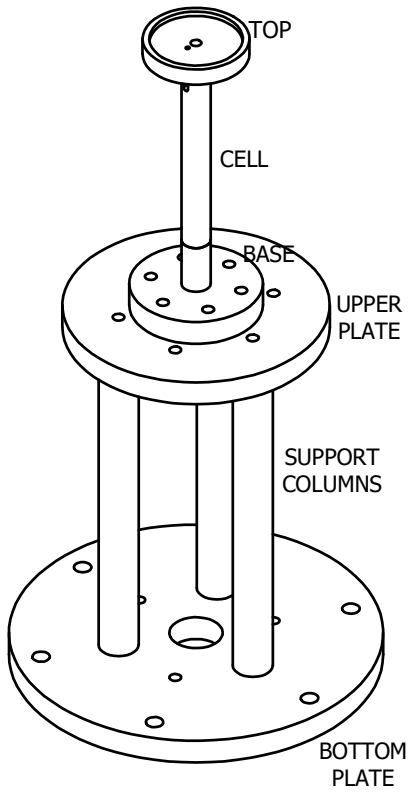
The apparatus comprises four main pieces:

- a support system (bottom plate, support columns, upper plate) to correctly install the apparatus on the rotation stage and to properly align it with the x-ray and neutron imaging setups. The pieces are made in steel;
- an aluminium base to support the cell and the specimen;
- a 7mm PTFE cylindrical cell that is substituted with an aluminium one for stability reasons (see Section 2.3.2 and 6.2.2);
- an aluminium ram to seal the cell and apply the desired stress.

Similarly to the 16 mm oedometer, the apparatus is equipped with O-rings and X-rings.

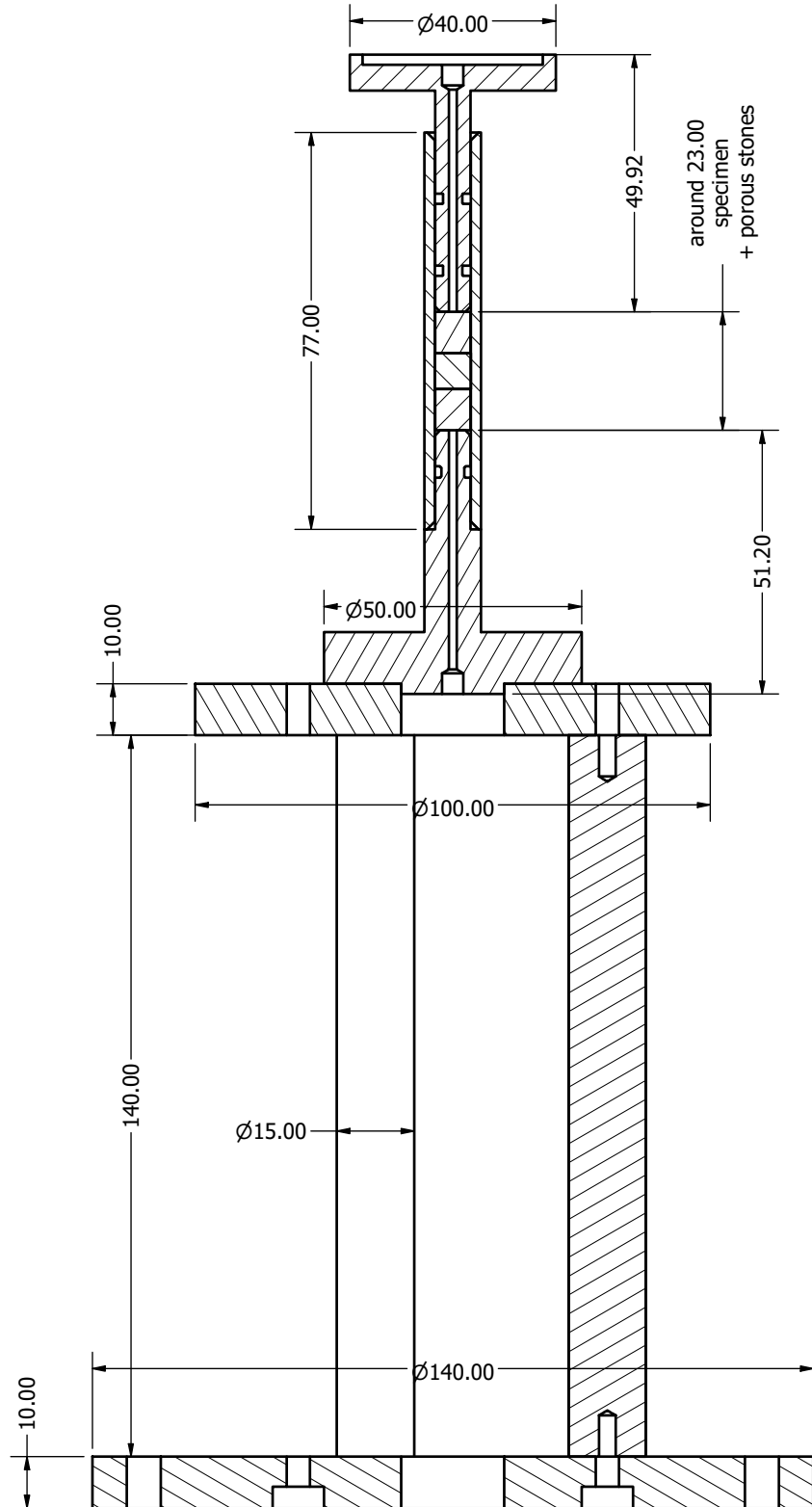
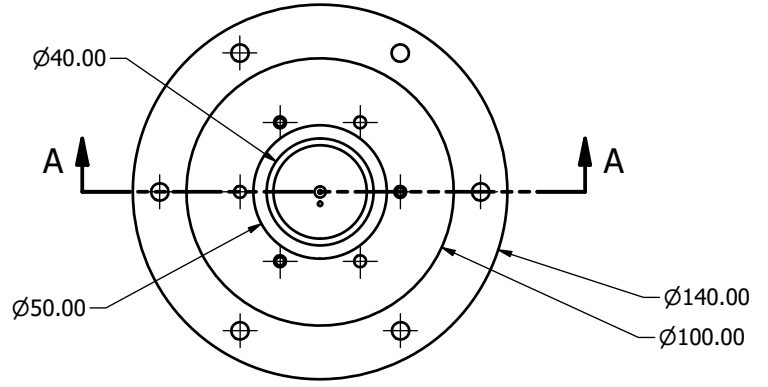
OEDOMETER

d=7mm



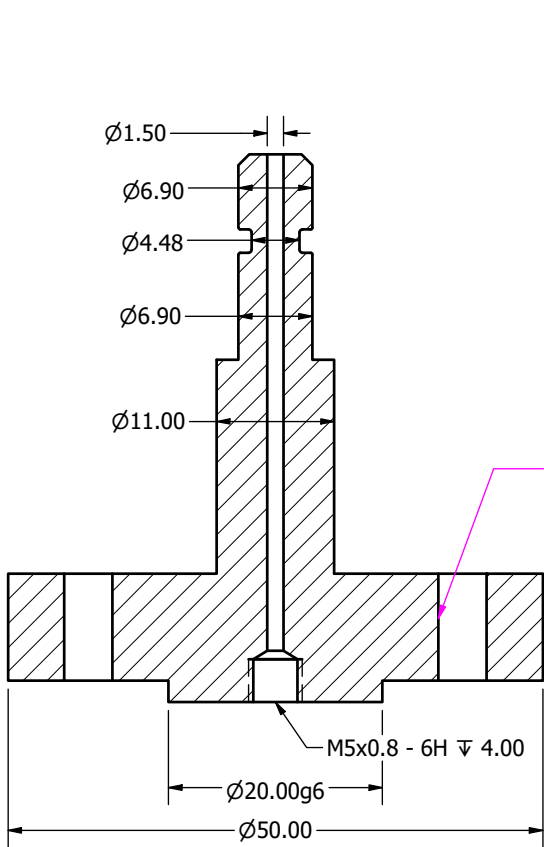
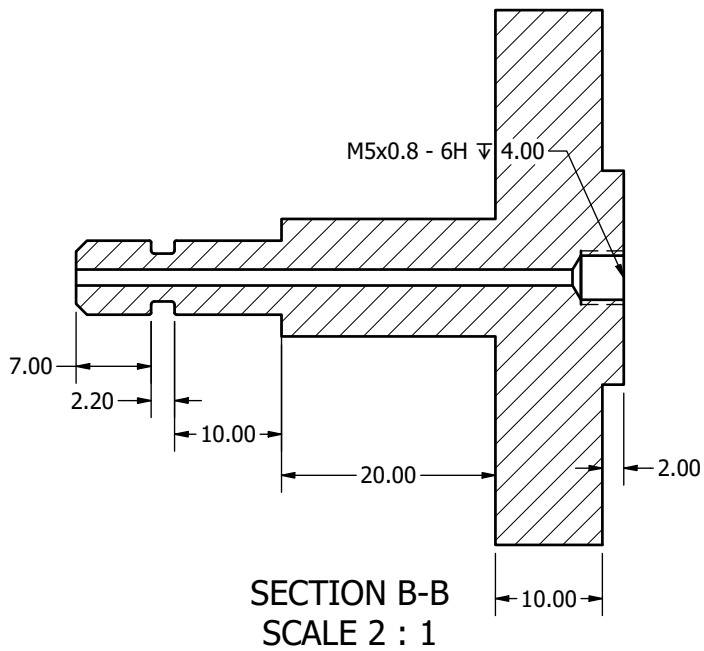
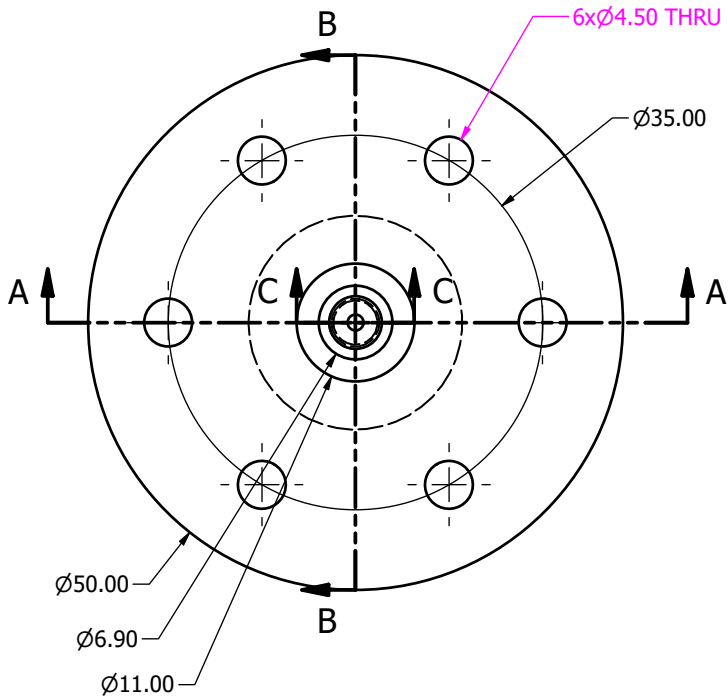
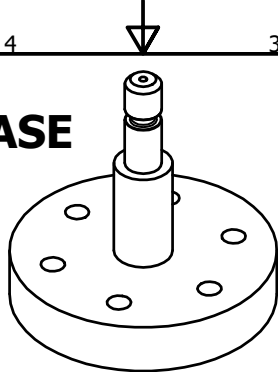
+ DEAD LOAD
total load:
 25 kPa
 35 kPa

+ 2xPOROUS STONE
 d=6.9mm

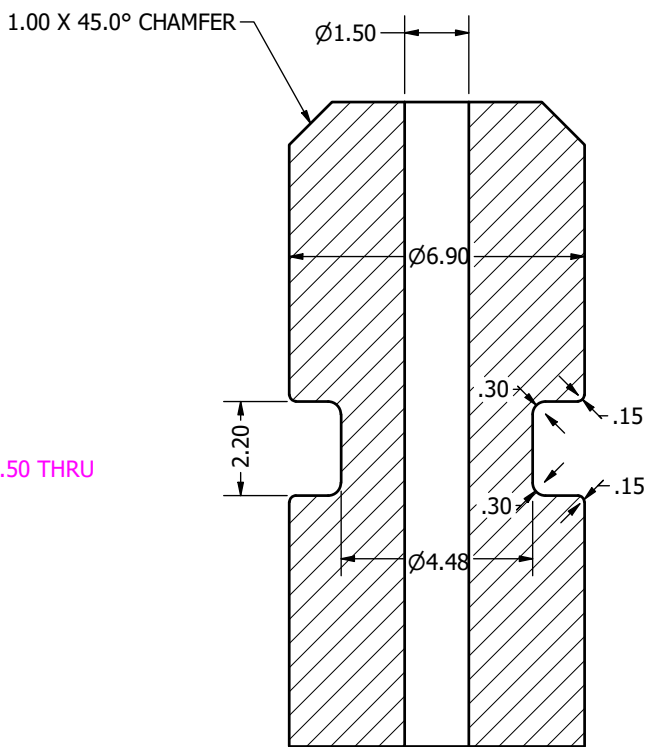


SECTION A-A
 SCALE 1 : 1

BASE

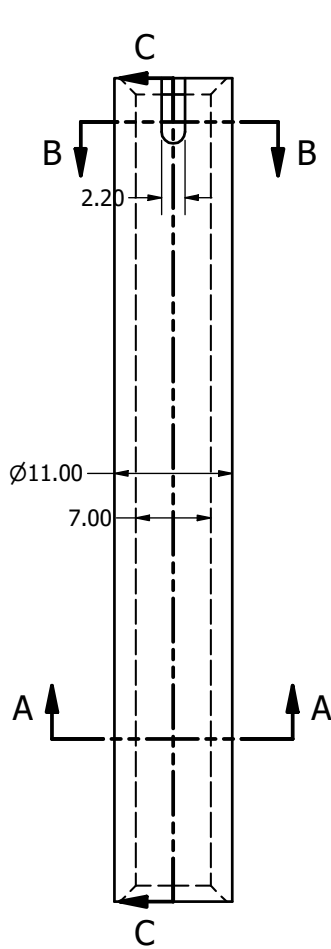
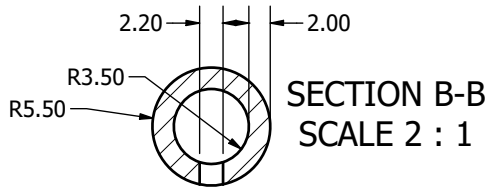


**SECTION A-A
SCALE 2 : 1**

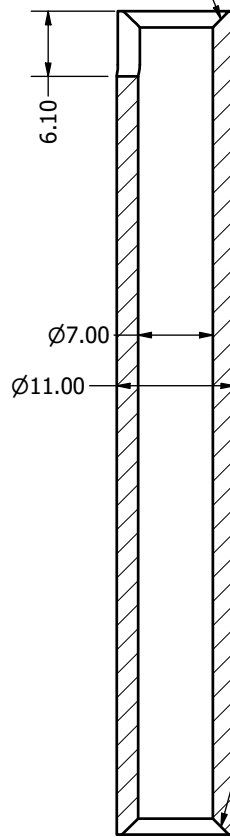


**SECTION C-C
SCALE 8:1**

CELL
(Teflon)

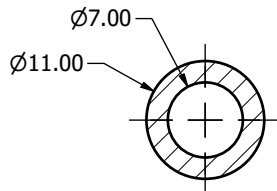


1.50 X 45.0° CHAMFER



1.50 X 45.0° CHAMFER

SECTION C-C
SCALE 2 : 1



SECTION A-A
SCALE 2 : 1

A.3 NMR compatible measurement cell

The measurement cell that is used for the TD-NMR relaxometry tests presented in Chapter 5 and it has been designed and fabricated at the Wageningen University & Research laboratories, in the Netherlands.

The presence of magnets in NMR spectrometers does not allow the use of metals, thus the apparatus is made of two main plastic pieces.

- a PTFE cylinder cell of 7mm internal diameter. At the bottom aperture, the internal diameter is slightly reduced to hold in place a glass porous stone;
- a PEEK rod that is connected to the RH unit control (see Section 2.3.1). The rod is equipped with an adjustable height ring, so that the analysed sample can be aligned within the homogeneous regions of the radio-frequency coil (Section 2.2.2).

Appendix B

Couscous particle stiffness dependency on water content

The main objective of the thesis is to quantify the microstructural changes in water-sensitive granular assemblies driven by variation of water content. The analysis of x-ray tomography and neutron images, combined with the TD-NMR relaxometry study, allows the quantification of particle volumes, inter-particle contacts and overall assembly volumetric response, and it is possible to relate them to increase of water content.

However, as mentioned in Chapter 1, the morphological changes are only one of the aspects characterising water-sensitive materials. The particle and bulk “strength” are also strongly affected by the presence of water. To fully understand and characterise the behaviour of such materials, it is necessary to also understand the influence of water on the material’s mechanical properties.

This Appendix presents an experimental campaign carried out in order to investigate the dependency of couscous individual particles stiffness on water content.

B.1 Experimental procedure

This Section describes the experimental setup used for the compression tests on individual couscous particles and the procedure followed to perform them.

B.1.1 Particle compression set-up

A schematic view and pictures of the experimental apparatus used to perform compression tests on individual couscous particle are shown in Figure B.1 and Figure B.2. The setup is composed of:

- a 6 mm diameter bottom plate of steel equipped with a 35 mm height and 5 mm diameter column to hold the particle in position;
- a PMMA transparent cell to contain the tested particle. The inner diameter of this cell is 10 mm. Air at specific RH is injected into the cell, to hinder infiltration of air at outer environmental conditions. The RH level of the air is kept stable using the WUR RH control unit (see chapter 2, section 2.3.1);
- a steel 8 mm steel piston which compresses the particle according to the imposed displacement;

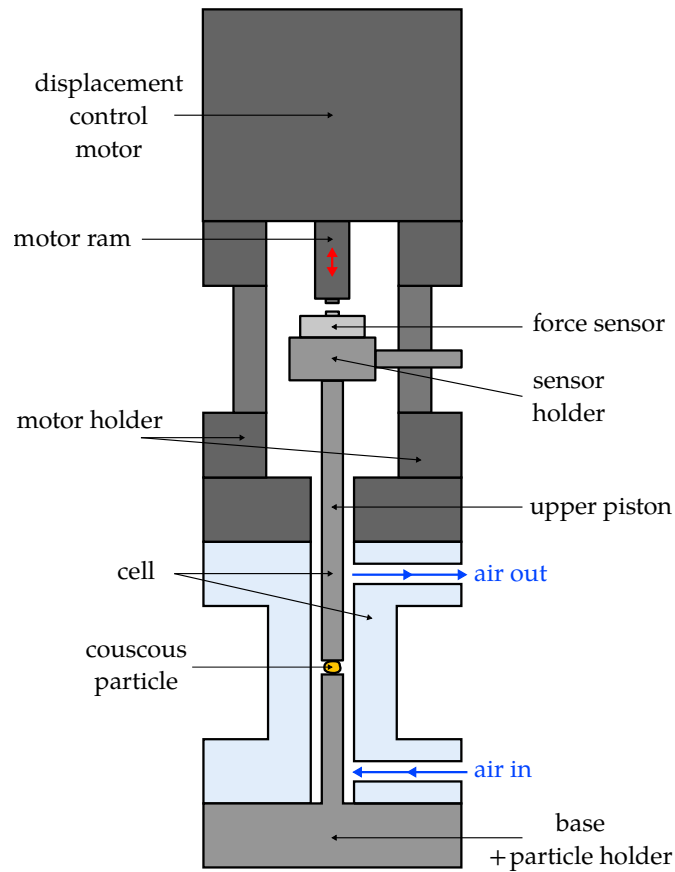


FIGURE B.1: Schematic view of the experimental setup used for the compression tests on individual couscous particles. Each particle is placed on a steel column. A rigid plastic cell contains the tested particle and prevents exposure to outer environment, also thanks to the injection of air from the RH control unit. On top of the particle another piston is placed, which compresses the particle according to the imposed displacement by the motor step. A force sensor is installed between the motor piston and the upper piston, and it records the particle mechanical compression resistance.

- a ELAF-BO-500N load cell (force sensor) to record the particle mechanical resistance to compression. The sensor is equipped with a holder to prevent sliding of the load cell and an adequate displacement control of the piston;
- a PI N-216.2A1 NEXLINE® piezo-walking Linear Actuator motor, equipped with a ram of which the displacement is controlled. By moving the ram downwards, the particle is compressed.

B.1.2 Sample preparation and test procedure

Before running the compression tests, couscous particles are sieved in order to obtain a relatively monodispersed size distribution. The particles used in this for the compression tests are from the same lot used in the experimental campaign presented in Chapter 5. There, the image analysis reveals an average particle equivalent diameter of $710 \mu m$ (Section 5.3.4).

The particles water content is stabilised and determined prior the tests. Two batches of particles are placed in a sealed vessel, where a flow of definite RH air dries or hydrates the particles. Once the particles weight stabilises, *i.e.*, equilibrium is reached with imposed RH, they are observed under a microscope. Only relatively convex particles are selected by eye



FIGURE B.2: Pictures of the compression setup used to test individual couscous particles. On the left, the whole mounted apparatus. On the right, a detail showing the particle positioned between the two pistons.

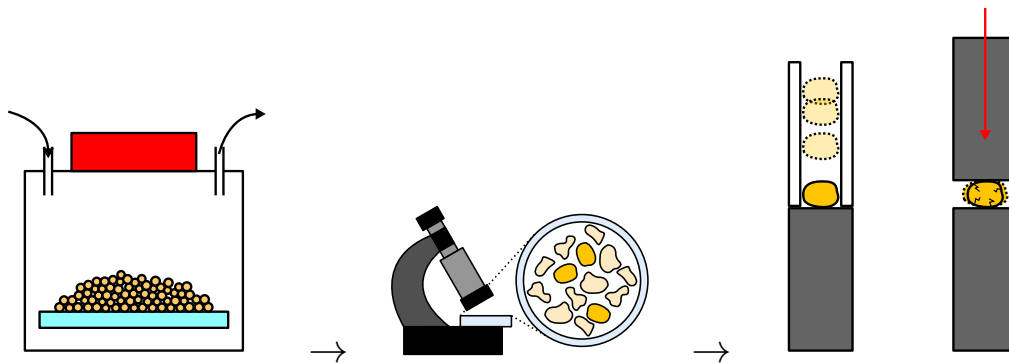


FIGURE B.3: The particles water content is stabilised in a sealed vessel with a flow of air at fixed RH. Then, convex particles are selected using an optical microscope and tested.

and used in the compression tests, to elude a shape effect on the results. Meanwhile, the other batch of particles is used to determine the water content with gravimetric measurements. The dry mass (*i.e.*, water content = 0%) is determined by drying the particles in an oven for 24 hours at 105 °C and measuring their weight.

The particles are tested one by one. Attention is paid to maintain a small distance between the force sensor and the motor ram, in order not to damage the particle or the delicate load cell.

The experimental investigation includes:

- simple compression tests;
- cyclic compression tests.

The simple compression tests are performed by moving downwards the piston at constant velocity ($1 \mu\text{m}/\text{s}$), while the sensor continuously records the force. The particle is compressed until its breakage. However, the analyses presented here focus only on the small displacements response.

In the cyclic tests, the procedure requires additional care. After an initial compression at the same rate as above, the motor-step is halted as soon as the load cell records a substantial increase of force. The system is left to relax for 3 minutes and then the piston is “unloaded”

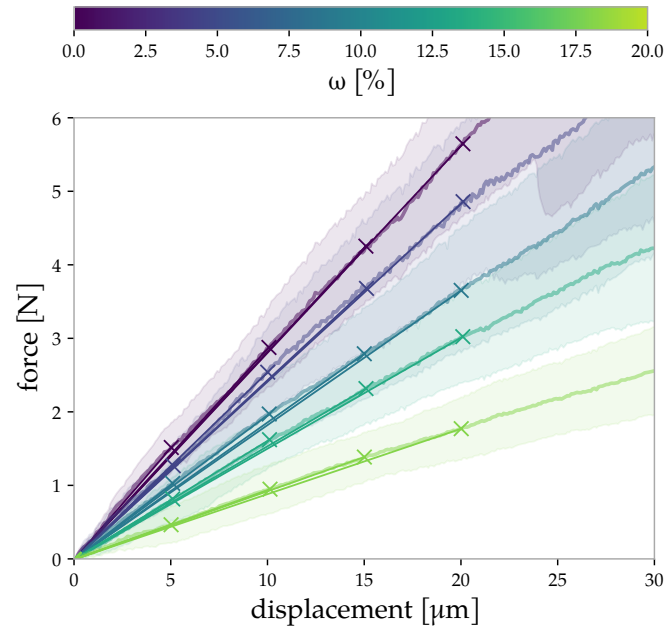


FIGURE B.4: Force-displacement curves from the simple compression tests at different water content levels (from 4.05 % to 18.1 %). Dry particles (purple lines) exhibit a higher stiffness than wet ones (greener lines). The force-displacement response can be describe as a linear relation.

back to the position corresponding to the first halt (displacement $0\mu m$). Next, the particle is compressed by imposing a displacement equal to $+10\mu m$ the maximum one of previous cycle. In total, 7 cycles are performed each time.

B.2 Results and discussion

B.2.1 Simple compression tests

Simple compression tests are performed at 5 different water content levels ω : 4.05, 7.89, 9.80, 11.55, 18.1 %. The investigation of higher water content is not possible due to the required long exposition to high RH air, which favours mould growth.

Several compression tests are performed for each of the water content levels, in order to examine the reproducibility of the tests and improve the characterisation of the particles response. Some tests are excluded from the analysis due to a sudden and early breakage of the particles.

At least 10 successful tests are collected for each water content level, and the results are then averaged. Figure B.4 shows the evolution with water content of force-displacement curves within $30\mu m$ displacement, a value approximately equal to 4% of the average particle diameter. Dry particles (purple lines) exhibit higher stiffness than wet ones. Moreover, the variance is found to be larger for low water contents, because of the higher material viscosity and more brittle response. Figure B.4 also highlights how the force-displacement curve can be described as a linear relation. The slight sub-linearity is well within the sensitivity of the force sensor.

The apparent stiffness $K(\omega)$ is measured as the ratio between the average force and respective displacement. Specifically, the operation is performed for displacements equal to 5, 10, 15 and $20\mu m$, as shown in Figure B.5. The apparent stiffness decreases with water content, and the overall evolution resembles the one found in other water-sensitive materials [GYP91;

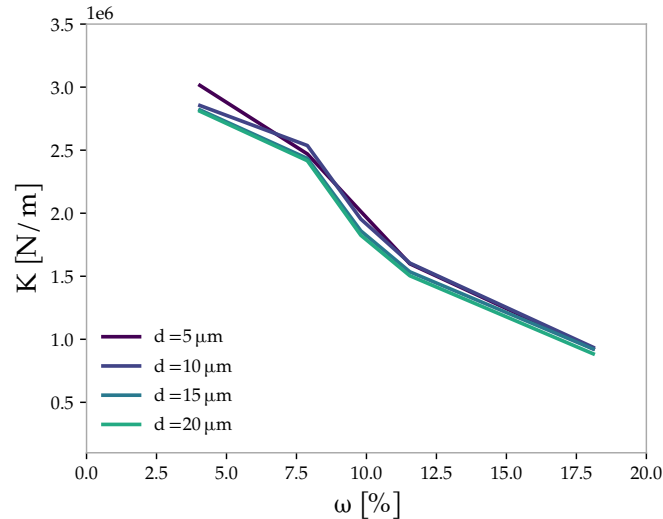


FIGURE B.5: Couscous particles apparent stiffness K as a function of water content ω . The simple compression tests reveal a strong dependency of couscous stiffness to water content. The particles become softer for high water content. No significant effect of (small) displacement is found on the value of K .

Kam+02; Cao+04] (see Figure 1.5). No displacement effect is observed on the simple compression tests.

B.2.2 Cyclic compression tests

The cyclic tests are carried out to investigate qualitatively the loading-unloading response, and establish the extent of recovered and irreversible deformation between cycles.

Here we present the results of two cyclic compression tests, one at 4 % water content and the other at 10 %. As mentioned earlier, 7 loading-unloading cycles are performed.

The force-displacement curves are shown in Figure B.6a and Figure B.6b. The results indicate that the material loading stiffness does not change between cycles. The inclination appears to be rather constant throughout the tests, at least until the sixth cycle, in which the particles are broken.

During the 3 minutes interval between loading and unloading a strong relaxation is measured, which indicates a significant non-recoverable deformation, even for small displacements. The relaxation is greater in the 4 % water content case, possibly because of the (more) fragile behaviour.

The unloading stiffness also appears to remain constant between cycles, although it is not equivalent to the loading stiffness. A strong component of non-recoverable deformation is therefore measured between cycles.

It can be noticed how the results highlight a brittle response in drier particles ($\omega = 4\%$), given that an “explosive” breakage is detected after the fifth cycle. Conversely, the response of the more hydrated particle ($\omega = 10\%$) is relatively ductile.

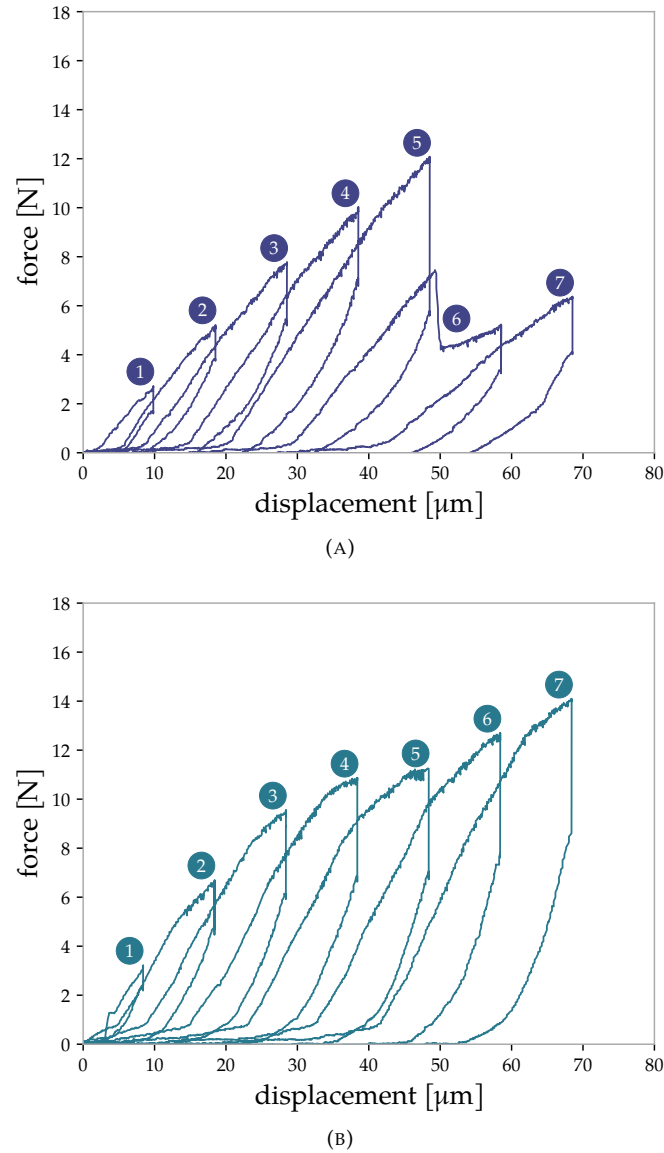


FIGURE B.6: Force-displacement curves of cyclic compression tests for particle at different water content: $\omega = 4\%$ (A) and $\omega = 10\%$ (B). The loading and unloading stiffnesses appear to remain constant during the tests. A strong relaxation is observed in either case between loading and unloading. The result show a strong non-recoverable deformation component, even for relatively small displacements.

B.3 Conclusions

The experimental campaign presented in this Appendix investigates the effect of water content on the stiffness of couscous particles.

Two different kind of tests are performed: simple compression tests and cyclic compression tests. The simple compression tests allow the measurement of the apparent stiffness K and its dependency on water content. The particle stiffness significantly decreases with water content. These results are used to calibrate the stiffness decay in the numerical DEM simulations presented in Chapter 8 (see Section 8.2).

From the cyclic compression tests it can be evinced that, unless the particle breaks, the loading and unloading stiffnesses do not vary between cycles. A strong relaxation and a significant

non-recoverable deformation are measured, indicating that a purely elastic assumption might not be sufficient to describe the inter-particle interaction.

In the future, the elastic and plastic deformation dependency on the applied load and on water content could be investigated. Additionally, experiments should be performed to further characterise the interaction of fewer [Wah+08; Hai+14].

Bibliography

- [Abe+12] J. Abecassis *et al.* "Other traditional durum-derived products". In: *Durum Wheat Chemistry and Technology*. Springer, 2012, pp. 177–199. DOI: [10.1016/B978-1-891127-65-6.50015-5](https://doi.org/10.1016/B978-1-891127-65-6.50015-5).
- [Abr61] A. Abragam. *The principles of nuclear magnetism*. 32. Oxford university press, 1961. DOI: [10.1119/1.1937646](https://doi.org/10.1119/1.1937646).
- [AVK95] J. Aguilera, J. del Valle, and M. Karel. "Caking phenomena in amorphous food powders". In: *Trends in Food Science & Technology* 6.5 (1995), pp. 149–155. DOI: [10.1016/S0924-2244\(00\)89023-8](https://doi.org/10.1016/S0924-2244(00)89023-8).
- [Als+17] K. A. Alshibli *et al.* "Influence of particle morphology on 3D kinematic behavior and strain localization of sheared sand". In: *Journal of Geotechnical and Geoenvironmental Engineering* 143.2 (2017), p. 04016097. DOI: [10.1061/\(ASCE\)GT.1943-5606.0001601](https://doi.org/10.1061/(ASCE)GT.1943-5606.0001601).
- [AHR04] M. Amin, M. Hossain, and K. Roy. "Effects of moisture content on some physical properties of lentil seeds". In: *Journal of Food Engineering* 65.1 (2004), pp. 83–87. DOI: [10.1016/j.jfoodeng.2003.12.006](https://doi.org/10.1016/j.jfoodeng.2003.12.006).
- [And+12] E. Andò *et al.* "Grain-scale experimental investigation of localised deformation in sand: a discrete particle tracking approach". In: *Acta Geotechnica* 7 (2012), pp. 1–13. DOI: [10.1007/s11440-011-0151-6](https://doi.org/10.1007/s11440-011-0151-6).
- [Ban+10] J. Banhart *et al.* "X-ray and neutron imaging—Complementary techniques for materials science and engineering". In: *International Journal of Materials Research* 101.9 (2010), pp. 1069–1079. DOI: [10.3139/146.110382](https://doi.org/10.3139/146.110382).
- [BK04] J. F. Barrett and N. Keat. "Artifacts in CT: recognition and avoidance". In: *Radiographics* 24.6 (2004), pp. 1679–1691. DOI: [10.1148/rg.246045065](https://doi.org/10.1148/rg.246045065).
- [BRC18] B. Bellocq, T. Ruiz, and B. Cuq. "Contribution of cooking and drying to the structure of couscous grains made from durum wheat semolina". In: *Cereal chemistry* 95.5 (2018), pp. 646–659. DOI: [10.1002/cche.10078](https://doi.org/10.1002/cche.10078).
- [Beu79] S. Beucher. "Use of watersheds in contour detection". In: *Proceedings of the International Workshop on Image Processing*. CCETT. 1979.
- [Beu82] S. Beucher. "Watersheds of functions and picture segmentation". In: *ICASSP'82. IEEE International Conference on Acoustics, Speech, and Signal Processing*. Vol. 7. IEEE. 1982, pp. 1928–1931. DOI: [10.1109/ICASSP.1982.1171424](https://doi.org/10.1109/ICASSP.1982.1171424).
- [Bik+05] D. Bika *et al.* "Strength and morphology of solid bridges in dry granules of pharmaceutical powders". In: *Powder Technology* 150.2 (2005), pp. 104–116. DOI: [10.1016/j.powtec.2004.11.024](https://doi.org/10.1016/j.powtec.2004.11.024).
- [Blo46] F. Bloch. "Nuclear induction". In: *Physical review* 70.7-8 (1946), p. 460. DOI: [10.1103/PhysRev.70.460](https://doi.org/10.1103/PhysRev.70.460).

- [BPP48] N. Bloembergen, E. M. Purcell, and R. V. Pound. "Relaxation effects in nuclear magnetic resonance absorption". In: *Physical review* 73.7 (1948), p. 679. DOI: [10.1103/PhysRev.73.679](https://doi.org/10.1103/PhysRev.73.679).
- [BAC21] K. Brockbank, B. Armstrong, and J. Clayton. "Measurement and quantification of caking in excipients and food products with emphasis on the non-homogeneous interaction with ambient moisture". In: *Particuology* 56 (2021), pp. 75–83. DOI: [10.1016/j.partic.2020.10.012](https://doi.org/10.1016/j.partic.2020.10.012).
- [Can+20] D. Cantor *et al.* "Compaction model for highly deformable particle assemblies". In: *Physical Review Letters* 124.20 (2020), p. 208003. DOI: [10.1103/PhysRevLett.124.208003](https://doi.org/10.1103/PhysRevLett.124.208003).
- [Cao+04] W. Cao *et al.* "Physicochemical, mechanical and thermal properties of brown rice grain with various moisture contents". In: *International journal of food science & technology* 39.9 (2004), pp. 899–906. DOI: [10.1111/j.1365-2621.2004.00849.x](https://doi.org/10.1111/j.1365-2621.2004.00849.x).
- [CB+21] M. Cárdenas-Barrantes *et al.* "Micromechanical description of the compaction of soft pentagon assemblies". In: *Physical Review E* 103.6 (2021), p. 062902. DOI: [10.1103/PhysRevE.103.062902](https://doi.org/10.1103/PhysRevE.103.062902).
- [CB+22] M. Cárdenas-Barrantes *et al.* "Three-dimensional compaction of soft granular packings". In: *Soft Matter* 18.2 (2022), pp. 312–321. DOI: [10.1039/D1SM01241J](https://doi.org/10.1039/D1SM01241J).
- [Car97] P. C. Carman. "Fluid flow through granular beds". In: *Chemical Engineering Research and Design* 75 (1997), S32–S48. DOI: [10.1016/S0263-8762\(97\)80003-2](https://doi.org/10.1016/S0263-8762(97)80003-2).
- [Car+16] M. Carpin *et al.* "Caking of lactose: A critical review". In: *Trends in Food Science & Technology* 53 (2016), pp. 1–12. DOI: [10.1016/j.tifs.2016.04.002](https://doi.org/10.1016/j.tifs.2016.04.002).
- [CH49] D. Carr and B. Harris. "Solutions for maintaining constant relative humidity". In: *Industrial & Engineering Chemistry* 41.9 (1949), pp. 2014–2015. DOI: [10.1021/ie50477a042](https://doi.org/10.1021/ie50477a042).
- [CP54] H. Y. Carr and E. M. Purcell. "Effects of Diffusion on Free Precession in Nuclear Magnetic Resonance Experiments". In: *Phys. Rev.* 94 (3 1954), pp. 630–638. DOI: [10.1103/PhysRev.94.630](https://doi.org/10.1103/PhysRev.94.630).
- [Cha+21] C. Chauhan *et al.* "Food loss and waste in food supply chains. A systematic literature review and framework development approach". In: *Journal of Cleaner Production* 295 (2021), p. 126438. DOI: [10.1016/j.jclepro.2021.126438](https://doi.org/10.1016/j.jclepro.2021.126438).
- [CW18] Z. Cheng and J. Wang. "A particle-tracking method for experimental investigation of kinematics of sand particles under triaxial compression". In: *Powder Technology* 328 (2018), pp. 436–451. DOI: [10.1016/j.powtec.2017.12.071](https://doi.org/10.1016/j.powtec.2017.12.071).
- [Chr+06] N. Christakis *et al.* "Aggregation and caking processes of granular materials: continuum model and numerical simulation with application to sugar". In: *Advanced Powder Technology* 17.5 (2006), pp. 543–565. DOI: [10.1163/156855206778440480](https://doi.org/10.1163/156855206778440480).
- [Chu+00] M.-S. Chung *et al.* "Study of Caking in Powdered Foods Using Nuclear Magnetic Resonance Spectroscopy". In: *Journal of Food Science* 65.1 (2000), pp. 134–138. DOI: [10.1111/j.1365-2621.2000.tb15968.x](https://doi.org/10.1111/j.1365-2621.2000.tb15968.x).
- [CI+08] T. Cleveland Iv *et al.* "The use of neutron tomography for the structural analysis of corn kernels". In: *Journal of Cereal Science* 48.2 (2008), pp. 517–525. DOI: [10.1016/j.jcs.2007.12.003](https://doi.org/10.1016/j.jcs.2007.12.003).

- [CB13] V. Cnudde and M. N. Boone. "High-resolution X-ray computed tomography in geosciences: A review of the current technology and applications". In: *Earth-Science Reviews* 123 (2013), pp. 1–17. DOI: [10.1016/j.earscirev.2013.04.003](https://doi.org/10.1016/j.earscirev.2013.04.003).
- [CB14] A. Crouter and L. Briens. "The effect of moisture on the flowability of pharmaceutical excipients". In: *Aaps PharmSciTech* 15.1 (2014), pp. 65–74. DOI: [10.1208/s12249-013-0036-0](https://doi.org/10.1208/s12249-013-0036-0).
- [CS79] P. A. Cundall and O. D. Strack. "A discrete numerical model for granular assemblies". In: *Géotechnique* 29.1 (1979), pp. 47–65. DOI: [10.1680/geot.1979.29.1.47](https://doi.org/10.1680/geot.1979.29.1.47).
- [DP17] S. Damodaran and K. Parkin. *Fennema's Food Chemistry (5th ed.)* CRC press, 2017. DOI: [10.1201/9781315372914](https://doi.org/10.1201/9781315372914).
- [DE06] G. Davis and J. Elliott. "Artefacts in X-ray microtomography of materials". In: *Materials science and technology* 22.9 (2006), pp. 1011–1018. DOI: [10.1179/174328406X114117](https://doi.org/10.1179/174328406X114117).
- [DR+22] S. K. De Richter *et al.* "Swelling of couscous grains under saturated conditions". In: *Journal of Food Engineering* 319 (2022), p. 110910. DOI: [10.1016/j.jfoodeng.2021.110910](https://doi.org/10.1016/j.jfoodeng.2021.110910).
- [DTR09] J.-Y. Delenne, V. Topin, and F. Radjai. "Failure of cemented granular materials under simple compression: experiments and numerical simulations". In: *Acta Mechanica* 205.1 (2009), pp. 9–21. DOI: [10.1007/s00707-009-0160-9](https://doi.org/10.1007/s00707-009-0160-9).
- [Des+18] J. Desrues *et al.* "How does strain localise in standard triaxial tests on sand: Revisiting the mechanism 20 years on". In: *Mechanics Research Communications* 92 (2018), pp. 142–146. DOI: [10.1016/j.mechrescom.2018.08.007](https://doi.org/10.1016/j.mechrescom.2018.08.007).
- [DAD19] J. Dijkstra, E. Andò, and C. Dano. "Grain kinematics during stress relaxation in sand: not a problem for X-ray imaging". In: *E3S Web of Conferences*. Vol. 92. EDP Sciences, 2019, p. 01001. DOI: [10.1051/e3sconf/20199201001](https://doi.org/10.1051/e3sconf/20199201001).
- [DB07] C. Doona and M.-Y. Baik. "Molecular mobility in model dough systems studied by time-domain nuclear magnetic resonance spectroscopy". In: *Journal of Cereal Science* 45.3 (2007), pp. 257–262. DOI: [10.1016/j.jcs.2006.07.015](https://doi.org/10.1016/j.jcs.2006.07.015).
- [DAAR16] A. M. Druckrey, K. A. Alshibli, and R. I. Al-Raoush. "3D characterization of sand particle-to-particle contact and morphology". In: *Computers and Geotechnics* 74 (2016), pp. 26–35. DOI: [10.1016/j.compgeo.2015.12.014](https://doi.org/10.1016/j.compgeo.2015.12.014).
- [EYDR05] M. S. El Youssoufi, J.-Y. Delenne, and F. Radjai. "Self-stresses and crack formation by particle swelling in cohesive granular media". In: *Physical Review E* 71.5 (2005), p. 051307. DOI: [10.1103/PhysRevE.71.051307](https://doi.org/10.1103/PhysRevE.71.051307).
- [Eme+09] E. Emery *et al.* "Flowability of moist pharmaceutical powders". In: *Powder Technology* 189.3 (2009), pp. 409–415. DOI: [10.1016/j.powtec.2008.06.017](https://doi.org/10.1016/j.powtec.2008.06.017).
- [EEC05] M. Erbaş, M. F. Ertugay, and M. Certel. "Moisture adsorption behaviour of semolina and farina". In: *Journal of Food Engineering* 69.2 (2005), pp. 191–198. DOI: [10.1016/j.jfoodeng.2004.07.017](https://doi.org/10.1016/j.jfoodeng.2004.07.017).
- [et 21] V. S. *et al.* *Yade Documentation 3rd ed.* <http://yade-dem.org/doc/>. The Yade Project, 2021. DOI: [10.5281/zenodo.5705394](https://doi.org/10.5281/zenodo.5705394).
- [FDK84] L. A. Feldkamp, L. C. Davis, and J. W. Kress. "Practical cone-beam algorithm". In: *Josa a* 1.6 (1984), pp. 612–619. DOI: [10.1364/JOSA.A.1.000612](https://doi.org/10.1364/JOSA.A.1.000612).
- [Fen96] O. R. Fennema. *Food chemistry*. Vol. 76. CRC Press, 1996.

- [Fig+11] J. Figueroa *et al.* "Evaluation of degree of elasticity and other mechanical properties of wheat kernels". In: *Cereal Chemistry* 88.1 (2011), pp. 12–18. DOI: [10.1094/CCHEM-04-10-0065](https://doi.org/10.1094/CCHEM-04-10-0065).
- [Fit+07] J. Fitzpatrick *et al.* "Glass transition and the flowability and caking of powders containing amorphous lactose". In: *Powder Technology* 178.2 (2007), pp. 119–128. DOI: [10.1016/j.powtec.2007.04.017](https://doi.org/10.1016/j.powtec.2007.04.017).
- [Fit+10] J. Fitzpatrick *et al.* "Comparing the caking behaviours of skim milk powder, amorphous maltodextrin and crystalline common salt". In: *Powder Technology* 204.1 (2010), pp. 131–137. DOI: [10.1016/j.powtec.2010.07.029](https://doi.org/10.1016/j.powtec.2010.07.029).
- [FA05] J. J. Fitzpatrick and L. Ahrné. "Food powder handling and processing: Industry problems, knowledge barriers and research opportunities". In: *Chemical Engineering and Processing: Process Intensification* 44.2 (2005), pp. 209–214. DOI: [10.1016/j.cep.2004.03.014](https://doi.org/10.1016/j.cep.2004.03.014).
- [FR93] D. G. Fredlund and H. Rahardjo. *Soil mechanics for unsaturated soils*. John Wiley & Sons, 1993. DOI: [10.1002/9780470172759](https://doi.org/10.1002/9780470172759).
- [Gam92] P. N. Gambhir. "Applications of low-resolution pulsed NMR to the determination of oil and moisture in oilseeds". In: *Trends in Food Science & Technology* 3 (1992), pp. 191–196. DOI: [10.1016/0924-2244\(92\)90188-3](https://doi.org/10.1016/0924-2244(92)90188-3).
- [GRHM05] R. Garcia-Rojo, H. Herrmann, and S. McNamara. "Powders and grains". In: *Proc. 5th Int. Conf. on Micromech. of Granular Media*. 2005. DOI: [10.1201/NOE0415383486](https://doi.org/10.1201/NOE0415383486).
- [GYP91] G. Glenn, F. Younce, and M. Pitts. "Fundamental physical properties characterizing the hardness of wheat endosperm". In: *Journal of Cereal science* 13.2 (1991), pp. 179–194. DOI: [10.1016/S0733-5210\(09\)80035-0](https://doi.org/10.1016/S0733-5210(09)80035-0).
- [Gre+77] L. Greenspan *et al.* "Humidity fixed points of binary saturated aqueous solutions". In: *Journal of research of the national bureau of standards* 81.1 (1977), pp. 89–96. DOI: [10.6028/jres.081A.011](https://doi.org/10.6028/jres.081A.011).
- [Hah50a] E. L. Hahn. "Nuclear induction due to free Larmor precession". In: *Physical Review* 77.2 (1950), p. 297. DOI: [10.1103/PhysRev.77.297.2](https://doi.org/10.1103/PhysRev.77.297.2).
- [Hah50b] E. L. Hahn. "Spin echoes". In: *Physical review* 80.4 (1950), p. 580. DOI: [10.1103/PhysRev.80.580](https://doi.org/10.1103/PhysRev.80.580).
- [Hah53] E. L. Hahn. "Free nuclear induction". In: *Physics Today* 6.11 (1953), pp. 4–9. DOI: [10.1063/1.3061075](https://doi.org/10.1063/1.3061075).
- [Hai+14] C. I. Haider *et al.* "Influence of environmental conditions on caking mechanisms in individual amorphous food particle contacts". In: *AIChE Journal* 60.8 (2014), pp. 2774–2787. DOI: [10.1002/aic.14490](https://doi.org/10.1002/aic.14490).
- [Hal+10] S. A. Hall *et al.* "Discrete and continuum analysis of localised deformation in sand using X-ray μ CT and volumetric digital image correlation". In: *Géotechnique* 60.5 (2010), pp. 315–322. DOI: [10.1680/geot.2010.60.5.315](https://doi.org/10.1680/geot.2010.60.5.315).
- [HS20] R. Hammami and M. Sissons. "Durum wheat products, couscous". In: *Wheat Quality For Improving Processing And Human Health*. Springer, 2020, pp. 347–367. DOI: [10.1007/978-3-030-34163-3_15](https://doi.org/10.1007/978-3-030-34163-3_15).

- [Ham+22] R. Hammami *et al.* "Durum Wheat Couscous Grains: An Ethnic Mediterranean Food at the Interface of Traditional Domestic Preparation and Industrial Manufacturing". In: *Foods* 11.7 (2022), p. 902. DOI: <https://doi.org/10.3390/foods11070902>.
- [Hat19] E. Hatzakis. "Nuclear Magnetic Resonance (NMR) Spectroscopy in Food Science: A Comprehensive Review". In: *Comprehensive Reviews in Food Science and Food Safety* 18.1 (2019), pp. 189–220. DOI: [10.1111/1541-4337.12408](https://doi.org/10.1111/1541-4337.12408).
- [He+09] J. He *et al.* "Effect of pressure on the adsorption rate for gasoline vapor on pitch-based activated carbon". In: *Journal of Chemical & Engineering Data* 54.5 (2009), pp. 1504–1509. DOI: [10.1021/je800809k](https://doi.org/10.1021/je800809k).
- [Heb+03] A. Hebrard *et al.* "Hydration properties of durum wheat semolina: influence of particle size and temperature". In: *Powder Technology* 130.1-3 (2003), pp. 211–218. DOI: [10.1016/S0032-5910\(02\)00268-1](https://doi.org/10.1016/S0032-5910(02)00268-1).
- [Hel01] P. Helnwein. "Some remarks on the compressed matrix representation of symmetric second-order and fourth-order tensors". In: *Computer methods in applied mechanics and engineering* 190.22-23 (2001), pp. 2753–2770. DOI: [10.1016/S0045-7825\(00\)00263-2](https://doi.org/10.1016/S0045-7825(00)00263-2).
- [HR12] F. Hild and S. Roux. "Comparison of local and global approaches to digital image correlation". In: *Experimental mechanics* 52.9 (2012), pp. 1503–1519. DOI: [10.1007/s11340-012-9603-7](https://doi.org/10.1007/s11340-012-9603-7).
- [Jaq+13] C. Jaquet *et al.* "Estimation of separating planes between touching 3D objects using power watershed". In: *International Symposium on Mathematical Morphology and Its Applications to Signal and Image Processing*. Springer. 2013, pp. 452–463. DOI: [10.1007/978-3-642-38294-9_38](https://doi.org/10.1007/978-3-642-38294-9_38).
- [JE+17] E. Juarez-Enriquez *et al.* "Effect of water content on the flowability of hygroscopic powders". In: *Journal of Food Engineering* 205 (2017), pp. 12–17. DOI: [10.1016/j.jfoodeng.2017.02.024](https://doi.org/10.1016/j.jfoodeng.2017.02.024).
- [Kam+02] G. Kamst *et al.* "Effect of deformation rate and moisture content on the mechanical properties of rice grains". In: *Transactions of the ASAE* 45.1 (2002), p. 145. DOI: [10.13031/2013.7857](https://doi.org/10.13031/2013.7857).
- [Kar+18] N. Kardjilov *et al.* "Advances in neutron imaging". In: *Materials Today* 21.6 (2018), pp. 652–672. DOI: [10.1016/j.mattod.2018.03.001](https://doi.org/10.1016/j.mattod.2018.03.001).
- [Kaw+18] R. Kawamoto *et al.* "All you need is shape: Predicting shear banding in sand with LS-DEM". In: *Journal of the Mechanics and Physics of Solids* 111 (2018), pp. 375–392. DOI: [10.1016/j.jmps.2017.10.003](https://doi.org/10.1016/j.jmps.2017.10.003).
- [Lab75] T. P. Labuza. "Sorptions phenomena in foods: theoretical and practical aspects". In: *Theory, determination and control of physical properties of food materials*. Springer, 1975, pp. 197–219. DOI: [10.1007/978-94-010-1731-2_11](https://doi.org/10.1007/978-94-010-1731-2_11).
- [LH98] T. Labuza and C. Hyman. "Moisture migration and control in multi-domain foods". In: *Trends in Food Science & Technology* 9.2 (1998), pp. 47–55. DOI: [10.1016/S0924-2244\(98\)00005-3](https://doi.org/10.1016/S0924-2244(98)00005-3).
- [Lam+11] R. Lamanna *et al.* "Geographical origin of durum wheat studied by ¹H-NMR profiling". In: *Magnetic Resonance in Chemistry* 49.1 (2011), pp. 1–5. DOI: [10.1002/mrc.2695](https://doi.org/10.1002/mrc.2695).

- [LBCL98] D. Le Botlan, F. Casseron, and F. Lantier. "Polymorphism of sugars studied by time domain NMR". In: *Analisis* 26.5 (1998), pp. 198–204. DOI: [10.1051/analisis:1998135](https://doi.org/10.1051/analisis:1998135).
- [Lei+20] T. Leißner *et al.* "3D ex-situ and in-situ X-ray CT process studies in particle technology – A perspective". In: *Advanced Powder Technology* 31.1 (2020), pp. 78–86. DOI: [10.1016/j.apt.2019.09.038](https://doi.org/10.1016/j.apt.2019.09.038).
- [Len+07] N. Lenoir *et al.* "Volumetric digital image correlation applied to X-ray microtomography images from triaxial compression tests on argillaceous rock". In: *Strain* 43.3 (2007), pp. 193–205. DOI: [10.1111/j.1475-1305.2007.00348.x](https://doi.org/10.1111/j.1475-1305.2007.00348.x).
- [Lew00] P. P. Lewicki. "Raoult's law based food water sorption isotherm". In: *Journal of Food Engineering* 43.1 (2000), pp. 31–40. DOI: [10.1016/S0260-8774\(99\)00130-2](https://doi.org/10.1016/S0260-8774(99)00130-2).
- [LWL21] L. Liu, K.-T. Wan, and K.-K. Liu. "Influence of Relative Humidity on Interparticle Capillary Adhesion". In: *Langmuir* 37.43 (2021), pp. 12714–12722. DOI: [10.1021/acs.langmuir.1c02167](https://doi.org/10.1021/acs.langmuir.1c02167).
- [LK81] B. D. Lucas and T. Kanade. "An iterative image registration technique with an application to stereo vision". In: *IJCAI'81: 7th international joint conference on Artificial intelligence*. Vol. 2. 1981, pp. 674–679. DOI: [10.5555/1623264.1623280](https://doi.org/10.5555/1623264.1623280).
- [LLRM07] T. Lucas, D. Le Ray, and F. Mariette. "Kinetics of water absorption and solute leaching during soaking of breakfast cereals". In: *Journal of Food Engineering* 80.2 (2007), pp. 377–384. DOI: [10.1016/j.jfoodeng.2005.11.006](https://doi.org/10.1016/j.jfoodeng.2005.11.006).
- [Lum+16] G. Lumay *et al.* "Effect of relative air humidity on the flowability of lactose powders". In: *Journal of Drug Delivery Science and Technology* 35 (2016), pp. 207–212. DOI: [10.1016/j.jddst.2016.04.007](https://doi.org/10.1016/j.jddst.2016.04.007).
- [Mat+07] M.-L. Mateus *et al.* "Characterization of water mobility in dry and wetted roasted coffee using low-field proton nuclear magnetic resonance". In: *Journal of Food Engineering* 81.3 (2007), pp. 572–579. DOI: [10.1016/j.jfoodeng.2006.12.015](https://doi.org/10.1016/j.jfoodeng.2006.12.015).
- [MAN11] D. McMorrow and J. Als-Nielsen. *Elements of modern X-ray physics*. John Wiley & Sons, 2011. DOI: [10.1002/9781119998365](https://doi.org/10.1002/9781119998365).
- [MG58] S. Meiboom and D. Gill. "Modified Spin-Echo Method for Measuring Nuclear Relaxation Times". In: *Review of Scientific Instruments* 29.8 (1958), pp. 688–691. DOI: [10.1063/1.1716296](https://doi.org/10.1063/1.1716296).
- [MS79] T. Morita and R. P. Singh. "Physical and thermal properties of short-grain rough rice". In: *Transactions of the ASAE* 22.3 (1979), pp. 630–636. DOI: [10.13031/2013.35074](https://doi.org/10.13031/2013.35074).
- [O'B48] F. E. O'Brien. "The control of humidity by saturated salt solutions". In: *Journal of Scientific Instruments* 25.3 (1948), p. 73. DOI: [10.1088/0950-7671/25/3/305](https://doi.org/10.1088/0950-7671/25/3/305).
- [Omi+98] H. Omidian *et al.* "A model for the swelling of superabsorbent polymers". In: *Polymer* 39.26 (1998), pp. 6697–6704. DOI: [10.1016/S0032-3861\(98\)00095-0](https://doi.org/10.1016/S0032-3861(98)00095-0).
- [Onl] *Online Interactive Psychrometric Chart*. URL: <https://www.flycarpet.net/en/psyonline>.
- [Ots79] N. Otsu. "A threshold selection method from gray-level histograms". In: *IEEE transactions on systems, man, and cybernetics* 9.1 (1979), pp. 62–66. DOI: [10.1109/TSMC.1979.4310076](https://doi.org/10.1109/TSMC.1979.4310076).

- [PP93] N. R. Pal and S. K. Pal. "A review on image segmentation techniques". In: *Pattern recognition* 26.9 (1993), pp. 1277–1294. DOI: [10.1016/0031-3203\(93\)90135-J](https://doi.org/10.1016/0031-3203(93)90135-J).
- [Pal05] S. Palzer. "The effect of glass transition on the desired and undesired agglomeration of amorphous food powders". In: *Chemical Engineering Science* 60.14 (2005), pp. 3959–3968. DOI: [10.1016/j.ces.2005.02.015](https://doi.org/10.1016/j.ces.2005.02.015).
- [PME00] H. T. Pedersen, L. Munck, and S. B. Engelsen. "Low-field 1H nuclear magnetic resonance and chemometrics combined for simultaneous determination of water, oil, and protein contents in oilseeds". In: *Journal of the American Oil Chemists' Society* 77.10 (2000), pp. 1069–1077. DOI: [10.1007/s11746-000-0168-4](https://doi.org/10.1007/s11746-000-0168-4).
- [Pen+20] H. Penvern *et al.* "How Bound Water Regulates Wood Drying". In: *Phys. Rev. Applied* 14 (5 2020), p. 054051. DOI: [10.1103/PhysRevApplied.14.054051](https://doi.org/10.1103/PhysRevApplied.14.054051).
- [Pet46] O. Peter. "Neutronen-Durchleuchtung". In: *Zeitschrift für Naturforschung A* 1.10 (1946), pp. 557–559. DOI: [10.1515/zna-1946-1002](https://doi.org/10.1515/zna-1946-1002).
- [PHW19] V. L. Popov, M. Heß, and E. Willert. *Handbook of contact mechanics: exact solutions of axisymmetric contact problems*. Springer Nature, 2019. DOI: [10.1007/978-3-662-58709-6](https://doi.org/10.1007/978-3-662-58709-6).
- [PY50] W. Proctor and F. Yu. "The dependence of a nuclear magnetic resonance frequency upon chemical compound". In: *Physical Review* 77.5 (1950), p. 717. DOI: [10.1103/PhysRev.77.717](https://doi.org/10.1103/PhysRev.77.717).
- [Rad+10] F. Radjai *et al.* "Force transmission in cohesive granular media". In: *AIP Conference Proceedings*. Vol. 1227. 1. American Institute of Physics, 2010, pp. 240–259. DOI: [10.1063/1.3435395](https://doi.org/10.1063/1.3435395).
- [RW09] A. S. Rathore and H. Winkle. "Quality by design for biopharmaceuticals". In: *Nature biotechnology* 27.1 (2009), pp. 26–34. DOI: [10.1038/nbt0109-26](https://doi.org/10.1038/nbt0109-26).
- [Ros+20] L. Rostom *et al.* "Investigation of the effect of aging on wood hygroscopicity by 2D 1H NMR relaxometry". In: *Holzforschung* 74.4 (2020), pp. 400–411. DOI: [10.1515/hf-2019-0052](https://doi.org/10.1515/hf-2019-0052).
- [RAR19] E. Roubin, E. Ando, and S. Roux. "The colours of concrete as seen by X-rays and neutrons". In: *Cement and Concrete Composites* 104 (2019), p. 103336. DOI: [10.1016/j.cemconcomp.2019.103336](https://doi.org/10.1016/j.cemconcomp.2019.103336).
- [RCA99] R. R. Ruan, P. L. Chen, and S. Almaer. "Nondestructive analysis of sweet corn maturity using NMR". In: *HortScience* 34.2 (1999), pp. 319–321. DOI: [10.21273/HORTSCI.34.2.319](https://doi.org/10.21273/HORTSCI.34.2.319).
- [Saa+05] M. Saadatfar *et al.* "The geometry and the number of contacts of monodisperse sphere packs using x-ray tomography". In: *Powders and Grains* (2005), pp. 33–36.
- [SAH10] M. Sadeghi, H. A. Araghi, and A. Hemmat. "Physico-mechanical properties of rough rice (*Oryza sativa* L.) grain as affected by variety and moisture content". In: *Agricultural Engineering International: CIGR Journal* 12.3-4 (2010), pp. 129–136.
- [SM98] T. Sasaki and J. Matsuki. "Effect of wheat starch structure on swelling power". In: *Cereal chemistry* 75.4 (1998), pp. 525–529. DOI: [10.1094/CCHEM.1998.75.4.525](https://doi.org/10.1094/CCHEM.1998.75.4.525).
- [Sch04] S. J. Schmidt. "Water and solids mobility in foods". In: *Advances in food and nutrition research* (2004). DOI: [10.1016/S1043-4526\(04\)48001-2](https://doi.org/10.1016/S1043-4526(04)48001-2).

- [Sch+16] L. Schoeman *et al.* "X-ray micro-computed tomography (μ CT) for non-destructive characterisation of food microstructure". In: *Trends in Food Science & Technology* 47 (2016), pp. 10–24. DOI: [10.1016/j.tifs.2015.10.016](https://doi.org/10.1016/j.tifs.2015.10.016).
- [Sei04] J. A. Seibert. "X-ray imaging physics for nuclear medicine technologists. Part 1: Basic principles of x-ray production". In: *Journal of nuclear medicine technology* 32.3 (2004), pp. 139–147.
- [SB05] J. A. Seibert and J. M. Boone. "X-ray imaging physics for nuclear medicine technologists. Part 2: X-ray interactions and image formation". In: *Journal of nuclear medicine technology* 33.1 (2005), pp. 3–18.
- [SK82] A. D. Sharma and O. R. Kunze. "Post-drying fissure developments in rough rice". In: *Transactions of the ASAE* 25.2 (1982), pp. 465–468. DOI: [10.13031/2013.33556](https://doi.org/10.13031/2013.33556).
- [SFS11] L. Shi, Y. Feng, and C. C. Sun. "Initial moisture content in raw material can profoundly influence high shear wet granulation process". In: *International journal of pharmaceutics* 416.1 (2011), pp. 43–48. DOI: [10.1016/j.ijpharm.2011.05.080](https://doi.org/10.1016/j.ijpharm.2011.05.080).
- [Sid+86] I. Siddiqui *et al.* "Mucilage in yellow mustard (*Brassica hirta*) seeds". In: *Food Structure* 5.1 (1986), p. 17.
- [Sim+14] C. Simmler *et al.* "Universal quantitative NMR analysis of complex natural samples". In: *Current opinion in biotechnology* 25 (2014), pp. 51–59. DOI: [10.1016/j.copbio.2013.08.004](https://doi.org/10.1016/j.copbio.2013.08.004).
- [Sle+21] H. C. Sleiman *et al.* "Simultaneous x-ray and neutron 4D tomographic study of drying-driven hydro-mechanical behavior of cement-based materials at moderate temperatures". In: *Cement and Concrete Research* 147 (2021), p. 106503. DOI: [10.1016/j.cemconres.2021.106503](https://doi.org/10.1016/j.cemconres.2021.106503).
- [SRWG01] M. Stading, Å Rindlav-Westling, and P. Gatenholm. "Humidity-induced structural transitions in amylose and amylopectin films". In: *Carbohydrate polymers* 45.3 (2001), pp. 209–217. DOI: [https://doi.org/10.1016/S0144-8617\(00\)00242-3](https://doi.org/10.1016/S0144-8617(00)00242-3).
- [Sta+20a] O. Stamati *et al.* "spam: Software for Practical Analysis of Materials". In: *Journal of Open Source Software* 5.51 (2020), p. 2286. DOI: [10.21105/joss.02286](https://doi.org/10.21105/joss.02286).
- [Sta+20b] E. Stavropoulou *et al.* "Dynamics of water absorption in Callovo-Oxfordian Claystone revealed with multimodal x-ray and neutron tomography". In: *Frontiers in Earth Science* 8 (2020), p. 6. DOI: [10.3389/feart.2020.00006](https://doi.org/10.3389/feart.2020.00006).
- [SR49] R. H. Stokes and R. Robinson. "Standard Solutions for Humidity Control at 25°C." In: *Industrial & engineering chemistry* 41.9 (1949), pp. 2013–2013. DOI: [10.1021/ie50477a041](https://doi.org/10.1021/ie50477a041).
- [SW93] D.-W. Sun and J. Woods. "The moisture content/relative humidity equilibrium relationship of wheat-A review". In: *Drying Technology* 11.7 (1993), pp. 1523–1551. DOI: [10.1080/07373939308916918](https://doi.org/10.1080/07373939308916918).
- [Swe+17] T. Sweijen *et al.* "Grain-scale modelling of swelling granular materials; application to super absorbent polymers". In: *Powder Technology* 318 (2017), pp. 411–422. DOI: [10.1016/j.powtec.2017.06.015](https://doi.org/10.1016/j.powtec.2017.06.015).
- [Tab03] A. Tabatabaefar. "Moisture-dependent physical properties of wheat". In: *International Agrophysics* 17.4 (2003), pp. 207–211.

- [TA15] A. Tengattini and E. Andò. “Kalisphera: an analytical tool to reproduce the partial volume effect of spheres imaged in 3D”. In: *Measurement Science and Technology* 26.9 (2015), p. 095606. DOI: [10.1088/0957-0233/26/9/095606](https://doi.org/10.1088/0957-0233/26/9/095606).
- [Ten+20] A. Tengattini *et al.* “NeXT-Grenoble, the Neutron and X-ray tomograph in Grenoble”. In: *Nuclear Instruments and Methods in Physics Research Section A: Accelerators, Spectrometers, Detectors and Associated Equipment* 968 (2020), p. 163939. DOI: [10.1016/j.nima.2020.163939](https://doi.org/10.1016/j.nima.2020.163939).
- [Ten+21] A. Tengattini *et al.* “Neutron imaging for geomechanics: A review”. In: *Geomechanics for Energy and the Environment* 27 (2021), p. 100206. DOI: [10.1016/j.gete.2020.100206](https://doi.org/10.1016/j.gete.2020.100206).
- [Tör+21] E. Törnquist *et al.* “Dual modality neutron and x-ray tomography for enhanced image analysis of the bone-metal interface”. In: *Physics in Medicine & Biology* 66.13 (2021), p. 135016. DOI: [10.1088/1361-6560/ac02d4](https://doi.org/10.1088/1361-6560/ac02d4).
- [Tre+06] E. Trezza *et al.* “Rapid phase-compositional assessment of lipid-based food products by time domain NMR”. In: *Magnetic resonance in chemistry* 44.11 (2006), pp. 1023–1030. DOI: [10.1002/mrc.1893](https://doi.org/10.1002/mrc.1893).
- [Tud+17] E. Tudisco *et al.* “An extension of digital volume correlation for multimodality image registration”. In: *Measurement Science and Technology* 28.9 (2017), p. 095401. DOI: [10.1088/1361-6501/aa7b48](https://doi.org/10.1088/1361-6501/aa7b48).
- [van+07] J. P. van Duynhoven *et al.* “A rapid benchtop NMR method for determination of droplet size distributions in food emulsions”. In: *European journal of lipid science and technology* 109.11 (2007), pp. 1095–1103. DOI: [10.1002/ejlt.200700019](https://doi.org/10.1002/ejlt.200700019).
- [van+10] J. van Duynhoven *et al.* “Time-domain NMR applied to food products”. In: *Annual reports on NMR spectroscopy*. Vol. 69. Elsevier, 2010, pp. 145–197. DOI: [10.1016/S0066-4103\(10\)69003-5](https://doi.org/10.1016/S0066-4103(10)69003-5).
- [Veg+22] I. Vego *et al.* “Effect of high relative humidity on a network of a water-sensitive particles (couscous) as revealed by in-situ x-ray tomography”. In: *Soft Matter* (2022). DOI: [10.1039/D2SM00322H](https://doi.org/10.1039/D2SM00322H).
- [VH12] G. Viggiani and S. A. Hall. “Full-field measurements in experimental geomechanics: historical perspective, current trends and recent results”. In: *ALERT Doctoral School* (2012), pp. 3–68.
- [VS91] L. Vincent and P. Soille. “Watersheds in digital spaces: an efficient algorithm based on immersion simulations”. In: *IEEE Transactions on Pattern Analysis & Machine Intelligence* 13.06 (1991), pp. 583–598. DOI: [10.1109/34.87344](https://doi.org/10.1109/34.87344).
- [Vir+20] P. Virtanen *et al.* “SciPy 1.0: Fundamental Algorithms for Scientific Computing in Python”. In: *Nature Methods* 17 (2020), pp. 261–272. DOI: [10.1038/s41592-019-0686-2](https://doi.org/10.1038/s41592-019-0686-2).
- [Wah+08] M. Wahl *et al.* “Understanding powder caking: Predicting caking strength from individual particle contacts”. In: *Powder technology* 188.2 (2008), pp. 147–152. DOI: [10.1016/j.powtec.2008.04.062](https://doi.org/10.1016/j.powtec.2008.04.062).
- [WH54] A. Wexler and S. Hasegawa. “Relative Humidity-Temperature Relationships of Some Saturated Salt Solutions in the Temperature”. In: *Journal of research of the National Bureau of standards* 53.1 (1954), pp. 19–26. DOI: [10.6028/JRES.053.003](https://doi.org/10.6028/JRES.053.003).

- [Wie+17] M. Wiebicke *et al.* "On the metrology of interparticle contacts in sand from x-ray tomography images". In: *Measurement Science and Technology* 28.12 (2017), p. 124007. DOI: [10.1088/1361-6501/aa8dbf](https://doi.org/10.1088/1361-6501/aa8dbf).
- [WS13] D. Wildenschild and A. P. Sheppard. "X-ray imaging and analysis techniques for quantifying pore-scale structure and processes in subsurface porous medium systems". In: *Advances in Water resources* 51 (2013), pp. 217–246. DOI: [10.1016/j.advwatres.2012.07.018](https://doi.org/10.1016/j.advwatres.2012.07.018).
- [WB60] P. W. Winston and D. H. Bates. "Saturated solutions for the control of humidity in biological research". In: *Ecology* 41.1 (1960), pp. 232–237. DOI: [10.2307/1931961](https://doi.org/10.2307/1931961).
- [You67] J. F. Young. "Humidity control in the laboratory using salt solutions—a review". In: *Journal of Applied Chemistry* 17.9 (1967), pp. 241–245. DOI: [10.1002/jctb.5010170901](https://doi.org/10.1002/jctb.5010170901).
- [Zaf+17] U. Zafar *et al.* "A review of bulk powder caking". In: *Powder Technology* 313 (2017), pp. 389–401. DOI: [10.1016/j.powtec.2017.02.024](https://doi.org/10.1016/j.powtec.2017.02.024).

Grenoble,
February 3, 2023

Sub: Doctoral thesis “Multi-modal investigation of hygroscopic granular media at high relative humidity” – Paper editing and resubmission commitment

To Whom It May Concern,

In case of acceptance of the two unpublished papers included in this doctoral thesis:

- “Heterogeneous swelling of couscous particles exposed to a high relative humidity air, as revealed by TD-NMR and X-ray tomography”;
- “The influence of water sorption on the microstructure of a hygroscopic granular material (couscous) deduced from simultaneous neutron and x-ray tomography”;

I hereby declare my commitment to edit and resubmit their manuscripts, in agreement with peer reviews.

Sincerely,



Ilija Vego

Ph.D. Candidate

Laboratoire 3SR

Université Grenoble Alpes (France)

Grenoble,
02-02-2023

Subject: Author contributions to the article

To whom it may concern,

I hereby acknowledge that the *Author Contributions* statement in the articles:

- “The effect of high relative humidity on a network of water-sensitive particles (couscous) as revealed by *in situ* X-ray tomography”;
- “Heterogeneous swelling of couscous particles exposed to a high relative humidity air, as revealed by TD-NMR and X-ray tomography”;
- “The influence of water sorption on the microstructure of a hygroscopic granular material (couscous) deduced from simultaneous neutron and x-ray tomography”;

follows the *CRedit* (Contributor Roles Taxonomy) convention and corresponds realistically to the authors contribution to the article.

Sincerely,



Alessandro Tengattini
A. Professor UGA, Laboratoire 3SR, alessandro.tengattini@3sr-grenoble.fr
Instrument Responsible for NeXT-Grenoble, ILL tengattini@ill.fr
+33 (0) 4 57 42 80 50

Lausanne, Switzerland,
03/02/2023

Subject: Author contributions to the article

To whom it may concern,

I hereby acknowledge that the *Author Contributions* statement in the articles:

- “The effect of high relative humidity on a network of water-sensitive particles (couscous) as revealed by *in situ* X-ray tomography”;

follows the *CRedit* (Contributor Roles Taxonomy) convention and corresponds realistically to the authors contribution to the article.

Sincerely,

A handwritten signature in black ink that reads "Edward Andò". The script is cursive and fluid, with the first letter of each name being capitalized and prominent.

Dr. Edward Andò
EPFL Center for Imaging
edward.ando@epfl.ch

Laboratoire 3SR, Grenoble (FRANCE)
01/02/2023

Subject: Author contributions to the article

To whom it may concern,

I hereby acknowledge that the *Author Contributions* statement in the articles:

- “The effect of high relative humidity on a network of water-sensitive particles (couscous) as revealed by *in situ* X-ray tomography”;
- “The influence of water sorption on the microstructure of a hygroscopic granular material (couscous) deduced from simultaneous neutron and x-ray tomography”;

follows the *CRedit* (Contributor Roles Taxonomy) convention and corresponds realistically to the authors contribution to the article.

Sincerely,



Dr Lenoir Nicolas
Laboratoire 3SR (CNRS)
1270 Rue de la Piscine, 38610 Gières (FRANCE)
nicolas.lenoir@3sr-grenoble.fr



Gioacchino (Cino) VIGGIANI

Laboratoire 3SR (Sols, Solides, Structures, Risques)

Tél. +33 (0)4 76 82 70 38

fax. +33 (0)4 76 82 70 00

E-mail : cino.viggiani@3sr-grenoble.fr



Grenoble, February 1st, 2023

Subject: Author contributions to the article

To whom it may concern,

I hereby acknowledge that the *Author Contributions* statement in the articles:

- “The effect of high relative humidity on a network of water-sensitive particles (couscous) as revealed by *in situ* X-ray tomography”;
- “The influence of water sorption on the microstructure of a hygroscopic granular material (couscous) deduced from simultaneous neutron and x-ray tomography”;

follows the *CRedit* (Contributor Roles Taxonomy) convention and corresponds realistically to the authors contribution to the article.

Sincerely,

Prof. Gioacchino (Cino) Viggiani, Ph.D.

Professor of Civil Engineering and Geomechanics at UGA

cino.viggiani@3sr-grenoble.fr

Wageningen,
01-Feb-2023

Subject: Author contributions to the article

To whom it may concern,

I hereby acknowledge that the *Author Contributions* statement in the article:

- “Heterogeneous swelling of couscous particles exposed to a high relative humidity air, as revealed by TD-NMR and X-ray tomography”;

follows the *CRedit* (Contributor Roles Taxonomy) convention and corresponds realistically to my contribution to the article.

Sincerely,

A handwritten signature in black ink, appearing to be 'Richard T. Benders', written over the word 'Sincerely,'.

Richard T. Benders
Wageningen University – Physical Chemistry and Soft Matter
Stippeneng 4, 6708 WE, Wageningen, The Netherlands
richard.benders@wur.nl

Wageningen,
02/February/2023

Subject: Author contributions to the article

To whom it may concern,

I hereby acknowledge that the *Author Contributions* statement in the article:

- “Heterogeneous swelling of couscous particles exposed to a high relative humidity air, as revealed by TD-NMR and X-ray tomography”;

follows the *CRedit* (Contributor Roles Taxonomy) convention and corresponds realistically to the authors contribution to the article.

Sincerely,

A handwritten signature in black ink, appearing to be 'Frank Vergeldt', with a long horizontal flourish extending to the right.

Frank Vergeldt
Laboratory of Biophysics, Wageningen University & Research
Stippeneng 4, 6708 WE Wageningen, The Netherlands
frank.vergeldt@wur.nl

Wageningen
3 Feb 2023

Subject: Author contributions to article

To whom it may concern,

I hereby acknowledge that the *Author Contributions* statement in the article:

- “Heterogeneous swelling of couscous particles exposed to a high relative humidity air, as revealed by TD-NMR and X-ray tomography”;

follows the *CRedit* (Contributor Roles Taxonomy) convention and corresponds realistically to the authors contribution to the article.

Sincerely,

A handwritten signature in black ink, appearing to be 'J.A. Dijkman', with a long horizontal line extending to the right.

Dr. Joshua A. Dijkman
University of Amsterdam
Science Park 904
1098 XH Amsterdam
j.a.dijkman@uva.nl

Wageningen University
Helix, 124
Stippeneng 4
6708 WE
Wageningen

Wageningen,
01/Feb/2023

Subject: Author contributions to the article

To whom it may concern,

I hereby acknowledge that the *Author Contributions* statement in the article:

- “Heterogeneous swelling of couscous particles exposed to a high relative humidity air, as revealed by TD-NMR and X-ray tomography”;

follows the *CRedit* (Contributor Roles Taxonomy) convention and corresponds realistically to the authors contribution to the article.

Sincerely,

A handwritten signature in blue ink, appearing to be 'J. van Duynhoven', written in a cursive style.

Prof Dr John van Duynhoven
Wageningen University, Unilever
Wageningen, The Netherlands
John.vanDuynhoven@wur.nl